UNIVERSIDADE
BEIRA INTERIOR

Multifunctional Advanced Ceramics for Aeronautical and Aerospace Applications

Study of $MgO–Al_2O_3$, $MgO–CaZrO_3$, and YSZ Ceramic Composites

Kateryna Oleksandrivna Shvydyuk

Dissertação para obtenção do Grau de Mestre em
Engenharia Aeronáutica
(mestrado integrado)

Orientador: Prof. Doutor Abílio Manuel Pereira da Silva
Co-orientador: Prof. Doutor João Nunes Pereira
Co-orientador: Prof. Doutor Frederico Rodrigues

Covilhã, outubro de 2022

Declaração de Integridade

Eu, Kateryna Oleksandrivna Shvydyuk, que abaixo assino, estudante com o número de inscrição a37708 de/o Mestrado Integrado em Engenharia Aeronáutica da Faculdade de Engenharia, declaro ter desenvolvido o presente trabalho e elaborado o presente texto em total consonância com o **Código de Integridades da Universidade da Beira Interior**.

Mais concretamente afirmo não ter incorrido em qualquer das variedades de Fraude Académica, e que aqui declaro conhecer, que em particular atendi à exigida referenciação de frases, extratos, imagens e outras formas de trabalho intelectual, e assumindo assim na íntegra as responsabilidades da autoria.

Universidade da Beira Interior, Covilhã 07/10/2022

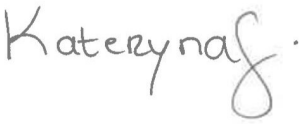

Everything that is not forbidden by laws of nature is achievable, given the right knowledge.

— David Deutsch, *The Beginning of Infinity*

Allow me to defend myself. I agree that man is preeminently a creative animal, predestined to strive consciously for an object and to engage in engineering that is, incessantly and eternally to make new roads, wherever they may lead.

— Fyodor Dostoevsky, *Notes from the Underground*

careful poetry
and careful
people
last
only long
enough
to
die
safely

— Charles Bukowski, *Bone Palace Ballet*

Acknowledgements

This dissertation is dedicated to everyone that, directly or indirectly, got involved throughout the attainment of this work, leaving me forever indebted and grateful.

First and foremost, I would like to express my sincerest appreciation to my supervisor, Prof. Abílio Silva, without whom I could not have undertaken this journey, for his tireless support, availability, tranquility, empathy, intellectual solidarity, and material security that made this work possible. My profound *thank you* for teaching me the knowledge of material science during these last months, which motivated me to continuously do my utmost, to fairly represent, the trust and opportunity given to me, to work with such an enthusiastic person in his field of proficiency.

This endeavor would also not have been possible without the incessant raising of precious points of view and discussions, as well as encouragement, to seek knowledge beyond the borders of my field of study and comfort zone, by Prof. João Nunes Pereira, thereby, I am forever grateful for his incentive, forbearance, and positivity.

Additionally, words cannot express my gratitude to Prof. Frederico Rodrigues for his generously provided knowledge and expertise, assistance, as well as thoughtfulness in carefully guiding me in the field of plasma actuators, without whom I would not have had the opportunity to learn, absorb and comprehend the topic, therefore, my deepest appreciation for the prompt availability, ceaseless feedback, and unlimited support.

I would like to extend my sincere thanks to the Centre for Mechanical and Aerospace Science and Technologies (C–MAST) for providing me with the laboratory resources, equipment, and raw materials, in addition to supporting me with rendered services.

Moreover, getting through this dissertation required more than academic support, thus I would like to express my gratitude, for providing a dynamic, cheerful, and wonderful working environment, where help was never denied, to my colleagues and friends, of the Material Science Laboratory, Ana Luísa Carvalho, Duarte Macedo, Paulo Santos, and João Parente.

I take this opportunity to namely show my gratitude to all of the closest people to me for their love, patience, and support. A big and warm *thank you* to my friends for their absolute and unbreakable friendship, and to my family for giving me the strength, means, and opportunity to undergo this fantastic journey in the city of Covilhã.

Resumo

A premissa de que os materiais são elementos essenciais e que moldam todos os aspetos do nosso dia-a-dia é bem reconhecida. A procura incansável das últimas décadas pelo aumento de desempenho nas indústrias de aeronáutica e aeroespacial forneceu uma força motriz sólida para o estudo, pesquisa e investigação das cerâmicas avançadas para inúmeras aplicações futuras. Acredita-se que o campo das cerâmicas avançadas seja uma tecnologia estimulante com potencial para fornecer contribuições de alto valor por forma a assegurar as necessidades e desafios futuros. Além disso, a indústria da cerâmica avançada é preconizada como sendo uma indústria significativamente distinta devido à sua diversidade característica e natureza interdisciplinar. Como consequência, um número elevado de diferentes metodologias de processamento, assim como uma ampla variedade de aplicações são parte integrante deste sector. Desta forma, esta dissertação teve como objetivo a realização de uma extensa e abrangente pesquisa de revisão de literatura, juntamente com a seleção, fabricação, teste e análise dos compósitos cerâmicos $MgO-Al_2O_3$, $MgO-CaZrO_3$ e YSZ que por sua vez se destinam a satisfazer a condição de cerâmica multifuncional nas áreas aeronáutica e aeroespacial. Para a concretização deste objetivo, sistemas de proteção térmica, revestimentos de barreira térmica e aplicações de atuadores a plasma de descarga de barreira dielétrica foram considerados e adotados como um ponto de partida. Uma abordagem sequencial foi empregue para a execução do procedimento experimental. Mais precisamente, inicialmente, as amostras de compósitos cerâmicos $MgO-Al_2O_3$, $MgO-CaZrO_3$ e YSZ foram fabricadas através de um processo subdividido em quatro etapas, isto é, preparação do material, processamento, sinterização e acabamento. Após a obtenção das diversas amostras, isto é, placas retangulares, barras e discos cerâmicos, para as três composições referidas, prosseguiu-se com o estudo das mesmas através da caracterização e análise das propriedades microestruturais, físicas, mecânicas, térmicas e elétricas. Em suma, conclui-se que muitas cerâmicas avançadas são na sua essência multifuncionais e, portanto, predestinadas a promover a resolução dos futuros desafios quer tecnológicos, assim como de engenharia. Por último, com o desenvolvimento desta dissertação, defende-se que as cerâmicas avançadas oferecem um proeminente potencial ainda por ser explorado com o auxílio do conhecimento da ciência dos materiais, ou seja, por meio de correlações entre características microestruturais, físicas, mecânicas, térmicas e elétricas.

Palavras–chave

Cerâmicas Avançadas Multifuncionais, Sistemas de Proteção Térmica, Revestimentos de Barreira Térmica, Atuadores a Plasma de Barreira Dielétrica de Descarga, Compósitos Cerâmicos, $MgO-Al_2O_3$, $MgO-CaZrO_3$, YSZ

Abstract

The premise that materials permeate all aspects of our day-a-day lives is well established. The relentless pursuit for increased performance in aeronautical and aerospace industries over the last decades has provided a solid driving force for the study, research, and investigation of advanced ceramics for numerous future investments. The advanced ceramics field is believed to be an enabling technology with the potential to deliver high-value contributions for meeting both future needs and challenges. Moreover, the advanced ceramics industry is quite distinctive due to its high diversity and interdisciplinary nature that encompasses an engaging number of different processing methodologies and a variety of applications. In this sense, this dissertation project focused to perform an extensive and comprehensive literature review research, in addition to further selection, fabrication, testing, and analysis of $MgO-Al_2O_3$, $MgO-CaZrO_3$, and YSZ ceramic materials which are intended to satisfy the condition of advanced multifunctional ceramic in the aeronautical and aerospace fields. Within this framework of thought, thermal protection systems, thermal barrier coatings, and dielectric barrier discharge plasma actuator applications were perceived and adopted as a jumping-off point. A step–by–step approach was adopted for the experimental procedure. More precisely, initially, ceramic composite$MgO-Al_2O_3$, $MgO-CaZrO_3$, and YSZ samples were manufactured through a four stages process, i.e., material preparation, processing, sintering, and finishing. After the rectangular plates, bars, and disc specimens were obtained for the three referred compositions, the in-depth study under the microstructural, physical, mechanical, thermal, and electrical characterization followed. Ultimately, many fine ceramics are multifunctional and therefore predestined to solve the forthcoming technological and engineering challenges. It is believed that ceramics offer an enormous potential to be exploited with the knowledge of material science, i.e., through correlations between microstructural, physical, mechanical, thermal, and electrical features.

Keywords

Multifunctional Advanced Ceramic, Thermal Protection System, Thermal Barrier Coating, Dielectric Barrier Discharge Plasma Actuator, Ceramic Composites, $MgO-Al_2O_3$, MgO-$CaZrO_3$, YSZ

Table of Contents

List of Figures

List of Tables

Acronyms and Abbreviations

3D MAT Three–Dimensional Multifunctional Ablative Thermal Protection System

AC Alternate Current

AC–SDBD Alternating–Current Surface Dielectric Barrier Discharge

AFM Atomic Force Microscopy

APS Atmospheric Plasma Spraying

APTD Atmospheric Pressure Townsend Discharge

ASTM American Society for Testing and Materials

AVCO Aviation Corporation

AVCOAT Coating by Aviation Corporation

BSE Back Scattered Electron

CDBD Coplanar Dielectric Barrier Discharge

CMAS Calcium–Magnesia–Alumina–Silicate

CMC Ceramic Matrix Composite

CNT Carbon Nanotube

CTE Coefficient of Thermal Expansion

CVI Chemical Vapor Infiltration

DBD Dielectric Barrier Discharge

DCS Differential Scanning Calorimetry

DTA Differential Thermal Analysis

EBC Environmental Barrier Coating

EB–PVD Electron–Beam Physical Vapor Deposition

EDA European Defense Agency

EHD Electrohydrodynamic

FEM Finit Element Method

FOD Foreign Object Damage

GCMC Graphene Ceramic Matrix Composite

GE	General Electric
HT	Hot Pressing
ICDD	International Center for Diffraction Data
ICTAC	International Confederation of Thermal Analysis and Calorimetry
IET	Impulse Excitation Technique
ISO	International Standardization Organization
ITPS	Integrated Thermal Protection Systems
JCPDS	Joint Committee on Powder Diffraction Standards
LDA	Laser Diffraction Analysis
LFA	Laser Flash Analysis
LHA	Lanthanum Hexaaluminate
LPPS	Low Pressure Plasma Spraying
LTCC	Low Temperature Co-Fired Ceramics
LVDT	Linear Variable Differential Transformer
LWC	Liquid Water Content
MS	Mega Sample
MI	Melt Infiltration
NACA	National Advisory Committee For Aeronautics
NBS	National Bureau Of Standards
ND–DBD	Nanosecond–DBD
nSDBD	Nanosecond Pulse Surface Dielectric Barrier Discharge
NTP	Non Thermal Plasmas
OM	Optical Microscope
PAPS	Protective Atmosphere Plasma Spraying
PDF	Power Diffraction Files
PIB	Poly–Isobutylene
PICA	Phenolic–Impregnated Carbon Ablator

PIP	Polymer Impregnation and Pyrolysis
PIXEL	Picure Element
PLA	Polylactic Acid
PMMA	Polymethyl Methacrylate
PS	Plasma-Sprayed
PSD	Particle Size Distribution
PVC	Polyvinyl Chloride
RE	Rare–Earth
SD	Standard Deviation
SDBD	Surface Dielectric Barrier Discharge
SE	Secondary Electron
SEM	Scanning Electron Microscope
SIRCA	Silicone–Impregnated Reusable Ceramic Ablator
SLA	Super Lightweight Ablators
SOEC	Solid Oxide Electrolysis Cells
SOFC	Solid Oxide Fuel Cell
SPPS	Solution Precursor Plasma Spraying
TA	Thermal Analysis
TBC	Thermal Barrier Coating
TGA	Thermo Gravimetric Analysis
TGO	Thermally Grown Oxide
TMA	Thermo Mechanical Analysis
TPS	Thermal Protection System
UDP	Uniaxial Die Pressing
UHTC	Ultra–High Temperature Ceramic
UHTCMC	Ultra High Temperature Ceramic Matrix Composite
UV	Ultraviolet radiation

USA United States of America

VAMAS Versailles Project on Advanced Materials and Standards

VDBD Volume Dielectric Barrier Discharge

VPS Vacuum Plasma Spraying

XRD X–Ray Diffraction

XRF X–Ray Fluorescence

YSZ Yttria-Stabilized Zirconia

Symbols

Chemical Symbols

$\mathbf{3\,Al_2O_3{\cdot}2\,SiO_2}$	Mullite
$\mathbf{Al_2O_3}$	Aluminum Oxide, or Alumina
AlN	Aluminum Nitride
$\mathbf{B_4C}$	Boron Carbide
Ba	Barium
$\mathbf{Ba(Mg_{1/3}Ta_{2/3})O_3}$	Complex form of perovskite compounds
$\mathbf{BaLa_2Ti_3O_{10}}$	Complex form of perovskite compounds
$\mathbf{BaZrO_3}$	Barium Zirconate
BN	Boron Nitride
C	Carbon
Ca	Calcium
CaO	Calcium Oxide
$\mathbf{CaZrO_3}$	Calcium Zirconate
Ce	Cerium
$\mathbf{Ce_2Zr_2O_7}$	Cerium Zirconium Oxide
Co	Cobalt
Cr	Chromium
Fe	Iron
Gd	Gadolinium
$\mathbf{Gd_2O_3}$	Gadolinium (III) Oxide
$\mathbf{Gd_2Zr_2O_7}$	Gadolinium Zirconate, or GZ
Hf	Hafnium
$\mathbf{HfB_2}$	Hafnium Diboride
HfC	Hafnium Carbide

HfO_2	Hafnium (IV) Oxide, Hafnium Dioxide, or Hafnia
La	Lanthanum
$La(Al_{1/4}Mg_{1/2}Ta_{1/4})O_3$	Complex form of perovskite compounds
$La_2(Zr_{0.7}Ce_{0.3})_2O_7$	Pyrochlore Oxide compound, LZ7C3
$La_2Hf_2O_7$	Dilanthanum Dihafnate (IV)
La_2O_3	Lanthanum Oxide, or Lanthana
$La_2Zr_2O_7$	Lanthanum Zirconate, or LZ
$LaMgAl_{11}O_{19}$	LHA compound, also named LaMa, or LMA
$LaTi_2Al_9O_{19}$	LHA compound
$LaZnAl_{11}O_{19}$	LHA compound
Mg	Magnesium
$MgAl_2O_4$	Magnesium Aluminum Oxide, or Magnesium Aluminate
MgO	Magnesium Oxide
Mn	Manganese
Mo	Molybdenum
$MoSi_2$	Molybdenum Disilicide
Nb	Niobium
Nd	Neodymium
Nd_2O_3	Neodymium (III) Oxide
$Nd_2Zr_2O_7$	Neodymium Zirconate
Ni	Nickel
Pt	Platinum
Re	Rhenium
Sc_2O_3	Scandium (III) Oxide, or Scandia
Si_3N_4	Silicon Nitride
SiC	Silicon Carbide
Sm	Samarium

$\mathbf{Sm_2FeTaO_7}$	Pyrochlore compound
$\mathbf{Sm_2O_3}$	Samarium (III) Oxide
$\mathbf{Sm_2Ti_2O_7}$	Samarium Dititanium Oxide
Sr	Strontium
$\mathbf{SrZrO_3}$	Strontium Zirconate
Ta	Tantalum
TaC	Tantalum Carbide
Ti	Titanium
$\mathbf{TiB_2}$	Titanium Diboride
TiC	Titanium Carbide
$\mathbf{TiO_2}$	Titanium Dioxide
Y	Yttrium
$\mathbf{Y_2O_3}$	Yttrium (III) Oxide, or Yttria
$\mathbf{Yb_2O_3}$	Ytterbium (III) Oxide
Zn	Zinc
Zr	Zirconium
$\mathbf{ZrB_2}$	Zirconium Diboride
ZrC	Zirconium Carbide
$\mathbf{ZrO_2}$	Zirconium Dioxide, or Zirconia
$\alpha-\mathbf{Al_2O_3}$	α–Alumina
$\gamma-\mathbf{Al_2O_3}$	γ–Alumina

Other Symbols

Latin Symbols

a	Thermal Diffusivity
b	Width
c	Constant (related to the elastic behavior of a material)
C	Capacitance
c_c	Average Length of the Diagonal Cracks
C_d	Diametrical Linear Contraction
c_p	Specific Heat Capacity
d	Thickness
D	Dry Weight
d_{50}	Particle Size at 50 % Percentile
d_{90}	Particle Size at 90 % Percentile
d_c	Average Length of the Diagonals
d_i	Initial Diameter
d_f	Final Diameter
d_p	Distance between Lattice Planes
E	Young's Modulus
E_P	Energy (of a particle of light)
E_{th}	Theoretical Young's Modulus
G	Shear Modulus
G_{th}	Theoretical Shear Modulus
h	Planck's Constant
HV	Vickers Hardness
i	Phase Element
I	Current
k	Calibration Coefficient
K_c	Fracture Toughness

l	Length
L	Outer Support Span Length
L^{ref}	Reference Material Length
L^{spec}	Specimen Length
m	Mass
n	Number (of)
P	Porosity
P_{el}	Power
P_l	Load Applied
px	Pixel
q	Charge
R	Resistance
S	Suspended Weight
S_d	Diametrical Linear Contraction
sin	Sine Function
t	Time
t_{50}	Half–Minimum
T	Temperature
T^{ref}	Reference Material Temperature
T^{spec}	Specimen Temperature
v	Frequency
V	Voltage
V_b	Breakdown Voltage
V_{ext}	Exterior Volume
v_i	Volume Fraction
W	Sutured Weight
w_i	Mass Fraction
x_i	Molar Fraction

x/l	Spacial Variation (x–axis)
y/w	Spacial Variation (y–axis)

Greek Symbols

α_m	Coefficient of Linear Thermal Expansion
α_{ma}	Coefficient of Linear Thermal Expansion in the x–direction
α_{mb}	Coefficient of Linear Thermal Expansion in the y–direction
α_{mc}	Coefficient of Linear Thermal Expansion in the z–direction
α^{ref}	Mean Coefficient of Linear Thermal Expansion for Reference Material
λ	Thermal Conductivity
λ_w	Wavelength of X–rays
ρ	Density
ρ_{th}	Theoretical Density
ρ_a	Apparent Density
ρ_b	Bulk Density
ρ_r	Relative Density
σ	Flexural Strength
σ_m	Linear Thermal Capacity
θ	Reflected Angle
ε	Strain
Δ	Variation

Chapter 1

Introduction

This chapter will focus on providing an overview of the importance of the ceramic materials in the aeronautical and aerospace industries with special emphasis on the advanced ceramics and their ability to fulfill extreme and differentiating application requirements. The motivation behind this work, its objectives and the documentation organization will all be mentioned and described as well.

1.1 Motivation

Nowadays, in material science and engineering, it is possible to identify four major classes of materials which are characterized and distinguished by the nature of their chemical bonding: metals, polymers, ceramics, and composites [1, 2].

The premise that materials permeate all aspects of our day-a-day lives is well accepted. The continuous research and investigation of atomic and molecular structures, as well as their understanding not only allows scientists to improve already existing materials, but also develop new and advanced ones. Therefore, interesting opportunities arise for meeting challenging requirements for different applications fields.

From an historical point of view, ceramics are the oldest man-made materials, dating back to the dawn of human civilization. While naturally available *ceramics*, such as hard rock and flint, were used for production of tools, with the advent of fire, soft and pliable clay, and loam raw materials, were changed eventually into hard, durable shapes that served as liquids recipient, storage containers as well as terracotta [1, 3]. Consequently, since ancient times the technology and applications of ceramics have been increasing and contributing to the progress of society. These materials possess an overwhelmingly wide variety regarding their origin, history, utilization, and properties. **Figure 1.1** shows the evolution and importance of the different classes of materials, namely ceramics.

Defining ceramics is not straightforward nor an easy task. Describing exactly what the term “ceramic” means is challenging since it strongly depends on the point of view that is being considered. The term will have different interpretations for a historian, a scientist, an engineer, or a manufacturer [4]. Despite what was mentioned before, there seems to be an agreement in the division between the so-called *traditional ceramics* and the *advanced ceramics*. Traditional ceramics are characterized by mostly silicate-based, porous microstructures that are quite coarse, nonuniform and multiphase; whilst advanced ce-

ramics are known for being crystalline materials of rigorously controlled composition and manufactured with detailed regulation from highly refined and characterized raw materials [5].

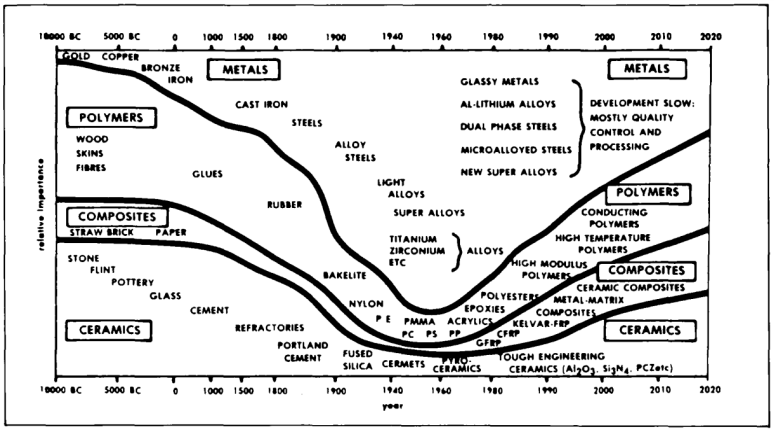

Figure 1.1: Historical evolution and applications of different existing material types [2].

Advanced ceramics may also be denominated as *high-performance ceramics*, *high-tech ceramics*, *engineering ceramics*, *fine ceramics*, and *technical ceramics*. They are recognized by their outstanding higher physical and mechanical properties, as well as great potential for use in sound, magnetism, heat, electricity, light, and other applications [5, 3]. **Figure 1.2** represents three levels of hierarchical triangles relating different groups of materials where level 1 consists of materials supergroups (metals, polymers, ceramics), level 2 regards ceramics *sensu lato* (glasses, hydraulic ceramics, ceramic *sensu strictu*), and, finally, level 3 represents ceramic subgroups formed by advanced oxide ceramics, non-oxide ceramics and classic silicate ceramics [1].

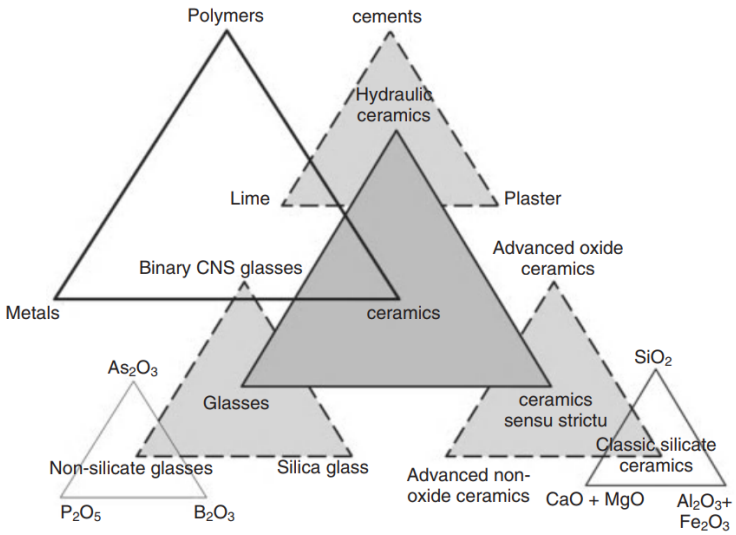

Figure 1.2: Different groups of materials and their relationship [1].

In concern to aeronautical and aerospace engineering, there are many properties of advanced ceramics-based materials that do them appealing. Modern advanced structures and components intended for these industries consist of highly complex geometries which require the use of materials capable of handling the extreme range of environmental conditions for an extended diversity of applications. The available metal alloys and conventional composites based on reinforced polymers can no longer meet these rising requirements for new applications. Consequently, a shift is being noticed to the use of ceramics that exhibit superior performances, reliability, and lifespan over those that are shown by the metal alloys [6]. Characteristics of ceramics such as their relatively low-density, high temperature resistance, electrical insulation, resistance to corrosion, chemical stability, wear resistance and ability to withstand vibration are all extremely desirable in this field of engineering. The main applications of ceramics in the aeronautical and aerospace industry, just to name a few, consist in components of engines and exhaust systems brakes, insulation tiles in space vehicles and nose cones, as well as high-temperature coatings in ultra-high-speed flying objects [7]. **Figures 1.3**, **1.4** and **1.5** are examples of engineered ceramics applications.

Figure 1.3 represents General Electric (GE) new ceramic matrix composite (CMC) component-assembly on the blades of a low-pressure turbine of a F414 model jet engine where some of the blades are covered with a specific yellow colored environmental barrier coating (EBC).

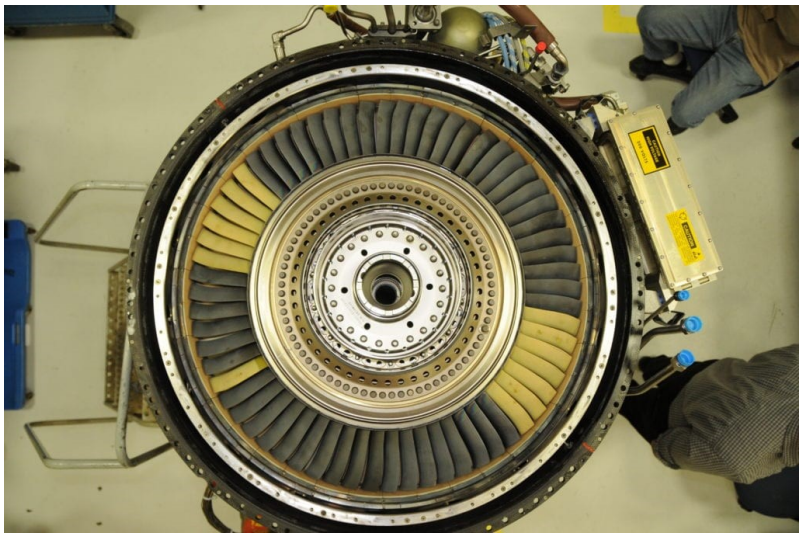

Figure 1.3: Low-pressure turbine of a F414 jet engine with blades from CMCs [8].

Figure 1.4 shows the most well-known example of heat tiles applied on the famous Space Shuttle Discovery, which served as a prevention of heat transfer to the underlying orbiter aluminum skin and vital structures not only at the time of the reentry of the vehicle in the atmosphere, but namely additional safeguard from cold temperatures of space while in orbit.

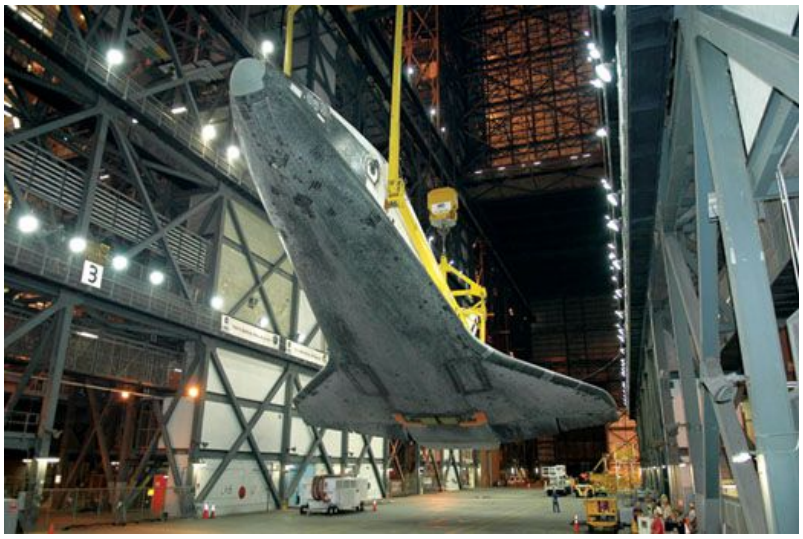

Figure 1.4: Space Shuttle Discovery heat shield tiles [9].

As a last example, **Figure 1.5** exhibits the ultra-careful and demanding process of application of ablative material to function as heat shield for the Orion spacecraft designed for the Artemis II lunar mission. This structure aims to protect the capsule itself and the astronauts inside from extremely high temperatures experienced during reentry through Earth's atmosphere.

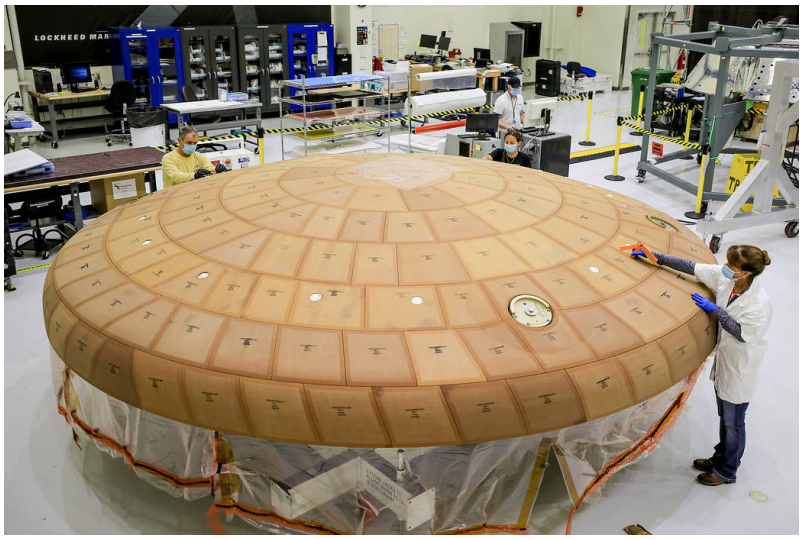

Figure 1.5: Application of 180 blocks of ablative material to serve as heat shield [10].

In summary, it is clear from the given examples the major role that ceramics play in today's world. Nevertheless, driven by the aeronautical and aerospace industries, engineers and material scientists will continue to develop new materials, processes, and applications that will take advantage of the powerful properties of the advanced ceramic materials [11].

1.2 Objectives

In this sense, this dissertation project aims to perform an extensive and comprehensive literature review research, in addition to further selection, fabrication, testing, and analysis of $MgO-Al_2O_3$, $MgO-CaZrO_3$, and YSZ ceramic composite materials which are intended to satisfy the condition of *advanced multifunctional ceramic* in the aeronautical and aerospace fields. Within this framework of thought, thermal protection systems, thermal barrier coatings, and dielectric barrier discharge plasma actuators applications were perceived and adopted as a jumping-off point.

To achieve the described objectives, the following tasks must be fulfilled:

- Overview of the global demand for ceramic materials, their wide-ranging field of application, as well as assessment of their dynamic and differentiating properties.
- Research of advanced ceramics in aeronautical and aerospace fields capable to fulfill extreme and differentiating application requirements.
- Further study, contextualization, and presentation of the state-of-art of thermal protection systems, thermal barrier coatings, and dielectric barrier discharges for plasma actuators.
- Identification, selection, and justification of adequate engineering ceramics systems for the purposes in view.
- Manufacturing of several samples, i.e., discs, bars, and plates, of $MgO-Al_2O_3$, $MgO–CaZrO_3$, and YSZ ceramic systems.
- Microstructural characterization of the ceramic composites fabricated via X–ray Diffraction, and scanning electron microscope analysis.
- Physical characterization of the ceramic composites fabricated through diametrical linear contraction, apparent porosity, in addition to bulk, apparent and relative densities.
- Mechanical characterization of the ceramic composites fabricated via dynamic Young's modulus, dynamic shear modulus, flexural strength, hardness and fracture toughness properties.
- Thermal characterization of the ceramic composites fabricated owing to thermal conductivity and coefficient of thermal expansion features.
- Proof of concept of the electrical feasibility, capability, and applicability of $MgO-Al_2O_3$, $MgO– CaZrO_3$, and YSZ ceramic systems as surface dielectric barrier discharge plasma actuator.

- Electrical characterization of the ceramic composites manufactured through electrical power consumption, capacitance via Lissajous figures, capacitance, induced flow velocities, and thermographic analysis.

- Consideration and crosscheck of the experimental results obtained with the reported in the literature by the scientific community.

1.3 Dissertation Outline

This dissertation work consists of a total of six chapters organized as follow:

- The current Chapter 1, **Introduction**, focuses on contextualizing advanced ceramics in the nowadays material science and engineering sciences. A distinction among traditional and advance ceramics is provided, as well as insight into the variety of these materials in terms of their origin, history, utilization, and properties. To conclude, an outline of the importance of ceramic materials in the aeronautical and aerospace fields is made.

- Chapter 2, **Literature Review**, consist of a brief discussion about engineering ceramics timeline evolution from a global perspective, as well as regarding their growing opportunities ascertained based on the technology foresight methodology.

- Chapter 3, **State–of–Art of Advanced Ceramics in Aeronautical and Aerospace Engineering**, offers an in–depth introduction, contextualization, and analysis, as the name itself suggests, of the state–of–art of advanced ceramics' role in three different domain of application within aeronautical and aerospace domains. Accordingly, the chapter is segmented into three main sections – 3.1 Thermal Protection Systems, 3.2 Thermal Barrier Coatings, and 3.3 Dielectric Barrier Discharges – with an additional one in which the concept of multifunctional advanced ceramic is addressed and the reasoning line of ceramic composite selection to be manufactured justified. For each main subsection, an introduction is performed to the technology topic being discussed, their corresponding brief history presented, classification systems provided, and, more importantly, a ceramic-oriented investigation and research reported to be performed by the scientific community to date described.

- Chapter 4, **Experimental Procedure**, which is divided in three section exposes the materials used, the experimental procedure for sampling manufacturing, and experimental procedure for sampling analysis. In a broad way, the selected raw powders and their corresponding characterization, step–by–step fabrication process and each testing methodology exploited are described. On top, a support explanation of the working principles of techniques announced is provided when considered necessary.

- To conclude Chapter 5, **Results and Discussion**, indicates the experimentally obtained microstructural, physical, mechanical, thermal, and electrical results. A comprehensive study and analysis of the findings achieved is acquired through illustrative charts, figures and tables. Additionally, a comparison and crosscheck with the literature is performed.
- To sum up, Chapter 6, **Conclusion and Future Work**, summarizes the conclusions reached throughout the elaboration of the present dissertation work and points out future work research guidelines.

Chapter 2

Literature Review

This chapter will start by introducing the technology foresight methodology focused on advanced ceramic materials. Followed by this brief discussion, an easy-to-analyze comparison is made between technical ceramics and other existing material in engineering, which aims to hone their full potential and areas of applications. To conclude, classification systems as well as roadmaps of evolving ceramics technology are shown.

2.1 Advanced Ceramics

Science and technology are advancing at a progressively rapid pace; hence it becomes crucial to identify, select and develop technology alternatives to satisfy future needs. *Technology foresight* is a mechanism for strategic decision making [12]. According to the European Defense Agency (EDA), "technology foresight provides a framework to think about the possible futures in a structured and constructive way. It is not about predicting a predetermined future, but about exploring how the future might evolve in different ways, depending on the actions and decisions taken today" [13]. In scope of this and within the immeasurable number of fields of application, tremendous growth opportunities for ceramics as an enabling technology is highlighted and manifold suggestions for future development of these materials come to light. In sum, advanced ceramics will have a major impact on addressing emerging key challenges in diverse domains.

A traditional definition of advanced ceramics consists in characterizing ceramics as inorganic, nonmetallic solids that are prepared from powdered materials and fabricated into products through the application of heat which display features as hardness, strength, low electrical conductivity, and brittleness.

On the other hand, advanced ceramics embody a furtherance over this previously mentioned definition. Through the employment of a modern science approach, new materials or new combinations of materials have been designed and orientated to present surprising variations on the properties traditionally ascribed to ceramics [14]. With the continuous maturing of advanced ceramics, a more detailed definition of the material originated by the 1993 Versailles Project on Advanced Materials and Standards (VAMAS), which described an advanced ceramic as "an inorganic, nonmetallic (ceramic), basically crystalline material of rigorous controlled composition and raw materials giving precise specific attributes.". Particular distinguished features of advanced ceramics are possible to withdraw from this definition: primarily, advanced ceramics tend to lack a glassy component;

then, their microstructures are highly controlled and engineered, which means that grain sizes, grain shape, porosity and phase distribution are meticulously and rigorously controlled, and additionally, advanced ceramics tend to exhibit unique and superior functional attributes that can be precisely specified by proper processing and careful quality control [14].

2.1.1 Advanced Ceramics and Other Materials

When compared to metals and some polymers, high-tech ceramics excel these materials in terms of their high temperature stability, low thermal expansion, high corrosion resistance and high hardness, as well as the variety of electrical properties offered. Despite the enumerated advantages, parameters such as fracture toughness and impact resistance of ceramics are low, driving science to the creation of transformed-toughened ceramics that show good performances even in adverse mechanical conditions [15]. **Table 2.1** gives an overview of some properties of metals, engineering plastics and advanced ceramics to illustrate their assets and weaknesses, allowing this way to perform a comparison among them.

Table 2.1: Comparison table of metals, engineering plastics and advanced ceramics [15]

Property	Metals	Engineering plastics	Advanced ceramics
Maximum temperature for continuous use (°C)			
Typical	1000	250	1200
Maximum	1500	350	2500
Hardness	Medium-high	Low-medium	High
Toughness			
Flexibility	Medium-high	High	Low
Impact resistance	High	Medium-high	Low
Corrosion resistance	Low-medium	Medium	High
Coefficient of thermal expansion	High	Medium	Low
Electrical properties	Conductive	Insulative to conductive (with fillers)[1]	Insulative to conductive
Density	High	Low	Medium

On the exposed basis, nowadays the term **advanced ceramics** refers to ceramic materials which are [15]:

- predominantly inorganic nonmetallic compounds;

[1]Adding fillers can transform plastic properties so it meets the intended use without sacrificing the qualities that made it attractive in the first place. Regarding specifically engineering plastics electrical properties, fillers lend the material electrically isolating or electrically conductive features.

- highly specialized by exploiting unique properties;
- performing outstandingly well under extreme conditions;
- capable of solving current manufacturing and use problems;
- high value-added products owing to their sophisticated processing technology;
- relatively expensive with properties and failure mechanism not yet fully understood;
- positioning at the beginning of the development cycle and not yet widely used with respect to their potential; and
- not presently profitable in terms of return investment, but with great promise for the future.

2.2 Classification Systems and Fields of Application

With respect to a high-performance ceramic division arrangement, a broad categorization system can be recognized, especially depending on the field or domain that is being considered. In general, these materials can be sorted by their function, their use or even by their atomic arrangement based on the principles of crystallography. The task becomes even more difficult since currently constantly new classes of technical ceramic materials have been fractionated to satisfy a profuse number of new emerging applications. Hence, two categories were adopted to simplify the division of advanced ceramics: one based on their application and another on their composition. From an *application* point of view, a two-subsection classification is assumed, and so these materials class is subdivided into:

- structural ceramics, and
- functional ceramics.

Advanced *structural* ceramics are conventionally best suited in mechanical, structural, tribological, thermal or chemical load applications, owing to their chemical inert nature, high compression and flexural strength, toughness, high corrosion, and thermal shock resistant as well as thermal oscillations. A consideration should be made regarding these structural ceramics during the fabrication process; this is, upon the manufacturing stage a defect free material should be obtained, which will eventually carry significant levels of load normally at high temperatures. Typical examples of these ceramics are alumina (Al_2O_3), zirconia (ZrO_2), mullite ($3\,Al_2O_3{\cdot}2\,SiO_2$), boron carbide ($B_4C$), silicon carbide (SiC) and titanium carbide (TiC), boron nitride (BN), silicon nitride (Si_3N_4) and aluminum nitride (AlN), and composites [1, 16]. Moreover, as the name suggests, the *functional* ceramics application is based on their functional capabilities ruled by microstructural effects, which involve semiconducting, piezoelectric, ferroelectric, pyroelectric, and superconducting properties. In case one desires a further categorization of this type of ceramics,

an analysis may be established on the basis of their functions, for example, mechanical, thermal, electrical, electronic, chemical, magnetic, optical, nuclear, or biological functions [1, 16]. **Table 2.2** shows some application fields, common components, and a few examples of advanced ceramics solutions to fulfill the requirements for the optimum component performance.

Table 2.2: Application fields, examples of components, properties desired and advanced ceramics alternatives for each [15]

Application field	Component	Properties utilized	Advanced ceramics
Processing technology	Chemical apparatus	Corrosion resistance	Aluminum oxide
	Sliding rings	Wear resistance	Silicon carbide
	Thread guides		Titanium oxide
	Wire-drawing dies		Zirconium oxide
Shaping of materials	Cutting tools	Wear resistance	Aluminum oxide
	Grinding disks	Hardness	Silicon nitride
	Sand-blasting nozzles		Silicon carbide Boron carbide
High temperatures	Burner nozzles	Heat resistance	Silicon nitride
	Welding nozzles	Corrosion resistance	Silicon carbide
	Heat exchanger	Heat conductivity	Aluminum oxide
	Crucibles		Carbon
	Heat pipes		Boron nitride
Engines	Valve seats	Heat resistance	Aluminum titanate
	Turbocharger	Corrosion resistance	Silicon carbide
	Gas turbine	Heat conductivity	Silicon nitride
	Catalyst support		Cordierite
	A-probe		Zirconium oxide
Electronics, electrical engineering, optics	Substrates	Special electrical and magnetic properties	Aluminum oxide
	Capacitors		Titanate perovskites
	Sensors		Ferrites
	Laser materials		
	Magnets		
Energy technology	Nuclear fuel	Radiation resistance	Uranium oxide
	Solid-state electrolyte	Ionic conductivity	Zirconium oxide
			β-Aluminum oxide
Medical technology	Hip joints	Mechanical resistance	Aluminum oxide
	Bone replacement	Surface finish	Calcium phosphate
		Biocompatibility	

On the other hand, from a *chemical* composition perspective, two classes are identified:

- oxide ceramics, and
- non-oxide ceramics.

Figure 2.1 subdivides the high-tech ceramics into *oxide ceramics*, *non-oxide ceramics*, and shows examples of specific components for each subgroup.

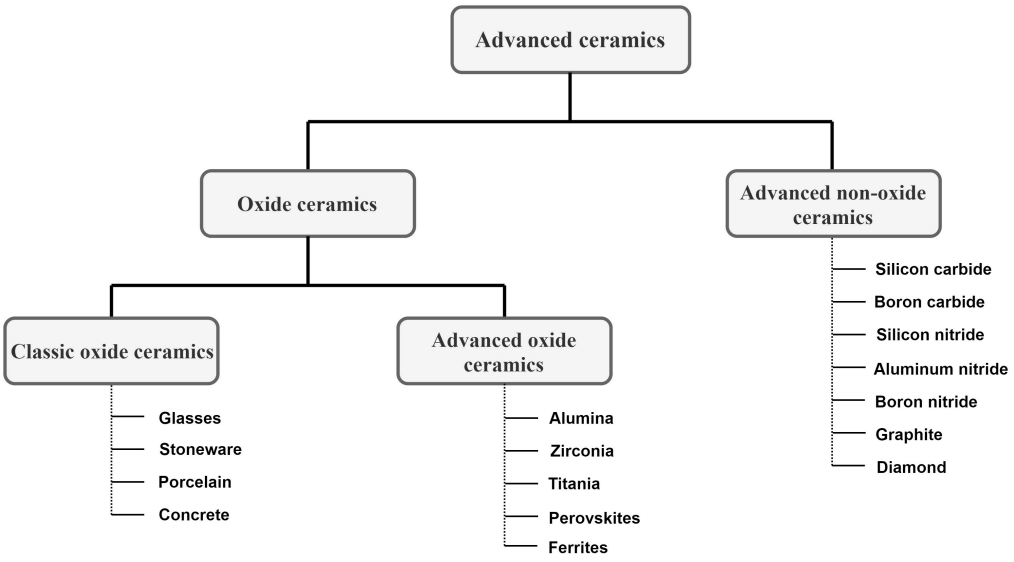

Figure 2.1: Advanced oxide and non-oxide ceramics, as well as their examples [1].

Table 2.3 presented below summarizes some important key guide properties of oxides, and non-oxides ceramics.

Table 2.3: Engineered ceramics classification by composition and their respective properties.

Technical ceramics	Properties
Oxide ceramics	Oxidation resistant
	Chemically inert
	Electrically insulating
	Generally low thermal conductivity
	Slightly complex manufacturing
Non-oxide ceramics	Low oxidation resistance
	Extreme hardness
	Chemically inert
	High thermal conductivity and electrically conducting
	Difficult energy dependent manufacturing
	High cost

As mentioned, the domain of advanced ceramics represents an important technology for a variety of industries, branches, and markets thanks to the numerous enhancements they have to offer. **Figure 2.2** represents a typical Japanese intuitive panorama of the interactions and synergetic relations of the *advanced ceramics* [15].

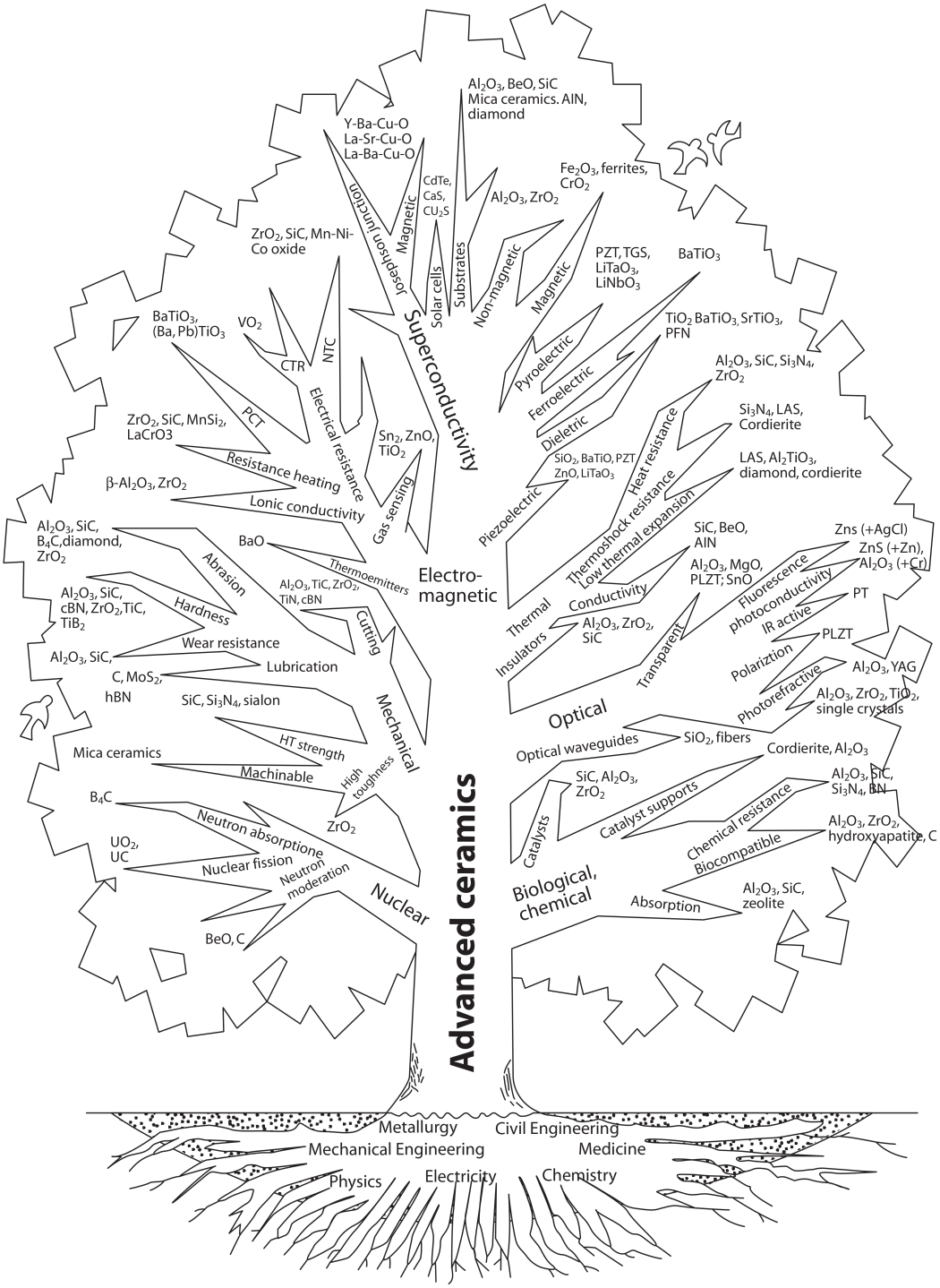

Figure 2.2: Properties and applications of fine ceramics according to a Japanese analysis methodology [15].

Overall, in the figure shown, i.e., **Figure 2.2**, the tree diagram of fine ceramics (according to the Japanese nomenclature) is divided into several phases of maturity. In other words, the advanced ceramic tree is nourished in terms of knowledge and expertise through its *roots* founded in the so designated (here) master disciplines such as physics, chemistry, mechanical engineering, electricity, metallurgy, civil engineering, and medicine. Further, from the trunk of the tree, *main branches* appear which will reunite the general properties of fields such as nuclear, mechanical, electromagnetic, thermal, optical, chemical, and biological depending on the domain that is being considered. Additionally, and in more detail, *smaller branches* are correlated to the union of secondary properties and applications, whilst finally the *leaves* of the tree symbolize examples of individual compounds adequate for tangible functions that one desires to assign to them [15].

2.3 Advanced Ceramics Timeline Evolution

The above presented scheme grants the possibility to learn that, from a global perspective, the advanced ceramics sector comprises different fields, and furthermore indicates that the continuing research and investigation of the ceramic materials, as well as the associated materials technologies is rapidly supplying more data to the knowledge bank [17]. With the aim to facilitate the visualization of the evolution of ceramic technologies, a time frame, based on "Development of a roadmap for advanced ceramics: 2010 – 2025." is followingly described. The authors proposed five roadmaps for advanced ceramics throughout the years, along with guidelines for future investments in policy makers, scientists, and industry as summarized in the scheme of **Figure 2.3**.

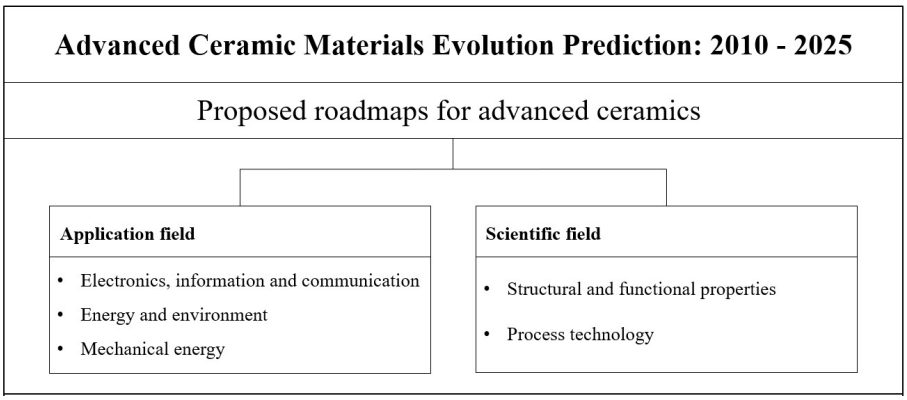

Figure 2.3: Five proposed roadmaps for advanced ceramics sectorized by fields as proposed by Rödel et al. (2009) [12].

As **Figure 2.3** shows, the top three initial roadmaps focused on the next application fields – *electronics, information, and communication; energy and environment*; and lastly, *mechanical engineering*. Regarding the bottom two, they were related to scientific fields, such as – *structural and functional properties*, and *process technology*. The methodology of information gathering, and meta-data structuring may be consulted in the article

itself. Here, the focus will lie specifically on the scientific fields and how these may be addressed in future challenges and needs.

Presently, and as described until now, it is well-established that high-ceramics are recognized by their broadest wide-spectrum of properties when compared to classes of materials such as polymers and metals. As mentioned, they impact an extensive variety of industries, so they can be functional structural, bioceramics, coating systems or even special glasses. Nevertheless, although the science and the market are already exploring the concept of multifunctional ceramics, these materials still offer an unexplored potential, specifically [12]:

- **Structural ceramics** where enhancement of the mechanical properties (based on affordable raw materials, optimized technologies, and simulations of the complete process chain), as well as exploration of the reliability of materials by auxiliar sensors integration for structural health controlling or even further self-healing ceramic are mandatory.
- **Miniaturization and integration** density of devices and systems is a current tendency and will clearly constitute a further pursuit. To this aim, better understanding, and the control of the corresponding changes of specific properties of materials, new testing and measurements methods are crucial.
- **Modelling** is a sensitive topic of uplift since complete chains of production and a faithful multi-scale modeling must be matured for new materials and devices with higher emphases in cases of coupled properties.
- **Functional ceramics defect structures dissemination** should be achieved to take advantage of a full temperature dependent influence study on atomic and electronic point defects.
- **Functional ceramics and properties enhancement** allows investigating multifunctional ceramics which normally do not simply exhibit additive effects, but especially a coupling of their properties. Unfortunately, the limitations of these effects are not yet explored, even so they promise to provide and stimulate scientific and technological advancements henceforward.

The roadmap displayed on **Figure 2.4** illustrates the evolution and its prediction from 2010 to 2025 of the concepts, materials, technologies and modelling and simulations of the structural and functional properties described above. This roadmap places its key topics on the axis centered at the year where the pioneer prototypes became available, and the length of the arrows suggest a time span for the setting developments.

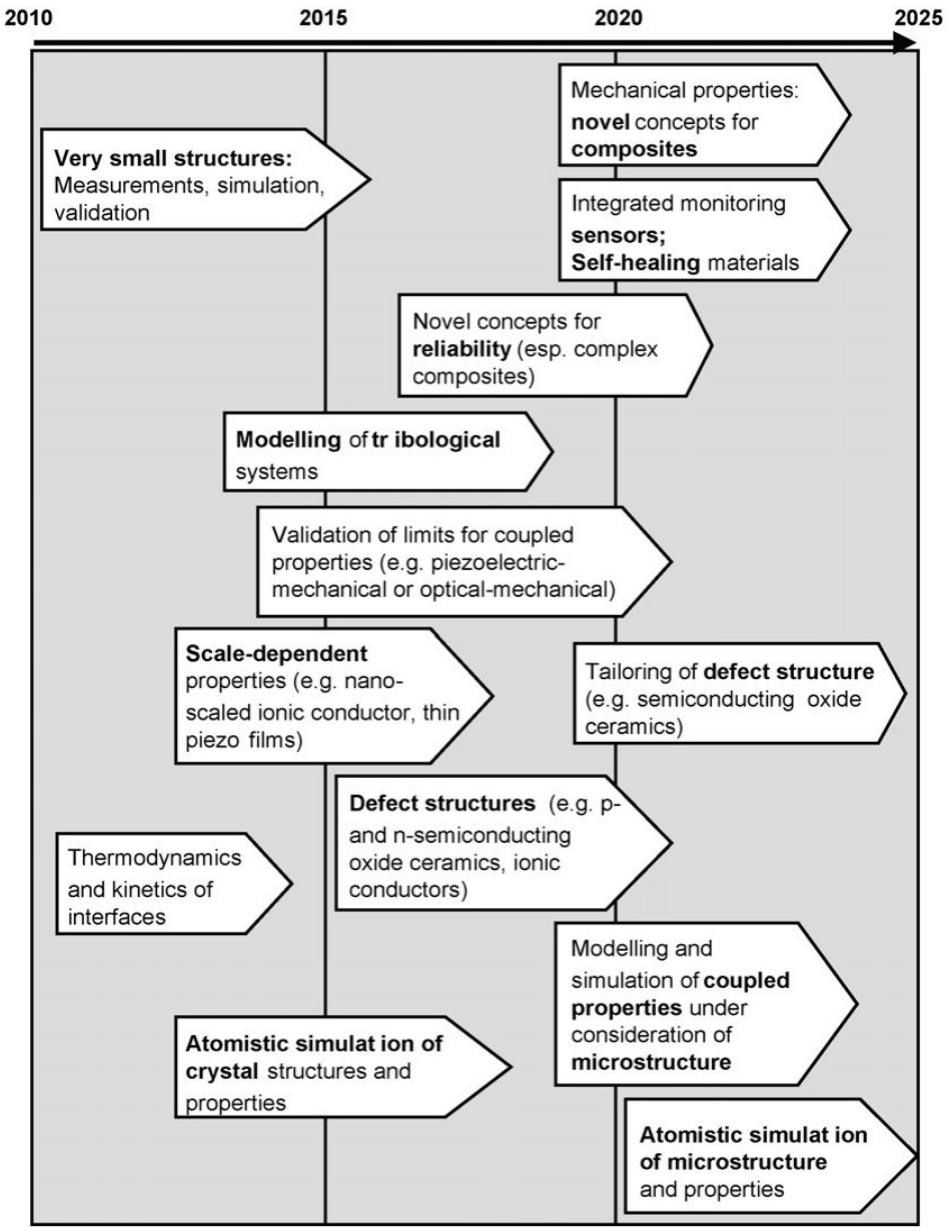

Figure 2.4: Roadmap evolution between 2010 and 2025 for structural and functional properties [12].

In conclusion, one can say that to leverage the entire innovative potential of advanced ceramics four major research topics should be approached to guarantee a sustainable development and growth of the advanced ceramic materials market. They are:

- novel ceramics with enhanced and new properties
- high performances key components for system applications
- highly efficient processing technology
- integral modelling and simulating techniques.

Chapter 3

State–of–Art of Advanced Ceramics in Aeronautical and Aerospace Engineering

The quest of increased performance in aeronautical and aerospace industries has provided the driving force for the development of high temperature ceramics with attractive combinations of thermomechanical properties, oxidation resistance, as well as low to moderate density [18]. In the aeronautical and aerospace fields, their main applications consist of *thermal protection systems*, *shielding purposes*, as well as *instrumentation and control*.

One of the most common and well-known use cases for high performance ceramics in aviation, rocketry and space technologies is as part of the *thermal protection systems*. This application of ceramics protects the intended components against hazard aerothermal environments ensuring the reliability, durability, and useful time life of the critical structures of a system it is protecting. Examples of the thermal protection systems can be encountered in coatings made of various heat-resisting materials for aircraft engine nacelle, thrust reverser fire protection, helicopter cowlings, gas turbine engines, satellites, rockets, and re-entry vehicles [19]. Besides thermal protection itself, another major advantage of this type of ceramics consists in being capable of enabling higher operating temperatures, consequently increasing, for example, an engine's combustion efficiency, which in turn reduces the fuel consumption and harmful residual emissions.

Additionally, another application of technical ceramics may be as means of *shielding*, since through the years they have been specifically tailored and designed to act as a ballistic shielding against foreign objects, both from internal and external sources. Examples of shielding purposes based on advanced ceramic materials are the conservation and safety of propulsion components from the existing particles in the surroundings or namely residuals resulting from poor combustion processes, space debris or micrometeoroid particles in case of a spacecraft or rockets [6].

A different, and lastly mentioned, important field of application of high-tech ceramics consists in a specific category of ceramics materials designed as electroceramics which are materials that combine specific characteristics such as piezoelectric and dielectric properties with corrosion and thermal resistance that are used in aircraft *instrumentation and control systems*, such as missile guidance systems, satellite positioning equipment, ignition systems, instrument display and engine monitoring equipment [11]. In essence, piezoelectric sensors consist of instruments that take advantage of the so-called piezoelectric effect which can be translated into an electrical charge across the crystalline structure of a crystal due to induced mechanical stress. In aeronautical and aerospace engineering,

accelerometers, gyroscopes, and level sensors are practical examples of piezoelectric sensors [20].

The subsequent three subsections of this chapter aim to provide an in-depth *introduction, contextualization, delineation* and *analysis* of the state-of-art of advanced ceramics' role in three different domains – Thermal Protection System (TPS), Thermal Barrier Coating (TBC) and Dielectric Barrier Discharge (BDB). The following review presented is specifically focused on the aerospace and aeronautical industries and academia research performed to date. Each subsection obeys more or less to the same structure. Initially, a brief preamble to the topic in addition to a brief historical framework are established. Then, a more technical and focused characterization of each mechanism/system or concept are made. Lastly, ceramic-oriented studies and investigations for each application are outlined with the help of current and even ongoing research. The fourth and last subsection of this chapter named Multifunctional Advanced Ceramics points out the fine ceramic systems that will be studied, as well as arguments the reasoning for which they were selected.

3.1 Thermal Protection System (TPS)

In the time of the atmosphere entry, hypersonic vehicles are subjected to strong mechanical stress and aerodynamic heating, equilibrium or non–equilibrium gas chemistry, large heat fluxes, which in consequence induce the vehicle's structure to reach very high temperatures. These adverse conditions make indispensable a proper *protection* and *insulation* subsystem for spacecrafts [21].

3.1.1 Introduction to TPS

Thermal protection systems (TPSs) play a crucial role in the aerospace and aeronautical industries as they are single–point–failure systems which work above all as thermal shields, i.e., a subsystem that protects the structure, aerodynamic surfaces, payload of probes, missiles, warheads, and space vehicles from severe aerothermodynamic heating. Accordingly, an *effective* TPS system must uphold a reliable shield against aerothermal loads, without adding significant weight penalties nor compromising the structure of the vehicle. Nonetheless, TPSs also work as structural component and aerodynamic body [21, 22, 23].

The idea of using a protection layer to prevent damage to interior parts of a vehicle dates back to 1920 and is attributed to Robert Goddart who developed the concept of a heat shield after observing the behavior of meteors entering the Earth's atmosphere. However, the origin of the modern protection systems as they are known nowadays can be traced back to the period of World War II. During this period, considered a golden age in space flight, ushered countries to invest in developing long range missiles and rockets capable of leaving the earth's atmosphere and hereinafter reentering to deliver payloads. Several studies were conducted during this period, and it was soon concluded that the vehicles had no capacity of reentering into the earth's atmosphere due to high heat loads and high reentry speeds, as well as lack of suitable TPS materials. From mid twentieth century to date, various TPS technologies have been developed and tested with the aim to ensure safety of space vehicles [24].

3.1.2 TPS Classification System

The type of protection on any space–venturing vehicle or, more precisely, on any given area of a vehicle depends largely on the magnitude and duration of the heat load as well as various operational considerations. In the broadest sense, thermal protection systems can be categorized into three major classes – passive methods, semi–passive methods, and active methods – as shown in **Figure 3.1** – based on their physicalmechanical working principle for the thermal management, which can be insulation, ablation, dissipation, or cooling [24, 25, 26]. The correct selection of a TPS includes considering first and foremost the propulsion system of the vehicle, its geometry, and the amount of heat flux on the surface as well as the time of exposure [27].

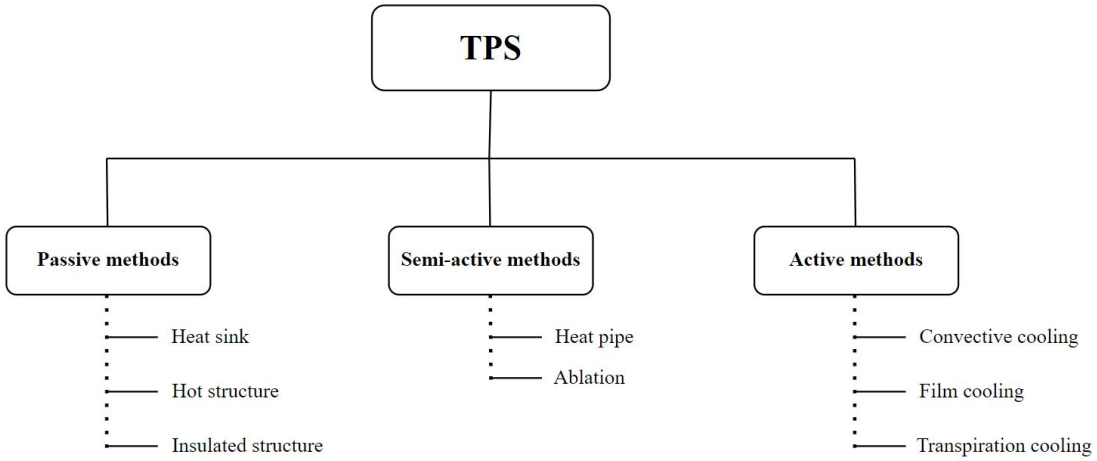

Figure 3.1: TPS classification based on their working principle and developed structures of each method.

The following subsections aim to explain in greater detail the methods – passive, semi–passive and active – of the TPS classification adopted.

(a) Passive methods

As the name itself suggests, passive thermal protection systems have no moving parts. Furthermore, they are the simplest thermal protection systems. The three different passive TPSs are *heat sink*, *hot structure*, or *insulated structure*. Concisely, *heat sinks* consist of a metallic structure that absorb almost all the incident heat and store it. This concept has the limitation that it is only suitable for short heat pulses. *Hot structures* on the other hand are systems characterized by high emissivity which allows the temperature of the structure to rise until the heat being radiated from the surface equals to the incident heating. Last passive method, i.e., *insulated structures* are composed by an outer shell that radiates most of the incident heat and an underlying structure protected by an insulative material, such as, for example, high–temperature ceramic matrix that slows down the heat transfer process [24, 25, 28].

(b) Semi–passive methods

The two semi–passive methods that have been explored and tested for TPS applications are *heat pipes* and *ablative surfaces*. Summarily, *heat pipes* are devices with very high thermal conductivity that enable transportation of heat while maintaining almost uniform temperatures along its heated and cooled sections. Heat pipes possess the great advantage that their show a wide variety of sizes and geometries that vary accordingly to the desired application [29]. On the other hand, *ablation* is a process in which the material – ablative layer – is sacrificed, i.e., consumed to protect the underlying structure. The term “ablative” refers to a number of physico-chemical processes, namely vaporization, chemical reaction, and erosion, leading to the surface material removal. Naturally, this method is limited by the duration of its

operation and eliminates the possibility of reuse [21, 24, 25]. Examples of ablative TPS materials are super lightweight ablators (SLA), phenolic–impregnated carbon ablator (PICA), silicone–impregnated reusable ceramic ablator (SIRCA), coating by Aviation Corporation (AVCO), AVCOAT, three–dimensional multifunctional ablative TPS (3D MAT) [30].

(c) Active methods

Convective cooling, *film cooling*, and *transpiration cooling* are three different active TPS technologies widely investigated in applications such as rockets and hypersonic vehicles' engines. Briefly, *convective, or regenerative cooling* uses a circulating coolant underneath the vehicle's surface to absorb the aerothermal heat load. In *film cooling* the selected coolant is injected at a discrete location on the surface of the vehicle, and followingly a thin film – cooling blanket – is created on the wall to be protected, ensuring that the melting temperature is not exceeded. Film cooling is widely used specially in blades of gas turbines. Lastly, *transpiration cooling* that is characterized by a higher efficiency and with a lower coolant consumption when compared to film cooling method, takes advantage of the flow of the coolant through a porous wall into the mainstream, protecting this way the intended surface of the body by forming a thin film that further decreases the heat flux. Transpiration cooling can be found as thermal protection of rocket engine throats [24, 25, 31].

Figure 3.2 illustrates the historical development of the thermal protection system methods between 1950 and 2020 and gives specific examples of application of materials applied in different space missions.

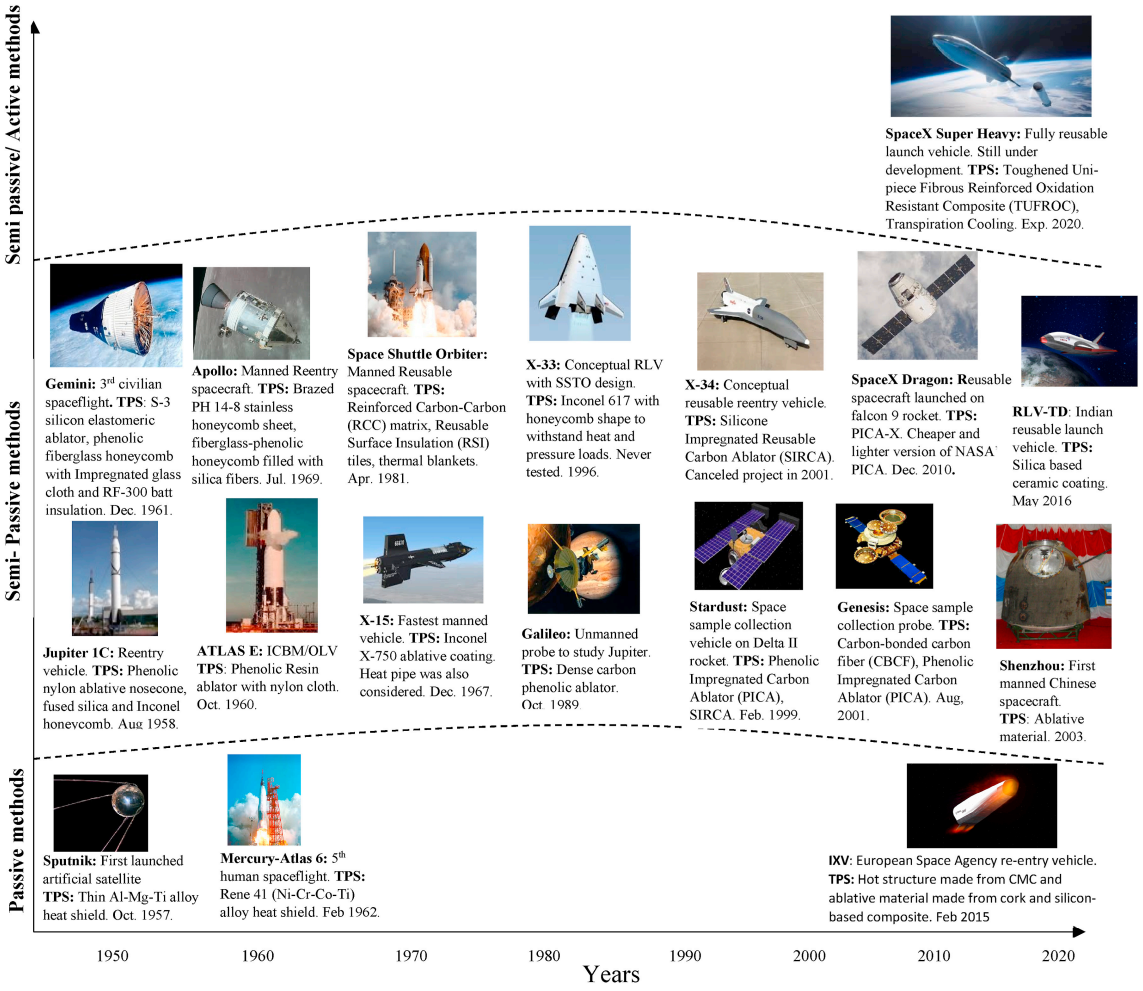

Figure 3.2: Examples of TPS methods and materials employed in different space missions between 1950 and 2020 [24].

Despite of the classification above, it is important to emphasize that some authors suggest different grouping of TPSs. Based on the properties and nature of application of TPS, a distinction is hence made between the thermal protection systems which are reusable, or also designated insulative or radiative TPS (i.e., non–ablative TPS), and the ablative TPS [26, 32, 33, 34, 35, 36]. It should be noted that this type of classification is rather a simplification since dissipation and cooling mechanisms are put aside [21]. To cover every aspect, usually reusable insulative systems are related to parts of the vehicle that experiences *less intense heating during reentry*. Reusable insulative systems consist of materials that are mechanically or chemically unchanged by flight mission – no mass variation or composition occurs of the materials during its exposure to the hazard environments – and can be relatively safely flown a number of times – with or without servicing. In contrast, when the vehicle is subjected to *very high heat fluxes*, ablative TPS is used since

they can withstand much higher heat loads through the process of phase change and mass loss [30, 32, 37]. The following **Figure 3.3** summarizes the different TPS material classes described.

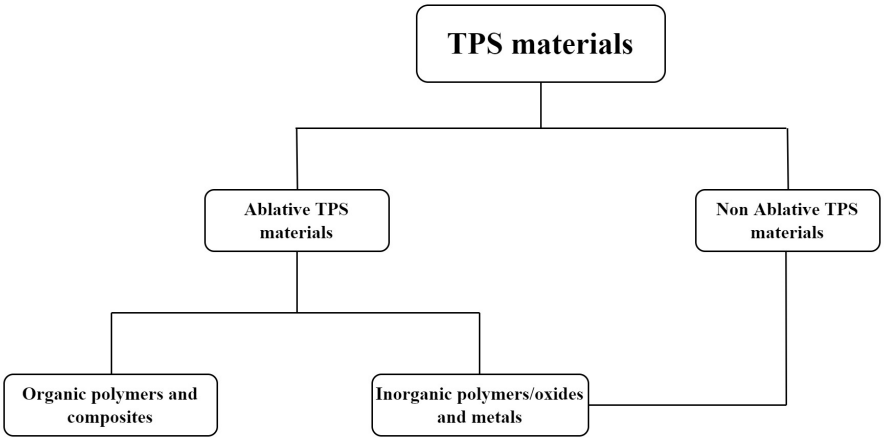

Figure 3.3: TPS classification based on their materials based on [35].

3.1.3 Advanced Ceramic Materials for TPSs

Aerospace insatiable aspirations are the source of intense demand for more efficient and powerful vehicle–structure thermal protection systems. To put it simply, the severe operating conditions, including higher temperatures, faster speeds, higher stresses, and hostile environments require the constant investigation and improvement of available materials in conjunction with cooling systems for TPSs applications [37]. Therefore, the TPS of next generation hypersonic and reentry space vehicles must offer a combination of suitable properties among them [30]:

- high melting point (>3000 °C)
- high softening temperature
- low areal density
- low recession rate
- high impact resistance
- high ablation resistance
- ability to withstand radiative heating
- superior oxidation resistance
- thermal shock resistance
- high fracture toughness

- high temperature strength
- low to moderate thermal conductivity (depending on areas of applications).

Accordingly, the introduction of *advanced structural ceramics* plays a key role in addressing these challenges considering the vast range of improvements they offer, such as weight reduction, longer lifetime, thus cost savings.

Intuitively, *oxide ceramics*, such as alumina, zirconia and mullite, appear ideal candidates for high–temperature structural applications due to their *high temperature stability*, *high hardness*, *good corrosion and erosion resistance* together with *comparatively low costs*. Nevertheless, relatively poor mechanical properties, videlicet, creep, fatigue, fracture toughness, large volume change (generated by phase transformation) and significant grain growth above 1000 °C severely limit oxide ceramics as structural components in high–temperature applications [30]. In contrast, *non–oxide ceramics* such as nitrides, carbides and borides can achieve *high–strength* and *excellent creep resistance up to elevated temperatures*, due to their predominant covalent bonding. Unfortunately, the fundamental drawback of these materials is their susceptibility to oxidation [38].

Thus, to overcome the problems associated to conventional technical ceramics, *ceramic matrix composites*, or CMCs, were developed to achieve *damage tolerance* and *favorable failure behavior*. In essence, CMCs consist of ceramic fibers or whiskers in a ceramic matrix and generally an interphase provided by a fiber coating. Both the fibers and the matrix can be made of any ceramic material. The choice of focusing on systems with similar matrices and fibers is mainly justified by the need of minimizing the residual stress associated with mismatch between the thermal expansion coefficients of the matrix and the reinforcement material. In spite of that, by carefully combining different ceramic matrix materials with special suitable fibers, new properties can be created and tailored [39].

It is interesting to mention that CMCs are referred to as “inverse composites” which means that contrarily to most polymer or metal matrix composites, the failure strain of the matrix is lower that the failure strain of the fibers. Hence, under load it is the matrix that fails first. Overall, long–term high–temperature stability, creep resistance, and oxidation stability are sought. The term “ceramic fibers” encompasses all non–metallic inorganic fibers – oxide and non–oxide – as pointed out in the **Figure 3.4** below. It should be noted that carbon fibers can namely be exploited in CMCs materials [38].

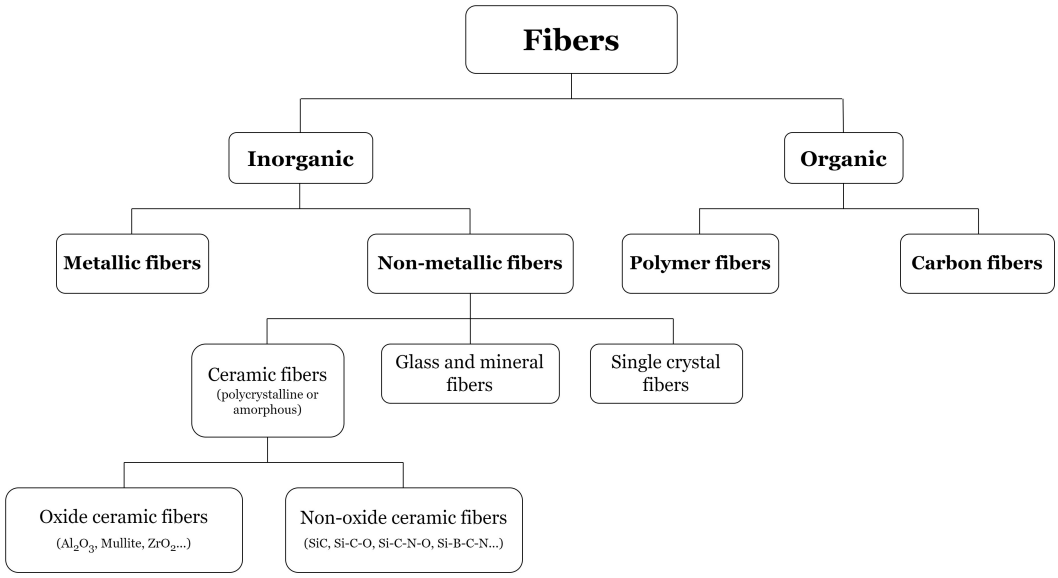

Figure 3.4: Classification of different groups of fibers.

The most commonly used CMCs are non–oxide CMCs, namely carbon/carbon (C/C), carbon/silicon carbide (C/SiC), and silicon carbide/silicon carbide (SiC/SiC). Hybrid composites and composites with nanostructured reinforcements, like *carbon nanotubes* (CNTs) and *graphene*, have paved the way to further investigation. For instance, Cho J. et al. (2009) [40] provides a review the status of the research and development of CNT–loaded ceramic matrix composite materials, whilst H. Porwal et al. (2014) [41] hands a comprehensive overview on the graphene ceramic matrix composite (GCMC) in comparison to polymer composites.

Nevertheless, *carbon fiber–reinforced silicon carbide* (C/SiC) CMCs are among the most famous composites for high–temperature structural applications.

In what concerns fiber/matrix behavior, L.B. Li et al. (2014) [42] studied the uniaxial tensile behavior of unidirectional C/SiC CMCs at room temperature. During conducted tests, the failure strength and the failure strain obtained 230 MPa and 0.24 %, respectively. Scattered cracks resulting from the thermal residual stress in the composites due to the mismatch of the thermal expansion coefficient of the matrix and fiber were seen in the matrix.

Additionally, Wei K. et al (2018) [43] focused its research rather on integrated thermal protection systems (ITPS) that are comprised of a cellular core sandwich panel and filling insulative material in the core. It was shown that compared to using metal sandwich panels, ITPS incorporating CMC sandwich panels gives notable advantages of high temperature resistance up to 1600 ^{o}C and areal density of 17.22–30.56 kg/m^2 which are much

lower than those of the reported ITPSs (23.66–88.84 kg/m^2). Notably, Heidenreich B. et al. (2021) [44] studied the shear properties of C/C–SiC sandwich structures on samples based on different core types. Results showed that sandwich samples with fold–cores offered higher specific stiffness and effective shear modulus of up to G_{eff}=6.4 GPa/(g/cm^3) compared to the sandwich samples based on grid–cores, G_{eff}=4.2 GPa/(g/cm^3). Hence, it was remarked that fold–cores are preferred.

Recently, Shi et al. (2021) [45] focused its work on experimental characterization and theoretical prediction of elastic and failure properties of continuous reinforced silicon carbide, C/C–SiC.

Interestingly enough, Huang J. et al. (2022) [46] investigated a novel SiC coating with a relatively high crack resistance property, in addition to outstanding thermal shock resistance achieved by means of pack cementation technique. ABSC2 coating (i.e., SiC coating with Al–B–C) was prepared on C/C composites. When compared to conventional AOSC2 (i.e., SiC coating with Al_2O_3), ABSC2 coating showed a refined and denser microstructure thanks to better effects in promoting SiC densification. Therefore, the improvements in microstructure results in superior mechanical capabilities, antioxidation performance (900 °C), and thermal shock resistance (between 1500 °C and room temperature).

Despite of this broad investigation on CMCs materials, over the last years, *to extend the temperature range capabilities of state–of–art materials* in addition *to develop components able to withstand larger and multiple aerothermal–chemical loads*, ultra–high temperature ceramic (UHTC) materials have been the focus of intensive research by the scientific community. Fundamentally, UHTCs encompass carbides, nitrides and borides of the transition metals, e.g., – zirconium diboride (ZrB_2), hafnium diboride (HfB_2), titanium diboride (TiB_2), zirconium carbide (ZrC), hafnium carbide (HfC), tantalum carbide (TaC), that are characterized by *melting points above 3000 °C*, *high temperature strength* and *excellent oxidation ablation resistance*. This portends that they can maintain non–ablative properties and structural integrity in hazard environments above 1800 °C for long periods [27, 47].

Among UHTC materials, ZrB_2, HfB_2 are the most widely investigated. Opila E. et al. (2004) [48] reported that the addition of SiC up to 30 vol. % is found to improve both the oxidation resistance and the mechanical properties of sintered ZrB_2–SiC and HfB_2–SiC composites. Likewise, Chamberlain A. L. et al. (2004) [49] investigated zirconium diboride, ZrB_2, composites containing 10 vol. %, 20 vol. %, and 30 vol. % of either SiC or molybdenum disilicide ($MoSi_2$) prepared by hot pressing. Results exhibited an improvement of strength of ZrB_2, reaching a maximum of approximately 1 GPa at 30 vol. % additives. In particular, SiC additives increased the fracture toughness to 5.25 MPa $\cdot$ $m^{1/2}$. Overall, the addition of $MoSi_2$ and SiC decreased the oxidation rate when com-

pared to monolithic ZrB_2. Latterly, Zhang H. et al. (2019) [50] proposed a novel eutectic engineered microstructural design of ZrB_2–SiC UHTCs to improve oxidation resistance by means of directionally solidification.

Notwithstanding the advances in the TPS materials already obtained, continuous investigation led to follow–up research on the *strengthening and toughening technology of UHTCs*. By combining the unique properties of the UHTCs with the concepts of CMCs, a new class of materials known as fiber reinforced UHTCMCs (Ultra High Temperature Ceramic Matrix Composite) are developed. This class of materials *focuses on overcoming the inherent brittleness and poor mechanical resistance of bulk UHTCs* as summarized in **Figure 3.5**. Therefore, UHTCMCs are very promising for application in extreme conditions and considered as the best candidates for a new generation of high–thermal protection materials [47].

CMCs		UHTCs	
Disadvantages	**Advantages**	**Advantages**	**Disadvantages**
Moderate erosion resistance	Low density	High temperature strength	High specific weight
Low oxidation resistance	Excellent damage tolerance	Extreme melting temperature	Very low damage tolerance
Low temperature capability	Excellent thermal shock resistance	Self-healing ability[2]	Low thermal shock resistance

UHTCMCs

Figure 3.5: UHTCMCs approach based on concepts of CMCs and UHTCs materials.

The EU–funded project C^3HARME aspires to combine the best features of CMCs and UHTCs to design, develop, manufacture and test UHTCMCs with self–healing capabilities. The self–healing capabilities desired to achieve is a formation *in situ* of an adherent, ultra–refractory solid oxide scales achieved by nanosized ceramic dopants. Sciti et al. (2018) [51] reported that the preferred matrix is essentially based on ZrB_2 enriched with secondary phases and different functionalities.

Carbon fiber reinforced UHTC composites, consisting of carbon fibers embedded in a UHTC–matrix or a C–SiC–UHTC matrix are also count a promising class of materials in order to surpass monolithic UHTC materials in terms of fracture toughness and thermal shock resistance. Tang S. et al. (2016) [52] elaborated an outright review on this topic including the design, preparation and properties of such materials for aerospace application.

[2] Self–healing ability mentioned refers to the capacity of partial or complete sealing of cracks thought a thermal treatment, also known as “crack–healing”.

Carbon reinforced ultra–high temperature ceramic matrix (C/UHTC) composites fabrication processes – hot pressing (HT), chemical vapor infiltration (CVI), polymer impregnation and pyrolysis (PIP) and melt infiltration (MI) – were reviewed by Arai et al. (2019) [53]. In detail, the fracture toughness, thermal conductivity and recession behavior in an oxidizing atmosphere of (C/UHTC) were evaluated. It was concluded that Zr– and Hf–based mechanical behavior and thermal conductivity can be tailored by varying their fiber volume fraction and by the formation of a "weak" interface by using fiber coatings. Further, MI was pointed out as an efficient approach for the preparation of C/UHTC composites.

Of late, an extensive aerothermodynamic characterization of UHTCMCs produced by sintering technology, including ZrB_2–SiC matrix reinforced with short random or continuous fiber was performed by Mungiguerra S. et al. (2022) [54]. Test conditions aimed to reproduce the typical heat fluxes (around 2 MW/m^2) and stagnation pressure (around 70 kPa) of a reference re–entry mission with a high amount of dissociated oxygen, i.e., about 22 wt. %. All the materials successfully passed the base qualification and cycling exposure for three times, achieving temperatures about 2000 – 2500 K. The materials developed and tested were *ZS–SF* and *ZSY* (i.e., 53 vol. % ZrB_2–SiC matrix, 45 vol. % chopped carbon fibres, with porosity below 2 %. The difference between the two samples was the SiC content with respect to the UHTC matrix); ZSY–LF: 45 vol. % ZrB2–SiC matrix, 50 vol. % continuous carbon fibres ($0^0/90^0$ configuration) with porosity of 5 %; and CS (baseline C–SiC material loaded with 10 vol. % ZrB_2 phase and a porosity of about 10 %. Altogether, the capability of these novel UHTCMCs to maintain their functionality and structural integrity after repeated exposure was confirmed which makes them extremely appealing for future reusable TPSs applications.

3.2 Thermal Barrier Coating (TBC)

Nowadays, higher efficiency in thermal conversion processes has been required to satisfy the global push for reliable green energy use, reducing this way the consumptions of fossil fuels. Consequently, today's competitive world economy makes vital the further research of engineering components with increased efficiency that operate in harsh environments. Advances in several techniques, such as superalloys, cooling processes, and coatings have been reported. Among them, thermal barrier coatings (TBCs) show promising potentials as a result of extensive research over the last decades to safeguard critical components under even the most demanding conditions [55, 56].

3.2.1 Introduction to TBC

As mentioned, strong renewable energy demands, (i.e., the urgent need in reducing the fossil fuel consumption) and continuously growing fuel costs are forcing – among other sectors – aerospace industries to focus their investigations on more efficient turbine and scramjet engines, turbine blades, rockets, reentry vehicles and space vehicles. Since the operating conditions of such structures are characterized by long periods in temperatures well above structures' superalloy substrate melting points, the development of new capable materials and coatings has been the target [56, 57].

Thermal barrier coatings, or TBCs, systems are generally explored to enhance energy durability and therefore efficiency of hot components of aero-engines, gas turbines and parts for combustion power plants. More specifically, TBCs serve as a protection for the substrate structure by preventing them from experience high temperature and harsh environments degradation. Consequently, thermal barrier coating, as a surface modification technique, provides wear, oxidation, thermal shock and corrosion resistance for prolonged service times and thermal cycles without failure, increasing this way both the efficiency and lifetime of the desired components [58, 59, 60]. Ultimately, TBCs are multifunctional systems that provide a wide range of benefits such as [56]:

- shielding of metallic structure,
- decreased thermal conductivity,
- high thermomechanical stability,
- increased exhaust gas temperature,
- increased engine power efficiency,
- decreased fuel consumption, and
- increased lifespan of parts through decreased fatigue and stress.

The concept of “thermal barrier coating” is believed to be firstly introduced by National Advisory Committee for Aeronautics (NACA) and National Bureau of Standards (NBS) with the publication of the earliest turbine blade-oriented ceramic coatings research entitled “Review of an Investigation of Ceramic Coatings for Metallic Turbine Parts and Other High–Temperature Applications” by W.N. Harrison, D.G. Moore, and J.C. Richmond in 1947 [61, 62, 63]. The pioneer ceramic coatings for aerospace applications were frit enamels used in aircraft engines throughout the 1950s [63]. With the development of the flame-sprayed ceramic coatings technique, further applications included the protection of sheet metal in jet engines and in rocket engine thrust chambers. With regard to the materials appraised for TBC purposes, the flame-sprayed zirconia-calcia coatings were widely applied on the regeneratively cooled XLR99 thrust chamber for the X-15 experimental rocket planes. In addition, in the 1970, “modern” plasma-sprayed TBCs began to be employed on hot section transition ducts and other hot section sheet metal components in commercial gas turbines [64]. Most recently, the morphology (i.e., microstructure) of the thermal barrier coatings, the materials applied, the coating preparation technologies and the failure mechanisms, as well as lifetime prediction models have all been part of the different branches of extensive and deep investigation in TBC technology [61].

3.2.2 TBC Structure, Fabrication Techniques and Failure Mechanisms

A great deal of effort has been devoted over the past few decades so that TBCs systems could enable higher operating temperatures and reduce cooling systems costs, thus improving the overall components’ capabilities and effectiveness [56]. Irrespective of the evolution achieved, the stability of TBCs systems continues to be a major concern of the scientific community. During the operating service, TBCs are exposed to complex phenomena, such as thermomechanical stress, corrosion by foreign objects, erosion, diffusion, oxidation, phase transformation, and sintering [60]. In essence, TBC are *complex*, *multilayered* and *multi-material* coatings systems composed of (1) a top coat, (2) a metallic bond coat (MCrAlY; M = Co, Ni, Fe and/or their combinations), a thin thermally grown oxide (TGO) layer, and a superalloy substrate (structure) as depicted in the **Figure 3.6** [56, 59].

Figure 3.6: Schematic illustration of a traditional TBC system (not to scale).

The **ceramic top coat**, also referred in the literature as the "TBC layer", is generally as the name itself implies a ceramic material layer that *provides more importantly thermal protection to the substrate*, but also *strain tolerance*, and *thermal shock resistance* for components through reduction of the heat transfer. Consequently, to decrease the temperature of the metal substrate this top coat should have essentially low thermal conductivity [56, 58, 59]. A state-of-art TBC top coat material is yttria–stabilized zirconia (YSZ) composed of ZrO_2 with 7–8 wt. % Y_2O_3 for the reason that it has excellent thermomechanical properties, such as [58, 59, 65]:

- very high mechanical strength,
- very high wear resistance,
- very high erosion resistance,
- high impact resistance,
- high corrosion resistance,
- high chemical resistance,
- very low thermal conductivity, and
- relatively high coefficient of thermal expansion when compared to other ceramics.

Followed, the **TGO layer** is created via diffusion of oxygen from the bond coat through the top coat of metallic elements during manufacturing and operation processes. The

TGO layer *acts as a protective layer to retard the further thermal and oxidation diffusion*. Nonetheless, the TGO layer may increase the internal stress in the TBC system, hence originating potential cracking at the interface between the bond and top coats. This phenomenon may eventually lead to the unwanted spallation or delamination of the top coat [56, 66, 67].

Lastly, the **metallic bond coat** acts as a precoating interface between the substrate and the top coat aims *to protect the superalloy substrate from oxidation and corrosion*, *increase both the adhesion between the layers*, and ultimately *guarantee the structural integrity of the coating* by matching the thermal properties and stress between the substrate and the ceramic coating [56, 66]. Two types of metallic bond coat may be identified. The well-known first-generation bond coat of Platinum (Pt) modified aluminide, which is recognized by having good stabilization and adhesive strength of the coating by reducing the inter-diffusion between the coating and the substrate layers. Unfortunately, Pt is an expensive component and does not possess a desirable mechanical robustness at high-temperatures [61, 68]. Another widely investigated second-generation bond coat that consist of MCrAlY coatings. These MCrAlY coatings include NiCrAlY, CoCrAlY, and NiCoCrAlY which have good oxidation, as well as hot corrosion resistances [55, 58, 61, 69]. Moreover, the composition of MCrAlY coating systems can be enhanced by adding Ta (Tantalum), Nb (Niobium), Re (Rhenium), Hf (Hafnium), Zr (Zirconium) and/or other components to improve the high temperature performance, extend the lifespan, and match specific requirements [55, 61]. Worth noting that new ultra-high temperature bond coat materials have become the focus of research in recent years [61].

Concerning the fabrication techniques of TBCs, several different methods are known and ready to be used e.g., atmospheric plasma spraying (APS) and electron bean physical vapor deposition (EB-PVD); whereas others are still under intensive research as promising candidates to achieve better results in the near future, for example, plasma spray physical deposition vapor deposition technology.

The plasma-sprayed (PS) TBCs were firstly invented in the 1960s. During the following years, several different variations of this technique appeared, including APS, low pressure plasma spraying (LPPS), solution precursor plasma spraying (SPPS), vacuum plasma spraying (VPS) and protective atmosphere plasma spraying (PAPS). Among them, the APS and LPPS are two main methods utilized in TBC deposition, since they are characterized by their low cost, rapid deposition rate, high efficiency and easily management [61]. The TBCs deposited by APS and LPPS are distinguished by their complex *laminated structure* containing horizontal to the surface pores and defects encountered in the form of microcracks of various sizes and shapes [69]. Substantially, the porosity of APS TBCs lays in the range of 3 – 20 %, however the acceptable range is 10 – 15 %, which serves essential for high strain compliance and effectively further reduce the thermal conductivity. Despite

of the advantages pointed out that these methodology offer, inter-lamellar pores, microcracks and microstructural defects give way to the possibility of delamination and spallation. Therefore, APS and SPPS are useful for structures with large volume and weaker mechanical properties needed, i.e., combustion chambers and stator vanes [56, 61, 70, 71].

In the 1980s, countries such as Germany, Britain, United States and the former Soviet Union, switched their focus in the TBC deposition techniques to EB-PVD and with the advent of low cost EB-PVD equipment in 1990s, it was subsequently popularized worldwide. Overall, the EB-PVD exhibits excellent aerodynamic properties, since they have better surface roughness than those of PS TBCs and do not block fine cooling holes. The EB-PVD coatings exhibit a *columnar morphology* within randomly distributed multi-scale porosity, as well as a thin layer in the form of equiaxed grains near the interface between the bond and ceramic top coat. The EB-PVD microstructure improves the TBCs system strain tolerance, thermal shock resistance, in addition to relax thermal expansion mismatch stresses. Nonetheless, EB-PVD TBCs result unfortunately in higher thermal conductivity and lower thermal insulation than those of APS TBCs [56, 61, 70, 71].

In summary, up to now, although various methods for TBCs deposition exist besides the described ones, APS and EB-PVD techniques are widely exploited [56, 61, 70, 71]. **Figure 3.7** illustrates the contrast in the coatings produced by the EB-PVD process which, as mentioned, exhibits a *columnar morphology* whereas the coating deposited via APS exhibits a *lamellar morphology*.

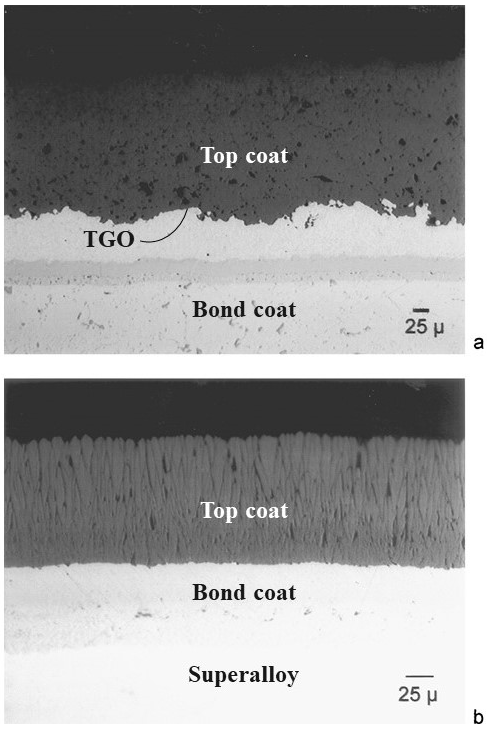

Figure 3.7: Photographs of (a) an APS TBC showing a laminar morphology and (b) an EB-PVD TBC showing a columnar morphology based on [72]

Based on the deposition techniques announced and in consequence different morphologies obtained, it can be highlighted that the porosity aspect of coatings which varies in size and location plays a major role in controlling the thermomechanical properties of TBCs systems. Therefore, it must be a topic of consideration when designing and implementing a TBCs structures for a specific application in order it will withstand the operating service conditions.

Both industry and research experience indicate that TBC failure can occur in a multitude of ways depending on the TBC system and the service conditions due to the sheer complexity of the interactions between the three primary layers described. It is important to note that all these layers have distinct physical, mechanical, and thermal properties. When the word "failure" is applied in the of TBC contexts, it implies that the coating is no longer capable of fulfill its functional requirements. Simply put, when the top coat spalls due to, for example, fatigue, corrosion or erosion, the TBC is considered unfit and "failed" [73, 74].

Generally, damage in the TBCs may result from, for example, thermal shocks and gradients, sintering, phase transformation, oxidation, external mechanical damage, calcium-magnesia-alumina-silicate (CMAS) attack, corrosion, as well as environment-induced erosion. **Figure 3.8** represents a schematic illustration of the major drivers of material failure in TBC structures when subjected to high-temperature and harsh conditions [56, 74].

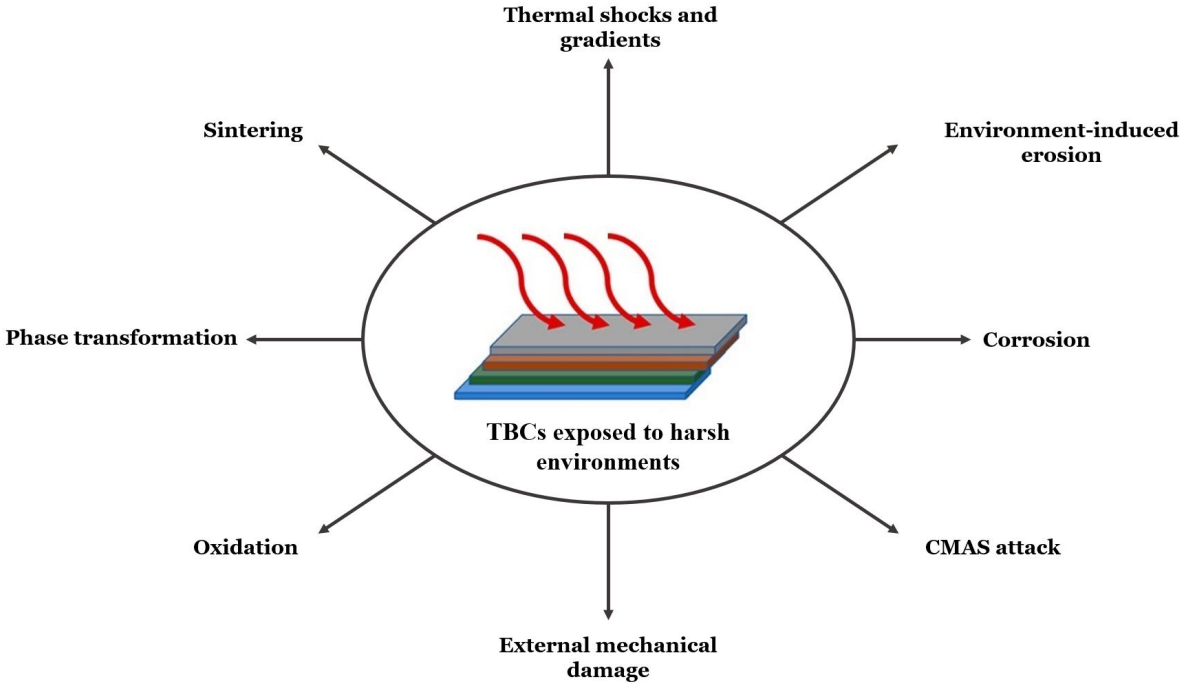

Figure 3.8: Different damage types that occur to TBCs in high-temperature and hazard environments based on [56].

Nevertheless, a regrouping may be considered to better categorize and understand the

different existing failure types of TBC structures, such as: thermal fatigue–, corrosion– and erosion–based damage–causing mechanisms [73, 74].

- **Thermal Fatigue–based failure mechanisms:** thermal fatigue is related to the impairment of the TBCs structure motivated by cyclic thermal stresses due to temperature oscillations. During thermal fatigue, different phenomena may occur, such as mismatch in the coefficient of thermal expansion (CTE), sintering of the top coat which refers to a process where densification of material occurs by the closing of the existing pores and micro-cracks, bond coat oxidation and interdiffusion.
- **Corrosion–based failure mechanisms:** corrosion is responsible for the destabilization of the coating by acceleration of oxidation and/or mechanical damage. Considering the dominant location of the dominant damage, corrosion can be divided into top coat corrosion or bond coat corrosion.
- **Erosion–based failure mechanisms:** erosion of the top coat may happen thanks to the impact of abrasive particles existing in the environment on the coating surface. Smaller particles normally are the origin of erosion, whilst, in contrast, the larger particles are the cause of the so–called foreign object damage (FOD). Both types of particles accelerate the deterioration, damage and reduction of the lifespan of TBCs.

3.2.3 Advanced Ceramic Materials for TBCs

The selection of effective materials for the TBC applications is highly restricted by many desirable properties, such as [57, 68, 75, 76]:

- high melting point,
- phase stability in the operating temperature range,
- chemical inertness,
- low thermal conductivity,
- low thermal diffusivity,
- thermal shock resistance,
- no oxygen transparent (i.e., permeable),
- good adherence to the metallic substrate,
- low sintering rate of the porous microstructures,
- thermal expansion match with the metallic substrate (matched CTE).

The following **Table 3.1** summarizes the material major requirements for thermal barrier coatings and briefly explains its importance [77].

Table 3.1: Material requirements for ceramic top coat of thermal barrier coatings [77].

Property	Requirement	Fundament
Melting point	High	Operating environment at high temperatures
Thermal conductivity	Low	Temperature reduction inversely proportional to thermal conductivity
Coefficient of thermal expansion	High	Expansion should be close to that of substrate and bond coat on which coatings are deposited
Phase	Stable	Phase change in thermocycle environment is structurally detrimental
Oxidation resistance	High	Operating environment highly oxidizing
Corrosion resistance	Moderate to high	Operating environment may be corrosive
Strain tolerance	High	Operating environment large strain ranges

Consequently, the number of materials that can be used as TBCs is very limited. So far, only a few ceramics have been found to satisfy the majority of these requirements. Naturally, a single compound ceramic can hardly meet all the requirements for TBCs applications, therefore the combination of two of more ceramics materials becomes mandatory. Among the properties referred, a special attention should be paid to the thermochemical stability, the thermal conductivity, as well as the thermal expansion coefficient.

As mentioned in the previous subsection, yttria-stabilized zirconia, YSZ, is the most successful top coat ceramic material and considered an industry standard. The development of YSZ started way back in the 1970s and continues to dominate the TBC field. The main reason behind this truth, is that YSZ gathers a considerable number of features that makes it an attractive top coat, including *relatively low density*, *high strain tolerance*, *high fracture toughness*, *high coefficient of thermal expansion*, *low thermal conductivity* attributed to its high concentration of point defects, *ability to stress relaxation caused by compatible CTE*, *high resistance to thermal shock* when compared to other ceramic top coats, as well as *thermochemically compatible with the protective TGO*. Hence, the superior successor of YSZ has not been developed yet [57, 68, 75, 76].

Better performance of YSZ is typically achieved by variation of Y_2O_3 content from 6 – 8 wt. % in ZrO_2. Nevertheless, by lowering Y_2O_3 content in ZrO_2 in a range between 7 – 8 wt. % improves both thermal and mechanical properties, i.e., high melting point, low thermal conductivity and high thermal expansion coefficient are obtained. Fundamentally, yttria is added to zirconia to stabilize its phase at high temperatures. Pure zirconia is allotropic (i.e., the existence of a chemical element in two or more forms). It exhibits a monoclinic

structure up to 1170 °C, tetragonal structure in the temperature range of 1170 – 2370 °C and cubic structure up to its melting point at 2690 °C, as shown in the phase diagram of ZrO_2–Y_2O_3 system in **Figure 3.9**. The phase transformation of zirconia from tetragonal to monoclinic is martensitic and leads to a significant volume expansion of about 4 – 6 %. This is sufficient to damage the mechanical integrity of the coating to a serious concern, due to fatigue failure when the coating is subjected to repeat thermal cycle and thermal expansion mismatch. Yttria, when added to zirconia in the range of 7 – 8 wt. %, forms a non-transformable tetragonal prime (*t'*) phase. This phase is stable up to 1200 °C above which a phase transition causes catastrophic delamination of the top coat [73, 75, 76].

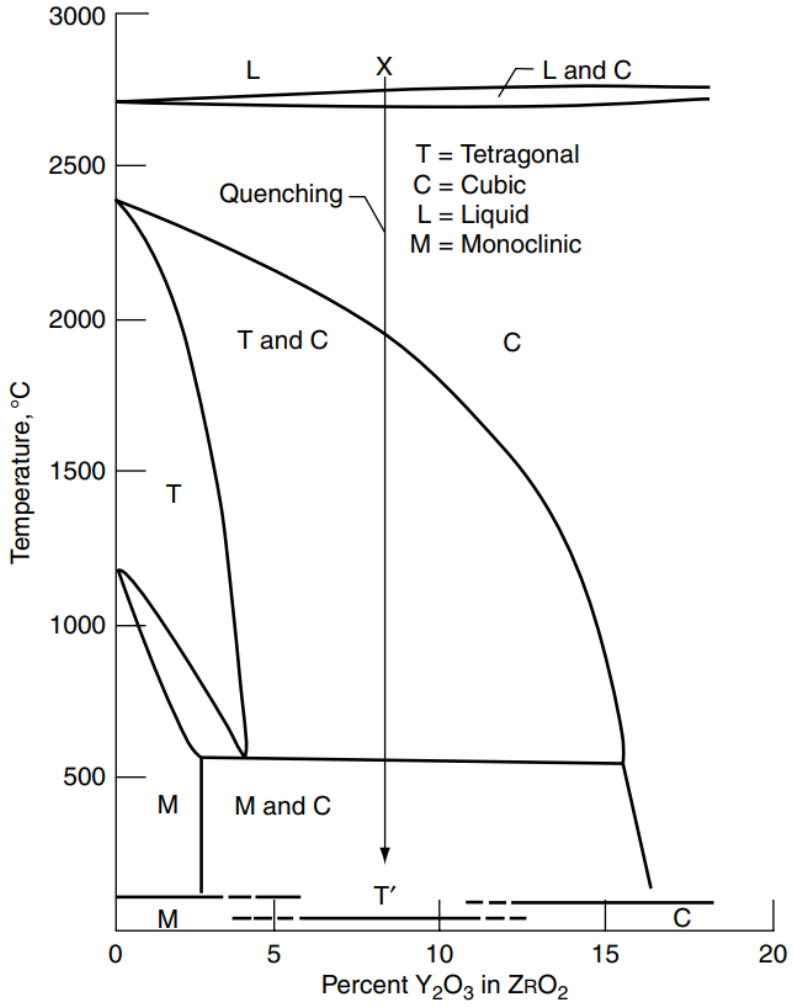

Figure 3.9: Phase diagram of ZrO_2–Y_2O_3 system [77]

For this reason, YSZ has a functional operation limit of about 1200 °C, which means that YSZ barrier coatings are unreliable for long-term use in temperatures of over 1200 °C, due to their catastrophic phase transformation, that in turn escalates thermal conductivity and boosts spallation in the TBCs. In addition, sensitivity to hot corrosion, sinterability and accelerated TGO formation caused by the extremely high ionic oxygen diffusion in the ZrO_2–based ceramics also restricts YSZ usage. Early studies suggested a double layer

coatings design of the top coat to minimize the delamination phenomenon by compensating the thermal expansion mismatch, whereas some authors claimed that to overcome the limited phase transition of YSZ, it was critical to change the stabilizing oxide or addition or components in YSZ, such as aluminum oxide, calcium oxide (CaO), titanium dioxide (TiO_2) and magnesium oxide (MgO) [73, 75]. As a result, many parallel research and investigations have been carried out on alternative materials to YSZ. Substantially, two approaches may be considered: **(1)** development of new structural coating materials with higher temperature resistance, i.e., advanced multicomponent oxide-doped ZrO_2 and HfO_2 (Hafnium Dioxide, Hafnium(IV) Oxide, or Hafnia) solid solution-based ceramics; and **(2)** multi-element modification and optimization of YSZ materials. From the literature, it is generally accepted that *defect cluster TBCs*, *crystal structures of perovskite*, *pyrochlore* and *lanthanum compounds* are regarded as the potential materials for advanced TBCs. Some other materials, such as mullite, silicates, and garnets were also considered as candidate materials through the years, but regrettably their typical low CTE precludes the likelihood of their implementation [57, 61, 78, 68, 75, 76].

3.2.3.1 Defect cluster TBCs

As referred, many new TBC materials have been proposed to achieve low thermal conductivity and high-temperature capability mandatory of a coating system. In particular, ZrO_2 and HfO_2 solid solutions based ceramic coatings co-doped with Y_2O_3 as primary stabilizer and additional paired rare-earth (RE) cluster oxides were detected to offer significantly better features. **Defect cluster** TBCs possess *much lower thermal conductivity*, and, consequently, *better thermal stability to the material*, since the resulting point defects are thermodynamically stable; and *better sintering resistance at high temperatures* than the state-of-art YSZ due to the reduction of effective defect concentration and the increase of activation energies by clustering [79].

Zhu et al. (2004) [80] studied the conventional furnace cyclic oxidation behavior of advanced multicomponent oxide-doped zirconia–based TBCs designed based on defect cluster concept. The aim was to report the furnace cyclic oxidation performance of plasma-sprayed multicomponent rare-earth (RE2O3) oxide doped zirconia thermal barrier coatings as a function of dopant concentration and processing variation. In essence, the coatings analyzed were the ZrO_2–based oxides, stabilized with the primary yttria, Y_2O_3, dopant and/or paired *Group A* and *Group B* RE oxide co-dopants. *Group A* dopants consisted in neodymium (III) oxide (Nd_2O_3), gadolinium (III) oxide (Gd_2O_3), and samarium (III) oxide (Sm_2O_3); whilst *Group B* ones were such as ytterbium (III) oxide (Yb_2O_3), scandium (III) oxide, or also known as scandia (Sc_2O_3). Results showed that the tested multicomponent, more precisely, multiphase coatings had significantly lower thermal conductivities and better thermal stability, mainly in the lower total dopant concentration (which varied between 4.5 to 52.5 % mol) when compared with ZrO_2–8 wt. % Y_2O_3 coating. The defect cluster coatings consisted of a 180–250 μm thick ceramic top coat, a 120 μm thick

NiCoCrAlY or NiCrAlY bond coat, and finally a 3.2 mm thick nickel superalloy. In summary, it was proven that the oxide defect cluster have the potential to achieve better cyclic performance than the binary ZrO_2–Y_2O_3 coatings owing to their high temperature stability, reduced grain growth, and hence increased toughness structures. Nevertheless, it was pointed out by the authors that the ceramic coating cyclic life generally decreases as the dopant concentration increases due to the reduced fraction of tetragonal phase and the increased fraction of the cubic phase. The fully stabilized cubic phase normally shows an enhanced grain growth behavior, and also lacks the additional grain-refining and toughening mechanism by the tetragonal to monoclinic phase transformation which is present in a partially stabilized tetragonal phase. Therefore, in high-dopant-concentration coating, a very low toughness of coating structure was distinguished.

In a subsequent research, Zhu et al. (2005) [81], proposed similarly an advanced alternative oxide ceramic compounds, low-conductivity and high stability TBC based on an oxide defect-clustering design approach, but obtained this time *by applying a laser high-heat-flux thermal conductivity technique*. The laser test approach emphasized real-time monitoring of the coating conductivity at high temperatures to evaluate its performance under engine-like heat-flux and thermal gradients. Briefly, the advanced oxide coatings were designed by incorporating multicomponent, paired-cluster rare–earth oxide dopants into conventional zirconia– and hafnia–yttria oxide systems. The dopant oxides were selected by considering their interatomic and chemical potentials, lattice elastic strain energy, polarization, as well as electro-neutrality within the oxides. Selected oxide cluster TBC systems including ZrO_2–Y_2O_3–Nd_2O_3(Gd_2O_3,Sm_2O_3)–Yb_2O_3(Sc_2O_3) were synthesized, and their conductivity and sintering behavior were investigated. The aim of the carried tests was to essentially promote a production of thermodynamically stable, highly defective lattice structures and/or nanoscale ordered phases which would in turn *reduce oxide coating thermal conductivity and improve coatings sintering resistance*. The study highlighted as conclusion that despite of similar trend between the advanced oxide cluster coatings and the binary ZrO_2–Y_2O_3 coatings in the *furnace cyclic behavior* (where, as discussed, the cyclic lifespan generally decreased with the increase of total dopant concentration), the oxide cluster coatings showed promise to have significantly better cyclic durability (comparable to that of zirconia–4.55 mol % yttria) than the binary ZrO_2–Y_2O_3 coatings with equivalent dopant concentrations.

Further improvements are expected in defect cluster TBC's by utilizing advanced coating architecture design, dopant type and composition optimization, and improved processing techniques [79, 80, 81].

3.2.3.2 Perovskites

Perovskite oxides are a class of **ABO_3** crystal structure which can accommodate a wide variety of ions in a solid solution including ions with large atomic mass. Perovskite-type

oxides have been favored by researchers because of their enthusiastic structure features and properties, especially ABO3 (A = Ca (Calcium), Sr (Strontium), Ba (Barium); B = Zr, Ti (Titanium), Ce (Cerium)) perovskites. The major advantage of using perovskite oxides as thermal barrier coatings is its 20 % lower thermal conductivity than YSZ, which provides good thermal stability at high temperatures [75, 82, 83, 84, 85].

In greater depth, materials exhibiting perovskite structure, have attracted much attention as YSZ replacement mainly due to their *high melting point* (higher than 1800 ^{o}C), *high thermal expansion coefficient* (higher than 8.5×10^{-6} K^{-1}), *relatively low thermal conductivity* (lower than 2.2 W/mK) and *low Young's modulus* (approximately 210 GPa). The biggest drawbacks of materials exhibiting *simple* perovskite structure are mainly their inferior fracture-related mechanical properties, as well as the partial evaporation of constituents of the perovskites phase during plasma spraying process, which leads to impurity phases in the coating, that, in turn, often have detrimental effects on the coating performance [83, 86].

Nonetheless, it is highly important to mention that perovskites offer the possibility of extensive substitution of ions at the A or/and B site, thus allowing their properties to be tailored towards specific requirements [87]. The well-known and studied simple perovskite oxides materials for TBC applications are strontium zirconate ($SrZrO_3$), barium zirconate ($BaZrO_3$), and calcium zirconate ($CaZrO_3$) [88].

The early candidate for TBC applications, **$BaZrO_3$**, draws attention in the first place due to its *high melting temperature of 2600 ^{o}C*, however both *relatively poor thermal expansion coefficient* and *interior chemical stability* induce the coating to failure in the course of thermal cycle tests, minimizing this way the TBC service lifetime [84]. Contrarily, **$SrZrO_3$** exhibits a better performance on these cyclic tests with surface temperatures above 1250 ^{o}C with respect to its *high melting temperature (2800 ^{o}C)*, *relatively low thermal conductivity*, and *high thermal expansion coefficient* of $\sim11\times10^{-6}$ K^{-1} (30–1000 ^{o}C). Therewithal both the sintering rate and Young's modulus of $SrZrO_3$ are lower than those of YSZ as well, which is of assistance to favorable mechanical responses [84, 87, 89]. Unfortunately, this perovskite has been reported to suffer temperature-induced phase transformation that has a detrimental effect on the performance of this type of TBC material. Some studies highlighted that such transformation could be suppressed by doping gadolinium oxide (Gd_2O_3) or ytterbium(III) oxide (Yb_2O_3) in addition to enhance thermophysical properties of the coatings [89].

Vassen R. et al. (2000) [82] investigated both $BaZrO_3$ and $SrZrO_3$ materials as new thermal barrier coatings, focusing on their properties. Similarly, Ma W. et al. (2008) [89] focused on both $SrZrO_3$ and $SrZrO_3$/YSZ double-layer coating thermophysical properties in addition to thermal cycling behavior. More recently, Qiao Z. et al. (2022) [85] con-

sidered the co-doping mechanism regarding the $BaZrO_3$ at A-B sites instead of limiting the doping modification of this material at either A or B sites. As outcome, a characterization was conducted on the composition, structure, mechanical properties and thermal conductivity.

Lastly, **$CaZrO_3$** on the other hand is the latest material to be considered for TBC application in this group. Although its melting temperature is lower than that of YSZ, it has an encouraging thermal conductivity of approximately 2 W/mK and excellent mechanical properties [85, 89, 90, 91]. For instance, Garcia E. et al. (2008) [90] carried out a comparative study of $CaZrO_3$ coatings prepared by air plasma and by flame spray processes. Results showed that the two techniques produced coatings with different microstructures and thus properties. All of coatings were porous, but the flame sprayed ones exhibited interplast cracks whereas atmospheric plasma spraying coatings had larger round pores. Nevertheless, all the $CaZrO_3$ coatings showed very low thermal conductivity.

Generally speaking, perovskites may be subdivided into the discussed *zirconates* and *complex forms*. Under the concept of compositional control of properties, complex substituted structures have also been a focus of studies as YSZ substitutes. In particular complex forms, with a $\mathbf{A(B'}_{1/3}\mathbf{B''}_{2/3}\mathbf{)O}_3$ structure, such as $BaLa_2Ti_3O_{10}$, $Ba(Mg_{1/3}Ta_{2/3})O_3$, and $La(Al_{1/4}Mg_{1/2}Ta_{1/4})$ have promising bulk properties for TBC applications [76, 84, 89]. However, the thermal expansion coefficients of these materials are still lower than those of substrates and bondcoats, leading to thermal stresses in TBC systems. Moreover, relatively low toughness values are observed. As a result, the thermal cycling properties are poorer than those of YSZ coatings and further improvements are necessary [78]. Application of complex perovskites as TBC was considered by Jarligo M. O. et al. (2009) [83] that concluded that these compounds show a promising TBC performance since the means to control the propagation of interfacial cracks from TGO along the interface of the coatings were proven possible.

3.2.3.3 Pyrochlores

Among the interesting candidates for TBCs applications, the group of pyrochlore-structured oxide compounds gained gradually importance as advantageous ceramic top coats to replace the state-of-art YSZ. The features that have drawn special attention is their distinctive arrangement of ions and vacations within the $A_xB_xO_z$ (or also sometimes found in the literature as $A_2B_2O_7$) compositional structure where the first metal cation A is a rare earth element, typically a lanthanide such as lanthanum (La), gadolinium (Gd), neodymium (Nd), yttrium (Y), etc., and the second metal cation such as Zr, Hf, titanium (Ti), or molybdenum (Mo). The vacancies at A^{3+}, B^{4+} and O^{2-} sites make the composition flexible to design for achievement of attractive material properties by incorporating of other RE elements [92]. Materials with pyrochlore structures show excellent thermophysical properties of these materials, i.e., *high melting point*, *stable phase conditions and morphology*

at temperatures up to 1400 °C, relatively high coefficient of thermal expansion, low thermal conductivity, and, mostly, *pronounced CMAS resistance*, which make them suitable for applications as high-temperature thermal barrier coatings. Conversely, the thermal expansion coefficient lower ($9–10\times10^{-6}$ K^{-1}) than that of YSZ ($10–11\times10^{-6}$ K^{-1}) may lead to higher thermal stresses in the TBC system as both substrate and bondcoat have higher thermal expansion coefficient (about 15×10^{-6} K^{-1}) [92, 93, 94, 95].

Out of pyrochlore materials, especially interesting candidates are lanthanum zirconate, LZ ($La_2Zr_2O_7$), gadolinium zirconate, GZ ($Gd_2Zr_2O_7$), cerium zirconium oxide ($Ce_2Zr_2O_7$), samarium dititanium oxide ($Sm_2Ti_2O_7$), dilanthanum dihafnate(IV) ($La_2Hf_2O_7$), and neodymium zirconate ($Nd_2Zr_2O_7$) [95].

Specifically, $\mathbf{La_2Zr_2O_7}$ seems to be one of the most promising for TBC application due to its outstanding bulk properties compared to standard YSZ with a high thermal stability up to 2000 °C, a low thermal conductivity of 1.56 W/(mK) and eminent sintering resistance. A major drawback however is the relatively low thermal expansion coefficient of about 9×10^{-6} K^{-1} compared to YSZ with $10–11\times10-6$ K^{-1}, which leads to higher thermal stresses from thermal expansion mismatch, and poor toughness responsible of lowering the thermal cycling life time use of LZ as TBCs. In this regard, the higher thermal expansion coefficient of 1.1×10^{-6} K^{-1} of $Gd_2Zr_2O_7$ is advantageous [92]. To overcome the thermal cycling lifetime issue of LZ pyrochlore, Vaßen R. et el. (2004) [95] suggested a pyrochlore/YSZ double layers systems based on $La_2Zr_2O_7$ and $Gd_2Zr_2O_7$ pyrochlores. Results showed similar performances to YSZ coatings at temperatures below about 1300 °C. At higher temperatures, however, double-layer systems coatings revealed excellent thermal cycling behavior, i.e., at the highest test conditions, lifetime was thereby orders of magnitude better than that of YSZ coatings.

In another study, Bansal N. et al. (2007) [96] focused on lowering even further the thermal conductivity of pyrochlore oxide compounds. An oxide doping approach was used where part of cation A was substituted by other cations, e.g., $A_{2-x}M_xB_2O_7$ (where x = 0–0.5 and M = RE or other cation) in the pyrochlore materials. Pyrochlore oxide powders of various compositions were synthesized by sol-gel process and hot-pressed into 2.54 cm diameters discs whereas the thermal conductivity was measured using a steady-state laser heat flux test method. It was concluded that the performed investigation was successful since doping with RE cations at the A sites in $La_2Zr_2O_7$ ($A_2B_2O_7$) pyrochlore greatly reduced the thermal conductivity. Yang et al. (2018) [97] investigated and synthesized the pyrochlore-related Sm_2FeTaO_7 compound as a potential material for TBCs top coat with low thermal conductivity, better mechanical properties, and high-temperature phase stability. It was concluded that the compound had low thermal conductivity values (approximately half of YSZ), due to a complex and distorted crystal lattice, high concentration of defects, and large differences in atomic mass of cations. Lastly, Che J. et al. (2021) [98] considered

and studied the sintering behavior of nanostructured pyrochlore-type $La_2(Zr_{0.7}Ce_{0.3})_2O_7$, designated as LZ7C3, using experiments and molecular dynamics. It was proven than the novel LZ7C3 compound exhibited significantly higher sintering resistance than the host $La_2Zr_2O_7$ and typical 8YSZ at temperatures up to 1773 K. Hence, it was concluded that LZ7O3 is a promising TBC topcoat at high temperatures that could substitute YSZ.

3.2.3.4 Hexaaluminates

Two important thermophysical properties influence the lifespan of a TBC materials, which are thermocycling and thermal shock resistance. These parameters are mainly influenced by the microstructure, the coefficient of thermal expansion and aging behavior of the TBC material [99]. Lanthanum hexaaluminate (LHA) with magnetoplumbite structure has proven to be a promising competitor to the state-of-art yttria stabilized zirconia as a TBC material, especially bearing in mind that most of zirconia-based coatings age significantly due to thermal loads, and thus include undesired densification at temperatures exceeding 1200 ºC. Fortunately, in contrast to zirconia, lanthanum hexaaluminate permits operating at high temperatures owing to its *high temperature thermal stability* (up to 1600 ºC), and *electrical insulating properties*. Besides these features, LHA particularly possess *high melting point*, *high thermal expansion*, *low thermal conductivity*, *high fracture toughness*, and *outstanding sintering resistance*, since such kind of oxides usually crystallize in hexagonal platelet-like grains [99, 100]. In conclusion, LHA materials have both superior thermochemical and thermophysical characteristics which grants them an attractive thermal cycling lifespan making them a sublime candidate material for TBC application. As last remark, oxides with magnetoplumbite structure have a nominal composition of $LnMAl_{11}O_{19}$ (Ln = La *to* Gd; M = Mg (Magnesium), Mn (Manganese) *to* Zn (Zinc), Cr (Chromium) or Sm (Samarium)) [101]. Some specific examples of investigated LHA materials for TBC applications are $LaMgAl_{11}O_{19}$, $LaZnAl_{11}O_{19}$, and $LaTi_2Al_9O_{19}$ [102].

In greater detail, among LHA materials, LaMgAl11O19 (also known as LaMA or LMA) is the one that has been the most widely studied during the last decades. LaMA with magnetoplumbite-type structure displays naturally as its analogues a high thermochemical stability, a superior sintering resistance, and a high fracture toughness [103]. Furthermore, LaMA single–layered coating is the only one that exhibits a close thermal cycling lifetime of the traditional YSZ coating at the similar testing conditions. However, the relatively lower CTE than traditional YSZ in combination with the recrystallization behavior – that reduces the bond strength between the ceramic coating and the bond coat – results in the single LaMA coating to be less durable under higher service temperatures. The recrystallization issue forces the LaMA to have some shortcomings [104]. On one hand, the ED-PVD LaMA coating, usually characterized by the columnar structure, with superior strain tolerance and service lifetime has shown difficulties in being successfully prepared; whereas, in the plasma sprayed LaMA coating, partial decomposition of LaMA oxide usually occurs, originating this way a large amount of amorphous phase due to the

rapid quenching from the molten state. Therefore, the following recrystallization of the coating during high temperature service may compromise the reliability of the LaMA layer in terms of variation of the heat capacity of the material, that consequently will have a strong influence on the thermal conductivity, as well as in CTE giving rise to the formation of residual stress [75].

Chen X. et al. (2011) [105] approached this problem and investigated the thermal aging behavior of plasma sprayed LaMgAl11O19 thermal barrier coatings. LaMA powders were synthesized by a solid-state reaction method. La_2O_3, $\gamma-Al_2O_3$, and MgO were selected to be the starting materials. Results showed that the recrystallization and grain growth rates can be significantly accelerated when LaMA coating is isothermally aged at temperature above 1173 K. The well crystallized LaMA coating exhibited improved properties, such as reduced microhardness with the consequence of enhanced strain tolerance and thermal shock resistance, as well as CTE and heat capacity close to its bulk counterpart. Furthermore, to overcome the mentioned drawbacks of LaMgAl11O19 – relative lower CTE than traditional YSZ in combination with the recrystallization behavior – double–ceramic top coat TBCs based on LaMA/YSZ systems were studied. For instance, Chen X. et al. (2011) [106] evaluated the thermal cycling failure of $LaMgAl_{11}O_{19}$/YSZ double ceramic top coat material, and with the help of two different types of LaMA/YSZ composite coatings, the weak bond strength at the interface of LaMA and YSZ were addressed. Preliminary results exhibited improved strain tolerance and thermal cycling lifetime in comparison to single layer YSZ and LaMA coatings. It was namely noticed that specific crystal chemistry in addition to the nano-crystallization of LaMA coating induced by recrystallization during thermal cycling also made contribution to further enhance the LaMA layer-containing LaMA/YSZ double ceramic TBCs. On top of that, functionally graded thermal barrier coatings systems based $LaMgAl_{11}O_{19}$ and YSZ designed and prepared by APS were introduced to improve the durability and temperature capability of LaMA top coat materials. For instance, Chen et al. (2012) [107] prepared a new five-layer quasi-gradient functionally graded thermal barrier coating based on $LaMgAl_{11}O_{19}$/YSZ whose microstructure, thermal and mechanical properties were investigated. It was proven that the burner-rig thermal cycling lifetime increased by approximately 50 % in comparison with the double-layered TBCs of the same ceramics. More recently and to further understand the factors related to thermal cycling lifetime, Chen et al. (2020) [108] analyzed three multilayered TBCs similarly based on LaMA/YSZ, but this time with different variations in composition and thickness of the intermediate gradient layers.

The following **Table 3.2** serves as a summary of properties, discriminated as *advantages* and *disadvantages*, of the materials and categories of materials discussed throughout this last subsection.

Table 3.2: Summary of parallel research on material alternatives to YSZ that could be used as TBCs based on [75, 76].

Category	Material	Advantages	Disadvantages
Zirconium oxide	7–8 wt. % Y_2O_3 + 92–93 wt. % ZrO_2	Low thermal conductivity High thermal expansion coefficient Thermal shock resistance High fracture toughness	Sintering above 1473 K Phase transition above 1443 K Corrosion resistance Oxygen transparent
Zirconium Oxide-doped	Al_2O_3 (Alumina)	High bond strength and hardness Corrosion resistance *No oxygen transparent*	Phase transition above 1273 K Low thermal expansion coefficient High thermal conductivity
	YSZ + CaO	Lower thermal diffusivity Corrosion resistance	Destabilization Sintering effect above 1300 K
	YSZ + MgO	Low thermal conductivity High thermal expansion coefficient	Low strength Low erosion resistance
	YSZ + CeO_2	Low thermal conductivity High thermal expansion High thermal shock resistance High corrosion resistance Low phase transition	High sintering rate CeO_2 precipitation (>1373 K)
Defect cluster (ZrO_2/HfO_2–Y_2O_3 -RE oxides)	ZrO_2–Y_2O_3–Gd_2O_3–Yb_2O_3	Low thermal conductivity High thermal stability High sintering resistance	Low toughness (with increasing dopant-concentration)
Perovskite oxides (simple form, ABO_3)	$BaZrO_3$ (Barium Zirconate)	Low sintering rate	Low thermal shock resistance Low thermal expansion coefficient Poor thermal and chemical stability
	$SrZrO_3$ (Strontium Zirconate)	Low thermal conductivity High thermal expansion coefficient Low sintering rate	Phase transition Low thermal shock resistance
	$CaZrO_3$ (Calcium Zirconate)	Low thermal conductivity Good thermal shock resistance High chemical stability	Anisotropic crystalline thermal expansion
Pyrochlore Oxides ($A_xB_xO_z$ or $A_2B_2O_7$)	$La_2Zr_2O_7$ (Lanthanum Zirconate)	High thermal stability Low thermal conductivity High hardness Low sintering rate High temperature capability	Highly prone to decomposition during plasma spraying Low thermal expansion Poor toughness Low lifetime
	$Gd_2Zr_2O_7$ (Gadolinium Zirconate)	Good resistance to CMAS attack Cost effective with YSZ	Prone to decomposition during plasma spraying Low lifetime
Lanthanum compounds	LHA (Lanthanum Hexaaluminates)	Low thermal conductivity High thermal expansion coefficient Better thermal stability Low sintering rate	Crystallization
	$LnMAl_{11}O_{19}$ (Lanthanum Aluminate)	Low thermal conductivity High thermal expansion coefficient Low sintering rate	Low hardness
	Rare Earth Oxides	High thermal expansion coefficient Lower thermal diffusivity Cheap Readily available	Phase instability Low thermal shock resistance

3.3 Dielectric Barrier Discharge (DBD)

At first sight, matter is assumed to exist only in three major states, this is, solid, liquid, and/or gas. Nevertheless, by increasing the kinetic energy of the particles, matter can change – in the mentioned sequence – its states. Specifically, when enough energy is added to a gas, it starts to get partially ionized and transforms into the so-called fourth state of matter, or simply put, *plasma* [109]. Plasma is often defined as *quasi-neutral gas containing charged and neutral particles* which possess collective behavior. The announced *collective behavior* allows to evaluate the reaction of plasma to deviations from neutrality and applied external electromagnetic fields, in addition to its ability to sustain many different forms of waves and oscillations [110, 111]. Essentially, one may say that plasma contains electrons, neutrals, electronically and vibrationally excited species, ions, radicals, and atoms [110]. Plasmas can be broadly classified into two major categories: thermal and non-thermal plasmas (NTP).

On one hand, *thermal plasmas* are considered to be in thermodynamic equilibrium and all their constituent particles have the same temperature. They are generated at high pressure with high excitation energy. Flame and fusion plasmas are clear examples of thermal plasmas. Also designated as hot plasmas, they can be detected in space whereas earthly applications are mainly constrained to astronomy research, fusion reactors, particle accelerators and other particles' physical research [109, 110]. On the other hand, *non-thermal plasmas* are not in thermodynamic equilibrium, and therefore different particles show different characteristic temperatures or degrees of freedom. Non-thermal plasmas have found extensive applications *at low and atmospheric pressures* due to their low enthalpy, which makes their study relatively simpler compared to the thermal ones. Also termed as *cold plasmas* or as *non-equilibrium plasma* – since the electrons temperature, T_e, is several orders of magnitude higher than the temperature of the ions, T_i, or of the neutral gas, T_g – they require smaller energy input and are generated by the application of electrical fields. Most plasmas of practical interest are non-equilibrium plasmas, considering that their usage is based on the high energy of electrons and chemically active species. Therefore, an increase in the gas temperature constitutes an unwelcome side effect because it misspends the input energy designed to generate plasma and originates additional complications, for example, the need for cooling techniques and devices [110, 111, 112, 113].

In many applications of plasmas and gas discharge techniques, it has been proven that atmospheric pressure conditions are favorable or even required [113]. These discharges (at atmospheric pressure) are found in the region between a *glow discharge* and an *atmospheric arc discharge*. To give better insight, glow discharge has a *low gas temperature* ($\sim 300K \approx 0.025$ eV), a *high electron temperature* ($\sim 11000K \approx 1$ eV), and a *low degree of ionization* (% of gas molecules or atoms that are ionized). Thermal arcs are *close to thermal equilibrium*, so electron and gas temperatures are within 1 % of each other ($T_e \approx T_g \sim 10000$ K) [111].

Finally, and as a last introductory remark, it is important to emphasize that an *electrical discharge* is a process employed to fabricate man-made plasma by inducing a high electrical voltage. These electrical discharges occur when an insulating medium becomes partially or completely ionized to an electrical field. Consequently, discharges produce plasma in some regions of the discharge area or/and at specific time intervals during the whole process [111, 114]. Different physical mechanisms of creating non-thermal plasma based on electrical discharge exist, including the mostly known corona discharge and dielectric barrier discharge [109, 110, 111, 112].

The following **Figure 3.10** summarizes some of the applications of man-made plasmas in several fields, such as catalysis, materials synthesis, cleaning, biochemistry and medicine, and fusion reactions studies.

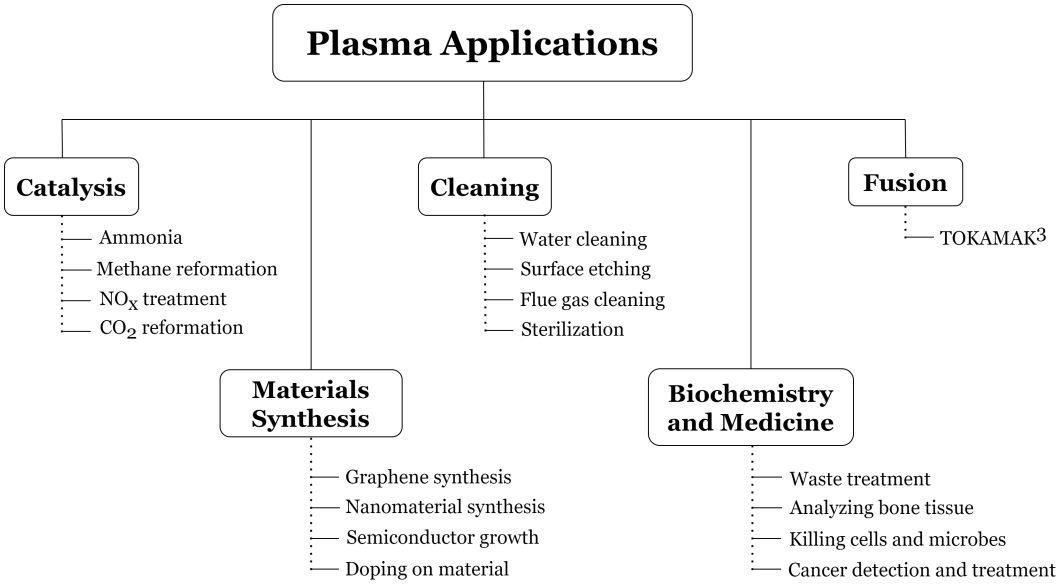

Figure 3.10: Plasma applications in different research fields.

3.3.1 Introduction to DBD

Dielectric barrier discharge, or DBD, mechanism has been introduced for more than a century and a half and its research continues to suffer ongoing technological development as well as industrial exploration on a large scale [114, 115, 116]. Dielectric barrier discharge (also known as *barrier discharge*, *silent discharge*, or *ozonizer discharge*) is a mechanism that is ignited by applying a high voltage – both at low and at atmospheric pressure

[3]The TOKAMAK (i.e., toroidal chamber with magnetic coils) is an experimental device which uses a powerful magnetic field to confine plasma in the shape of a torus. In essence, a TOKAMAK consists in thermonuclear fusion power,or, in other words, a machine designed to harness the energy produced through fusion of atoms, which is absorbed as heat in the walls of the vessel.

– between two electrodes wherein at least one of the electrodes is insulated by a dielectric, as depicted in **Figure 3.11** [115, 117, 118]. Typically, the dielectric materials used – of low dielectric loss and high breakdown strength – may be glass, quartz, ceramics, enamel, mica, plastics, silicon rubber, or teflon [109, 115, 116].

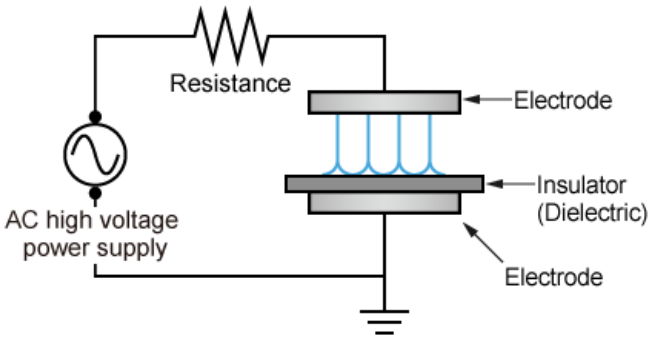

Figure 3.11: Scheme of a dielectric barrier discharge setup [118].

By using an insulator – that works in the same way that a capacitor (i.e., a passive electronic component (with two terminals) which is a device that stores electrical energy in an electric field), – many fine plasma *filaments* usually are formed between the electrodes; and the formation of a spark or an arc discharge is thus prevented[4] [117, 118, 119, 120]. Worth emphasizing that these filaments (also called *microdischarges*) have a *random distribution over the dielectric surface*, as well as a very *short lifetime*, more precisely in the range of a few nanoseconds. This happens due to the accumulation of the charge carriers on the dielectric surface, which generates an opposite field to the externally applied voltage so that the discharge disappears again. Consequently, DBD microplasmas are often considered and recognized as *self-limited* in time and space, and, as pointed by Bruggeman and Brandenburg, *intrinsically transient* [113]. Additionally, in DBDs, microdischarges are observed in every half cycle of the applied voltage, as shown in **Figure 3.12**.

For this reason, DBDs are operated with AC (alternate current) voltage typically at several kilohertz [117]. Namely, as a consequence of the low lifetime of the discharge, the heavy particles are able to absorb far less energy from the alternating field than the lighter and faster electrons. Therefore, the DBD gives rise to a non-thermal cold plasma in which, as already described, the electrons have an elevated temperature, but the ions and the neutral gas are at room temperature [117, 118].

[4]With increasing pressure and neutral gas density, gas discharge have the tendency to become non-uniform, unstable and constricted. Consequently, a glow-to-spark/arc transition occurs. This way, it is fundamental to accurately design and control some parameters, such as the use of special geometries, the electrode arrangements, the excitation methods and other techniques to obtain non-equilibrium plasmas at elevated pressures [113].

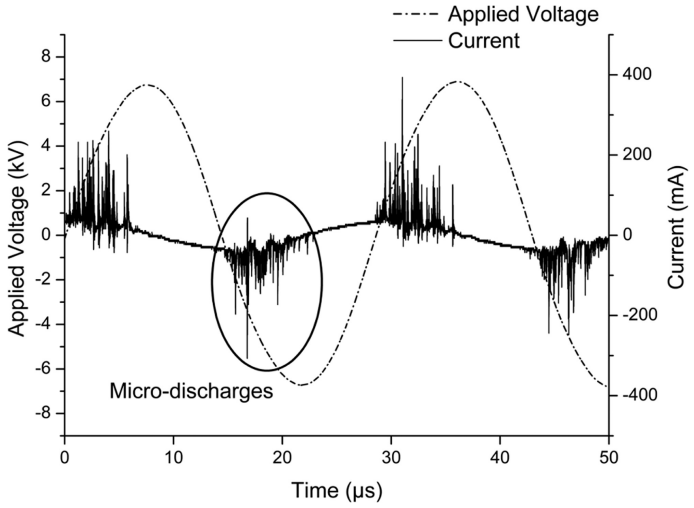

Figure 3.12: Microdischarges (filaments, or channels) typical representation based on a graph of applied voltage (left axis) and resulting current (right axis) as a function of time [118].

Table 3.3 presented below summarizes and highlights some of the characteristic properties of a microdischarge channel in air, at atmospheric pressure, for clarification purposes on the parameters involved in the described process.

Table 3.3: Properties of microdischarge channels [111, 121].

Characteristic properties of microdischarge channels	
Duration (lifetime)	a few nanoseconds
Radius of filament	50 - 100 μm
Peak current	0.1 A
Current density	10^6 - 10^7 A/m^2
Total transported charge	10^{-10} - 10^{-9} C
Electrons density	10^{14} - 10^{15} cm^{-3}
Mean electron energy	1 - 10 eV
Gas temperature of microdischarge	near room temperature, about 300 K

In summary, the main aspects that must be considered, since they influence the general performance of dielectric barrier discharge plasma actuators, are (a) geometry (configuration), (b) dimensions of the electrodes, (c) gap between the electrodes, (d) dielectric thickness, (e) dielectric material, (f) applied voltage, (g) voltage waveform, as well as (h) AC frequency. It is important to realize that the influence of these parameters is highly nonlinear and interdependent which regrettably makes it more difficult to design, optimize and mathematically model these devices. For this reason, the continuous investigation of dielectric barrier discharge plasma actuators is crucial to guide their future implementa-

tion for several applications. Despite the above mentioned, the most important characteristic of DBD devices is that non-equilibrium plasma conditions can be provided in a much simpler way than based on other existing alternatives – for instance, low-pressure discharges, fast pulsed high-pressure discharges, or electron beam injections. Its flexibility concerning geometrical configurations, operating medium, and operating parameters is unprecedented [122]. Therefore, advantages such as low costs associated with the construction of reactors, low-frequency power supply needed, as well as easy scalability by numbering-up make dielectric barrier discharge an attractive and easily adaptable technology to a particular desired application [109, 117].

In the literature can be found that the DBDs are predestined for a large volume of applications, including ozone and UV generation, plasma display panels of large-area flat television screens, pollution control by air and wastewater treatment, sterilization of packing and food, as well as activation, cleaning, etching, and coating of surfaces [117, 121, 122, 123].

3.3.2 DBD Actuators Classification System

Based on the described general working principle of the DBDs mechanism, as well as the different existing applications, dielectric barrier discharge designs may be divided into *two main categories*. It is noteworthy that the classification of configurations is distinguished by the *presence* and *usage* of insulating material in the discharge path [109, 124].

- If the space between the electrodes includes both a dielectric and a discharge gap, the plasma is therefore ignited in the *volume* existing between the two electrodes. In that case, the DBD is considered a *volume dielectric barrier discharge*, or *VDBD geometry*. As shown in **Figure 3.13**, the schemes (a) to (c) represent the so-called *planar configurations* of VDBDs in which the dielectric(s) is (are) placed in different positions, in (h) is depicted a cylindrical setup, and, lastly, in (i) a packed-bed DBD setup may be observed [109, 115].

- Otherwise, in case the space between the electrodes is completely filled by a dielectric, the plasma is consequently ignited on the *surface* of the dielectric exposed to the gas volume. In that case, the DBD is named a *surface dielectric barrier discharge*, or *SDBD geometry*. Still in **Figure 3.13**, in (d) and (e) a symmetric and an asymmetric single-sided SDBD are shown, respectively, in which the plasma is ignited around the powered electrodes, in (f) a coplanar design is represented, and, finally, in (g) a symmetric double-sided setup is illustrated [109, 115].

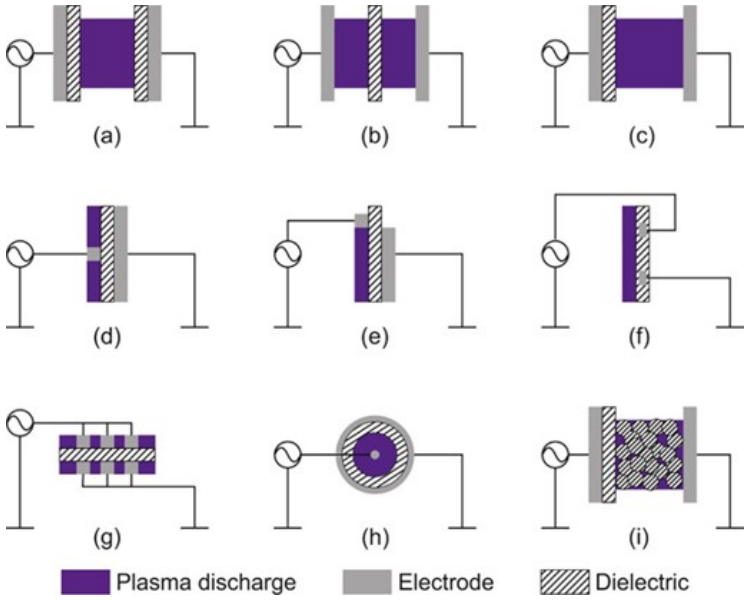

Figure 3.13: Different configurations of VDBD and SDBD geometries [109].

It is important to highlight that the SDBDs, **Figure 3.14**, have been considered for space applications for decades. Since the 1990s, the surface dielectric barrier discharge actuators – which are non-equilibrium plasma devices capable of generating forces in air without any moving parts – are considered an engaging technology in the aerospace sector. Overall, their appealing features, such as their *mechanical simplicity*, *lightweight*, *planar and low drag-structure*, as well as *relatively low-performance power levels consumption* make them a great choice for, for example, aerodynamic flow control and aircraft propulsion investigations [123].

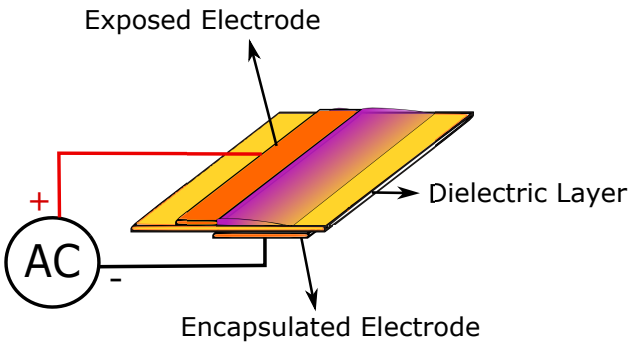

Figure 3.14: Schematic representation of a surface DBD (SDBD) plasma actuator configuration [125].

As a last remark of this subsection, it is noted that the various investigations and adaptations of DBDs on different problems have directed this technology towards the adoption of several *special configurations*. Just to name a few, *DBD-based plasma jets actuators*, *multiple encapsulated electrode plasma actuators*, *nanosecond-DBD* (i.e., NS-DBD), *sliding discharges*, and *capillary plasma electrode discharges* have been demon-

strated and applied in numerous studies over the last few years with special focus on the aeronautical and aerospace fields [115, 124].

3.3.3 DBD Technology in Aerospace and Aeronautical Sectors

The origin of the dielectric barrier discharge is attributed to Ernst Werner von Siemens in 1857 [114, 115, 116, 122]. The first experimental investigations performed by Siemens et al. were focused on the generation of ozone and the experiment discharge apparatus design featured many novel traits, including the electrodes positioned outside the discharge chamber, as well as they were not in contact with the plasma. For this reason, DBDs were considered *ozone discharges* for a long time [114, 116, 122, 126]. A few years after the original publications, in 1860, Andrew and Tait also conducted studies on the topic called the system *silent discharge* because of its quiet and silent discharge process. Such nomenclature is still frequently used in English, German and French scientific literature [114, 116, 126]. Later, in 1932, K. Buss made a notable contribution to characterize the discharge by reporting that the breakdown of atmospheric pressure air between planar parallel electrodes covered by dielectrics always gives origin to a large number of tiny short-lived current channels. First photographic traces – Lichtenberg figures – of these channels (or microdischarges); and oscilloscopes recording of current, in addition to the voltage applied were obtained [116, 122]. Further investigation on more detailed information on these channels (or filaments) was collected by several research groups, such as Klemenc et al. (1937), Suzuki (1950) Honda and Naito (1955), and later by Gobrecht et al. (1964), Bagirov et al. (1971), Tanaka et al. (1978), Hirth (1981) and Heuser (1984) [116, 122]. Despite all ongoing research mentioned through the years, in 1943, another key contribution was made by T.C. Manley who proposed a method for determining the dissipated power in DBDs by using closed voltage/charge Lissajous figures (i.e., a pattern shown in a graph of a system of parametric equations that describes the complex harmonic motion) and derived an equation that became known as the *power formula for ozonizers* [115, 126].

Over the last years, plasma actuators based on the dielectric barrier discharge mechanism have attracted much attention for aerospace and aeronautical applications [127]. Broadly speaking, the DBD actuators may be applied in conducting research regarding aerodynamic active flow control and heat transfer purposes [124].

(a) Plasma actuators for aerodynamic flow control and aerodynamic drag reduction

Active flow control is an important subject of study since it allows to improve the efficiency of several mechanical systems by enhancing their performance through both fuel consumption and environmental impact reduction [128, 129]. Thus, the ability to manipulate a flow field is crucial for the scientific community worldwide. Particularly, dielectric barrier discharge plasma actuators are a technology with great

characteristics for this aim, once it is characterized by an easy implementation (i.e., simple construction), absence of moving parts, extremely low mass, robustness, low power requirements, and fast response to electrical signals [128, 129, 130, 131]. From the practical point of view, this type of actuator allows modification of the airflow owing to the *electrokinetic conversion mechanism* which is called the *electrohydrodynamic (EHD) phenomenon*. The exploited *electrohydrodynamic force* originating from the electrohydrodynamic phenomenon is produced due to momentum transfer from charged species accelerated by an electrical field to neutral molecules by collision [128, 129]. On the whole, research regarding the plasma actuators for active flow control includes *turbulent boundary-layer separation control*, *steady airfoil leading-edge separation control*, *oscillating airfoil dynamic stall control*, and *circular cylinder wake control* [128].

- **Drag reduction:**
  Since the 1930s extensive research has been carried out on aerodynamic flow control, specifically on retaining laminar flow along with an aircraft's primary structures, such as wings and fuselage. The final goal is to through active flow control techniques, reduce the skin friction associated with the transition of laminar boundary-layer flow to the turbulent state to reduce the overall aircraft drag [132]. The need for minimizing the aerodynamic drag is justified by the limitations that it imposes on the fluid dynamic performance of any vehicle and consequently on its *stability*, *safety*, and *power consumption*, in addition to its general *efficiency* [133, 134, 135, 136]. For instance, the aerodynamic drag for commercial air vehicles, heavy highway vehicles, and high-speed trains may be compromised by up to 50 %, 65 %, and 70 %, respectively. Therefore, controlling the flow around vehicles for drag reduction purposes is vital and can have a profound impact on transportation applications [134, 136]. In the literature, to reduce skin-friction drag, flow control methods can be roughly divided into two categories, i.e., *passive* and *active tools* – in which the active approaches are based on the manipulation of the near-wall flow properties [136, 137]. Ever since its first reported success that plasma actuators have been the focus of detailed investigations for improving the authority of flow control in a wide range of industries – owing especially due to their applicability on a surface without significant change of geometry, fast time-response, small size, and static parts [134, 135, 136]. In the field of drag reduction, DBD plasma actuators have proven to be capable of *modifying the laminar-to-turbulent transition*, *enhancing jet vectoring*, and *reattaching separated flows* [135].

- **Noise reduction:**
  Furthermore, the noise produced by an aircraft and, consequently the emerging need for noise reduction, has been proven to be a relevant topic of research, in modern aeronautics, both by academic, as well as industrial centers over the

past few decades [137, 138]. Specifically, due to urban expansion (shift of urbanized sectors closer to airports), and an increasing number of aircraft operations, noise owing to airport activities has negatively impacted the environment. Consequently, this phenomenon has been forcing authorities to implement restrictions on tolerable levels of noise [138]. The source of the aircraft noise is its different components, and the interaction of external flow and the aircraft parts produced during the different phases of flight according to the aircraft performance studies [137, 138, 139]. Therefore, an approach that considers different noise sources is required for effective noise reduction [140]. Two types of solutions may be applied for this end (similarly to the drag reduction issue): *passive flow control* or *active flow control*. On one hand, *passive flow control* is unfortunately shown to be a mechanically complex mechanism that possesses high mass (i.e., it is heavy), is difficult to manufacture and maintain, and, even worse, degrades the aerodynamic performance of the vehicle once they are not capable to adapt to different conditions. On the other hand, *active flow control* demands the addition of energy to manipulate the airflow [138]. Bearing all this in mind, one proposed mean of accomplishing noise reduction is by using the dielectric barrier discharge plasma actuators due to all their key assets previously mentioned (i.e., among others, characteristic simplicity of the mechanism, absence of mechanical moving parts, and lack of need to physically alter or adjust the shape of the aerodynamic surfaces) [124, 137, 138, 139, 141]. Overall, the principle of using plasma actuators for aeroacoustic control relies on sufficiently modifying the flow field to disrupt or modify the mechanism of the generation of flow-induced noise – as flow and surface interaction represents one of the dominant sources of aerodynamic noise. Examples of aeroacoustic control are *cavity noise attenuation*, *noise control model development*, and *bluff body noise control* [139].

(b) Plasma actuators for heat transfer

Apart from the main described aerodynamic applications, dielectric barrier discharge plasma actuators devices can be considered and used within the field of heat transfer, for example, for film cooling of gas turbine blades, and heat generation for deicing or anti-icing objectives [131, 141]. In essence, the thermal behavior of DBD plasma actuators has great importance for these types of applications. Nevertheless, there have been a relatively limited number of studies reporting these applications [89].

- **Gas turbine film cooling:**
  As mentioned in the subchapter of 3.1, Thermal Protection Systems, film cooling is used in hypersonic vehicles by injecting a coolant at a discrete location on a surface of a structure that aims to protect it from high thermal stresses. Therefore, the fluid acts as a thin cool insulating blanket on the component to

be cooled, ensuring that the melting temperature is not exceeded. This type of cooling is considered an active cooling method with a relatively high degree of complexity since it depends both on the geometry and the flow parameters. Film cooling has become the main method applied to modern gas turbines that shields them from hot combustion gasses and thus increases the blades' lifetime [131, 142, 143]. Furthermore, the behavior of the actual turbine flow highlights the need for an active cooling technology that is able to adjust in time to maintain an efficient performance [142]. The concept of using plasma actuators for active flow control in case of film cooling enhancement was introduced by Roy and Wang in 2008, and it was shown by numerical simulations that – with the classical hole geometry – the application of plasma discharges could improve the film cooling efficiency up to 26 % [124, 142]. Other studies were conducted over the years; however, the general conclusion is the same: despite different boundary conditions or geometries of components to be cooled, the plasma aerodynamic actuation allows to improve the overall efficiency of the film cooling process by enhancing the adherence of the coolant working fluid (also called "coolant jet") [124, 144].

- **Plasma actuators for aircraft icing mitigation:**
  For years, aircraft icing has been recognized as a well-known weather hazard to flight performance, and consequently a threat to the overall flight safety [145, 146]. In more detail, the icing on critical parts of an aircraft, especially ice accretion on the airframe surfaces may cause large-scale flow separation due to airfoil and rotating blades geometry deformation – owing to contamination of the streamlined profile –, and thus significantly reduce aerodynamic performance. Aircraft icing occurs when small, supercooled, airborne water droplets impinge and freeze upon impact on the airframe components [147, 148, 149, 150]. In case the aircraft is exposed to icing conditions during a prolonged interval of time, it may even lose the ability to continue a stable flight [145, 146, 147, 148, 149, 150]. In fact, according to statistics, it was reported that of all the in-flight accidents due to weather, approximately, 12 % are related to the icing of aircraft, which may give rise to loss of both personnel and property [147]. Ice accretion may occur *on the ground* or *in flight* and can follow either by *dry growth* or *wet growth*. For the sake of clarity, during *dry growth* impinging droplets release latent heat quickly and freeze on impact. Dry growth is therefore related to *rime ice* that is characterized as white and opaque. Contrary, during *wet growth* droplets do not lose the latent heat quickly, so they can deform and run back along the incident surface. As a consequence, wet growth is related to *glaze ice* that is clear and glossy [149]. The ice accretion process is affected by several parameters, such as the *geometry of the componen*, *surface type*, *airspeed of the aircraft*, *temperature of the surface*, *droplet size*, as well as *liquid water content* (LWC) [149]. In an attempt to prevent

unwanted icing outcomes, several anti-/de-icing systems and methods have been developed for icing mitigation. Nevertheless, currently applied strategies and technologies are not sufficient to address the ever-evolving requirements in aerodynamics, materials, and energy consumption, since they are too complex, too heavy, or consume too much power to be effective [145, 148, 150]. Examples of these methods are freezing point depressants, pneumatic boots, hot-bleed-air anti-icing systems, and electrothermal heating, along with, hydrophobic materials or, also designated, superhydrophobic coatings [147, 149]. As a result, novel methodologies and techniques are sought to extend the durability and efficiency of anti-/de-icing strategies to ensure safer aircraft operation specifically in cold weather [145, 148, 150]. Van den Broecke was the first to conduct research on the feasibility and effectiveness of using DBD plasma actuators to remove ice accretion from a stationary flat plate. Currently, more studies were carried out on this topic and plasma actuation has gained great attention concerning icing mitigation due to its unique features [148, 150]. Finally, SDBD was defined by Jia Y. et al. (2022) [147] as a "novel anti-icing method featuring low energy consumption, geometrical simplicity, and rapid heating effect" and that depending on the driving waveform, both nanosecond pulse SDBD (nSDBD) and alternating-current SDBD (AC-SDBD) have been proven a verified through experiments technologies for anti-icing purposes.

3.3.4 Advanced Ceramic Materials for DBDs

DBD plasma actuators' performance may be predominantly considered in terms of their *three major features*, i.e., their *electrical parameters*, the *geometry chosen*, and *material properties*, of particular interest, the dielectric barrier materials properties. Despite the several advantageous features of DBD plasma actuators – listed through this subchapter –, one of the major weaknesses of these devices is their ***longevity***. As previously explained, when high voltages are applied between two electrodes separated by a dielectric to promote the ionization of encompassing air, the charged particles are therefore accelerated in the electric field and transfer momentum occurs through collisions of the surrounding air molecules. Naturally, during this plasma microdischarge process, the charged particles interact with the dielectric barrier and, consequently, after a sufficient period of time, may lead to its degradation or even premature dielectric breakdown, i.e., electric charging in the sense it no longer maintains its semiconductor properties.

Authors such as Moreau E. (2007) [151] Corke T.C. et al. (2009) [152], and Bernard and Moreau (2014) [153] have elaborated and published comprehensive reviews of physics, modeling, and experiments, as well as applications of the plasma actuators [149, 154]. In addition, several papers have namely elaborated on the properties of dielectric materials, as described by Bian D.L. et al. (2017) [154] and Rodrigues, F.M.F. (2018) [124]. For instance, parameters such as *dielectric thickness* and its influence on the DBD plasma ac-

tuator performance, the relationship between the concentration of *discharge filaments and the consequent dielectric breakdown*, as well as the *surface temperature* of the dielectric and its impact on the transition from glow to filamentary discharge have all been addressed on conducted investigations by several authors. Furthermore, both *novel dielectric barrier materials* and *material modifications*, focusing mainly on polymers – due to their simplicity of use – have also been part of current research regarding DBD devices [152]. Nevertheless, polymers have been reported to be very vulnerable to ion bombardment, radical species, and ultraviolet radiations that are emitted by plasma filaments in air at atmospheric pressure, thus making them extremely susceptible to material degradation, in addition to discrete thickness, and partial discharge between layers [124, 155].

As a result, ceramics appear a suitable substitute for the widely used polymers, since this type of materials offers several superior and favorable traits such as *corrosion resistance*, *high- and low-temperature resistance*, *excellent dielectric properties*, and *heat conduction* – which clearly highlights its possibility of being a good dielectric barrier in the years to come [154]. In spite of today's advancements in many technical and scientific fields, in standard applications of dielectric barrier discharges, a significant effort for extensive research in dielectric barrier layers is lacking in the literature [156].This becomes particularly concerning since physical properties and plasma-chemical efforts are highly dependent on the material of the dielectric barrier used. In other words, both surface and electrical properties of the DBD actuator are particularly influenced by the chemical composition of the dielectric barrier. These features are of utmost importance since they affect *charge accumulation*, *charge traps*, and *electric field distribution* in the vicinity of the dielectric surface [157, 158].

In an attempt to put emphasis on the most prominent investigations detected during the database and comprehensive searching on dielectric barrier materials, some studies will be summarized below.

Pons et al. (2008) [155] analyzed the surface degradation for two types of polymers as a dielectric barrier on a DBD actuator, i.e., polymethyl methacrylate (PMMA) and polyvinyl chloride (PVC) materials, and an afterward comparison with a borosilicate glass exposed to the same test conditions was performed. Images taken of both polymers showed clear degradation after operation in terms of roughness and burning. Pictures of PVC polymers showed color changing. Contrary to the evaluated polymers, images taken of borosilicate glass plates presented no obvious modification of the surface. It was concluded that this material is indeed more robust to chemical and radiation exposure. Additionally, glass (ceramic) dielectric barriers have been successfully utilized in many DBD experiments and have demonstrated improved resilience over organic materials, including epoxies and polymers, such as Kapton tape and polyimide film [154, 159].

In their studies, Zito J. et al. (2013) [159] fabricated microscale dielectric barrier discharge plasma actuators and experimentally characterized silicon dioxide for the dielectric barrier. Power, velocity, and thrust/force data were reported for several device geometries. In the final conclusions, it was stated that by using SiO_2 as a dielectric barrier the lifetime of the actuators was extended when compared with the first generation of DBD actuators, i.e., polymer dielectric material. Nevertheless, the authors also emphasized that, according to the results of induced velocities and thrust data, the increased device reliability – from using a ceramic dielectric – shows a clear trade-off with device performance. Furthermore, Fine N.E. and Brickner S. (2010) [160] proposed the addition of a heterogeneous catalyst on the surface of the dielectric exposed to the plasma as an approach to increase actuators' thrust. It was reported, according to the results obtained, that the use of titania (TiO_2) as a plasma catalyst allowed to increase the actuator thrust by 120 % when compared to a catalyst-free actuator.

In addition, in order to determine the time-resolved body force induced by a DBD plasma actuator motivated by the conflicting results in the literature on the correlation between induced body force, flow behavior and phase of the dielectric discharge, Neumann et al. (2013) [161] performed flow studies captured with a high spatial and temporal resolution. All measurements were carried out in a DBD placed in quiescent air. A ceramic dielectric manufactured using the low temperature co-fired ceramics technology (LTCC) was applied which, according to the authors, allowed the use of a very durable and lasting ceramic, which possibly will enable the future application of this material in harsh environments, such as turbomachines. In turn, Segawa et al. (2007) [162] elaborated a study on the characteristics of a dielectric barrier discharge plasma actuator under elevated temperatures – up to 600 ºC. In their study, the authors developed a DBD plasma actuator with ceramic and quartz insulators. Overall results verified the performance deterioration of both dielectric materials – alumina ceramics and quartz ceramics – with the increasing temperature from the room temperature to 500 ºC.

On top of all the investigations described, to obtain a homogeneous DBD in air at atmospheric pressure, many methods – including different types of barrier materials, different types of power supply, and different types of electrode arrangements – have been explored [59]. Ran J. et al. (2018) [163] focused their work on the factors that influence the formation of homogeneous dielectric barrier discharges at atmospheric pressure in air with a greater focus on dielectric properties on discharge modes. The experimental set-up featured plane-parallel electrodes which were covered with quartz plates of 0.5 mm to 1 mm thick or Al_2O_3 ceramic plates of 0.5 mm to 3.25 mm thick. It was found that the dielectrics play a crucial role in the formation of Atmospheric Pressure Townsend Discharge[5], or APTD, in the open air. Three dielectric characteristics were distinguished of major importance: *type of dielectric material*, *the thickness of the dielectric barrier*, and *surface roughness of the dielectric barrier*. Nevertheless, it was highlighted by the authors that

the rougher the dielectric material, the more the number of shallow traps, so the more electrons can be provided for the next half-cycle discharge of the DBD. In addition, it was shown that the surface roughness of the dielectric also reduces the breakdown electric field due to its uneven surface. The ceramics used in this study had more shallow traps than quartz glass, which explains the difficulties quartz has in generating homogeneous DBD in air.

As a follow-up, in their article, Ran et al. (2020) [164] approached the factors that affect the transition of discharge mode for obtaining a homogeneous atmospheric pressure dielectric barrier discharge in air. The surface morphology of different dielectric materials – quartz glass and ceramic – was given special attention. It was once again concluded that the surface morphology of different applied dielectric has indeed a remarkable influence on discharge mode and emission spectrum of the discharge.

A particularity of interest about DBD actuators is the efficiency of DBD plasma chemical reaction. In fact, this efficiency is expected to increase by increasing the permittivity of the barrier material, since the transported charge of plasma reaction is proportional to the permittivity of the dielectric material. Ceramics with high permittivity tend to break by supplying a high voltage thanks to their modest dielectric strength, and therefore SiO_2 which has a low permittivity is generally used as a dielectric material [165]. Nevertheless, $MTiO_3$ (M = Ca, Sr, Ba) ceramics are actually recognized as a typical dielectric material possessing a variety of dielectric properties. Li R. et al. (2004) [165] investigated the sinterability, mechanical and dielectric properties of $Ca_{0.7}Sr_{0.3}TiO_3$ using $L_2Si_2O_5$ as a sintering additive. Followingly, the produced ceramic was applied as a dielectric barrier for the decomposition of CO_2. For comparison purposes, alumina and silica glass were also used as dielectric barriers. Results pointed out that the permittivities of the three types of ceramics at 100 ºC and 10 MHz were $Ca_{0.7}Sr_{0.3}TiO_3$ (207) $\gg$ alumina (10.4) > silica glass (4.6); and the CO_2 conversions greatly changed depending on the barrier materials in the same order as the permittivity, i.e., $Ca_{0.7}Sr_{0.3}TiO_3 \gg$ alumina > silica glass.

In the same train of thought, Song X. et al. (2016) [158] evaluated the $Ca_{0.8}Sr_{0.2}TiO_3$ ceramics' performance as a dielectric barrier, based on different amounts of glass addition, in the decomposition of carbon dioxide at atmospheric pressure. Several conclusions were reached, including the feasibility of using $Ca_{0.8}Sr_{0.2}TiO_3$ for the decomposition of CO_2, both the conversion rate and the conversion efficiency increase with increasing glass content, and, lastly, the high glass content may increase the number of electrons near the surface of the dielectric barrier.

[5]The Townsend discharge consists in a gas ionization process where an initially small amount of free electrons, accelerated by a sufficiently strong electric field, give rise to electrical conduction through a gas by avalanche multiplication. Once the number of free charges drops or the electric field weakens, the phenomena ceases.

Moreover, in the literature is stated that alumina ceramics are widely applied as a ceramic dielectric barrier, since they are still considered sufficient for DBD actuators applications due to their advantageous features, such as *high mechanical and dielectric strength*, *high resistivity*, and *small dielectric losses* [156, 157].

In their study regarding the influence of the DBD actuator above the construction threshold on the two-dimensional subsonic boundary layer, Moravel et al. (2018) [166] used an actuator design with a two-layer underlying electrode to stabilize the position of the filaments; and between these two electrode layers, as well as above them dielectric plates of alumina ceramic 1 mm thick were placed. Recently, in their research, Keral et al. (2020) [156] studied and determined the ignition and quenching voltage of the DBD regarding the effect of adding several types of oxides into a pure alumina ceramic. The aim was to determine the impact of the chemical composition of the dielectric barrier. In addition, changes in surface morphology of the coplanar arrangement of the DBD (CDBD) barrier layer were verified. Overall, the final findings showed, in the form of graphs and atomic force microscopy (AFM) images, that the addition of small amounts of oxide dopant into pure alumina ceramics affects both ceramic's chemical composition, as well as surface structure, which in turn influence plasma parameters. Similarly, the investigations carried out by Pribyl R. et al. (2020) [157] consisted of a complex study on alumina-based ceramics barriers doped with spinel, i.e., $MgAl_2O_4$. It was concluded that the change in the sample composition resulted in a nonlinear response of physical properties for coplanar DBD. In summary, it was remarked that the determination of bulk and surface properties is necessary for complex analysis of the suitability of materials to be used as a dielectric barrier for CDBD; however, based on the knowledge and experience already acquired, the alumina-based ceramics with a small addition of $MgAl_2O_4$ are a promising compound for effective cold nonthermal plasma generation.

Lastly, a remarkable investigation was carried out by Bian D.L. et al. (2017) [154] that reports the material characterization and performance evolution of an AlN ceramic-based DBD plasma actuator. A conventional Al_2O_3 ceramic was also investigated as a control material. The plasma images, thermal characteristics, and electrical properties of the two actuators were compared and studied. Afterward, the evolutions of the surface morphologies, power consumption, and plasma images were monitored and analyzed at various operating intervals of time. A digital microscope imaging system was further used to characterize changes in the surface morphology. In addition, the induced velocities of the actuators were measured using a Pitot tube before and after plasma discharge aging. Lots of conclusions were therefore extrapolated, but, in general, it was highlighted by the authors that the AlN-based actuator can produce a more uniform discharge whilst the discharge of the Al_2O_3 actuator is easier to become filamentary. The later condition unfortunately leads to higher power consumption and earlier failure due to electrode oxidation.

3.4 Multifunctional Advanced Ceramics

The function of an engineering ceramic material may be defined as the specific purpose for which it is used in a particular application. Moreover, multifunctional ceramic systems composed of different materials – each offering primarily a single function – are namely well known. Nevertheless, sometimes even for a monofunctional application, a fine ceramic is frequently able to fulfill a set of *secondary purposes* based on their *secondary properties* [167].

Taking the above into consideration, the three aforementioned and reviewed applications of advanced ceramics in aerospace and aeronautical engineering fields – i.e., Thermal Protection Systems, Thermal Barrier Coatings and Dielectric Barrier Discharges –, in addition to the materials assessed in each subsection, three chemical compositions of ceramic systems were selected to be fabricated and further carefully studied. Specifically, the three ceramic systems are Mg-doped aluminum oxide, Mg-doped calcium zirconate oxide, and yttria stabilized zirconia.

3.4.1 Mg–doped Aluminum Oxide, $Mg{-}Al_2O_3$

Aluminum oxide, commonly referred to as alumina, is one of the most widely cost effective material in the family of fine ceramics. With an excellent combination of properties and reasonably priced available raw materials it is instinctive that fine grain technical alumina has a very wide range of applications. In detail, this material possesses strong ionic interatomic bonding, which consequently gives rise to its desirable key properties, such as:

- high temperature stability,
- excellent size and shape molding capabilities,
- high strength, stiffness, hardness and wear resistance,
- good corrosion and erosion resistance,
- resistant to strong acid and alkali attacks at elevated temperatures[6],
- high dielectric strength and small dielectric losses, and
- commercial availability in purity ranges from 94 % to 99.8 % for the most demanding high temperature application.

[6]The issue of ceramic corrosion is widely considered and investigated. Contrarily to the metal corrosion, which is mostly a consequence of electrochemical processes, in ceramics it is related to the dissolution phenomenon in different media. Many studies have been conducted to fulfill the urge for new applications possibilities of advanced ceramics, especially for engineering structures exposed to high-temperature environments, i.e., power generation industries and hot sections of the gas turbine engines. As consequence, it has been proven that alumina withstands both acid and alkali attacks at relatively large temperature ranges.

Moreover, the listed characteristics make alumina-based ceramics the material of choice for a wide range of applications, including *high temperature and aggressive environments*, *wear and corrosion resistance*, *metal cutting tools*, *microwave components*, and *electrical insulation*, as illustrated in **Figure 2.2**.

Furthermore, authors such as Pribyl R. et al. [157], Mollá J. et al. [168], and Ramírez-González J. et al. [169] studied and evaluated the addition of magnesium-based dopants on standard alumina ceramics. It was reported and highlighted that Mg-based dopant components are usually used as a sintering aid in alumina fabrication process since it produces an inhibition of the grain growth, as well as an increase in the final density of the material. Accordingly, and bearing in mind two crucial considerations described in 3.1.3 and 3.3.4, respectively, this is, (a) oxide ceramics are intuitively a good candidate for passive TPS application, (b) alumina is the state-of-art ceramic dielectric barrier material of DBD actuators; Mg-doped Al_2O_3 was therefore appraised a suitable material for a ceramic system to be produced and thereafter analyzed.

3.4.2 Mg–doped Calcium Zirconate Oxide, Mg–$CaZrO_3$

Calcium zirconate oxide, also named calcium zirconate, or simply, CZ, is reported to be a potential candidate for many purposes in mechanical, coating and electrical applications. As described in 3.2.3, calcium zirconate has appealing and exciting thermal properties, rendering this ceramic material to be a convenient candidate for thermal barrier applications. Besides, CZ is a material with a perovskite structure that is of fundamental significance for its electrical properties. All in all, some of attractive properties of calcium zirconate oxide are:

- excellent mechanical properties,
- low thermal conductivity,
- high thermal and chemical stabilities,
- good thermal shock resistance,
- high melting point, and
- excellent dielectric properties, i.e., high dielectric constant, low loss factor[7], and both of the qualities are well stable between 1 kHz and 1 MHz.

Calcium zirconate has been applied in different sectors, for example, as a sensor material in aluminum melts, as a refractory material for titanium metallurgy, in addition to as a microwave dielectric ceramic in modern communication systems. Nonetheless, in aeronautical and aerospace fields, it is considered as an alternative material to YSZ to be used

[7]The dielectric loss factor is a parameter used to evaluate the energy absorbed in the medium as an electromagnetic wave passes through. Considering an ideal case, the losses are zero, and consequently the dielectric loss factor is also zero.

in thermal barrier coating as pointed out by Ma W. et al. [89] and Garcia E. et al. [90] and explained in 3.2.3.

Additionally, it is also found in the literature that simple perovskite structured materials are of essential significance for their electrical properties including ferroelectricity, piezoelectricity, and superconductivity. Studies showed that perovskite ceramics increase the efficiency of the dielectric barrier discharge process. Li R. et al. [165] and Song X. et al. [158] focused their studies on the family of $CaTiO_3$–based compositions as described in 3.3.4, however these ceramics have a drawback consisting in a lower temperature stability when compared to that of $CaZrO_3$. Taking the above aspects into account, Mg–doped $CaZrO_3$ ceramic system was as well considered a reasonable and suitable material to be fabricated and studied. It is relevant to highlight that calcium zirconate was also chosen to be doped for the reasons mentioned in 3.4.1, i.e., as a sintering aid in the fabrication process for inhibition of the grain growth, and densification of the ceramic produced.

3.4.3 Yttria Stabilized Zirconia, YSZ

As described in 3.2.2, YSZ is widely considered and adopted material for thermal barrier coatings on gas turbine blades typically made of an Ni-based superalloy, considering its attractive properties, such as high thermal stability, low thermal conductivity, and a relatively large thermal expansion coefficient, which is close to that of the metal substrate. In addition, it is known that zirconia, or ZrO_2 has a very high melting point (3053.15 K), high temperature resistance, wear resistance, as well as corrosion resistance. Nonetheless, pure zirconium dioxide undergoes a phase transformation from monoclinic (stable at room temperature) to tetragonal (at about 1170 °C) and then to cubic (at about 2370 °C). Therefore, in order to obtain stable zirconia ceramic products *stabilized zirconias* are developed and studied by the process of doping ZrO_2. Particularly, by adding yttrium oxide, or yttria (Y_2O_3), which has excellent chemical inertness and high corrosion resistance, a fully stabilized zirconia is possible to obtain. Precisely, ZrO_2 with 7–8 wt. % Y_2O_3 composition has been studied for years for TBC applications due to its unique properties enumerated along the subsection of Thermal Barrier Coatings, but reconsidered once again:

- very high mechanical strength and wear resistance,
- very high erosion resistance,
- high impact resistance,
- high corrosion resistance,
- high chemical resistance,
- very low thermal conductivity, and
- relatively high coefficient of thermal expansion when compared to other ceramics.

Balça F. (2021) [170] studied specifically the optimization of multiphase composites of zirconium oxide for thermomechanical aeronautical applications. On the whole, the research consisted on the fabrication and microstructural, physical, mechanical and thermal characterization of seven multiphase distinct ceramic compositions in which pure zirconia ZrO_2 (monoclinic phase), 3YSZ (tetragonal phase) and 8YSZ (cubic phase) served as base materials. After performing an analysis, it was concluded for this work that based on mechanical and thermal results the composition named as P7 (i.e., 33.3 wt. % ZrO_2, 33.3 wt. % 3YSZ, 33.3 wt. %, and 8YSZ) would be a best fit to reproduce and study both as a Thermal Barrier Coating and as a passive Thermal Protection System. It is important to emphasis that the decision made was mainly influenced by the high mechanical resistance and notably low thermal conductivity which is a crucial parameter for the two applications referred.

To sum up, **Figure 3.15** outlines the three ceramic systems chosen to be investigated, i.e, Mg-doped Al_2O_3, and Mg-doped $CaZrO_3$, and YSZ in addition to their intended applications based on the aeronautical and aerospace implementations exploited throughout the course of this chapter, i.e., TPS, TBC and DBD. The selection was made in the sense that, when possible, one of functions of each candidate ceramic system should be based on their usual state-of-art application – YSZ is a state-of art material for TBCs, whereas alumina ceramic is for DBD –, whilst the second application should be an alternative one according to the literature revision performed. The third and remaining employment, which in the diagram is always opposite to the material considered, serves as a suggestion and, therefore, conducted studies are expected to answer regarding to its suitability – Mg-doped calcium zirconate as a TPS, Mg-doped alumina for TBC usage, and lastly YSZ as a dieletric barrier for DBD actuators.

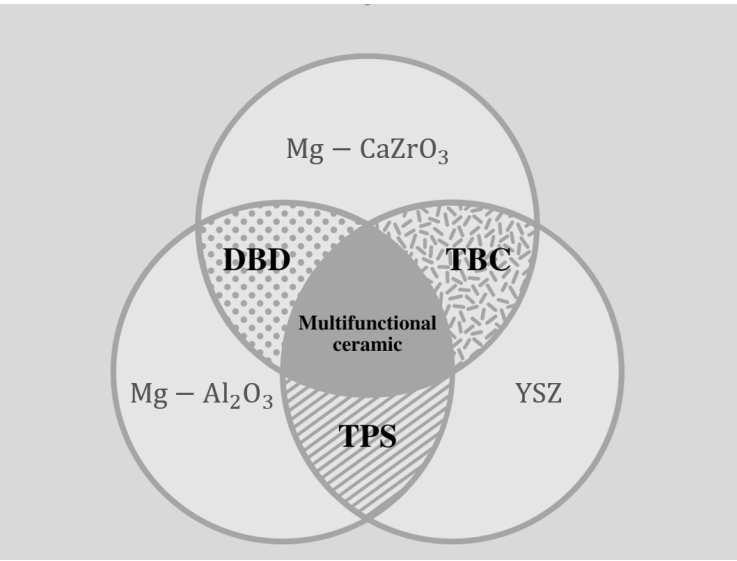

Figure 3.15: Ceramic systems selected to be investigated in addition to their *state–of–art*, *proposed by the literature* and *likely possible* applications in aeronautical and aerospace fields.

Chapter 4

Experimental Procedure

Ceramic components can be configured in various geometries through several fabrication processes, which in turn are achieved via different techniques. Despite the large manufacturing technique options, all of them can somehow be divided into four common stages including *material preparation*, *processing*, *sintering*, and *finishing* – **Figure 4.1**. Moreover, it is important to acknowledge that one of the most significant steps in preparing fine ceramics involves the heating process of ceramic powders, also known – and mentioned above – as sintering. Specifically, the sintering stage must undergo special handling control of the heterogeneity, chemical compositions, purity, particle size, particle size distribution (PSD), and part shape as the aforementioned factors play a significant role in the properties of the ceramic material components obtained [5, 171].

Accordingly, this part of the dissertation, i.e., Chapter 4, sets a general characterization of the selected raw powders for the ceramic materials fabricated in terms of their chemical properties. Furthermore, a description of the experimental procedure regarding both the specimens' manufacturing routine and samples analysis with respect to their physical, mechanical, thermal, and electrical properties is given. On top of that, when needed, a support explanation of the working principles of the techniques exploited is also provided.

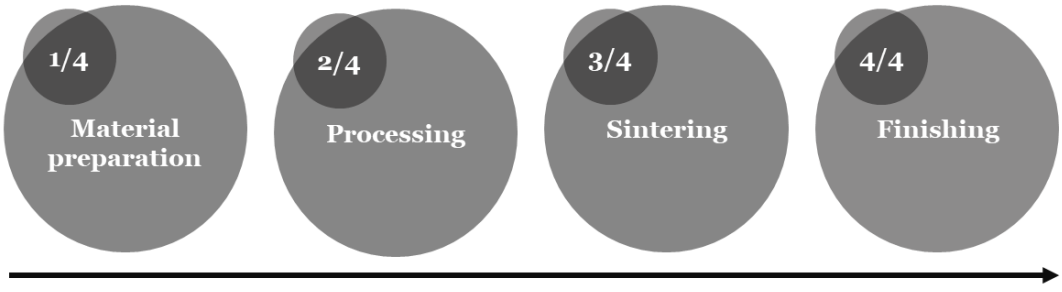

Figure 4.1: Fabrication process of advanced ceramics segmented into stages.

4.1 Materials

As detailed in the subsection entitled Multifunctional Advanced Ceramics, 3.4, the ceramic materials chosen to be fabricated and subsequently submitted to extensive study and analysis processes were Mg-doped Aluminum Oxide ($Mg-Al_2O_3$), Mg-doped Calcium Zirconate Oxide, ($Mg-CaZrO_3$) and Yttria Stabilized Zirconia (YSZ). The following tables

summarize the nomenclature adopted, as well as the detailed compositions in molar fraction (x_i), mass fraction (w_i), and volume fraction (v_i) for each ceramic system aimed to be studied. In addition, theoretical density values of the initial raw powders utilized are namely provided since they were used for the calculation of the theoretical density of each ceramic system material mixture.

For the oxide magnesium-doped alumina ceramic system – **Table 4.1** – commercial (Acros Organics, Belgium) aluminum oxide (Al_2O_3, A) and (Alfa Aesar, USA) magnesium oxide (MgO, M) powders of extra high and high purity (wt. %: 99 and 96, for A and M, respectively) were used as starting materials to prepare Mg-doped Al_2O_3 (designated as MA).

Table 4.1: Mg–doped Alumina, MA, ceramic system data.

Mg–doped Alumina (MA)	**MgO**	**Al_2O_3**
Molar fraction, x_i	1/3	2/3
Mass fraction, w_i [wt. %]	15.7	84.3
Volume fraction, v_i [vol. %]	17.2	82.8
Theoretical density, ρ [g/cm^3]	3.57 †	3.99 †
Theoretical density of the ceramic composite, ρ_{MA} [g/cm^3]	3,92	

Furthermore, for the magnesium-doped calcium zirconate ceramic system – **Table 4.2** – commercial (Alfa Aesar, USA) calcium zirconate ($CaZrO_3$, CZ) and magnesium oxide (MgO, M) powders of extra high and high purity (wt. %: 99.2 and 96, for CZ and M, respectively) were used as starting materials to produce Mg–doped $CaZrO_3$ (named as MCZ).

Table 4.2: Mg–doped Calcium Zirconate, MCZ, ceramic system data.

Mg–doped Calcium Zirconate (MCZ)	**MgO**	**$CaZrO_3$**
Molar fraction, x_i	1/3	2/3
Mass fraction, w_i [wt. %]	10.1	89.9
Volume fraction, v_i [vol. %]	12.7	87.3
Theoretical density, ρ [g/cm^3]	3.57 †	4.62 †
Theoretical density of the ceramic composite, ρ_{MCZ} [g/cm^3]	4.49	

Lastly, and similarly, for the three-phased yttria-stabilized zirconia ceramic system – **Table 4.3** – commercial (Tosoh-Zirconia, Japan) 3 mol % yttria-stabilized zirconia (t-3YSZ) – in which the tetragonal phase is predominant – 8 mol % yttria-stabilized zirconia (c-8YSZ) – in which the cubic phase is predominant – in addition to (Acros Organics, Bel-

† Theoretical densities values based on the XRD files indicated on **Table 4.4**.

gium) monoclinic zirconia (m-ZrO_2) powders of extra high purity (wt. %: 99.8, 99.7 and 98.5 for t-3YSZ, c-8YSZ, and m-ZrO_2, respectively) were used as starting materials to make YSZ.

Table 4.3: Yttria Stabilized Zirconia, YSZ, ceramic system data.

Yttria Stabilized Zirconia (YSZ)	**t-3YSZ**	**c-8YSZ**	**m-ZrO_2**
Molar fraction, x_i	1/3	1/3	1/3
Mass fraction, w_i [wt. %]	33.3	33.3	33.3
Volume fraction, v_i [vol. %]	32.6	33.0	34.4
Theoretical density, ρ [g/cm^3]	6.13 †	6,07 †	5.82 †
Theoretical density of the ceramic composite, ρ_{YSZ} [g/cm^3]	6.00		

What's more, theoretical values of each powder were used for the calculation of the theoretical density ρ_{th} (g/cm^3) of the three ceramic composite materials. Based on the following **Equation 4.1** where v_i indicates the volume fraction of the element i, ρ the theoretical density of the element i, and n the number of ingredients of the mixture.

$$\rho_{th} = \sum_{i=1}^{n} v_i \times \rho_i \quad (4.1)$$

Table 4.4 summarized the XRD files from which values of theoretical densities were accessed. These XRD files, formerly known as ASTM (American Society for Testing and Materials) and JCPDS (Joint Committee on Powder Diffraction Standards), are supplied in the form of power diffraction files (PDF) by the International Centre for Diffraction Data (ICDD). The XRD files/cards here mentioned and used were collected from the DMAX III/C (Rigaku, Japan) apparatus based on the X-ray diffraction principle. For clarity, it is worth mentioning that some mismatches between the values applied in the calculation performed and the values provided by the manufacturers' data spreadsheets may occur. This happens mainly due to each manufacturer's techniques adopted to sinter the specimens and the following applied calculation routines. Having this in mind was assessed as a reasonable and consistent approach to take into consideration the theoretical densities indicated by the XRD cards.**Table 4.5** summarizes the manufacturer and the theoretical densities by them listed.

† Theoretical densities values based on the XRD files indicated on **Table 4.4**.

Table 4.4: Powders' theoretical densities based on XRD files/cards.

Material	**XRD file**	**Theoretical density, ρ, [g/cm^3]**
Magnesium oxide, M	XRD file/card #71-1176	3.570
Aluminum oxide, A	XRD file/card #46-1212	3.987
Calcium zirconate, CZ	XRD file/card #35-0790	4.619
t-3YSZ	XRD file/card #50-1089	6.134
c-8YSZ	XRD file/card #49-1642	6.069
m-ZrO_2	XRD file/card #37-1484	5.817

Table 4.5: Powders' theoretical densities based on manufacturers' data spreadsheet.

Material (powder)	**Manufacturer data**	**CAS**	**LOT**	**Theoretical density, ρ, [g/cm^3]**
Magnesium oxide, M	Acros Organics, Belgium	1309-48-4	B02Y033	3.58
Aluminum oxide, A	Alfa Aesar, USA	1344-28-1	A0383004	3.97
Calcium zirconate, CZ	Alfa Aesar, USA	12013-47-7	U25D020	n/a [8]
t-3YSZ	Tosoh-Zirconia, Japan	n/a [8]	Z308782P	6.05
c-8YSZ	Tosoh-Zirconia, Japan	n/a [8]	Z807724P	5.95
m-ZrO_2	Acros Organics, Belgium	1314-23-4	A0387501	5.60

The XRD files are obtained based on an X-ray analysis technique, i.e., in many production or research and development centers, X-rays can be used to characterize materials and samples. This electromagnetic radiations of extremely short wavelength – ranging from about 10^{-8} and 10^{-12} m –, and high frequency – 10^{16} and 10^{20} Hz – make them exceptionally suitable to analyze structures and elements at the atomic level. Among the techniques that incorporate X-ray analysis for sample analysis, two stand out for their non-destructive nature: X-ray Fluorescence (XRF) and X-ray Diffraction (XRD). Both of the announced techniques allow to measure a sample's response to the X-rays, however, each of them provides a different type of measurement [172, 173, 174].

On one hand, the X-ray Fluorescence [9] technique is applied to determine the element composition of materials that are being analyzed. XRF analyzers determine the chemistry of a sample by measuring the fluorescent, also named secondary, X-ray emitted from a sample when it is excited by a primary X-ray source. Consequently, each of the elements present in a sample produces a set of characteristic fluorescent X-rays that is unique for that spe-

[†]Theoretical densities values based on the XRD files indicated on **Table 4.4**.

[8]Information not available by the manufacturer.

[9]The XRF method is only described for the sake of completeness. It is outlined that the XRF analysis was not performed.

cific element. XRF analyzers are available in models designed to provide instant elemental evaluation for immediate feedback in the field, or in lab-based systems designed to provide qualitative and quantitative analysis. Unfortunately, the XRF examination determines the elemental composition of a sample but does not provide information regarding how the various elements in a sample are combined. Such information is only available through X-ray Diffraction. X-ray Diffraction, or XRD, is a powerful technique regularly used to recognize the different phases in a polycrystalline sample, i.e., XRD provides an analysis of crystalline phases in materials. More specifically, information on structures, phases, preferred crystal orientations, and other structural parameters – such as average grain size, crystallinity, strain, and crystal defects –, can be obtained from a careful examination of the diagram patterns which work as fingerprints as they are unique for a single substance. In other words, from a standard database for X-ray powder diffraction patterns, an easy phase recognition and identification for a large variety of crystalline samples is enabled. Within this framework of thought, it can be considered that the XRD technique is complementary to XRF since by using both of them it is possible not only to obtain the detailed chemical composition of a sample but namely the presence and amounts of minerals species, as well as phases identification [172, 173, 174].

As the name itself indicates, XRD analysis is performed with the aid of X–ray radiation. Considering the entire electromagnetic spectrum, this is justified by the fact that the wavelengths λ_w of X–rays range from 0.01 nm to 10 nm, which corresponds to energies E in the range from 0.125 to 125 keV, and in turn are in tune with the crystal atomic distances and lattice parameters [175, 176]. These quantities – X–rays wavelengths and their energies – are inversely proportional as indicated by **Equation 4.2** where h is the Planck's constant, v is the frequency, and c the velocity of light.

$$E_P = h \times v = h \times \frac{c}{\lambda_w} \quad (4.2)$$

In addition, XRD tests are carried out with X–ray diffractometers that generally consist of three components, this is, a source, also designated as an X–ray tube, a sample holder, and an X–ray detector [174]. At its basics, when a specimen is fired with the X-ray beam, the crystalline constituent atoms of a given material cause its diffraction in several directions. The term *diffraction* is usually used to explain the deviations of rays propagation from a trajectory dictated by a geometrical optical setup [175]. In other words, when X–ray radiation collides on a specific periodic crystal structure a characteristic diffraction effect is observed since X–rays diffract treating inter-atomic distances as slits. These X–ray diffraction patterns are thus exploited to assess the composition of a sample of study [174, 175, 176, 177, 178, 179].

In physics, the relation between the spacing of atomic planes in crystals and the angles of incidence – at which these planes produce the most intense reflections of radiation,

known as *peaks* – is expressed by the Bragg law. This law states that for maximum intensity of reflected wave trains (wave sequences are formed by crests and troughs) they must stay in phase to produce constructive interference – i.e., corresponding points of the wave must arrive simultaneously. Contrarily, if the wave trains do not stay in phase, destructive interference is produced, and the signal is destroyed creating background noise in the measurements. The Bragg law allows this way to compute both the lattice spacing of crystals and the wavelengths of incident X–ray beams illustrated in **Figure 4.2** [174, 175, 176, 177, 178, 179].

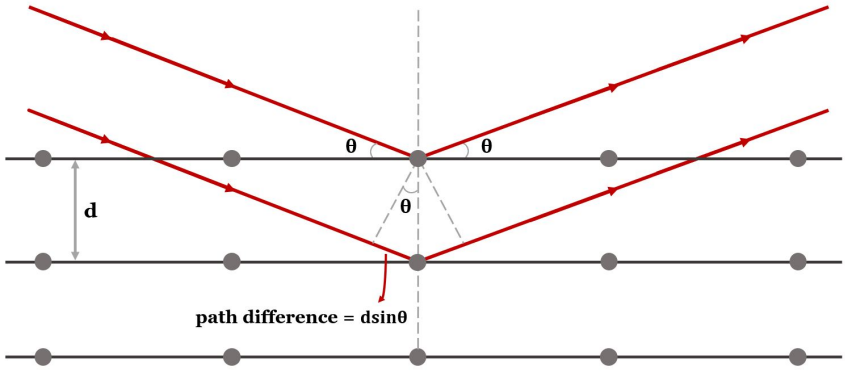

Figure 4.2: Bragg law diagram illustration.

The diagram of **Figure 4.2** illustrates a two-dimensional incident two X–ray waves (depicted by red arrows) on a crystal structure (represented by grey dots and dashed lines) with a separation distance d_p – the distance between the lattice planes – at a reflected angle θ that originates diffraction in phase, i.e., as previously explained, constructive interference in the distance traveled – path difference – and determined by the expression $2d_p \sin\theta$. Accordingly, Bragg law is given by **Equation 4.3**.

$$n\lambda_w = 2d_p sin\theta \quad (4.3)$$

Moreover, it is important to note that after the waves are reflected, they can only be in phase if the path length $2d_p \sin\theta$ is an integer number of wavelengths, $n\lambda_w$. Otherwise, in the case of fractional n lengths of wavelengths, the reflected waves are naturally out of phase and destructive interferences are created giving rise to noise instead of the desired sharp peaks for crystallographic determination [179].

4.2 Experimental Procedure - Sample Manufacturing

4.2.1 Material Preparation Stage

The samples' manufacturing process adopted was overall similar to the production of all-ceramic materials previously announced – MA, MCZ, and YSZ. The fabrication procedure commenced with the weighing of the corresponding proportion of every powder with the help of a single pan analytical balance (Oertling, United Kingdom) with a maximum capacity of 200 g and readability of 0.0001 g. Thereafter, the starting powders were milled for 3 h at 500 rpm in a high-energy planetary mill (Fritsch, Pulverisette 6, Germany) in alumina – for the MA mixture – and zirconia – for the MCZ and YSZ mixtures – griding bowls of 250 mL capacity. In addition, alumina and zirconia balls of 1 mm diameter (Fritsch) were added to the powder mixtures using isopropyl alcohol as a media in a powder/alcohol/balls ration of 1/1/2. Specifically, the mixtures were composed of 100 g of powder, 100 g of isopropyl alcohol, and 200 g of balls – which are responsible for the homogenization of the mixture and therefore their higher weight. The milling process aimed to reduce the characteristic particles' sizes. It must be highlighted that during the milling process cycles of 30 min were made with intervals of rest so that the mixture would not overheat inside the griding bowls which would have adverse consequences on the chemical composition of the ceramic produced. Afterward, all the mixtures were dried at 50 ^{o}C for 24 h in air (Carbolite, NR200-F, United Kingdom) – with the purpose of isopropyl alcohol complete evaporation – and, in due course, sieved with a vibratory shaker machine (Retsch, AS200, Germany) in 63 μm mesh so that the collected fine particles would be free, first and foremost, of alumina/zirconia balls, and namely some unintended agglomerates and impurities.

It must be remarked that due to unexpected high relative porosity values obtained for the MA specimens during physical properties determination – explained in the following sections – an optimized fabrication approach was then adopted. In greater detail, a fourth ceramic material, named MA2, was fabricated with the difference that its milling time was doubled, i.e., extended to 6 h instead of 3 h as for the rest of the compositions. Furthermore, during the milling process, an analysis of the particle size of the mixture was also performed based on the laser diffraction principle with a multifunctional particle characterization tool (Coulter LS-200, CA, United States of America) to ensure that a proper improvement regarding the particle size was being achieved when compared to MA1. This awareness regarding particle size worked as a quality control process and was fundamental since the ceramic materials that were being fabricated aimed to fulfill a range of applications common to the three of them. Naturally, the more alike the process of fabrication and its results, the more accurate characterization can afterward be performed for the ceramic materials studied through the course of this dissertation work.

Laser diffraction analysis, LDA, also called laser diffractions spectroscopy, is a technology – grounded on the Fraunhofer diffraction theory – that exploits diffraction patterns of a laser beam passed through any sample – ranging from nanometers to millimeters in size – to measure relatively quickly the geometrical dimensions of the particles composing the sample that is being analyzed. To put it in another way, at its very most basic, laser diffraction is about the relationship between *particle size* and the *angle and intensity of the scattering light*. The measurements are made when a sample is passed through a measurement chamber which is where a laser beam illuminates the particles. The intensity of light scattered by the particles within the sample is detected over an extensive range of angles. Large particles scatter light at small angles relative to the laser beam and small particles scatter light at large angles. Furthermore, a major advantage of this process is that it does not depend on volumetric flow rate, i.e., the number of particles that pass through a surface over time [180, 181, 182, 183]

For the apparatus available in the laboratory – Coulter LS-200 – the light intensity levels are first measured with no sample in the system, and then subtracted out. The background must always be measured before adding the sample to the system. Only this way, a comparison is possible based on the obtained light intensity patterns from which the size distribution is calculated. **Figure 4.3** consists of a schematic illustration of the working principle of a laser diffraction analysis methodology, whereas **Figure 4.4** shows a schematic diagram of the Counter LS model laser granulometer.

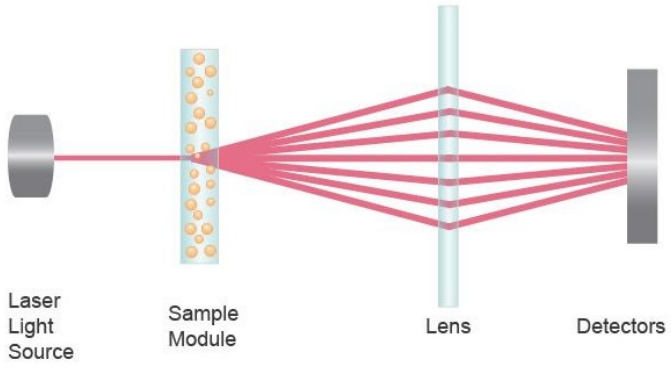

Figure 4.3: Schematic illustration of the optical working principle of the LDA particle size detector [184].

On the whole, laser diffraction analysis is characterized by *rapid measurements*, *repeatability* since a large number of particles can be sampled in each measurement, *elevated sample throughput*, i.e., a high number of measurements may be conducted, for example, per day; and it is considered a *well-established technique* as it is covered by ISO13320 (International Organization for Standardization).

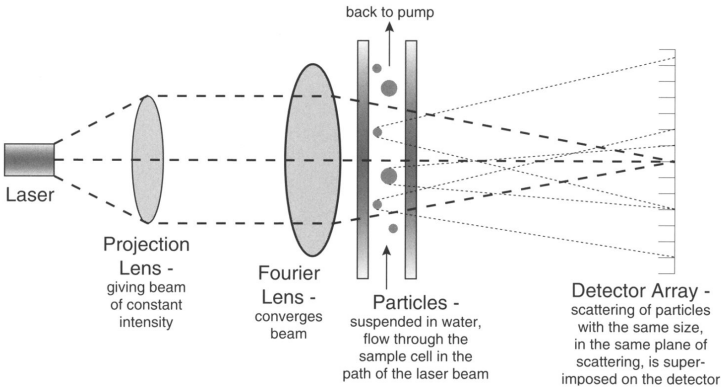

Figure 4.4: Schematic diagram of the Coulter LS model laser granulometer [185].

4.2.2 Processing Stage

After all the fine-powder mixtures were obtained, the next step consisted of the pressing process for the shape-forming of three types of specimens, i.e., two rectangular (one of them was intended to be transformed, i.e., cut into several rectangular bars) and one disc specimens. The uniaxial pressing technique was adopted in a universal testing machine using rectangular (Instron 8800, 100 kN electromechanical actuator capacity, United States of America) and cylindrical (Shimadzu, AGS-X, 50 kN electromechanical actuator capacity, Japan) dies of high strength steel – previously lubricated with thin oil (Connex COX591109, Germany) – at 25 MPa for both rectangular specimens (60 × 60 mm), and disc specimens (diameter of 28 mm) which correspond to, approximately, 90.0 kN and 15.4 kN, respectively. A total mass of 40 g for the rectangular specimens and 4 g for the discs were used. **Table 4.6** summarizes the information mentioned.

Table 4.6: Uniaxial pressing technique parameters for the rectangular and disc specimens powder compaction.

Specimen type	**Powder mass [g]**	**Force applied [kN]**	**Strength [MPa]**	**Mold dimensions [mm]**
Rectangular	40	≈ 90.0	25	60 × 60
Disc	4	≈ 15.4	25	Ø 28

The uniaxial die pressing or UDP is one of the dry forming techniques type that is considered to be the most common forming process of ceramic components for their mass production. The great benefit of dry forming – when compared for instance to wet forming methods – is that it eliminates problems related to drying shrinkage, as well as associated energy and costs. When the procedure takes place at room temperatures it is designated as cold pressing. Concisely, UDP consists of the powder compaction methodology involving uniaxial pressure applied to the powder deposited in a die between two stiff punches [5, 186]. **Figure 4.5** shows the uniaxial die pressing process divided into three stages: (a) die fill stage, (b) compaction, and (c) component or part ejection.

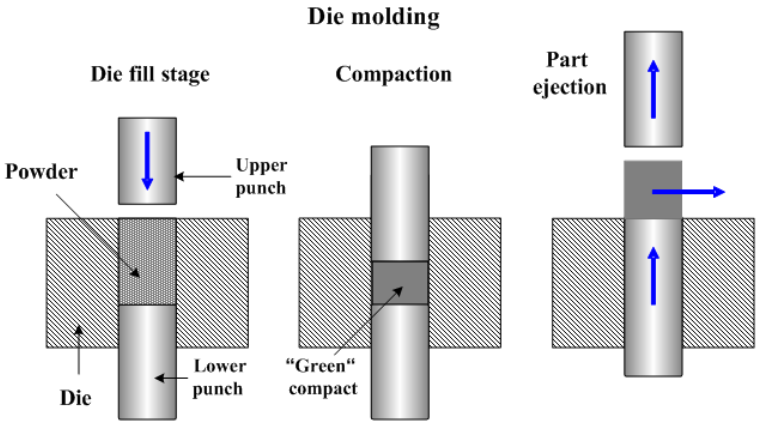

Figure 4.5: UDP methodology illustration divided into three stages: (a) die fill, (b) compaction, and (c) part ejection [187].

4.2.3 Sintering Stage

After the compaction process achieved by uniaxial die pressing, the following stage consisted of the sintering process that aims to convert fine-sized materials into an agglomerated product. In its essence, sintering is a thermal behavior of materials where particles bond together through a mass transport mechanism – mass transit due to species concentration gradient, i.e., the spatial difference in the abundance of a specific chemical species – in a mixture [188]. The goal of the sintering phase is to obtain a fully dense solid component, however, in most cases, some residual porosity remains. As pointed out by Otitoju et al. (2020) [5] sintering correlates with many factors, such as sintering temperature, time, atmosphere, heating, and cooling rates, shrinkage, pressure, grain size, agglomerates, and porosity. For this reason, it is a very critical stage in the fabrication of advanced ceramics [5, 189].

For the MA1, MA2, MCZ, and YSZ advanced ceramic materials the sintering process was carried out in air (Termolab, MLR, Portugal) and it was composed of pre-sintering (for rectangular specimens cut into bars) and sintering (for all the specimens) steps. The pre-sintering phase started with the rectangular specimens being heated with a rate of 5 ^{o}C/min from room temperature to the maximum temperature of 1200 ^{o}C, 120 min dwell, and 5 ^{o}C/min cooling rate from pre-sintering to room temperature. After the pre-sintering was completed, the specimens were cut into rectangular bars with a diamond wheel (Buehler IsoMet 15LC, United States of America) set on a laboratory precision cut-off machine (Accutom-2, Struers, Denmark), and their surfaces smoothened and uniformized with a silicon carbide paper of grid #1000 (Struers, Denmark).

Lastly, the sintering stage comprised the following steps common to the rectangular, the bar, and disc specimens: heating rate of 5 ^{o}C/min from room temperature to the sintering

temperature (1450 ºC for the MCZ and YSZ, and 1600 ºC for the MA1 and MA2 ceramic mixtures), 120 min dwell, and 5 ºC/min cooling rate from referred sintering temperatures to room temperature.

Bearing in mind that owing to the thermochemical reactions that take place during the sintering stage, a strengthening and densification of the engineering ceramic occur. Consequently, this leads to a reduction in porosity of the material which in turn diminish its volume. The process described is known as sintering shrinkage [190]. To ascertain the sintering shrinkage, diametrical linear contraction C_d (%) was evaluated on the disc samples based on the following **Equation 4.4** where d_i corresponds to the initial diameter of the disc specimens, whereas d_f is the final one.

$$C_d = \frac{d_f - d_i}{d_i} \times 100 \quad (4.4)$$

Moreover, to analyze any deviation and/or associated error with the, at least, three measurements, n, taken of the diametrical linear contraction, mean value $\overline{C_d}$ and standard deviation SD for the two manufactured disc specimens were established according to the following **Equations 4.5** and **4.6**, respectively.

$$\overline{C_d} = \frac{\sum_{i=1}^{n} C_d}{n} \quad (4.5)$$

$$SD = \sqrt{\frac{\sum_{i=1}^{n} (C_d - \overline{C_d})^2}{n-1}} \quad (4.6)$$

4.2.4 Finishing Stage

The concluding step in the ceramic component fabrication was the finishing stage. All ceramic components in their processed state have some individual physical characteristic features due to minor uncontrollable changes. Therefore, a finishing stage becomes mandatory to eliminate possible imperfections on the surface of the specimens. To overcome this phenomenon manual surfaces optimization grinding and polishing procedures were performed with the help of materialographic equipment (Struers DAP-V, Denmark) and silicon carbide paper #1000 (Struers, Denmark), followed by silicon carbide paper #2400 (Struers, Denmark) designated for materials wet grinding.

All in all, **Figue 4.6** summarizes the four steps and their determining parameters for the MA1, MA2, MCZ, and YSZ technical ceramics production covered in greater detail throughout this sample manufacturing description section, i.e., 4.2.

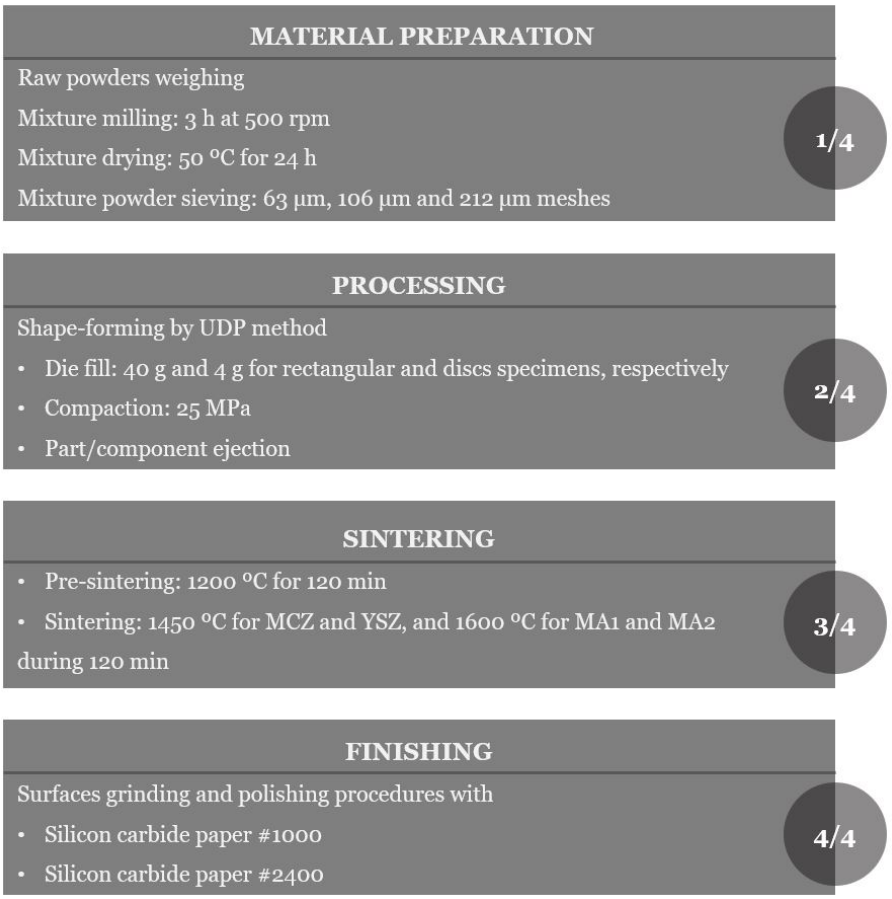

Figure 4.6: MA1, MA2, MCA, and YSZ manufacturing process summary.

4.3 Experimental Procedure - Sample Analysis

4.3.1 Physical Properties

4.3.1.1 Apparent Porosity, Bulk Density, Apparent Density and Relative Density

Apparent porosity and bulk density were measured following the ASTM C-20 – 00 [191] standard test methodology using deionized water and the – previously mentioned – single pan analytical balance (Oertling, United Kingdom) with a maximum capacity of 200 g and readability of 0.0001 g. The analysis of these parameters is essential once they are considered to be the primary properties of advanced ceramics, i.e., they are strongly correlated to the mechanical, thermal, and electrical performance of the finished technical ceramics. Both apparent porosity and bulk density parameters are widely applied in the evaluation exercises of different ceramic materials and serve namely as criteria of comparison, or benchmark, for distinct purposes, such as quality control, research, and development, as well as compliance assessment based on particular specifications. Therefore, it becomes appropriate and significant to note that during the fabrication process factors such as raw powders used, the particle size of the fine grain of mixtures obtained and, ultimately, the sintering temperature in addition to its duration, will dictate and govern the apparent porosity and bulk density of the fine ceramics manufactured. In summary, and simply put, the fabrication process influences the physical properties of a particular ceramic, which in turn will be decisive for the overall performance of an engineering structure, or component, that that specific ceramic integrates.

Thereby, the apparent porosity and bulk density determination procedure began with the measurement – in grams (g) – of three individual weigh for each bar specimen of every composition – MA1, MA2, MCZ, and YSZ, in the following sequence: dry weight, D, after the specimens were dried in air with the help of a laboratory oven (Carbolite, NR200-F, United Kingdom); saturated weight, W, after the samples were maintained in deionized water for 12 h and slightly wiped with absorbent paper so that remaining residual water drops would not impair the measurements, but also with special caution to avoid excessive withdrawing of water from their pores; and lastly, suspended weight, S, also performed in water and accomplished by suspending the specimen in a wire arm from a hung set on the balance. In between, i.e., after equipment assembly and before the weighing for the suspended weight determination, the calibration of the balance was done since the wire aimed to support the specimens is intended to be immersed in water to the same depth as when the sample is in place which naturally impacts the exercise described.

Once all measurements were made, a calculation routine was implemented to obtain the desired physical parameter values. The referred routine started with the exterior volume determination based on **Equation 4.7**, i.e., the exterior volume V_{ext} (cm^3) was given by subtracting the suspended weight S from the saturated weight W

$$V_{ext} = W - S \quad (4.7)$$

Next, the apparent porosity P (%) computation – **Equation 4.8** - (i.e., the percentage of open pores of the specimens) followed and was obtained by the subtraction of the dry weight D from the saturated weight W and divided by the exterior volume V_{ext}. In addition, the bulk density ρ_b (g/cm^3) – **Equation 4.9** - or, in other words, the quotient of the sample's dry weight D divided by their corresponding exterior volume V_{ext} was also computed as presented below

$$P = \frac{W - D}{V_{ext}} \times 100 \quad (4.8)$$

$$\rho_b = \frac{D}{V_{ext}} \quad (4.9)$$

Additional calculation of the apparent density were performed ρ_a (g/cm^3) which consists of the quotient of the specimen dry weight D (i.e., the sum weight of the compact fraction of material and the open pores or voids) divided by the difference between the dry D and the suspended weights S as depicted **Equation 4.10**

$$\rho_a = \frac{D}{D - S} \quad (4.10)$$

And, lastly, for the relative density ρ_r (%) **Equation 4.11** was applied that represents the quotient samples bulk density ρ_b divided by the previously calculated theoretical density ρ_{th} of in agreement ceramic material

$$\rho_r = \frac{\rho_b}{\rho_{th}} \times 100 \quad (4.11)$$

For the four ceramic composites produced, to ascertain any deviation and/or associated error with the measurements taken of each bar sample, mean value $\overline{P}$ and standard deviation SD of the apparent porosity for, at least, seven specimens, n, were established according to the following **Equations 4.12** and **4.13**, respectively

$$\overline{P} = \frac{\sum_{i=1}^{n} P}{n} \quad (4.12)$$

$$SD = \sqrt{\frac{\sum_{i=1}^{n}(P - \overline{P})^2}{n-1}} \quad (4.13)$$

4.3.2 Mechanical Properties

4.3.2.1 Dynamic Young's Modulus and Dynamic Shear Modulus

The Young's modulus also called the elastic modulus, E, and the dynamic shear modulus, modulus of rigidity, or torsional modulus, G, were experimentally determined based on the impulse excitation technique according to the standard test method ASTM C1198 – 20 [192]. On one hand, Young's modulus parameter consists of the elastic modulus of a material in tension or compression. On the other, the shear modulus property of a material describes its elastic modulus to shear or torsion. The reasoning behind choosing the method of impulse excitation technique, IET, for the calculation of the dynamic elastic modulus is described as follows. Primarily, the traditional method considering the typical stress-strain curve and its slope on the linear-elastic regime usually applied on metals and polymers is not suitable for ceramics. In more detail, according to Robert Hooke's law, the quotient of stress divided by strain is equal to a constant which is approximately the elastic modulus of a material. In other words, for metals and polymeric materials, the modulus of elasticity – which measures the stiffness of material – is defined as the ratio of stress σ to strain ε in the linear elastic region and mathematically it equals to $E = \Delta\sigma/\Delta\varepsilon$. Therefore, it is assumed that the linear Young's modulus is the slope of the linear-elastic regime within a stress-strain curve – **Figure 4.7**. Since the advanced ceramics of high stiffness possess a very low deformation rate, the *accurate* analysis of the elastic modulus by $E = \Delta\sigma/\Delta\varepsilon$ technique becomes extremely hard to perform, and therefore high associated errors will dictate the results which in turn would lead to misleading conclusions.

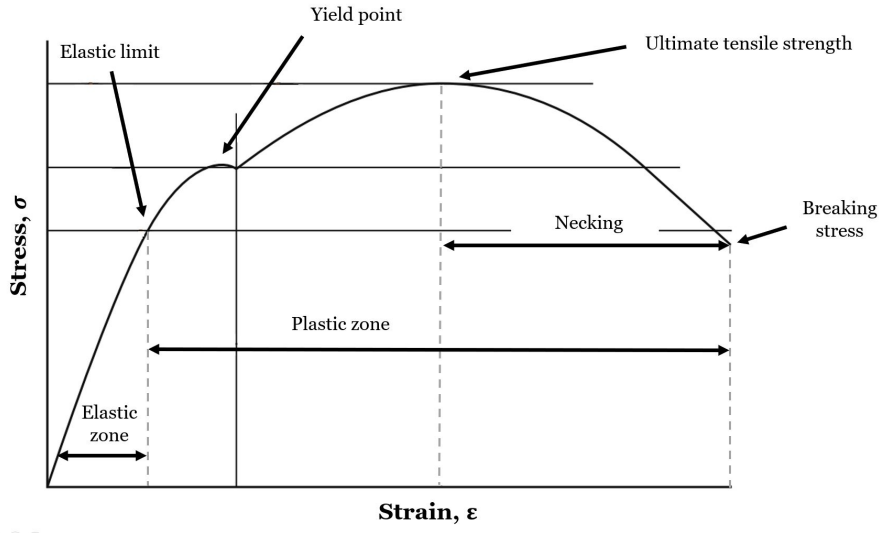

Figure 4.7: Typical stress–strain curve for metals.

Besides this, one has namely to be aware of the phenomenon of the *complacency* of the equipment at disposal. The Shimadzu AGS-X (Japan) equipment (supports, wedge, among other components) is made of steel that has a modulus of elasticity of 210 GPa. This value is inferior to the ones of the studied ceramic constituents, i.e., alumina (430 GPa) [57], calcium zirconate (228 GPa) [193], magnesium oxide (280 GPa) [193] and YSZ (210 – 220 GPa) [194]. Consequently, elevated repeatability of test would be necessary to properly measure the deformation rate of both the specimens and the machine's structure so that the last one could be subtracted to the first and elasticity modulus of the ceramic systems thus determined. This way, a constrain is immediately identified since relatively few specimens of each ceramic system material were fabricated. In summary, the IET technique is the natural method to apply in the dynamic Young's modulus experimental determination.

The impulse excitation technique, or simply named IET, is a non-destructive test method based on the analysis of the vibration of a test sample after it is impulse excited. In other words, the component to be analyzed is mechanically excited by a single elastic strike with the appropriate equipment, i.e., an impulse tool – **Figure 4.8**.

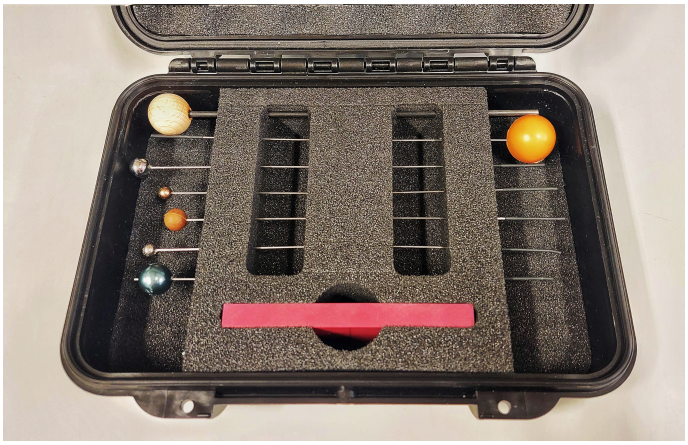

Figure 4.8: IET impulse hammers.

It is known that the resonance frequencies are characteristic of a test object or specimen, as they are related to its *elastic modulus*, *mass*, and *geometry*. The relation between these parameters is accurately identified for isotropic objects of simple shape such as bars or disks, thus making IET a standard method to determine material key properties such as Young's modulus, and shear modulus of advanced ceramics at ambient or high temperatures. Based on the awareness that small geometrical distortions, density fluctuations, or cracks influence the resonance frequencies values, IET may also be used for quality control and quality assurance in material processing.

For room temperature conditions, a high-performance IET device was used, i.e., GrindoSonic MK7, GrindoSonic, whose core equipment – widely used by the industrial and re-

search laboratory – measures various natural vibration frequencies, ranging from 100 Hz to 50 kHz, on an ample variety of test objects. Overall, IET GrindoSonic MK7 equipment measures the fundamental resonant frequency of test specimens of suitable geometry by exciting them mechanically with an impulse tool. Specimen supports, impulse locations, and signal pick-up points are selected to induce and measure specific modes of the transient vibrations – i.e., dynamic Young's modulus is determined using the resonant frequency in the flexural mode, whilst the dynamic shear modulus is found thanks to the torsional resonant vibrations.

In its core, a transducer senses the resulting mechanical vibrations of the specimen imposed by a single elastic strike and thereafter transforms them into electric signals. Next, the appropriate fundamental resonant frequencies, dimensions, and mass of the specimen are used to calculate either Young's modulus or shear modulus. Noteworthy to highlight that a standard MK7 shipment includes two vibration transducers. On one hand, the piezo-probe, or the piezoelectric detector, is sensitive over the entire operating frequency range of the GrindoSonic MK7, since the probe is most sensitive to movement back and forth in the direction indicated by the black dot on the probe making it easier to isolate particular vibrational modes. On the other, vibrations can also be measured using an acoustic microphone. The detection sensitivity of the microphone decreases for frequencies above about 20 kHz and it doesn't have the directional sensitivity of the piezo-probe sensor. An advantage of the microphone is that it is a non-contact detector and so will not introduce any additional damping of vibrational. **Figure 4.9** shows the IET technique working principle with the two GrindoSonic MK7 equipment vibration transducers discussed above.

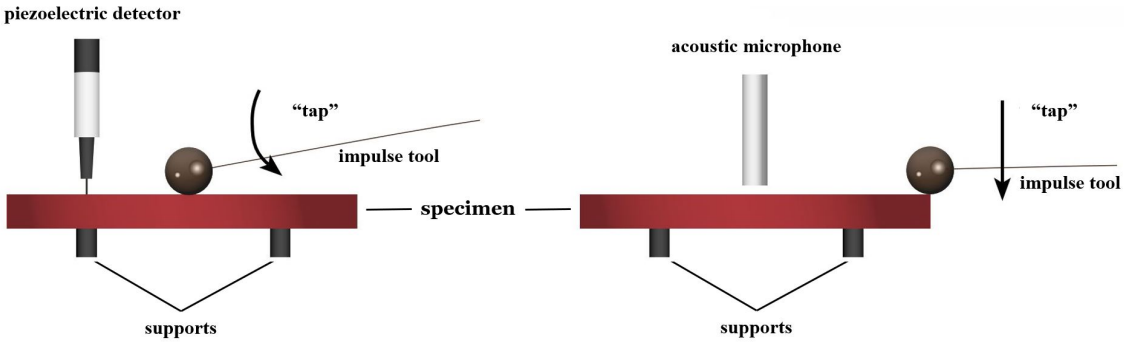

Figure 4.9: IET method impulse illustration with two types of GrindoSonic MK7 vibration transducers – piezo-probe and acoustic microphone sensors.

To optimize the measurement of the flexural (or bending mode) vibration mode, the ceramic rectangular bars specimens were rested on two resin supports – one at each end at a distance of approximately 22.4 % of the length of the bar. These points – where the bars are supported – are the vibrational nodes of the fundamental flexural vibration i.e., points of minimal vibrational amplitude. Consequently, resting the specimens on the nodes has a minimal damping effect on the vibrations. The bars were then tapped in the center with

proper excitation hammers. The resonant vibration was measured using either one of the vibration sensors, i.e., the piezo-probe vibration sensor or microphone equipment. At the end of this procedure, values of E-modulus measurements were obtained as the output of the MK7 device.

Lastly, for the measurements of the shear modulus, the rectangular samples were supported on the cross-shaped nodal support instead and excited not at the center as performed with bars in the flexural vibrational mode, but close to the edge along the node line. The procedure described excites preferentially the torsional mode allowing this way the G-modulus measurements.

For experimental results comparison, a Voigt model, **Equation 4.14**, was analytically used to estimate the theoretical Young's modulus E_{th} (GPa) of the ceramic composites

$$E_{th} = \sum_{i=1}^{n} v_i \times E_i \quad (4.14)$$

where E_i is the elastic modulus of the phase element i, and n the number of phases, i.e., the ingredients of the mixture of the ceramic.

Lastly, to ascertain any deviation and/or associated error with the, at least, fifteen measurements performed, n, mean value $\overline{E}$ and standard deviation SD of the experimentally obtained Young's modulus were established according to the following **Equations 4.15** and **4.16**, respectively. Alike computation was performed for G-modulus data assessment also for the, at least, fifteen measurements made.

$$\overline{E} = \frac{\sum_{i=1}^{n} E}{n} \quad (4.15)$$

$$SD = \sqrt{\frac{\sum_{i=1}^{n} (E - \overline{E})^2}{n-1}} \quad (4.16)$$

4.3.2.2 Flexural Strength

The determination of flexural strength also known as modulus of rupture, or bend strength, of advanced ceramic material at ambient temperature was performed accordingly to the ASTM C1161 – 18 [195] standard test method. In its essence, flexural strength consists of a measure of the ultimate strength of a specific beam in bending which depends on the ceramic inherent resistance to fracture and the size, severity, and concentration of flaws. Three-point loading test configuration was conducted using the universal testing machine Shimadzu AGS-X (Japan). This type of flexural strength analysis – contrary to

the four-point flexural strength test – exposes only a very small portion of the sample to the maximum stress. **Figure 4.10** illustrates a schematic setup of the three-point loading test where L is the supporting span and l is the specimen's length.

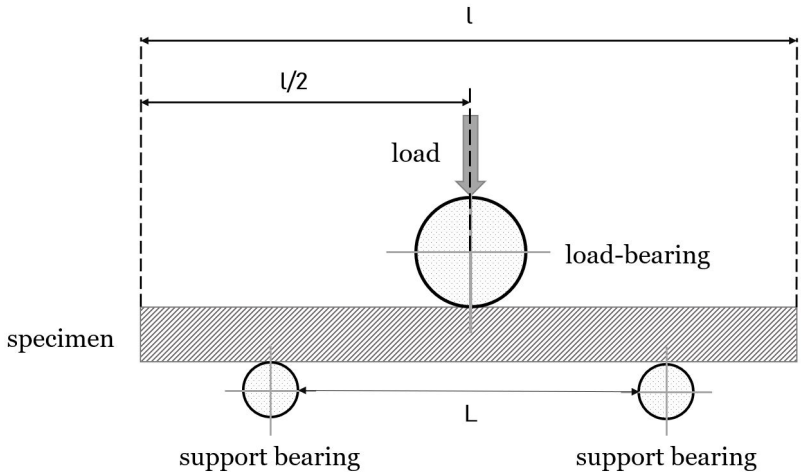

Figure 4.10: Three-point flexural strength test for advanced ceramics at ambient temperature set up illustration.

At least three specimens of each type of material – MA1, MA2, MCZ, and YSZ – were tested. Taking into consideration the bar specimens dimensions – measured in mm – of approximately 5.0 × 4.5 × 45 in a sequence of width (b) × thickness (d) × length (l), the selected crosshead speed for displacement-controlled testing was of 0.5 mm/min, and an outer support span (L) of 40 mm. During the testing process, special attention to the supports (diameter of 10 mm) and the wedge (diameter of 20 mm) of the testing machine was paid so that the ceramic surfaces would not be in direct contact with the metallic components. Therefore, to protect the ceramic specimens, the metallic components' surfaces were covered with polymeric film.

The flexural strength σ (MPa) of a beam in three-point flexure was calculated from the load exerted by the applied force P_l (N) as a function of the geometric parameters of the specimens above-listed. The standard calculation formula is thus represented by **Equation 4.17** as follows

$$\sigma = \frac{3P_l L}{2bd^2} \quad (4.17)$$

In addition, values of the flexural strength mean $\overline{\sigma}$ and standard deviation SD for error associated evaluation of, at least, three specimens tested, n, were computed by **Equations 4.18** and **4.19**, respectively, as expressed below

$$\overline{\sigma} = \frac{\sum_{i=1}^{n} \sigma}{n} \quad (4.18)$$

$$SD = \sqrt{\frac{\sum_{i=1}^{n} (\sigma - \overline{\sigma})^2}{n-1}} \quad (4.19)$$

4.3.2.3 Hardness and Fracture Toughness

After the three-point flexural strength tests were performed, the recovered shreds of the rectangular bar specimens were reused. The half-parts of material were embedded in a two-part mixture of epoxy resin (EpoxiCure 2 Epoxy Resin, Buehler, United States of America) and hardener (EpoxiCure 2 Epoxy Hardener, Buehler, United States of America), in a ratio of approximately 4:1, that gave rise to a chemical reaction which transformed the obtained solution from liquid into solid state after 24 h of resting at room temperature.

Thereafter, a surface optimization area process was conducted which aimed to reduce the samples' rugosity and repair minor scratches or imperfections. Firstly, the excess of epoxy mixture with hardener was removed through wet grinding with the help of manual materialographic apparatus (Struers DAP-V, Denmark) and silicon carbide paper #400 (BUEHLER, United States of America). Then, a semi-automatic RotoPol-21 (Struers, United States of America) apparatus (discs with a diameter of 250 mm and 150 rpm rotational speed) was used equipped with a RotoForce-4 arm (Struers, United States of America), and a rotary speed of 8 rpm, for the polishing procedure which was conducted in the sequence specified on **Table 4.7** below.

Table 4.7: Semi-automatic polishing in sequence of procedures performed.

Polishing cloth	Diamond suspension	Total duration [min]	Force applied [N]
MD-PLAN	6 μm	120	25
MD-DAC	3 μm	120	20
MD-DUR	1 μm	60	15

Polishing cloths with magnetic backings were used to expose the ceramic material structure for analysis by surface deformation removal through surface treatment along with an abrasive. More specifically, MD-PLAN (catalog number 40500087), MD-DAC (catalog number 40500075), and MD-DUR (catalog number 40500095) polishing cloths (Buehler, United States of America) with a diameter of 250 mm were used with a polycrystalline diamond suspension (MetaDi, Buehler, United States of America) of 6 μm (item number 40-6632), 3 μm (item number 40-6631F), and 1 μm (item number 40-6630F), respec-

tively. Worth mentioning that the diamond suspensions are routinely used for material preparation since they allow high-quality surface finishing due to the diamond's high removal rates.

The polishing of specimens was conducted as described since the surface's smoothness highly influences the accuracy of the Vickers indentation hardness test which is one of many properties that is used to characterize fine ceramics and allows to determine the resistance of deformation, densification, and fracture of ceramics.

The Vickers indentation hardness of advanced ceramics test was performed as described in the standard test method ASTM C1327-15 [196] documentation. At its core, the indentation hardness test is performed by using a calibrated hardness tester (Mitutoyo AVK – C2, Japan) to force a pointed and pyramidal diamond indenter under a predetermined load into a surface of the ceramics, i.e., the fragments embedded in resin with hardener. After the indentation is done and the load removed, the surface-projected diagonals of the obtained impression are measured.

During the test special attention was paid to the load applied, i.e., the test force is intended to be sufficiently large that a mark is made, but not so large as to introduce cracking of the material, since, as described in the literature, the Vickers indentations are quite likely to cause fractures or even excessive damage to the samples.

Therefore, taking into consideration the load applied as well as its time of application of 15 s ($\pm$ 2), a proper selection of the acceptable indentations was made according to the guidelines provided in the ASTM C1327-15 norm [196]. For instance, the indentations with irregularities such as *large tip cracks*, *asymmetrical impressions*, *spalled edges*, *pores presence*, *tip region displacement*, or *ragged edges*, were discarded.

After making a considerably reasonable number of impressions, the Vickers hardness HV (GPa) was computed as follows by **Equation 4.20**

$$HV = 0.0018544 \times \frac{P_l}{{d_c}^2} \quad (4.20)$$

where P_l (N) is the load applied and d_c (mm) is the average length of the two diagonals of the indentation.

Similarly to other conducted tests, to evaluate any deviation and/or associated error with, at least, five measurements taken, n, the mean value $\overline{HV}$ and standard deviation SD of the Vickers hardness of the ceramic specimens were established according to the following **Equations 4.21** and **4.22**, respectively

$$\overline{HV} = \frac{\sum_{i=1}^{n} HV}{n} \quad (4.21)$$

$$SD = \sqrt{\frac{\sum_{i=1}^{n} (HV - \overline{HV})^2}{n-1}} \quad (4.22)$$

In addition to the Vickers hardness, the radial median crack system fracture toughness K_C (MPa.m$^{1/2}$) which describes a material's capacity to resist to fracture when enduring a crack was namely calculated with the help of **Equation 4.23** proposed by Anstis et al. (1981) [197]

$$K_C = 0.016 \times \frac{P_l}{{c_c}^{1.5}} \times \left(\frac{E}{HV}\right)^{0.5} \quad (4.23)$$

where P_l (N) is once more the load applied, c_c (mm) is the average length of the two diagonal cracks that emerged from the corners of the indentation made, E (GPa) is the elastic modulus previously calculated, and HV (GPa) the hardness determined.

Lastly, the same methodology, as previously described, was adopted for the calculation of mean value $\overline{K_C}$ and error computation SD of fracture toughness for, at least, five measurements, n, performed. **Equations 4.24** and **4.25** were therefore used as follows

$$\overline{K_C} = \frac{\sum_{i=1}^{n} K_C}{n} \quad (4.24)$$

$$SD = \sqrt{\frac{\sum_{i=1}^{n} (K_C - \overline{K_C})^2}{n-1}} \quad (4.25)$$

4.3.3 Microstructural Analysis

4.3.3.1 X–Ray Diffraction

XRD analysis was performed based on CuKα radiation on the bulk ceramic bar specimens by utilizing a diffractometer (Rigaku DMAX III/C, Japan). The aim of this experimental procedure was to carry out the crystalline phases identification, as above-described, in detail, in section 4.1. For careful examination, data was collected between 5º and 90º (2θ), and furthermore the results obtained, in the diffractograms form, analyzed on a basis of comparison with the theoretical XRD cards, enunciated on **Table 4.4**, in addition to magnesium aluminum oxide card, i.e.,

- Magnesium oxide, M – XRD file/card #71-1176,
- Aluminum oxide, A – XRD file/card #46-1212,
- Calcium zirconate, CZ – XRD file/card #35-0790,
- t-3YSZ – XRD file/card #50-1089,
- c-8YSZ – XRD file/card #49-1642,
- m-ZrO2 – XRD file/card #37-1484 ,
- Magnesium aluminum oxide, $MgAl_2O_4$ – XRD file/card #77-1193.

It is highlighted that the range of measurements between 5º and 90º was selected to ensure the validity and viability of the data subject to be analyzed and studied.

4.3.3.2 Microstructure

In the human body, the optical system is composed of the eye. Nonetheless, this organ has natural limitations in terms of visual acuity dictated both by the biology of the visual system and the physical optical phenomena. Therefore, to overcome the limitations of human eyesight, efficient magnifying tools become mandatory to bring some specific images into focus [198, 199]. Analogically to the human eye, the microscope's resolving power (also known as angular resolution, or simply resolution) efficiency – which denotes the smallest detail that a microscope can resolve when imaging a specimen – depends on the design of the instrument (quality and number of operating lenses) in addition to the properties of light used in the image formation process [198, 199, 200].

Microscopes are instruments that are conventionally used to provide clarity while inspecting objects profoundly, i.e., they produce extremely detailed and enlarged pictures of the smallest objects. Roughly, they can be divided into two main categories – based on the source to produce an image – optical microscope (OM) and electron scanning microscope (SEM). The main difference between the optical microscope and the scanning electron microscope is the source to produce images, more precisely, the type of beam of

light applied to the sample. For the optical microscope, the visible light beam is applied, whilst for the electron scanning microscope, an accelerated electron beam is used instead [201, 202, 203].

As pointed out by Zhou et al. (2006) [204] the SEM "is one of the most versatile instruments available for the examination and analysis of the microstructure morphology and chemical compositions". The interaction of the electron beam with the sample dictates the quality of the signal acquisition produced which in turn influences the image formation. This relationship may be categorized as *elastic interactions* – consequence of the deflection of the incident electron by the specimen atomic nucleus or outer shell electrons of similar energy – and *inelastic interactions* – an outcome of several interactions among the incident electrons and the electrons and atoms of the sample [203, 204].

The incident electrons that are *elastically scattered* by the specimen give rise to the so-called back-scattered electrons (BSEs) in a wide-angle directional change characterized by negligible energy loss. The BSEs provide compositional information, i.e., a contrast in multiphase samples composition is exhibited for speedy phase judgment. On the other hand, *inelastic electron scattering* originates primary beam electrons and substantial energy to the atoms of the specimen is consequently transferred. The amount of energy loss relies on whether the specimen electrons are excited singly or collectively and on the binding energy of the electron to the atom. Thereby, the excitation of the electrons by the primary beam strike of the sample surface generates secondary electrons (SEs) which consists of the loosely bound electrons of the atoms of the material. The SEs are normally considered the most important electrons since they strongly interact with the surface and therefore hand sample topographical and morphological information. Besides the signals mentioned – back-scattered electron and secondary electron detectors – other signals are produced when an electron beam strikes a sample, for instance, X–rays, Auger electrons, and cathodoluminescence. Moreover, the X-rays – that are generated by the inflexible impacts of the incident electron beam with the electron available in the orbital levels of the sample atom – may serve for the so-called elemental analysis of surfaces in SEM using energy dispersive spectroscopy [201, 202, 203, 204].

To conclude, SEM analysis is an advanced technique with a greater focus depth, i.e., greater depth of field when compared to standard optical microscopy and magnification power for small features, such as texture (morphology), chemical composition, crystalline structure, and material orientation evaluation. **Figure 4.11** shows a schematic illustration of the SEM working principle, i.e., the different signals - BSE, SE, X–rays – generated by the incident primary electron beam and the corresponding regions from which each signal can be detected.

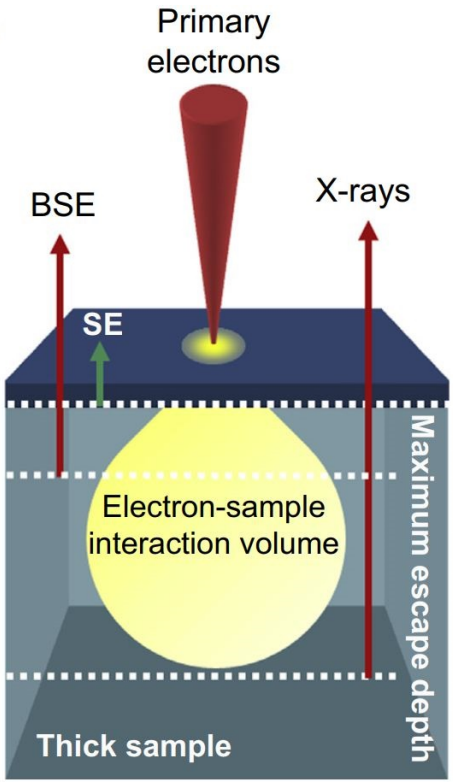

Figure 4.11: Illustration of the working principle of the scanning electron microscope: electron-sample interaction in function of the specimen volume [205]

Accordingly, for the microstructure imaging attainment, SEM methodology was exploited with a scanning electron microscope (Hitachi S-2700, Japan) - and by applying an accelerating voltage of 20 kV - after performing careful specimen surface preparation, as described in 4.3.2.3, once the microscope time and image analysis are highly impacted by the quality of the surface being examined. To put it in another way, the quality of the imaging obtained is strongly affected by the quality of the surface of the specimen being studied. Furthermore, thermal etching was also conducted for microstructure – *grain boundary* – contrasting for 30 min at 1305 ºC and 1440 ºC for the zirconia and alumina samples, respectively, i.e., at a temperature 10 % lower than the sintering temperature (referred in 4.2.3). Both, the heating and cooling rates were of 10 ºC/min.

Once optimized, the surface of the ceramics bar specimen being analyzed – MA1, MA2, MCZ, and YSZ – was gold-sputtered, as shown in **Figure 4.12**. The ultra–thin gold coating was applied with a turbomolecular pump coater (Emitech K550 Gold Sputter Coater, Quorum Technologies, United Kingdom) - **Figure 4.13** - to enhance the conductivity of the sample, which in turn will boost the interaction between the bombarded electron beam and the specimen surface.

Figure 4.12: Ceramic samples with an ultra-thin gold coating.

Lastly, and to conclude, gold – which is not easily oxidized – is considered one of the most widely used materials to coat non-conducting or poorly conducting specimens. Overall, the coating procedure offers benefits for the samples subject to SEM analysis, such as diminishing microscope beam damage, protection of beam-sensitive specimens, increased thermal conduction, reduced sample charging, and improved secondary electron emission [206].

Figure 4.13: Ultra-thin gold coating deposition.

4.3.4 Thermal Properties

When evaluating material characteristics, it is necessary to use different techniques or even a combination of multiple techniques depending on the purpose sought. According to the definition provided by the International Confederation for Thermal Analysis and Calorimetry (ICTAC), thermal analysis (TA) – which is a branch of physicochemical science – is "a group of techniques in which a property of a sample is monitored against time or temperature while the temperature of the sample, in a specified atmosphere, is programmed" [207, 208]. In other words, TA focuses on the study of the relationship between a sample property and its temperature, as the sample is heated or cooled, in a controlled manner. Each TA technique is defined according to the types of physical changes being analyzed, that is to say, temperature, enthalpy, mass and dimensional variation [207, 209].

Complementary to stated, depending upon the physical properties of the material being measured and studied (as referred, temperature, enthalpy, mass, or deformation), the most common thermal analytical techniques are as follows [209]:

- Differential Thermal Analysis (DTA) which evaluates the *temperature* difference,
- Differential Scanning Calorimetry (DCS) that analyzes the *enthalpy* variations,
- Thermo Gravimetric Analysis (TGA) that assess the *mass* (weight) changes, and
- Thermo Mechanical Analysis (TMA) which studies the *dimensional variations* (deformation) of the material investigated.

Generally, thermal analysis is mainly used in the field of research and development, and the instruments applied comprise a *detection unit* which includes a sample and reference holder, furnace, and sensors; a *temperature control unit* that rules the furnace temperature; and lastly, a *data recording unit* responsible for recording the signals initiated by the sensors and analyzing them [209].

4.3.4.1 Thermal conductivity

Thermal conductivity was computed throughout thermal diffusivity and specific heat experimental determination according to the thermal diffusivity by the flash method standard test method ASTM E1461 – 13 [210] of primarily homogeneous isotropic solid material. On one hand, *thermal conductivity* may be defined, according to Ratna (2012) [211], as "the rate at which heat is transferred by conducting through a unit cross-section area of a material when a temperature gradient exists perpendicular to the area". On the other, *thermal diffusivity* can be described as the parameter that describes the rate of temperature spread through a material. Consequently, thermal diffusivity is a *material property* that gives an insight into the ability of a material to conduct thermal energy relative to its

ability to store it [212].

In thermal characterization, many questions – for instance, related to development of new materials and designs, process control and optimization, safe operating temperatures, quality assurance, in addition to numerical simulation – may be solved when these two fundamental thermophysical properties are accurately known. To summarise, it is possible to state that the two main properties related to heat conduction are thermal conductivity and thermal diffusivity [213]. Mathematically, thermal diffusivity, a [mm^2/s], is the thermal conductivity λ [W/(m.K)] divided by the volumetric heat capacity, c_p [J/(g.K)], and the sample's density ρ [g/cm^3], at constant pressure, as follows in **Equation 4.26**

$$a(T) = \frac{\lambda(T)}{c_p(T) \times \rho(T)} \iff \lambda(T) = a(T) \times c_p(T) \times \rho(T) \quad (4.26)$$

To solve the equation enunciated, and thus determine the thermal conductivity λ the Laser Flash Analysis (LFA) technique – introduced by W. J. Parker et al. [214] in 1961 – was considered. The LFA method is particularly advantageous thanks to the *simple specimen size and geometry requirements*, *rapidity of measurement* [9] and *ease of handling*. Moreover, it is found a *non-destructive and non-contact method* [210].

From the theoretical point of view, the physical model of the pulse method is established on the thermal behavior of the specimen being analyzed, in adiabatic conditions[10], at a constant temperature, whose bottom side has been exposed to a light flash. Accordingly, it is important to highlight that an analytical solution for LFA thermal diffusivity measurements is only considered valid if the following conditions are fulfilled [210]:

- one-dimensional heat flow,
- no heat losses from the specimen surfaces,
- uniform pulse absorption at the bottom surfaces,
- absorption of the pulse energy in a very thin layer,
- infinitesimally short pulse duration (when compared to the time required for heat diffusion), and
- property invariance with temperature within the experimental conditions.

For a detailed explanation of the working principles and fundamentals of the flash test method, the ASTM E1461 – 13 Annex X2 [210], which provides additional support, should

[9] The LFA method conducts tests at a range of a few seconds for a given temperature. Measurements over a wide temperature range may take some hours to perform [213].

[10] By convention, an adiabatic process transfers energy to the surrounding only as work.

be considered.

In principle, the thermal diffusivity is attained from the *thickness of the specimen* and from a *characteristic time function describing the propagation of heat* from the bottom to the top surface. In this *discontinuous measuring technique*, the bottom surface of the specimen is heated to defined temperature steps by a short laser pulse. After the temperature stabilization, the temperature rise verified on the top surface is recorded by an infrared detector [213, 210]. **Figure 4.14** shows a schematic representation of the working principle of the LFA method, whilst **Figure 4.15** illustrates a typical curve of temperature variation as a function of time.

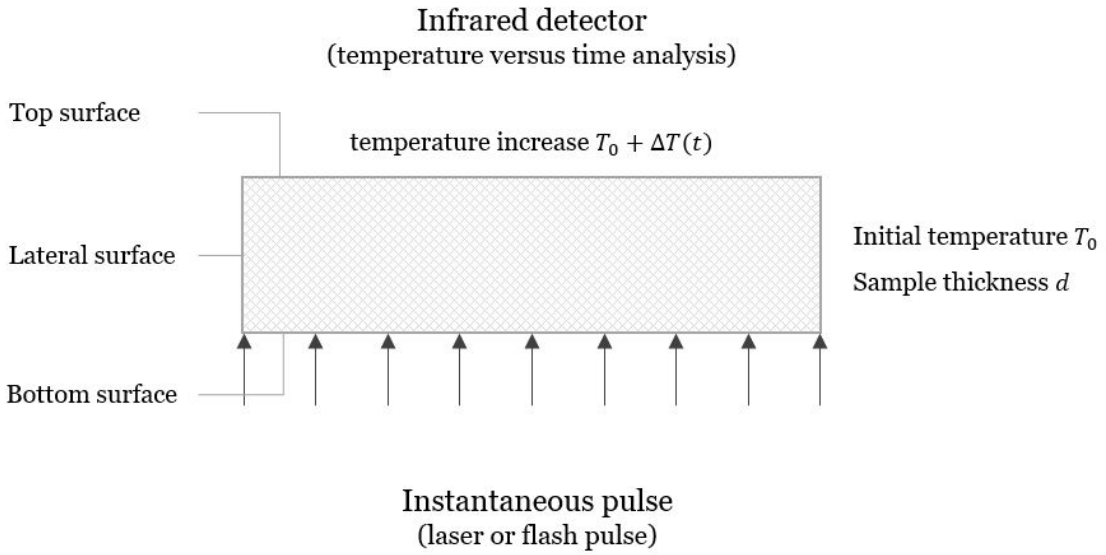

Figure 4.14: LFA working principle schematic illustration.

Mathematically, the graph of temperature variation in function of time allows the determination of the thermal diffusivity as follows in **Equation 4.27**

$$a(T) = 0.13879 \times \frac{d^2}{t_{0.5}} \quad (4.27)$$

with d [mm] being the thickness of the sample, and $t_{0.5}$ [s] the so-called *half-minimum* that consists of the time needed for the temperature on the top side of the sample to rise half of its maximum value.

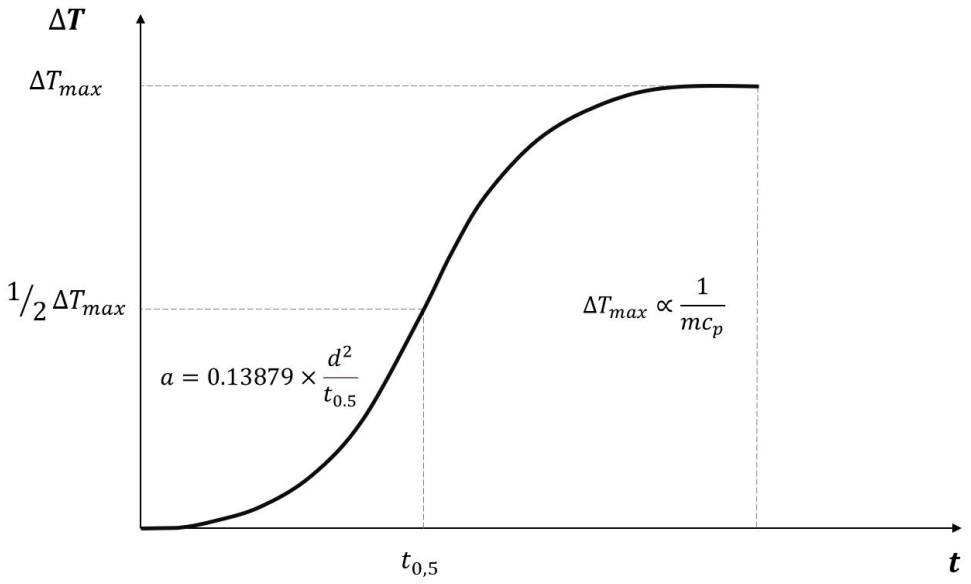

Figure 4.15: Characteristic thermal curve (temperature in function of time) for the FLA method.

Consequently, based on the information described, for the accomplishment of the thermal diffusivity determination, the disc specimens originally with a diameter of 28 mm and a thickness of 2.5 mm were cut with the help of water jet to adapt and adequate them to the sample carrier dimensions of the laser flash apparatus, i.e., diameter of 12.55 ± 0.5 mm. Afterward, a high emissivity coating (Kontakt-Chemie 76009-AG, Graphit 33 Spray, Belgium) was applied to the surface of the ceramic specimens to improve their capability to absorb the energy applied. **Figure 4.16** shows the ceramic specimen (right side picture) encapsulated in the circular sample carriers (left side picture) and then mounted on the integrated motorized sample changer with a capacity of taking up to three sample measurements simultaneously (middle picture).

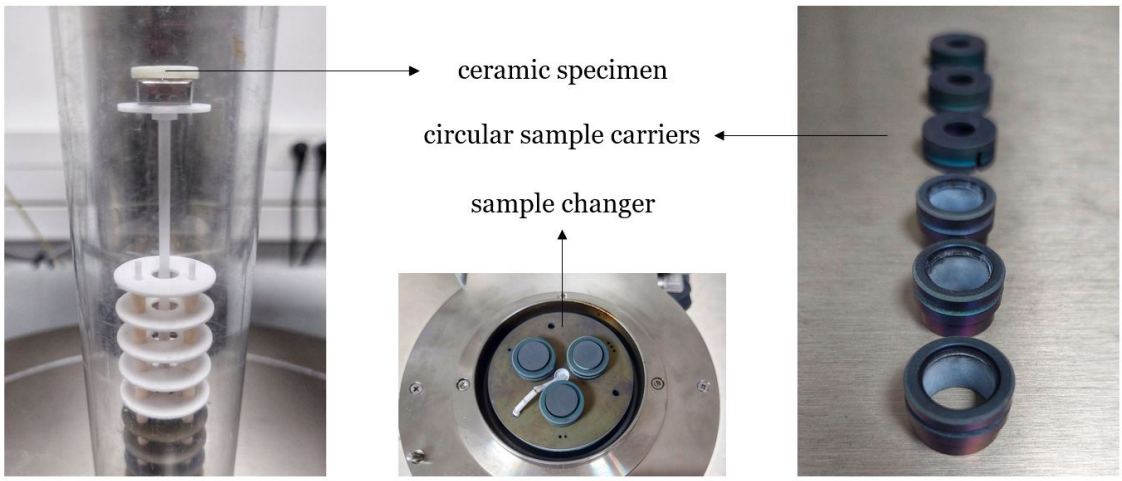

Figure 4.16: Ceramic sample (left), circular sample carriers (right), and integrated motorized sample changer (middle).

As already described and to put it succinctly, the thermal diffusivity was obtained by heating the bottom surface of the plane-parallel disc specimen with a short energy light (i.e., laser) pulse of the laser flash apparatus (LFA 457 MicroFlash, Netzsch, Germany). Next to the temperature stabilization, the resulting temperature exchange (rise) on the top side of the sample – which was recorded by performing seven measurements – as a function of time was obtained. The thermal diffusivity of the ceramic samples – MA2, MCZ, and YSZ – was tested upon a temperature interval ranging from room temperature 298.15 K (25 ºC) to 1273.15 K (1000 ºC) in a controlled inert atmosphere composed of argon or nitrogen .

In addition, a reference material (Pyroceramic, Order number 6.256.1-94.0.03, Netzsch, Germany), with a diameter of 12.7 mm and thickness of 2.5 mm, was tested simultaneously with the ceramic samples to compute the specific heat of the ceramic specimens and to serve as a calibration and verification control practice. Since the total temperature increase, i.e., step height is indirectly proportional to the heat capacity of the sample, as shown in **Figure 4.15**, the specific heat of the sample may be determined. The method applied for the specific heat c_p determination is known as a *comparative method* in which two samples are measured under the same conditions: a *test sample* under investigation and a *reference sample* with specific heat values already established [215]. The computation of the ceramic specimen specific heat for a given temperature was therefore computed as shown by **Equation 4.28** below

$$c_p^{sample} = \frac{T_{max}^{ref}}{T_{max}^{sample}} \times \frac{\rho^{ref}}{\rho^{sample}} \times \frac{d^{ref}}{d^{sample}} \times c_p^{ref} \quad (4.28)$$

where c_p^{sample} and c_p^{ref} [J/(g.K)] are the specific heat, T_{max}^{sample} and T_{max}^{ref} [K] the maximum temperature recorded, ρ^{sample} and ρ^{ref} [g/cm^3] the density, and, lastly, d^{sample} and d^{ref} [mm] the thickness of both sample and reference material, respectively.

Finally, having calculated the *thermal diffusivity* through **Equation 4.27** and the specific heat thanks to **Equation 4.28**, **Equation 4.26** was used to withdraw the thermal conductivity of the three ceramics studied in the thermal analysis – MA2, MCZ, and YSZ.

4.3.4.2 Coefficient of Thermal Expansion

The coefficient of thermal expansion was determined through thermomechanical analysis. In its simplest, thermomechanical analysis is one of the crucial tools in thermal analysis that evaluates the change in the dimensions of a sample as a function of temperature, time, and (nonoscillatory) load. Bearing in mind that many materials during cooling and/or heating processes suffer modifications in their (thermomechanical) properties, the TMA analysis grants information about the expansion or contraction of the sample in addition to its softening or deformation [216, 217]. In other words, the ICTAC

defines the thermomechanical analysis technique as “a technique whereby the deformation of a sample is measured under constant load” [208]. The TMA methodology is extremely advantageous since it allows the computation of several different properties of a sample being studied in the same test. Examples of these properties may be the coefficient of thermal expansion, melting temperature, phase transition temperatures, and elevated temperature creep or stress relaxation behavior, among others. Therefore, TMA delivers valuable information regarding the composition, structure, production conditions, and feasible applications for various materials. As a last remark, it is highlighted that in case a load is not applied during TMA measurements, the technique is named *thermodilatometry* [216, 217].

Overall, the TMA analyzer consists of a rigid *specimen holder*, a *weight or force transducer*, a *sensing element* (i.e., usually a linear variable differential transformer (LVDT)), a rigid *expansion probe* that contacts the specimen with an applied expansion/compression force, a *furnace* that generates a constant force, *temperature controller and sensor*, a *cooling system*, a *recording device*, and a *micrometer*. In addition, the TMA technique is performed in a controlled atmosphere [218].

The TMA test performed according to the ASTM E831 – 06 [218] standard test method, used a thermomechanical analyzer device – which can be conceptualized as a caliper in an oven – to determine the linear thermal expansion of solid materials when subject to a constant heating rate. The change of the specimen length was electronically recorded as a function of temperature, and, consequently, the mean coefficient of linear thermal expansion α_m [μm/(m.°C)] calculated from the collected data, as shown in the following **Equation 4.29**, where ΔL^{spec}[μm] is the change of specimen length, L^{spec} [m] is the specimen length at room temperature, ΔT^{spec} [°C] is the temperature difference over which the change in specimen length is measured, and k is the calibration coefficient given by **Equation 4.30** where, in turn, α^{ref} [μm/(m.°C)] is the mean coefficient of linear thermal expansion for reference material, L^{ref} [m] is the reference material length at room temperature, ΔT^{ref} [°C] is the temperature difference over which the change in reference material length is measured, and, lastly, ΔL^{ref} [μm] is the change of reference material length due to heating

$$\alpha_m = \frac{\Delta L^{spec} \times k}{L^{spec} \times \Delta T^{spec}} \quad (4.29)$$

$$k = \frac{\alpha^{ref} \times L^{ref} \times \Delta T^{ref}}{\Delta L^{ref}} \quad (4.30)$$

The linear thermal coefficient is a vital parameter to be studied since it gives insights into the material’s response to a change of temperature and hence allows to infer if failure by

thermal stress may occur [219].

Experimentally, a TMA analyzer (TMA 402 F1/F3 Hyperion, Germany) was used for the thermal expansion coefficient determination with a pretest applied load in the interval of 0.2 N. The tests performed used rectangular ceramic specimen type with approximately 5.0 × 4.5 × 25 mm dimensions in a sequence of width (b) × thickness (d) × length (l), respectively. In addition, a reference material (Fused Silica, Serial number 35859, Netzsch, Germany), with a diameter of 6 mm and length of 25 mm was also used to establish the validity of the obtained data, accuracy assessment, and calibration purposes through the calibration coefficient enunciated in **Equation 4.30**, i.e., the observed expansion must be corrected for the difference in expansion between the specimen holder and a probe test obtained from a control specimen – **Figure 4.17** [218]. The apparatus allowed to have a software-controlled, protective atmosphere of inert gas, i.e., more specifically, nitrogen gas. A temperature interval ranging from 173.15 K (-100 °C) to 1253.15 K (980 °C) was considered and a heating rate of 5 K/min was applied. The reasoning behind starting the CTE determination with 173.15 K relies on two grounds: the first being the apparatus' steel furnace capacity to achieve 123.15 K (-150 °C), and the second is the interesting data it would offer to analyze.

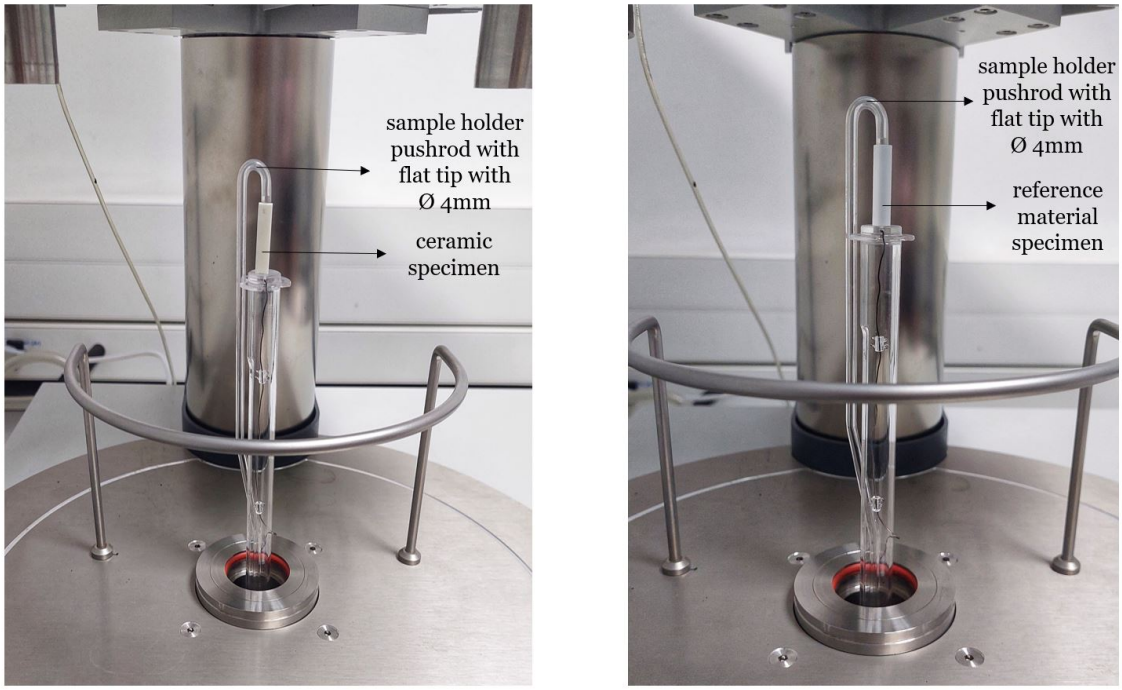

Figure 4.17: TMA sample holder with a diameter of 4 mm, ceramic specimen (left), and reference (right) material specimen.

4.3.5 Electrical Properties

To conduct the experimental study regarding the feasibility of the different ceramic materials produced – MA1, MA2, MCZ, and YSZ – as dielectric barriers for DBD plasma actuators, electrical tests were performed. For this aim, several types of equipment were used to operate and evaluate the DBD plasma actuators in terms of electrical, mechanical and thermal performance. **Figure 4.18** shows the experimental setup applied.

Specifically, the DBD plasma actuators were supplied by an AC high-voltage and frequency power source (PVM 500, Information Unlimited, United States of America) that allows producing signals with voltage amplitudes up to 20 kV peak to peak (kVpp) – this is, the distance from a crest and a trough of an AC voltage waveform –, frequencies between 20 and 50 kHz, and the power may reach up to 200 W. Furthermore, to monitor and record the voltage and current waveforms, a digital oscilloscope (PicoScope 5443A, Pico Technology, United Kingdom) of high signal integrity was used and connected to a high-voltage probe named "Secondary Ignition Pickup" (MI074 Secondary Ignition Pickup, United Kingdom). The high voltage probe is typically designed to safeguard the measuring instrument since attempting to make a direct connection would almost surely damage the equipment due to high voltages involved in the performed tests.

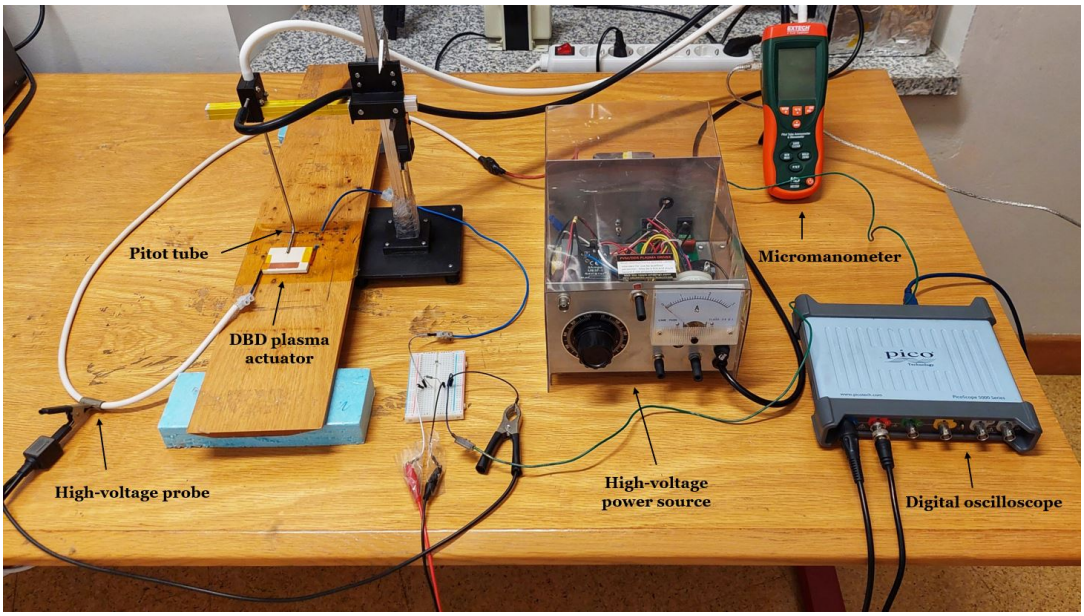

Figure 4.18: Experimental setup and materials used for the DBD plasma actuator characterization.

Additionally, the plasma actuator electrodes were made of copper tape and asymmetrically mounted on both sides of the dielectric, as depicted in the previous scheme presented in **Figure 3.14**, with a gap of 1 mm between them. The electrodes had a length of 30 mm and a thickness of 80 μm. The width of the exposed electrode was 10 mm, whereas of the enclosed one was 20 mm to certify that the plasma discharge extension would not be

limited by the end, i.e., the shortest length of the covered electrode.

In the literature, several studies conducted to infer about the optimum gap distance between the exposed and covered electrodes may be found. Commonly, three arrangements stand out, including the *overlapping design*, the *gapless design* and the *variable gap design*. It was shown by Roth and Dai (2006) [220] that the variable gap setup with an interval range of 1 – 2 mm maximizes the generated horizontal electrostatic pressure and consequently the horizontal flow velocity. Within the same framework of though, Forte et al. (2007) [221] emphasized that a gap with values higher than 5 mm gives rise to *strongly modified electric field distribution*. In addition, Rigit et al. (2009) [222] concluded that with the augmentation of the gap distance, degradation of the DBD actuator may be reduced by the lesser concentration of ion bombardment that is weakened at a specific area. In conformity with the above described a trade-off was therefore made between the degree of degradation of the dielectric and the performance to be achieved. Accordingly, 1 mm gap, as mentioned previously, was implemented.

Figure 4.19 represents the ceramic dielectrics glued with the copper tape electrodes and Kapton tape as protection material to shield the covered electrode and therefore ready to be tested. The electric experimental tests were conducted under environmental conditions of approximately 22 ^{o}C and 40 – 50 % relative humidity.

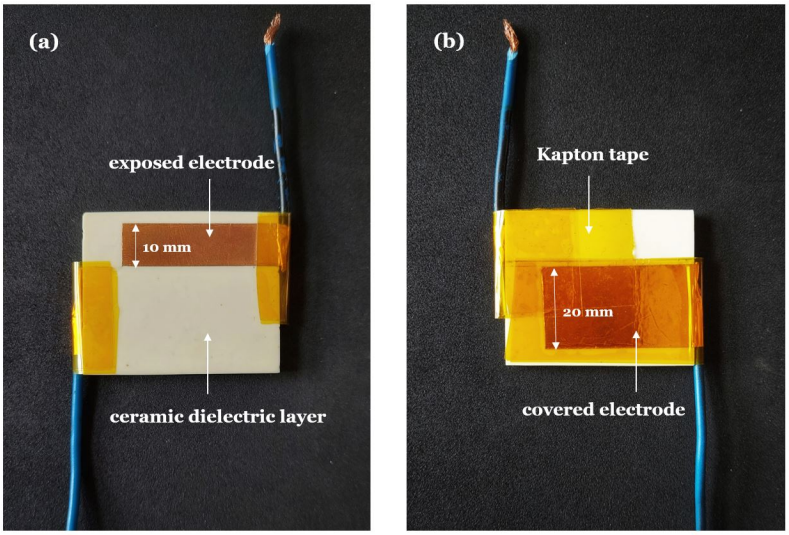

Figure 4.19: Plasma actuator ready to be tested: (a) top and (b) bottom surfaces.

In undertaking electrical tests, it shall be understood that due to their nature and characteristic features, DBD plasma actuators are devices that make it impossible to use some of the recurrent experimental techniques or equipment without considering certain safety measures. More precisely, during the plasma actuator operation, high-frequency and high-voltage signals are engendered, which in addition to the generated strong electrical field make accurate experimental analysis extremely difficult.

For these reasons, two methods from the literature were applied to perform the electrical characterization analysis, i.e., the *electrical current method* and the *electric charge method* based on a digital oscilloscope aforenamed that worked as a signal digitizer, i.e., an instrument that – by using the analog to digital converters – captures the fast-changing electrical signals and stores digitized waveform data in fast memory [223, 224].

The waveforms were collected with a sampling rate of 125 MS/s (mega samples per second) and a vertical resolution of 14 bits, which results in an uncertainty of approximately 1 %.

4.3.5.1 Electrical Current Method

In greater detail, once high voltages were to be imposed, and consequently, conventional laboratory equipment is not suitable to directly measure the resulting current, the *electric current method* (also named *current measurement using a shunt resistor*) was employed to calculate the current of the input signal and, in turn, perform the average power determination.

As result, to conduct this test method, a metal film resistor (Robert Mauser, Lda., Portugal), with an impedance of 100 Ω and 1 % of tolerance, was placed in series with the plasma device allowing this way the voltage across the resistor to be low enough, and thus to be measured by a conventional probe – **Figure 4.20**. From the literature, the resistor utilized in this method shall present a typical impedance in the range of 1 – 100 Ω.

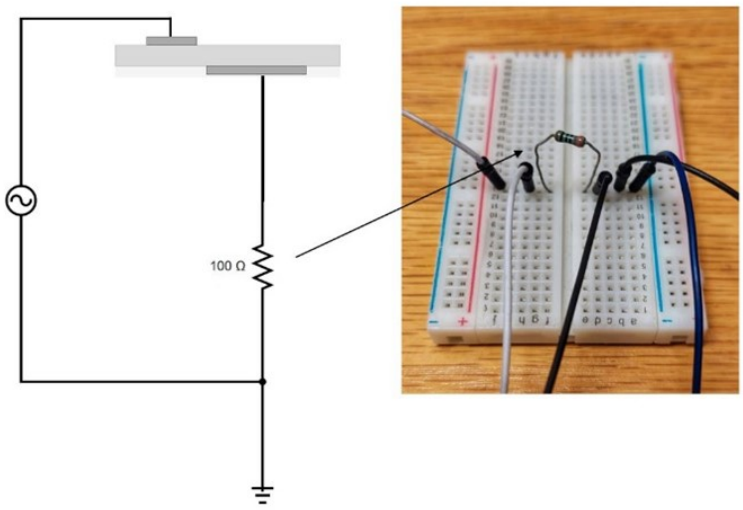

Figure 4.20: Electric current method setup diagram.

The resistor used was selected based on its temperature coefficient of 50 ppm, i.e., 0.00005 Ω/ºC which by being low can be neglected in the power consumption analysis and namely denotes that the impedance[11] remained almost constant under temperature variations. Furthermore, since the impedance is very low when compared with the actuator's impedance, it can be considered that no influence on the actuator operation was imposed.

Once the voltage across the resistor was measured, the current passing through the resistor was quantified employing the Ohm's law as follows in **Equation 4.31**

$$I_r = \frac{V_r}{R} \quad (4.31)$$

In addition, bearing in mind that the two components (actuator and resistor) were placed in series, their current value were equal, i.e., $I_r = I_a$. The determination of the consumed electrical power from the electric current method consisted initially of the described experimental measurement of the voltage and current waveforms, and afterwards by the multiplication of the two recorded signals. Consequently, the instantaneous power $P_{el}(t)$ (W) was computed through **Equation 4.32** as follows

$$P_{el}(t) = V_a(t) \times I_a(t) \quad (4.32)$$

where V(t) (V) and I(t) (A) are the input voltage and the input current, respectively, on the actuator. Lastly, for the electrical current method, the average consumed power by the actuator $\overline{P_{el}}$ (W) of n signal periods T was determined by **Equation 4.33**

$$\overline{P_{el}} = \frac{1}{nT} \int_0^{nT} V(t) \times I(t) dt \quad (4.33)$$

4.3.5.2 Electrical Charge Method

On the other hand, the *electric charge method* (also designated as *charge measurement using a monitor capacitor*) was performed for further detailed analysis of the plasma actuator electrical characteristics by replacing the previously used resistor with a ceramic disc capacitor E222M (Robert Mauser, Lda., Portugal) – **Figure 4.21**. In this method, the capacitor known as *monitor*, *measurement* or *probe* capacitor is chosen to have a large capacitance when compared to the capacitance of the actuator without plasma discharge.

[11] Electrical impedance measures the total opposition that a circuit or part of a circuit offers to the passing through electrical alternating current. In other words, the electrical impedance is the combined effect of both resistance component which arises from collision of the current-carrying charged particles with the internal structure of the conductor; and reactance component that is an additional opposition to the movement of electric charge that arises from the changing magnetic and electric fields in circuits carrying alternating current.

Once the capacitance of typical actuators is very low, i.e., 5 – 200 pF, monitor capacitors with values that fall within the range of 10 – 330 nF are chosen. The selected ceramic capacitor E222M had a characteristic capacitance of 10 nF and a tolerance of 10 %.

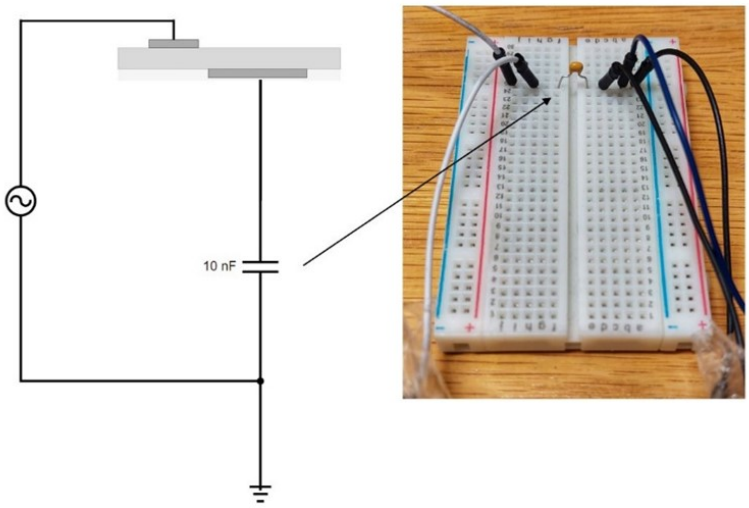

Figure 4.21: Electric charge method setup diagram.

The instantaneous charge q(t) (C) accumulated in the monitor capacitor was calculated by the following **Equation 4.34**

$$q(t) = C_c \times V_c(t) \quad (4.34)$$

where C_c (F) is the capacitance of the ceramic capacitor and V_c (t) (V) is the voltage across it. The variation of the maximum and minimum charge measured by the monitoring capacitor is an important feature for the electrical characterization of the DBD plasma actuators – considering, for instance, ice sensing and deicing performance aims [225]. The current I_c (t) (A) passing through the capacitor was given by **Equation 4.35**

$$I_c(t) = C_c \times \frac{\partial V_c(t)}{\partial t} \quad (4.35)$$

Since the capacitor was placed in series with the actuator between the covered electrode and the ground, the current passing through it is equal to the one in the actuator, i.e., $I_c = I_a$. Thus, the instantaneous power $P_{el}(t)$ (W) dissipated by the actuator was computed by **Equation 4.36** as indicated next

$$P_{el}(t) = V_a(t) \times I_a(t) = V_a(t) \times C_c \times \frac{\partial V_c(t)}{\partial t} \quad (4.36)$$

where V_a (t) (V) is the voltage and I_a (t) (A) is the current at the actuator. Finally, the

average consumed power $\overline{P_{el}}$ (W) of n signal periods T was determined by the following **Equation 4.37**

$$\overline{P_{el}} = \frac{1}{nT}\int_0^{nT} V_a(t) \times C_c \times \frac{\partial V_c(t)}{\partial t} dt = \frac{1}{nT}\int_0^{nT} V_a \times C_c \times dV_c \quad (4.37)$$

It should be emphasized that the power consumption is one of the most important parameters to be calculated and considered since it allows *comparative characterization of the performance* of the various ceramic actuators produced, as well as in terms of practical implementation the actuator consumption data grant the opportunity for *cost-benefit evaluation*.

By plotting the instantaneous charge accumulated in the capacitor, previously calculated by **Equation 4.34**, against the instantaneous voltage of the actuator, Lissajous curves, i.e., voltage-charge plot are thus obtained. Mathematically, the Lissajous curves can be used to analyze the properties of any two simple harmonic motions that are at right angles to each other. **Figure 4.22** shows the voltage-charge filtered data graph – black continuous line – of a surface DBD plasma actuator discharge attained from the collected experimental data – represented by the black dots.

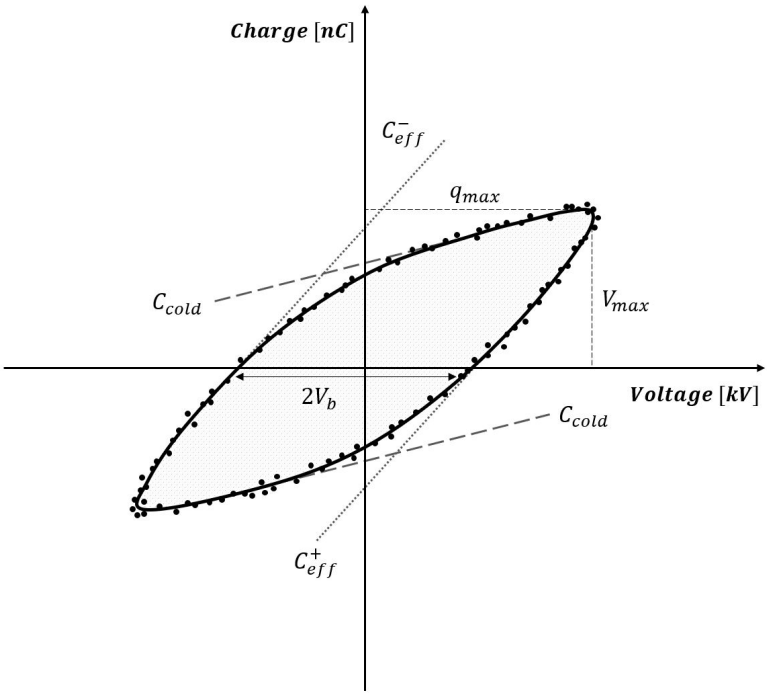

Figure 4.22: Lissajous diagram of a surface DBD plasma actuator discharge.

Typically, the Lissajous curves allow determining relevant electrical parameters of the actuators, i.e., cold C_{cold} and effective C_{eff} capacitance through specific local slopes of the curves, the breakdown voltage V_b, and the charge transferred dq for different applied operating voltages. In the interest of clarity, C_{cold} concerns the pure passive component

capacitance of the actuator device, therefore it represents the capacitance of the actuator when no plasma is generated. In turn, the C_{eff} refers to a combination of the passive component capacitance, i.e., C_{cold} in addition to the contribution of the produced plasma itself capacitance. In other words, and simply put, the C_{eff} is related to the capacitance of the device during the plasma discharge phenomenon [224, 226].

After the power consumption was determined, the fluid dynamic characterization was performed to study the mechanical performance of each plasma actuator. Fundamentally, the velocity of the plasma-induced flow was assessed by using the stainless-steel Pitot tube (167-6 model, Dwyer, United States of America) with inner and external diameters of 1.19 and 3.18 mm, respectively. It is important to highlight that once the Pitot tube is made of stainless steel, a special precaution had to be considered in the distance set – in the x-axis as shown in **Figure 4.23** – between the exposed electrode and the Pitot tube in order to avoid an arc discharge – i.e., arc discharge produces a prolonged electrical discharge and would therefore modify the plasma discharge actuation nature which is highly undesirable. As consequence, experiments were conducted for distances (between the exposed electrode and Pitot tube) of 1 cm and 1.5 cm namely to establish in which of these two positions higher velocities would be recorded. For the measurement of the flow velocity originating from the plasma discharge, a micromanometer (Extech HD 350, United Kingdom) with a resolution of 0.01 m/s and an accuracy of 1 % full-scale (FS) was used directly connected to a computer, thus allowing live streaming data. For the sake of completeness, when an instrument has the accuracy specified as % FS then the associated error, i.e., the percentage of variation will be constant for all the readings performed. This is different to the usually recognized percentage of reading accuracy since it is represented with respect to the true value of the measurement. In other words, the accuracy of reading value is dependent on the actual reading, thus the error may change linearly, whilst for the full-scale accuracy it remains constant.

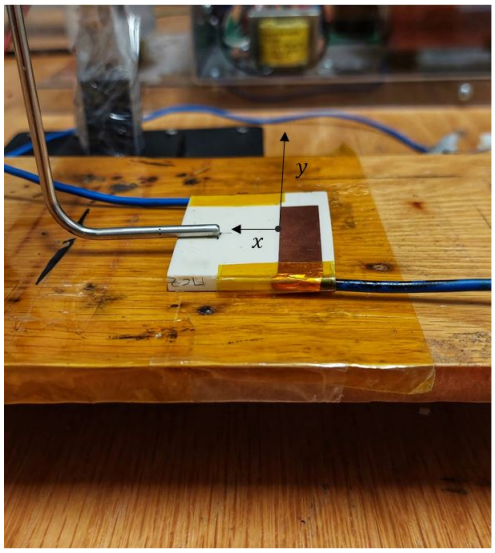

Figure 4.23: Illustration of the induced flow velocity measurements setup.

Lastly, thermal properties and the temperature effect on the plasma discharge were studied. The thermal examination allowed to infer regarding the plasma discharge extension which is an important parameter since it is associated with the body force generated by the plasma actuator. For this aim, a thermal imaging camera (FLIR E50, Teledyne FLIR, United States of America) was used with a resolution of 240 $\times$ 180 pixels and 2 % of uncertainty. The measurement was performed on the upper side of the dielectric plasma actuator – from 13 cm and 21 cm height for the zirconia– and alumina–based ceramics due to their respective sizes – immediately after the stoppage of plasma discharge for a total interval of time of operation of 300 s to ensure temperature stabilization. For the thermal properties analysis, the plasma actuators were painted with a black matte ink with an emissivity (i.e., effectiveness in emitting energy as thermal radiation) of 0.97 as shown in **Figure 4.24** . The black ink was previously tested, validated, and certified so that no impairment in the measurements would occur thanks to the ink's temperature field interference during the actuator operation.

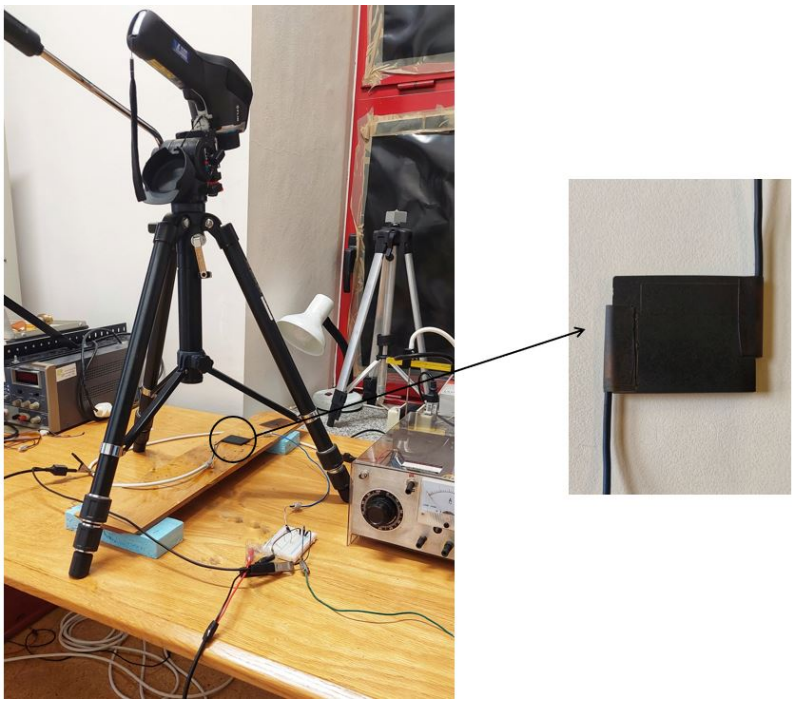

Figure 4.24: Illustration of thermal properties test setup.

Chapter 5

Results and Discussion

5.1 Microstructural Analysis

In this section the evaluation of the particle size distribution, the X-ray diffraction, as well as scanning electron microscopy imaging data for the manufactured ceramic composites will be presented. In addition, conclusions reached will be reported and described as well.

5.1.1 Particle Size Distribution

Determining particle size distributions (PSDs) is one of the key elements in ensuring the performance and consistency of a product since the particle size of a component highly influences many materials' properties. In its essence, by evaluating the PSD data, it is possible to infer the frequency of particles of a determined size in a sample. PSD is therefore a statistical concept in which percentages may be indicated per size interval or cumulative data. As mentioned in the last chapter in section 4.2.1, Material Preparation Stage, monitoring of the PSD was conducted throughout the fabrication stage to ensure that the ceramic systems produced – MA1, MA2, MCZ, and YSZ – would have a manufacturing process as similar as possible to foster greater confidence in the analysis of their physical, mechanical, thermal, and electrical results. The following **Figures 5.1** and **5.2** show the particle size distribution of MA1, MCZ, and YSZ powder mixtures after 3 h and MA2 after 6 h milling in number and volume, respectively.

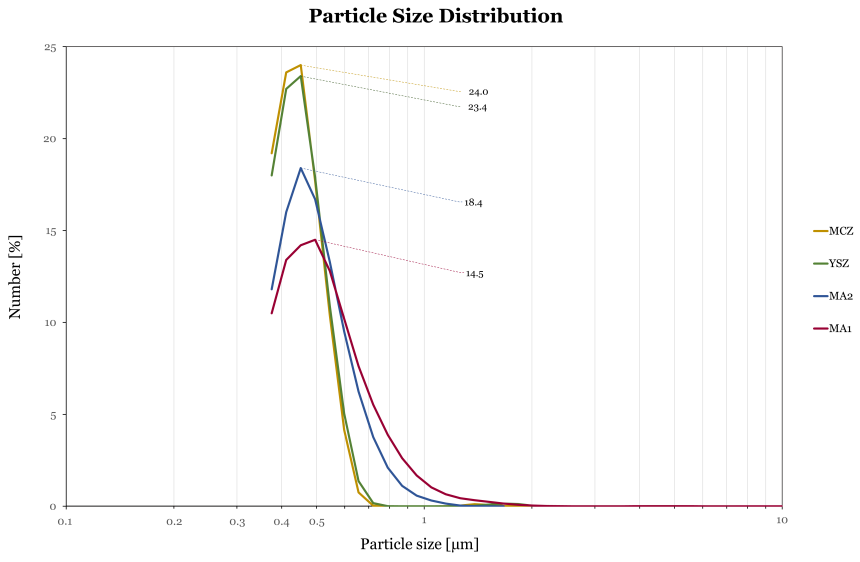

Figure 5.1: Number-weighted PSD of the fabricated ceramic systems.

From the *number-weighted PSD analysis* – in which all particles have the same contribution – is possible to conclude that all the mixtures present a particle size distribution roughly lesser than 1.5 μm. More specifically, all the powders show a mean maximum number percentage of particle size of 0.5 μm. In addition, two slightly different behaviors may be identified in **Figure 5.1**. Both MCZ and YSZ ceramic mixtures exhibit a higher percentage of particles in the range of 0.5 μm, i.e., 24 % and 23.4 %, respectively, whereas MA2 and MA1 show a maximum of about 18.4 % and 14.5 %, respectively. This means that alumina-based systems have a higher content of residual particles bigger than 1.5 μm when compared to MCZ and YSZ compositions. In **Figure 5.27** this is represented by the horizontal relatively noticeable gap between the pair composed of the yellow and green function lines and the pair of the blue and red ones.

On top of that, a slimmer gap also exists between the blue and red lines, this is the MA2 and MA1 powders. From here, is possible to surmise that the milling time augmentation from 3 to 6 h for MA2 has homogenized to a certain degree the MA2 powder. In essence, smaller particle size gives rise to a higher surface area, which, in turn, boosts an increased number of points of contact among the particles of the mixture. Consequently, a lesser relative porosity is expected in this ceramic composite.

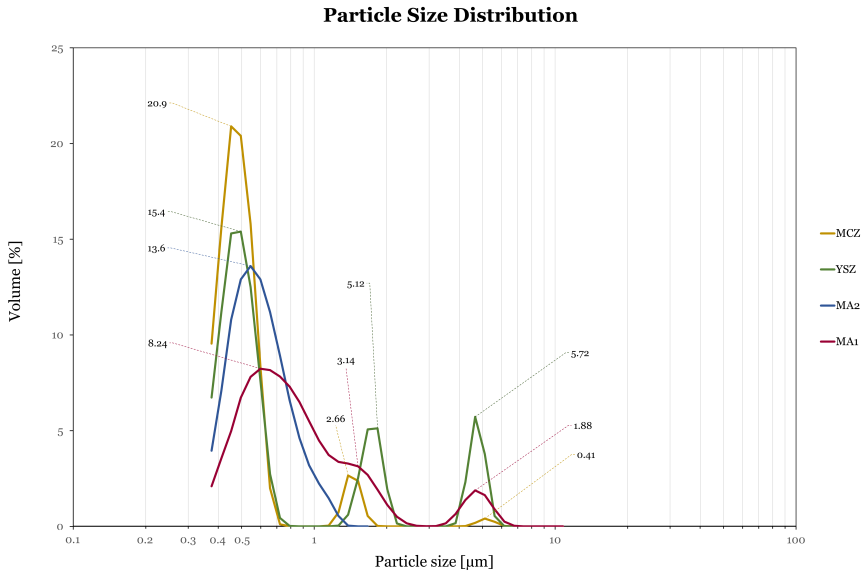

Figure 5.2: Volume-weighted PSD of the fabricated ceramic composites.

From the *volume-weighted PSD analysis* – in which the contribution of each particle relates to its volume – is possible to verify that MCZ, YSZ and MA1 powder have a multimodal behavior, whilst the MA2 has a monomodal one. This is evidenced by the number of relative maximums in the frequency distribution shown in **Figure 5.2**. This is to say, one peak is displayed for MA2 powder (blue line) and three relative maximums for the remaining compositions (yellow, green and red lines). Based on the more or less similar locations

of maximums, it is possible to state that the different particle sizes present in the mixtures coexist. By examining more closely the multimodal mixtures (MCZ, YSZ and MA1), the most frequently identified sizes are in the, approximately, [0.30, 0.60], [1.25, 1.80], and [4.0, 6.0] interval ranges. Additionally, by further inspecting **Figure 5.2**, the multimodal MA1 function line (red) compared to the monomodal MA2 (blue) strongly highlights the milling process efficiency improvement which agrees with the analysis made previously based on the number-weighted PSD.

Additionally, **Table 5.1** displays the d_{50} and d_{90} percentile values which correspond respectively to 50 % and 90 % of the volume of the four ceramic systems mixtures measured according to the Fraunhofer Diffraction Theory method. The d_{50} and d_{90} are statistical parameters which indicate the cumulative PSD and, therefore, the particle size below 50 % and 90 % of the entire spectrum of size particles found in the granulometer.

Table 5.1: MA1, MA2, MCZ, and YSZ mixture powders and their respective d_{50} and d_{90}.

Ceramic Composite	**Percentile**	
	d_{50} $[\mu m]$	d_{90} $[\mu m]$
MA1	1.150	2.217
MA2	0.655	1.805
MCZ	0.835	2.502
YSZ	0.931	1.642

On the whole, d_{50} percentile mostly evinces the drop from 1.150 μm of MA1 to 0.655 μm of MA2 which, in turn, indicates, as stated above, that by augmenting the milling timing of the alumina ceramic, smaller particle size was achieved. Similarly, d_{90} data supports this conclusion, once 90 % of the volume of the MA1 is constituted of particles with a size up to 2.217 μm, whereas for MA2 the maximum size recorded is of 1.805 μm. As a result, owing to the smaller size of the MA2 sample's particles, low porosity is foreseen, and in accordance, denser bulk ceramic.

For zirconia-based sintered ceramics d_{50} data shows relatively strong similarity among the particle size, i.e., 0.835 μm and 0.931 μm for MCZ and YSZ, respectively. However, with the d_{90} percentile data, it is possible to conclude that the tendency became different, i.e., the compositions depict heterogeneous behavior. Contrary to the verified in d_{50} column in which MCZ shows a similar, but lower characteristic particle size, in the d_{90} column MCZ and YSZ became very divergent. In other words, 90 % of the MCZ mixture analyzed a particle size up to 2.502 μm, whilst YSZ mixture goes up to 1.642 μm. From this information, one may suppose that the MCZ mixture will show some occasional bigger particles in the SEM imaging, whereas YSZ will exhibit matching – in size – particles.

In conclusion, it is highlighted that the PSD, which unequivocally and straightforwardly, consists of a quality assessment tool parameter, confers direct insights into the condition/status of the final ceramic composites to be produced once the level of homogeneity of the mixture influences the ceramic overall properties.

5.1.2 X–Ray Diffraction

The XRD patterns were obtained, as explained in section 4.3.3.1, with the aim of crystalline phases identification for the sintered ceramics composites MA2, MCZ and YSZ, as shown in **Figure 5.3**, **5.4** and **5.5**, respectively. The analysis of the XRD diffractograms started by the identification step of the 2θ angles in which main intensity peaks occurred, i.e., diffraction of crystalline planes corresponding to the different phases present in the samples. Then, a comparison to the crystallographic intensity peaks of the individual constituent materials for every sintered ceramic was performed based on the XRD theoretical cards.

It is highlighted that when two or more crystalline phases are identified for the same intensity peaks – on the following figures – it means that very close diffraction angles were obtained, and, therefore, doubling or tripling of crystalline phases is assumed. This phenomenon is represented with a "+" sign. Consequently, the following **Tables 5.2**, **5.3** and **5.4** of crystallographic intensity peaks of the ceramic samples and their constituents materials are presented to ease the diffractograms interpretation.

The following **Figure 5.3** and **Table 5.2** present the XRD analysis of MA2 ceramic composite.

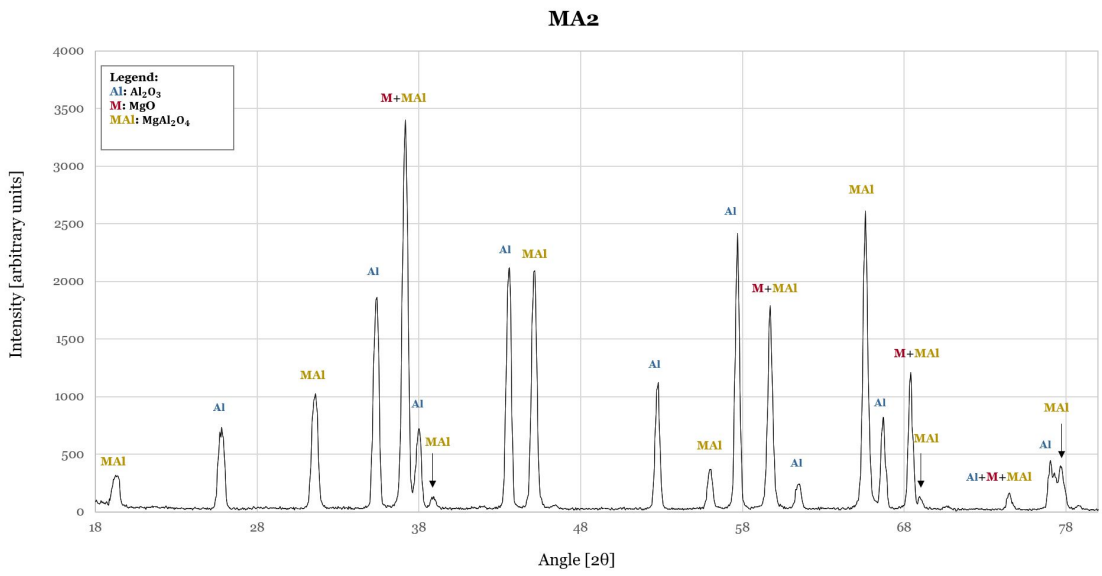

Figure 5.3: XRD pattern of MA2 ceramic composite.

For MA2, several intensity peaks were identified. Nevertheless, the majority of them corresponded mainly to alumina (Al_2O_3) – XRD card #46-1212 – or magnesium aluminum oxide ($MgAl_2O_4$) – XRD card #77-1193. In terms of stronger intensity peaks the same tendency is evidenced by **Figure 5.3**, i.e., alumina and magnesium aluminum oxide crystalline phases stand out. Only the highest peak corresponding to an angle of 2θ to, approximately, 37.15º deviate from the stated by presenting, besides the magnesium aluminum oxide, a magnesium oxide (MgO) – XRD card #71-1176 – phase. **Table 5.2** provides detailed additional information about peaks identification 2θ angles and the corresponding crystalline phases for MA2 bulk ceramic composite.

Table 5.2: Diffraction angles of the crystallographic intensity peaks and the XRD theoretical cards data for MA2 composite.

2θ	Al_2O_3	MgO	$MgAl_2O_4$	Crystalline Phase[12]
19.10	-	-	19.001	MAl
25.70	25.578	-	-	Al
31.55	-	-	31.273	MAl
35.35	35.152	-	-	Al
37.15	-	36.888	36.849	M + MAl
37.95	37.776	-	-	Al
38.75	-	-	38.551	MAl
43.55	43.355	-	-	Al
45.10	-	-	44.814	MAl
52.80	52.549	-	-	Al
56.00	-	-	55.66	MAl
57.70	57.496	-	-	Al
59.70	59.739	-	59.362	Al + MAl
61.50	61.298	-	-	Al
65.60	-	-	65.241	MAl
66.70	66.519	-	-	Al
68.40	68.212	-	68.635	Al + MAl
69.10	-	-	69.748	MAl
74.60	74.297	74.576	74.127	Al + M + MAl
77.00	77.224	-	-	Al
77.65	-	-	77.349	MAl

The following **Figure 5.4** and **Table 5.3** show the XRD analysis of MCZ ceramic composite.

[12]The nomenclature adopted in this column is coincident with the legend provided in **Figure 5.3**.

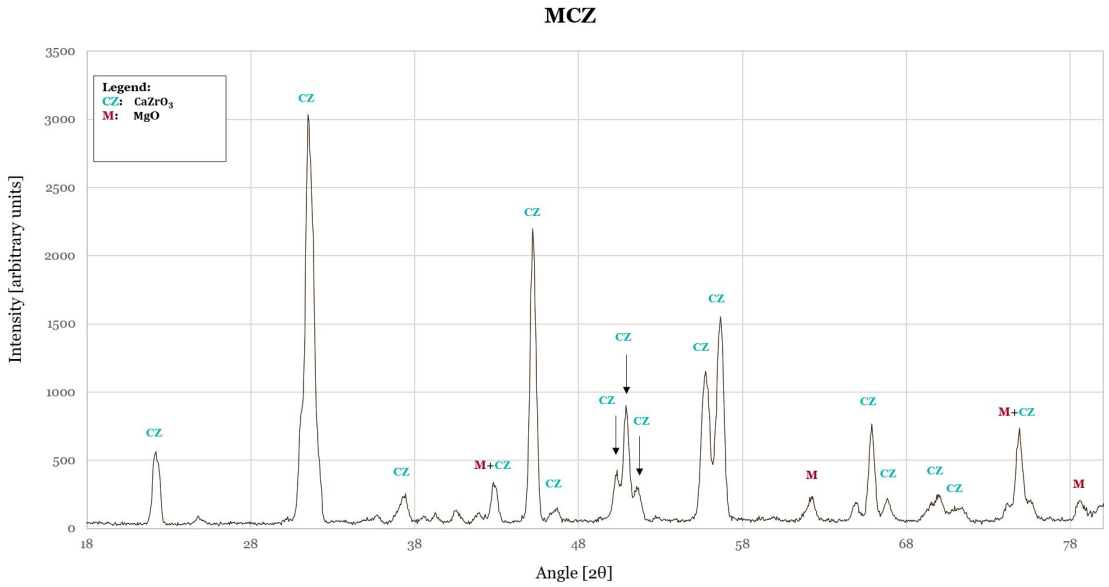

Figure 5.4: XRD pattern of MCZ ceramic composite.

In the MCZ sample, various intensity peaks were found. The majority of the diffraction peaks are coincident with the peaks of calcium zirconate ($CaZrO_3$) – XRD card #35-0790 – whereas only some are of magnesium oxide (MgO) – XRD card #71-1176. Concerning the diffraction intensity, alike behavior is depicted by **Figure 5.5**, i.e., calcium zirconate crystalline phase evidently emerge. In addition, in some specific 2θ angles, i.e., approximately for 42.85°, 62.15°, 74.90°, and 78.45° angles, magnesium oxide (MgO) – XRD card #71-1176 – phase is found. **Table 5.3** provides detailed additional information about peaks identification 2θ angles and their corresponding crystalline phases for MCZ bulk ceramic composite.

Table 5.3: Diffraction angles of the crystallographic intensity peaks and the XRD theoretical cards data for MCZ composite.

2θ	MgO	$CaZrO_3$	Crystalline Phase [13]
22.10	-	22.154	CZ
31.50	-	31.539	CZ
37.40	-	37.436	CZ
42.85	42.855	42.413	M + CZ
45.20	-	45.183	CZ
46.75	-	46.639	CZ
50.25	-	50.227	CZ
50.90	-	50.89	CZ
51.45	-	51.496	CZ
55.75	-	55.857	CZ
56.65	-	56.729	CZ
62.15	62.215	61.763	M
65.90	-	65.847	CZ
66.95	-	66.838	CZ
69.90	-	69.873	CZ
70.80	-	70.933	CZ
74.90	74.576	74.814	M + CZ
78.45	78.508	-	M

The following **Figure 5.5** and **Table 5.4** are regarding the XRD analysis of YSZ ceramic composite.

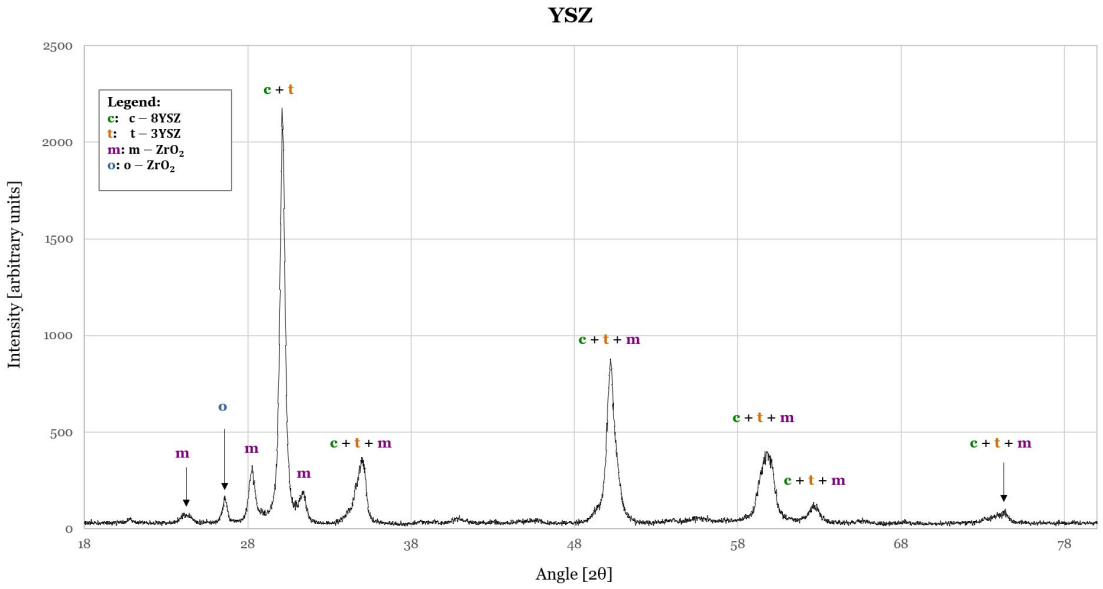

Figure 5.5: XRD pattern of YSZ ceramic composite.

The XRD analysis for YSZ specimen reveals that all three possible phases, i.e., c-8YSZ (XRD card #49-1642), t-3YSZ (XRD card #50-1089), and m-ZrO_2 (XRD card #37-1484)

[13]The nomenclature adopted in this column is coincident with the legend provided in **Figure 5.4**.

are present in the ceramic composite. The occurrence of doubling and tripling of crystalline phases, specifically in this ceramic composite, adds complexity to the sharp and precise identification of the intensity peaks. In other words, is not possible to establish, with the desired optimum accuracy, a unique correlation between a specific value of diffraction angle and a single exact phase, as shown in **Figure 5.5**. Notwithstanding, the monoclinic phase is distinctly identified for 24.54°, 28.28° and 31.34°; in the middle, the higher intensity diffraction peak for 30.1° shows a close diffraction angle for the c-8YSZ and t-3YSZ phases; and the remaining majority of peaks in the angle range from 33° to 80°, exhibit the tripling particularly of the crystalline phases justified by the very close diffraction angles. Once again, **Table 5.4** provides detailed additional information about peaks identification 2θ angles and their corresponding crystalline phases for YSZ bulk ceramic composite. Lastly, it must be highlighted that in the **Figure 5.5**, the second identified peak at, approximately, 26.58°, does not correspond to any previously mentioned crystalline phases, i.e., c-8YSZ (XRD card #49-1642), t-3YSZ (XRD card #50-1089), and m-ZrO_2 (XRD card #37-1484). As a result, further investigation for the comprehension of the phenomenon occurred took place. It was concluded that an additional phase named orthorhombic zirconia o–ZrO_2 (XRD card #49-1746) must have emerged due to the significantly high density of the material (owing to the low apparent porosity achieved). More specifically, the absence of significant open pores or voids, has not allowed the complete transformation – due to the lack of volume (space) – of the monoclinic phase to the tetragonal, or cubic, and, as a result, an intermediate orthorhombic zirconia phase appeared. The theoretical XRD card #49-1746, points out a peak of 2θ at 27.489°.

Table 5.4: Diffraction angles of the crystallographic intensity peaks and the XRD theoretical cards data for YSZ composite.

2θ	c-8YSZ	t-3YSZ	m-ZrO_2	Crystalline Phase [14]
22.54	-	-	24.440	m
28.28	-	-	28.174	m
30.10	30.119	30.270	-	c + t
31.34	-	-	31.467	m
35.00	34.959	34.811	35.308	c + t + m
50.20	50.219	50.377	50.115	c + t + m
59.90	59.738	59.61	59.773	c + t + m
62.70	62.678	62.967	62.836	c + t + m
74.22	73.938	74.538	74.680	c + t + m

It should be emphasized, as last consideration of XRD analysis, that short (in height) peaks may be visualized in the diffractograms – **Figure 5.3**, **5.4** and **5.5** – of the data collected, particularly in the initial (up to, approximately, 20°) and last few (about 80°) angles. The reason behind may be justified by the inherent noise in the measuring process

[14]The nomenclature adopted in this column is coincident with the legend provided in **Figure 5.5**.

registered, in addition to the adjustment and/or calibration of the diffractometer equipment.

Overall, the XRD results provide support to the information described in the section 4.1 entitled Materials where the ceramics composited to be manufactured were characterized in terms of volume and mass fractions.

5.1.3 Microstructure

Bearing in mind that the structure of the surface of the ceramic composites controls the interaction of the material with its surroundings, performing SEM analysis becomes consequently of utmost importance. Representative SEM micrographs, obtained via BSE mode, of the cross-section of four sintered ceramic composites – MA1, MA2, MCZ, and YSZ – with the grain size distributions are presented in the following **Figures 5.6**, **5.7**, and **5.8**. In greater detail, **Figure 5.6** shows the *alumina-based* compositions, i.e., MA1 and MA2, whilst **Figures 5.7** and **5.8** represent, in turn, the *zirconia-based* ones, i.e., MCZ and YSZ. The SEM surface micrographs a) and c) were achieved with a magnification of 5000X, the micrographs b), d), and g) with a magnification of 10000X, whilst e) and f) micrographs with 15000X.

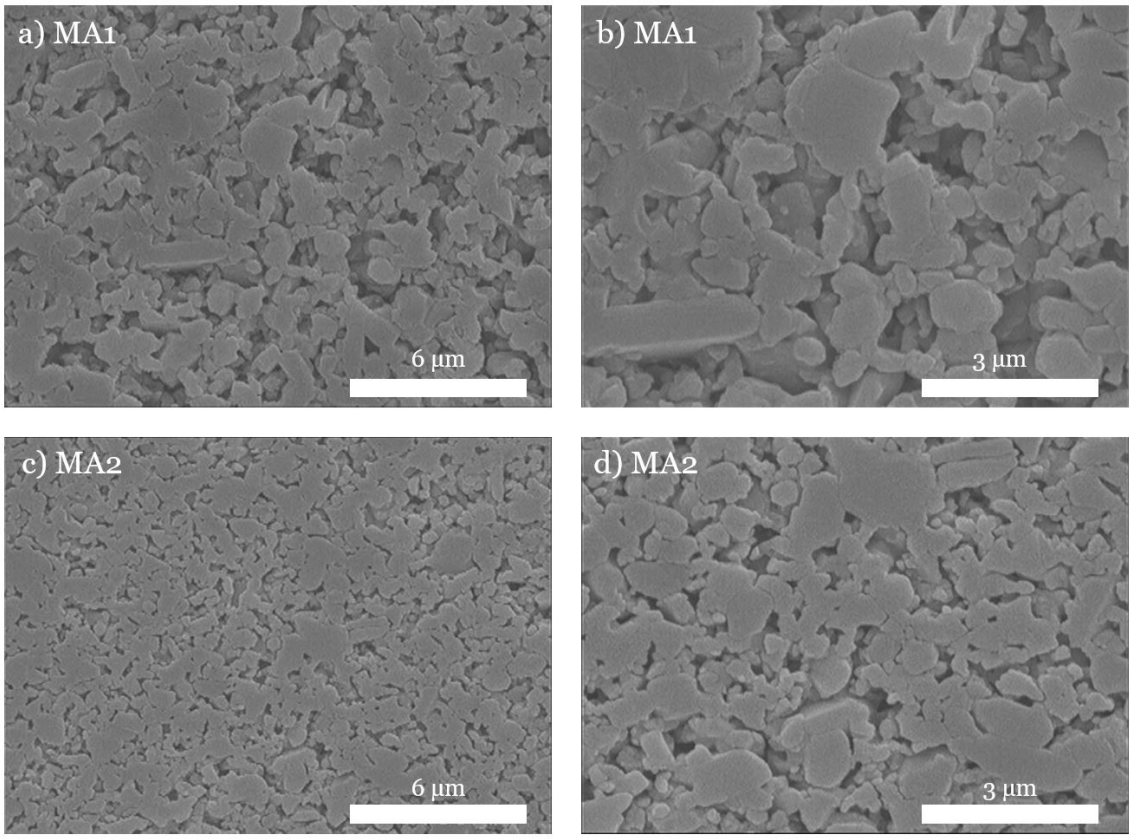

Figure 5.6: Scanning electron micrographs of polished and thermally etched surfaces at high magnifications: a), b) MA1, and c), d) MA2. Magnification factors of 5000X for a) and c); and 10000X for b) and d) micrographs.

Figure 5.7 emphasizes the difference between the two alumina ceramics produced – one with a higher content of porosity (to be evaluated in the following section), lesser points of contact among grains, and as pointed out, during PSD analysis, higher microstructure heterogeneity – a) and b) for MA1 versus c) and d) for MA2. In other words, what emerges distinctly, is a greater compaction degree (densification of the material) in micrograph c) of MA2 in comparison with the micrograph a) of MA1. Additionally, it is possible to highlight that altogether both alumina micrographs show a multiformity of grains, this is, in size and geometry: some are more elongated and longer (chord length < 2 μm), whereas others are circular and much minor (chord length < 1 μm), in addition to the uneven ones (variable chord length). Generally, MA1 and MA2 microstructures show a chord length lower than 3 μm. Additionally, in both ceramic composites MA1 and MA2 microstructures, an irregular shape of the grains and high porosity may be observed, which is illustrative of an incomplete sintering [157, 227]. Thus, although the decrease in the particle size of the MA2 mixture contributed to increase (to some extent) the atomic diffusion and, consequently, the porosity, in comparison with the MA1, the sintering time should have been increased for the composite MA2. By doing so, a high diffusivity would be obtained, and a clearer (better-defined) crystal structure achieved.

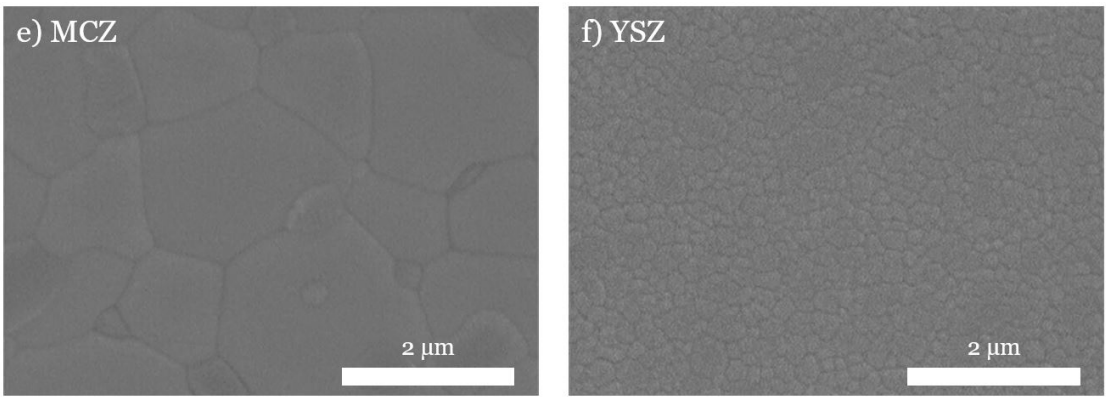

Figure 5.7: Scanning electron micrographs of polished and thermally etched surfaces at high magnifications: e) MCZ, and f) YSZ. Magnification factors of 15000X for e) and f) micrographs.

Figure 5.7 depicts the micrographs for the zirconia-based ceramic composites, i.e., micrograph e) shows MCZ microstructure, whereas micrograph f), YSZ. By comparing the two, it is evident that the milling process of YSZ fomented a notably homogeneous grain size distribution (chord length <1 μm), which contributed to higher densification of the ceramic (no evidence of empty pores exist). Extremely low porosity values are therefore expected. Contrastingly, MCZ microstructure features differences in crystalline phases of the materials which compose the ceramic, i.e., grains of dissimilar size and morphology can be visualized and promoted by: the larger and brighter grains (chord length < 1 μm) corresponding to the calcium zirconate, whereas smaller, darker, and textured (rugged) ones (chord length > 1 μm) to the magnesium oxide. This is evidenced to some degree better through color contrasting in micrograph g), **Figure 5.8**. Despite the described and

stated above, this is, the polycrystalline nature of MCZ demonstrable by the perceptible distinct grain size and contour (the boundary between two adjacent grains), similarly to YSZ, extremely low porosity values are anticipated for MCZ since inexistence of intergranular and intragranular microfractures is displayed.

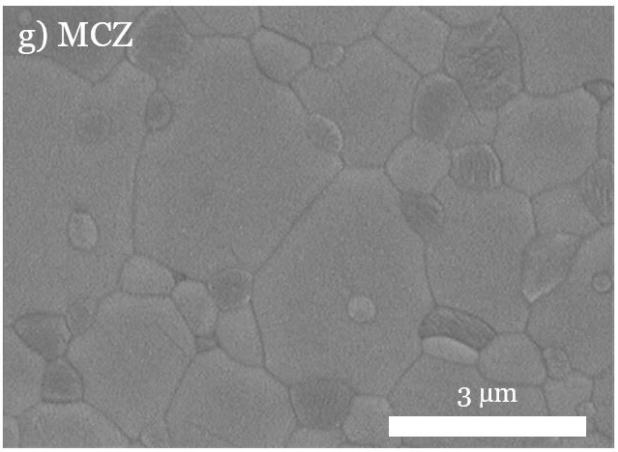

Figure 5.8: Scanning electron micrograph of polished and thermally etched surfaces at high magnifications: g) MCZ. Magnification factor of 10000X.

On the whole, and as the last conclusion, zirconia-based ceramic microstructures do not provide evidence of microstructural flaws, or defects, as microcracks due to their high level of densification, which cannot be assured for the alumina-based ceramics. The revealed presence of pores in alumina micrographs points out that incomplete densification during the sintering process was carried out. Moreover, the presence of pores will interfere with the functional and structural properties of the advanced ceramic. Therefore, the relationship should be derived between the microstructural data obtained – which will be determining the overall performance of the fine bulk ceramic manufactured – and further analyzed mechanical, thermal, and electrical properties.

5.2 Physical Properties

In this section the physical properties of the sintered bulk ceramics will be discussed, including the diametrical linear contraction, the apparent porosity, as well as the bulk, apparent and relative densities. A bridge between the microstructure analysis results and the physical parameters will also be performed.

5.2.1 Diametrical Linear Contraction

After processing (die pressing) of ceramic powders, sintering step took place where the resultant densification – achieved through porosity reduction – is the primarily responsible (in the advanced ceramics manufacturing) parameter for the achievement of the final dimensions and properties of the ceramic composites. The densification leads to volume diminishing, i.e., shrinkage which is a commonly recognized phenomenon that takes place during sintering. As a result, **Table 5.5** summarizes the studied diametric linear contraction of the specimens analyzed of each of the three ceramic composites sintered – MA2, MCZ, and YSZ. The calculation was performed as explained in 4.2.3 with the aim to asset and characterize the sintering step in the manufacturing of the fine ceramics.

Table 5.5: Diametrical linear contraction mean values and associated error of sintered ceramic composites.

Ceramic Composite	C_d [%]
MA2	13.0 ± 0.2
MCZ	24.0 ± 0.1
YSZ	27.4 ± 0.3

From **Table 5.5** it is valid to state that, during the sintering phase of the ceramic composites, a relatively accentuate shrinkage phenomenon occurred ranging from, approximately, 13.0 to 28 %, where MA2 suffered the lowest value of 13.0 %, and MCZ in addition to YSZ the highest percentages, i.e., 24.0 and 27.4 %, respectively.

According to the literature, and it must be highlighted, ceramic shrinkage may depend on several different factors such as the *composition of powder used*, their (powders) *density*, t*he processing method involved*, more specifically in case of die pressing the *compaction pressure applied*, in addition to *sintering method adopted* (for instance, one or several firings), *sintering temperature*, *dwell time*, as well as *heating and cooling rates* [170, 227, 228, 229, 230, 231].

Somton K. et al. (2020) [227] studied the shrinkage and properties of die pressed alumina produced from different powders source. The shrinkage values have been reported to in-

crease with the increasing of the sintering temperature up to 1600 ºC. In their study, bar samples showed a sintered shrinkage range of 14.4 % to 18.0 % at a compaction pressure of 133 MPa.

Ropuš I. et al. (2021) [228] compared the properties of cold isostatically high-purity of 99.83 wt. % alumina samples sintered by electrical (at 1600 ºC for 6 h) and hybrid microwave (1600 ºC for 1 h) techniques. It was verified that all cylindrical pellets shrunk both radially and axially of about 16 – 17 %.

Similarly, Shui A. at al. (2002) [229] verified that, in height and diameter directions, alumina-based ceramic pointed out values for linear contraction in between 15 to 20 %. Since the 13.0 % for the MA2 is slightly out of the range of the values found in the literature, this may indicate that the sintering step conducted at 1600 ºC was not totally completed. Therefore, to some extent, porosity is expected to be found in these samples. To overcome this undesirable drawback and considering the furnace at disposal, an increase of dwell interval of time at the maximum sintering temperature is suggested for future works.

Szczerba K. et al. (2011) [230] studied the synthesis of spinel and calcium zirconate by sintering natural dolomite, zirconia and alumina. Sintering was carried out in two ways. The first one, the *one-step process* in which the ceramic mixtures were exposed to several maxima temperatures and a dwell time of 120 min. The second one, *the two-step process* in which the powders were first heated to 1200 ºC, maintained at this temperature for 60 min, then pressed (for a second time) under 120 MPa and sintered again at a maxima of 1400, 1500 and 1600 ºC for 120 ºC. It was reported that spinel-calcium zirconate showed a significant densification and, consequently, shrinkage after firing from 1400 ºC and above. In the two-step process, the materials showed shrinkage about 20 % and 22 % at 1500 ºC and 1600 ºC, respectively.

Thus, it is concluded that, for the MCZ ceramic composite, sintered at a temperature of 1450 ºC, a diametrical linear contraction of 24 % is quite achievable once high-purity MgO (96 %) and $CaZrO_3$ (99 %) powders were used as starting materials. This value indicates that very high densification was accomplished and that, as a result, the material with low-porosity could be obtained.

Lastly, YSZ diametrical linear contraction was of 27.4 %. From the literature, this value was to some degree higher than the expected. Hu L. and Wang C. (2010) [231] studied the effect of different sintering temperatures in the yttria-stabilized zirconia compressive strength as a potential heat-insulation material. The evaluation was performed based on few parameters, including linear shrinkage after bulk ceramic fabrication applying gel-casting technique. All in all, the variation of linear shrinkage of YSZ samples increased from 15.4 to 31.8 % as the temperature increased from 1350 to 1550 ºC. The authors high-

lighted that between 1400 ºC and 1450 ºC the shrinkage rate was most prominent. Additionally, for 1450 ºC – which coincides with the sintering rate adopted in the sintering of YSZ specimens (section 4.2.3) – the linear contraction registered was of, approximately, 24 %.

Furthermore, Balça F. (2022) [170], reported values of C_d between 19 and 25 % for different yttria-stabilized zirconia composition studied. The composition which is theoretically equal to the manufactured YSZ ceramic composite (in this dissertation work) – 33.3 wt. % t-3YSZ, 33.3 wt. % c-8YSZ and 33.3 wt. % m-ZrO2 – showed a linear contraction of 24.4 %.

It is believed that the reasoning behind the values obtained in the experimental analysis may be justified as follows. In comparison to Hu L. and Wang C. (2010) [231] the fabrication procedure adopted for the ceramic specimens was different. Authors used gel-casting technique whereas, in this dissertation, uniaxial die pressing (as described in 4.2.2) was applied. According to Otitoju T. (2020) [5] gel casting does not lead to shrinkage of the powder compacted in a mold or removes any component. It rather solidified the medium through polymerization or trapping voids or molecules in the system.

Besides, although Balça F. (2022) [170] studied *a priori* an equal YSZ composition, when comparing the grain dimensions of the ceramic composite powders – in terms of d_{90} percentile values – a difference is noted. More specifically, Balça F. (2022) reported a d_{90} of 2.36 μm which is, approximately, 30 % higher in comparison to the 1.64 μm verified for the YSZ specimens manufactured (section 5.1.1). In other words, 90 % of the YSZ mixture fabricated showed a significant lesser grain size to the indicated in the literature which most likely enabled a higher shrinkage percentage due to higher densification of the material.

Moreover, considering that all the samples of MA2, MCZ and YSZ were fabricated having the same amount (mass) of initial powder – i.e., 4.0 g (section 4.2.2) – it is interesting enough to note that the final height of the cylindrical specimens were of, approximately, 3.23 (± 0.07), 2.44 (± 0.01), and 2.03 (± 0.04), respectively. These values are reasonable and in conformity to the expected based on the compaction percentage announced in **Table 5.5**.

5.2.2 Apparent Porosity, Bulk Density, Apparent Density and Relative Density

As explained in section of Physical Properties, i.e., 4.3.1, the study and examination of the apparent porosity and the different densities is of vital importance, since these parameters are closely related to the overall performance of the manufactured advanced ceramic composites. Thus, it is highlighted once more that the apparent porosity and the density of the bulk sintered ceramics are their primary properties. The following **Table 5.6** summarizes the primary properties enunciated above of the four sintered fine ceramics MA1, MA2, MCZ, and YSZ, this is, apparent porosity P (%), theoretical densities (for comparison purposes) (g/cm^3), bulk densities (g/cm^3), apparent densities (g/cm^3) and relative densities (%).

Table 5.6: Primary properties of ceramic composites manufactured: apparent porosity P, in addition to theoretical ρ_{th}, bulk ρ_b, apparent ρ_a, and relative ρ_r densities.

Ceramic Composite	P [%]	ρ_{th} [g/cm^3]	ρ_b [g/cm^3]	ρ_a [g/cm^3]	ρ_r [%]
MA1	34.62 ± 4.63	3.92	2.46 ± 0.05	3.77 ± 0.20	62.73 ± 1.15
MA2	7.03 ± 0.93	3.92	2.79 ± 0.04	2.66 ± 0.25	71.14 ± 1.03
MCZ	0.05 ± 0.05	4.49	4.48 ± 0.03	4.51 ± 0.03	99.95 ± 0.59
YSZ	0.16 ± 0.19	6.00	5.88 ± 0.02	5.89 ± 0.03	97.95 ± 0.35

Broadly speaking, and although different ceramic composites – MA, MCZ and YSZ – were fabricated (which precludes the possibility of direct comparison among them) a tendency exists. More specifically, alumina-based bulk ceramics show an undesired high porosity: approximately, 34.62 % for MA1 and 7.03 % for MA. Contrastingly, zirconia-based ceramics, exhibit minimum – less than 0.5 % – values of porosity. In greater detail, MA1 porosity data besides of a very high percentage exhibits also the higher dispersion in experimentally measured results, i.e., 4.63 %.

In summary, the column dedicated to apparent porosity reinforces and underpins the conclusions taken through **Figure 5.6** and **5.7**. MA1 reports very high apparent porosity values when compared to MA2 specimens. This is justified by the longer milling process to which the mixture was exposed. Oppositely, MCZ and YSZ samples have a very low porosity percentage which indicates that a strong compaction was achieved, i.e., no empty considerable voids were found.

Figure 5.10 depicts the apparent porosity of each ceramic composite manufactured as well as the associated error of the experimental measurements taken. It is noted that when no vertical bar is associated to each marker of each specimen type this means that the dispersion of data is very low, and, therefore, housed by the marker.

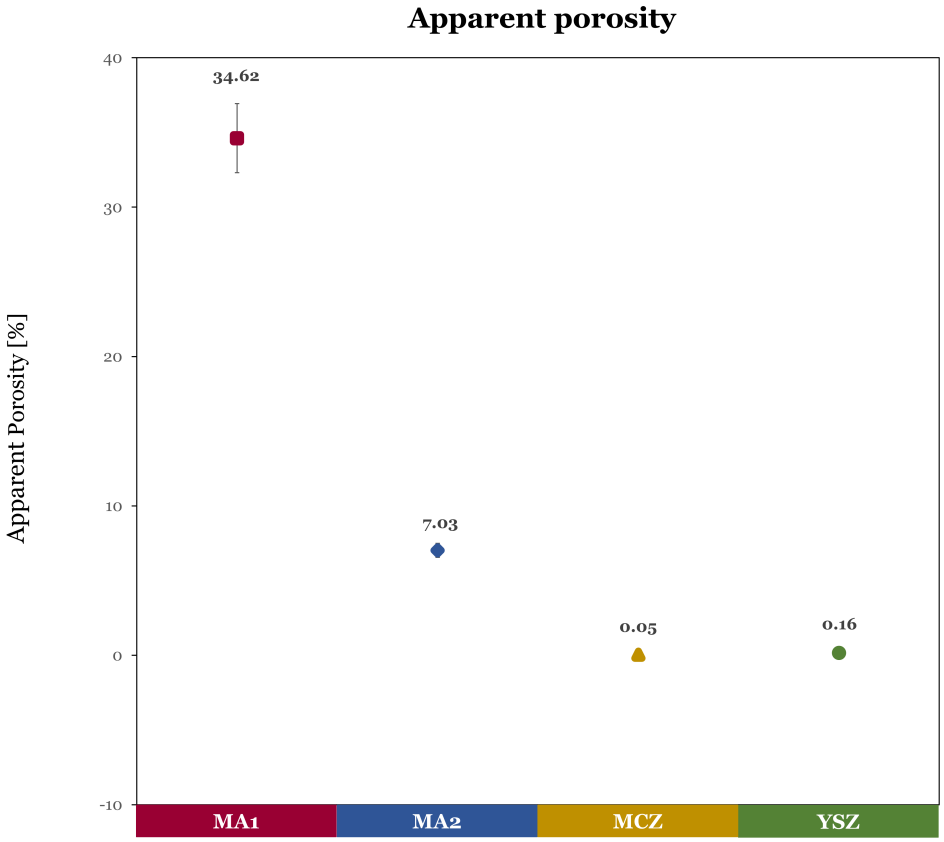

Figure 5.9: Apparent porosity, P, of the manufactured ceramic composites and the associated error of measurements.

Regarding the density data, very different behaviors were verified. For MA2, the compaction process was lower than expected due to the existing apparent porosity of approximately 7.0 %. Consequently, both bulk 2.79 g/cm^3 and apparent 2.66 g/cm^3 densities are considerably lower than the theoretical value 3.92 g/cm^3 used as reference. For MCZ and by deeming the theoretical density value of 4.49 g/cm^3, the bulk density of 4.48 g/cm^3 is very close to the reference, whereas the apparent density figure 4.52 g/cm^3 is believed to be slightly atypical since it is higher than the theoretical one. Lastly, YSZ showed a good compaction, and therefore densification during sintering phase, once both bulk and apparent densities are quite similar, i.e., 5.88 g/cm^3 and 5.89 g/cm^3 and, in turn, alike to the theoretical density of 6.00 g/cm^3. In addition, the error associated to the measurements taken is considered to be very low, i.e., below 5 %.

Figure 5.10 illustrates the relative density of each ceramic composite manufactured as well as the computed error through standard deviation parameter. Identically to apparent porosity graph, when no vertical bar is associated to each marker of each specimen type this means that the dispersion of data is very low and, therefore, is contained inside the marker.

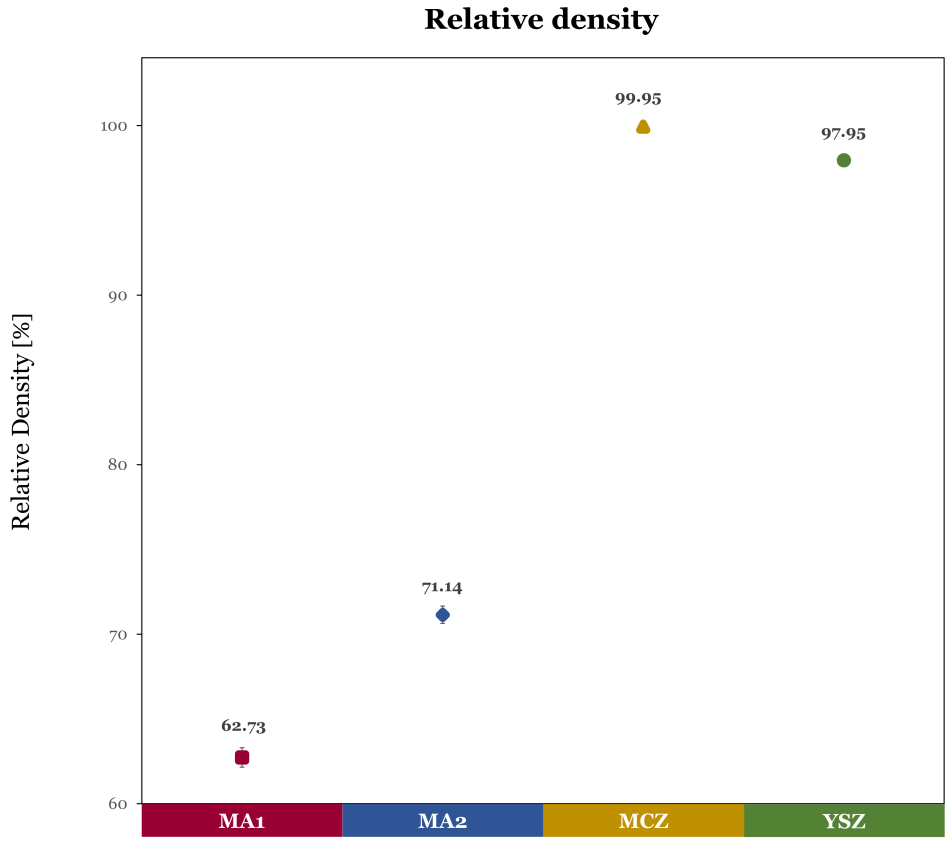

Figure 5.10: Relative density, ρ_r, of the manufactured ceramic composites and the associated error of measurements.

Many specific properties depend critically on the manufacturing conditions, including grain size (assessed through PSD analysis), purity of the material (evaluated based on the XRD analysis), in addition to apparent porosity and relative density (experimentally measured). In further detail, the fabrication process and parameters involved in each stage – material preparation, processing, sintering and finishing – influences and dictates the ceramic composites physical characteristics, which in turn rule their performance in terms of mechanical, thermal and electrical properties. On the whole, it should be remarked that to achieve better mechanical and thermal properties as well as higher corrosion resistance of fine ceramics, the maximum particle density must be combined with a minimum total porosity and, particularly, absence of large pores should be sought.

Bearing in mind the application purposes exploited in Chapter 3, in case of passive TPSs and TBCs applications, in which, the insulative material and coatings are intended to slow down the heat transfer process, high-level porosity may be extremely harmful since the materials become more prone to both mechanical and thermal related in-service failure. In other words, the existing open pores and voids lessen the mechanical strength, corrosion and scratch resistance, as well as temperature strength and thermal shock resistance of bulk ceramics. From the mechanical point of view, shielding is impaired for both TPS

and TBC applications. From the thermal one and still considering TPS and TBS applications, higher than expected thermal conductivity is obtained due to accentuated thermal gradients; whereas thermal expansion mismatch is induced thanks to mismatches in CTE between the metallic bond coat and ceramic top coat for (particularly-) TBCs applications. Therefore, on the whole, increased apparent porosity in the ceramic composites gives rise to decreased lifespan of parts owing to increased fatigue and stress.

On the other hand, as observed by Kelar J. et al. (2020) [156], the type of dielectric barrier material in addition to its surface morphology are closely related to the plasma discharge parameters. Moreover, it is recognized by the scientific community that the behavior of any surface electric discharge is affected by the trapping and de-trapping complex phenomenon of the charges in the surface layer [232]. Thus, it is expected that the apparent porosity, relative density as well as particle size parameters will be influencing features for the DBD plasma actuators overall performance.

Therefore, further study and evaluation of the influence of porosity in the ceramic composite performance as dielectric barriers, in addition to a trade-off establishment of the effects of porosity in different applications, studied in detail is expected in the following sections.

Lastly, since distinct ceramic composites were manufactured, as previously stated, this consideration makes impossible of performing their direct comparison. Notwithstanding, they may be exploited in the fabrication process characterization and serve as a forecast tool of the overall performance of an engineering structure, or component, that the ceramic composites studied may integrate.

5.3 Mechanical Properties

In this subsection, the mechanical characterization of the manufactured advanced ceramics composites, i.e., MA1, MA2, MCZ, and YSZ is presented. The mechanical tests conducted were, as enunciated throughout the Experimental Procedure chapter, dynamic Young's and dynamic shear moduli, flexural strength, hardness, and fracture toughness. In both functional as well as structural ceramics, the mechanical properties of these fine materials are of fundamental importance, as first and foremost, among other features, engineering ceramics are highlighted by their high hardness, high wear, and corrosion resistance. However, a significant predisposition to brittle fracture and low endurance limits – when compared to metals and engineering plastics, as shown in **Table 2.1** – strongly conditions their applications. Accordingly, to properly tailor and target the ceramic's properties to predefined engineering structures, or components, mechanical characterization shall primarily be assessed and carefully conducted.

5.3.1 Dynamic Young's Modulus and Dynamic Shear Modulus

Figure 5.11 shows Young's modulus measured by impulse excitation technique at room temperature of the four different manufactured ceramic systems. Broadly speaking, Young's modulus describes the strain response ability of a specific material to withstand uniaxial stress or bending stress. Young's modulus involves both, volume and shape changes of the material. By analyzing the plot, it is possible to easily infer that Young's modulus of 317 GPa of the denser alumina strongly surpasses in magnitude the rest of the materials, i.e., 213 GPa and 197 GPa of MCZ and YSZ ceramic composites, respectively. It is noted that when no vertical bar is visibly associated with each marker of each specimen type this means that the dispersion of data is very low, and, therefore, the vertical black bar housed by the marker.

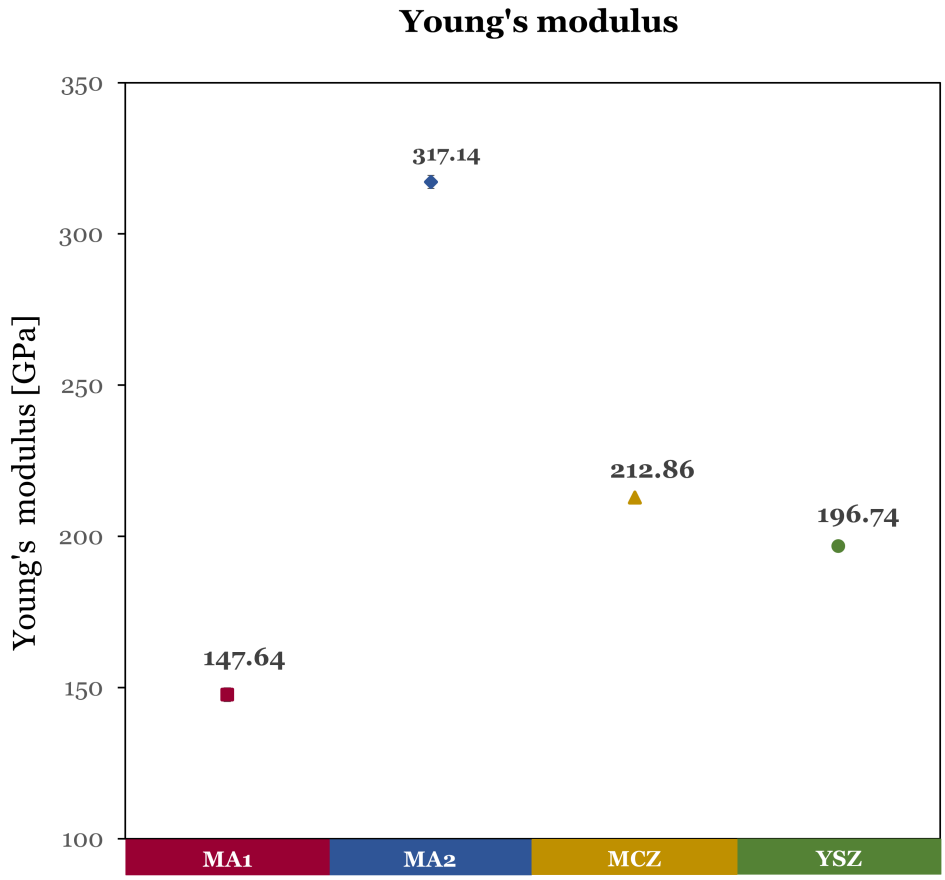

Figure 5.11: Young's, E, modulus experimentally obtained for MA1, MA2, MCZ, and YSZ ceramic composites.

Figure 5.12 represents the shear modulus of the MA1, MA2, MCZ, and YSZ ceramics namely measured by impulse excitation technique at room temperature. Shear modulus, on the other hand, describes the strain response of a body to shear stress or torsional stress in which a change of shape may occur but not in volume. Through examination of the graph below, once again, the alumina MA2 ceramic composite shows a higher value in magnitude, this time, however, for the shear modulus, of 130 GPa than the rest of the zirconia-based materials, i.e., 84 GPa and 69 GPa for MCZ and YSZ, respectively. Identically to Young's modulus graph, when no vertical bar is associated with each marker of each specimen type this means that the dispersion of data is very low and, therefore, the vertical black bar is contained inside the marker.

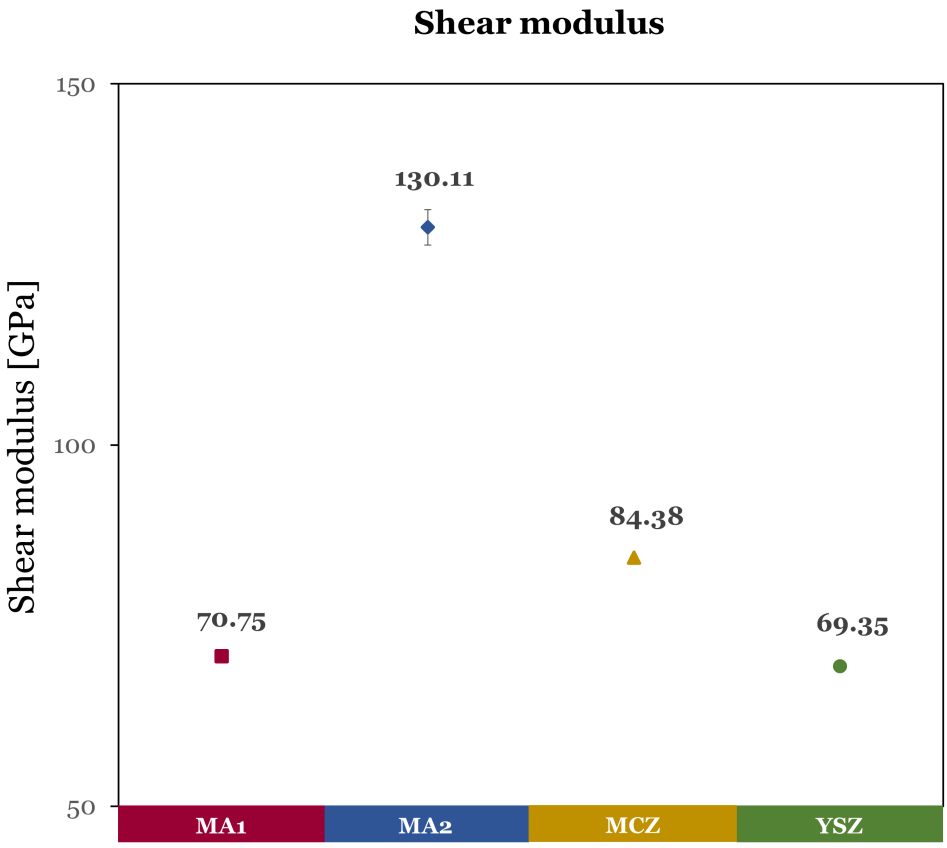

Figure 5.12: Shear modulus, G, experimentally obtained for MA1, MA2, MCZ, and YSZ ceramic composites.

It must be strongly emphasized that, in the literature, it is well established and long studied – both experimentally and analytically – the *porosity dependence of materials properties*. Particularly, porosity in brittle materials, i.e., ceramics, can have significant drawbacks on their physical properties, which in turn influence their mechanical, thermal, and electrical features [233, 234]. Consequently, numerous relationships may be encountered proposed by several researchers that allow computing the variation of the elastic properties – i.e., Young's and shear moduli, bulk modulus, and Poisson's ratio – of the ceramic materials in terms of *porosity content or volume fraction of pores* [235]. Moreover, in materials with constituents of different natures, additional complexity is added to the so-called modulus-porosity relationship since divergent responses from the characteristic single ceramic composite's phases may be found. Shortly, it may be stated that the *porosity dependence of material properties* is a large and complex field that has a great impact on elastic properties. Hence, it plays a key role in dictating the mechanical response of ceramic materials [236].

More specifically for the materials used, in the analytical models, the values of the elastic and rigidity moduli of single phases of ceramic materials, i.e., magnesium oxide, alumina, calcium zirconate, and magnesium aluminate, in addition to the polycrystalline yttria-stabilized zirconia were considered as the starting point. Further, the Voigt model was applied, as specified by **Equation 4.14**, to analytically estimate the theoretical modulus of the ceramic composite materials. Lastly, relative porosity was namely considered to contextualize possible deviations in experimental and theoretical data. **Table 5.7** summarizes the single-phase ceramic theoretical values considered for zero-porosity, whereas **Table 5.8** represents the elastic E_{exp} and shear G_{exp} moduli experimentally obtained, theoretically computed without considering porosity content and considering porosity for each respective manufactured ceramic system, i.e., MA1 (35 %), MA2 (7 %), MCZ (0 %), and YSZ (0.2 %). The computation of the influence (i.e., impact) on the elastic and rigidity moduli on the composite ceramics was computed adopting the formulation proposed by Rice W. R. et al. (1996) [234] through**Equation 5.1** and **5.2**, respectively, as follows:

$$E = E_0 \times e^{-cP} \quad (5.1)$$

$$G = G_0 \times e^{-cP} \quad (5.2)$$

where E is the modulus of elasticity, GPa, E_0 is the modulus of elasticity for zero porosity, GPa, P is the apparent porosity, and c is a constant related to the elastic behavior of the material. Adopting the alike notation for the shear modulus, comes that G is the modulus of rigidity, GPa, G_0 is the modulus of rigidity for zero porosity, GPa, P is the apparent porosity, and c is again a constant related to the elastic behavior of the material. It is noted that the YSZ Voigt computation was not performed for the determination of theoretical values, rather directly data from the literature was adopted for fully dense ceramics (i.e., with zero-porosity content ceramics).

Table 5.7: Single–phased ceramic elastic and rigidity theoretical moduli.

Single Phase Ceramics	**Young's modulus,** E **[GPa]**	**Shear modulus,** G **[GPa]**
Magnesium Oxide	280 [193]	130 [237]
Magnesium Aluminate	187 [238, 239]	109 [238, 239]
Alumina	405 [237, 240, 241]	163 [237]
Calcium Zirconate	228 [193]	87.9 [242]
Yttria-Stabilized Zirconia	210 – 220 [241, 243, 194]	76.5 [244]

Table 5.8: Ceramic composites elastic and rigidity moduli experimentally obtained; and theoretically computed exploiting Voigt model for MA1, MA2, and MCZ, whereas directly retrieved from literature sources for YSZ[†].

Ceramic Composite	E_{exp} **[GPa]**	E_{Voigt} **[GPa]** (without porosity)	E_{Voigt} **[GPa]** (with porosity)	G_{exp} **[GPa]**	G_{Voigt} **[GPa]** (without porosity)	G_{Voigt} **[GPa]** (with porosity)
MA1	148 ± 2.3	384	161.9	71 ± 0.01	154	63.8
MA2	317 ± 2.2	384	311.3	130 ± 2.5	154	127.3
MCZ	213 ± 0.2	235	–	84 ± 0.2	93	–
YSZ	199 ± 0.2	210 – 220[†]	208.7 – 218.7	69 ± 0.1	76.5[†]	72.1

Considering Young's modulus of alumina-based – MA – materials, i.e., MA1 and MA2, strong discrepancies are verified between the experimental (148 GPa and 317 GPa, respectively) and theoretical (384 GPa) values. The reasoning behind this consists of the high and relatively high porosity obtained in the bulk MA1 and MA2 sintered ceramics of approximately 35 % and 7 %, respectively [245]. If considering existing models to estimate the influence of the porosity, it is concluded that the values experimentally obtained are somehow reasonable. Similarly, the same dissimilarities were found for the shear modulus, and it is namely believed that the approximately 15.5 % lower experimental value obtained for the MA2 ceramic composite is due to the relatively high porosity contained in the ceramics. Auerkari P. (1996) [246] reported that the usual ranges of elastic properties at room temperature for engineering alumina ceramic of 99 % purity with 1 – 5 % porosity level are of 340 – 380 GPa for elastic modulus and 130 – 145 GPa for rigidity modulus. In turn, Asmani M. et al. (2001) [247] focused on the study of the influence of the porosity level on Young's modulus and Poisson's ratio properties of a sintered alumina using a non-destructive technique, this is ultrasonic waves. For this aim, a correlation was made by the authors between the transverse and longitudinal ultrasonic wave velocities data with measured density and porosity. From the obtained results it was concluded that Young's modulus of almost 400 GPa – with less than 0.05 pore volume fraction – drastically dropped to nearly 150 GPa with a total pore volume fraction of, approximately, 0.25. Moreover, for a ore volume fraction of 0.1, Young's modulus corresponded to, approximately, 300 GPa [247]. Based on the described data from the enunciated sources, it is, therefore, possible to infer that the values obtained are quite achievable since the characteristic relative porosity, as referred to, of MA2 is higher than 5 %. Moreover, not only the amount, but the character (i.e., pore characteristic, for instance, closed or opened, spherical or cylindrical) of the porosity content heavily influences the mechanical response and properties of ceramic materials under study.

Considering the MCZ ceramic composite, the experimental values for both moduli, i.e., elastic and rigidity, are slightly lower than the computed by the Voigt model through the single-phase constituent ceramics. More precisely, the 213 GPa for Young's modulus and the 84 GPa for the shear modulus measured are, approximately, both 91 % of the 235 GPa

and 93 GPa computed, respectively. Although this slight difference exists, it was considered that the experimental results fall within the range of the several reported values obtained in other studies. Additionally, it must be remarked that in some of the studies found, different theoretical values for single-phase materials are assumed and this may be justified by several factors, such as the manufacturer, the purity of the raw materials, and the measuring techniques exploited, among others.

Lastly, for YSZ a resembling trend as of MCZ was recorded. This is to say, that the experimental data of 199 GPa and 69 GPa, is, roughly, 90 – 95 % of the reported in the literature, i.e., 210 – 220 GPa and 76.5 GPa for Young's modulus and shear modulus, respectively. As previously explained, the data computed is consistent with the indicated by other investigations and therefore considered valid.

In short, the values obtained for Young's modulus and shear modulus parameters studied – of the magnesium oxide-doped alumina, magnesium oxide-doped calcium zirconate, and yttria-stabilized zirconia – are considered reasonable which signifies that they are in consonance with the announced by the scientific community.

On top of the discussion above provided, the elastic properties of polycrystalline materials are commonly envisioned to be isotropic. Under such conditions, the elastic properties – elastic modulus, shear modulus, bulk modulus, and Poisson's ratio – have well-known relationships. These elastic quantities are usually computed through ultrasonic methods under the relationships drawn between the longitudinal and shear velocities and the characteristic bulk density of the specimens under study [248]. It is emphasized that for a more detailed description of these relationships, Munro R. G. (1997) [248] article is advised. Furthermore, Phani K. K. and Sanyal D. (2008) [237] studied the relationships between the elastic properties – shear modulus, bulk modulus, and Young's modulus – for porous isotropic ceramic materials. For isotropic materials, as stated previously, the relations between these characteristics are given by the theory of elasticity. By plotting the variation of the shear modulus with Young's modulus (i.e., G versus E) – for various porous materials including more than twenty-five datasets retrieved from the literature – the authors concluded that a similar relationship to the rough proportionality of G/E = 0.375 for polycrystalline metallic materials may also exist for ceramic porous materials. The derived relationship defended that, if ignoring the variation of Poisson's ratio with porosity, then G/E becomes constant for a material. For the oxide materials studied, a proportionality of G/E interval ranging between 0.369 and 0.424 was provided. Considering the experimentally Young's and shear moduli values obtained for MA2, MCZ, and YSZ, the relationship between these parameters is, approximately, 0.410, 0.396, and 0.349, respectively, which are considered to be about consistent with the proportionality derived in the Phani K. K. and Sanyal D. (2008) [237] study.

5.3.2 Flexural Strength

Figure 5.13 depicts the flexural strength of the MA1, MA2, MCZ, and YSZ sintered ceramic systems. In general, flexural strength may be pointed out as the ability of a material to resist bending deflections applied perpendicularly to its longitudinal axis [249].

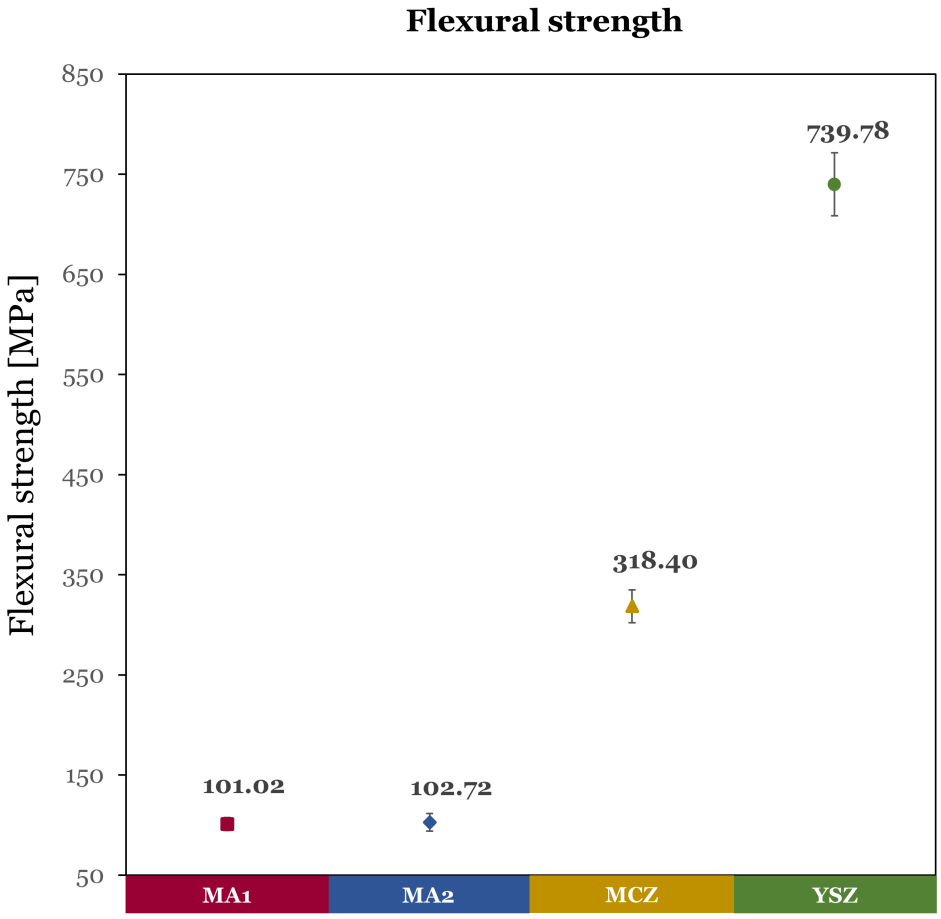

Figure 5.13: Flexural strength, σ, experimentally obtained for MA1, MA2, MCZ, and YSZ ceramic composites.

The graph represented in **Figure 5.13** depicts the flexural strength of the ceramic materials sintered, i.e., the alumina-based MA1 and MA2; as well as the zirconia-based MCZ and YSZ. Overall, the YSZ specimens showed the highest flexural strength in the magnitude of, approximately, 740 MPa, followed by the MCZ samples with, approximately, 318 MPa, and lastly MA2 and MA1 ones with, approximately, 101 MPa and 103 MPa, respectively.

It is highlighted that when no vertical bar is associated with each marker of each specimen type this means that the dispersion of data is very low and, therefore, the vertical bar is housed inside the marker. Additionally, the largest dispersion in the experimental results achieved (in comparison to other mechanical tests conducted and described in this

section) was somehow expected since the flexural strength is heavily dependent on microcracks and/or internal flaws of the specimens, as well as on the quality of their surfaces.

Based on studies found in the literature and commercially available material's datasheet, both MA1 and MA2 ceramic samples possess a very low flexural strength versus the expected. Heimann R. (2010) [250] indicates a range varying between 280 MPa and 420 MPa. In turn, Otitoju T. A. et al. (2020) [5] point out a value of 379 MPa, whereas the commercial datasheets suggest an interval of 310 – 455 MPa [251, 250]. On the other hand, for alumina with a purity of 99 % and 1 – 5 % porosity level, Auerkari P. (1996) [246] reported a drop for the lower limit of the interval range of flexural strength for 150 MPa. Therefore, it is not unexpected that – for MA1 and MA2 specimens with considerably high content of porosity – the flexural strength parameter would be highly impacted, and its value in magnitude greatly diminished.

For the MCZ ceramic composites, a much higher flexural strength data was recorded when compared to alumina-based ceramics. Bearing in mind parallel investigations on MgO – $CaZrO_3$ mixtures, slightly lower figures – to the ones experimentally obtained in this dissertation work, i.e., 318 MPa (with an apparent porosity of 0.05 $\pm$ 0.05) – of 270 MPa (with an apparent porosity of 0 $\pm$ 0.1 %) and 251 MPa (with an apparent porosity of 0.03 $\pm$ 0.1 %) were reported by Cabral A. (2021) [252] and Mamede et al. (2022) [253], respectively. It is believed that the differences of, around, 15 – 18 % may be justified by the chemical composition of the samples studied. Both Cabral A. (2021) [252] and Mamede et al. (2022) [253] investigated MgO – $CaZrO_3$ mixtures with 22.5 vol. % of MgO and 77.5 vol. % $CaZrO_3$. The magnesium-doped calcium zirconate ceramic composites manufactured, as described in section 4.1 Materials, had 12.7 vol. % of MgO and 87.3 vol. % of $CaZrO_3$. In other words, the authors here discussed used a higher content of magnesium oxide. Lang J. F. et al. (2018) [254] studied the effect of MgO on the thermal shock resistance of $CaZrO_3$ ceramic. Four batches containing 0 wt. %, 2 wt. %, 4 wt. %, and 8 wt. % were fabricated by solid-state reaction and further mechanically and thermally analyzed. It was concluded by the authors that, by adding MgO dopant, the flexural strength of the specimens at room temperature was improved due to grain refinement. However, after undergoing thermal shock, the samples with higher content of MgO proved to be more prone to microcracks due to mismatches in thermal expansion coefficients between MgO and $CaZrO_3$ (i.e., 13.8×10^{-6}/°C and 10.4×10^{-6}/°C, respectively). This study, therefore, suggests that, in the course of the sintering process, the residual strength of the MgO–$CaZrO_3$ specimens of Cabral A. (2021) [252] and Mamede et al. (2022) [253] was lowered due to the emergence of internal microcracks. Consequently, the highest flexural strength value of 318 MPa of MCZ manufactured specimens – with lower content of MgO dopant – is very much plausible to be recorded.

Lastly, YSZ samples showed to have the greatest flexural toughness among the ceramic composites manufactured and studied. According to the Tosoh powder manufacturer datasheet [243], yttria-stabilized zirconia may achieve a bending strength of 1200 MPa, whereas Heimann R. (2010) [255] indicates a range varying between 900 MPa and 1300 MPa for commercially available zirconia with an yttria content of 3 – 5 %. Amarante V. J. E. et al. (2019) [256] evaluated in their investigation the biaxial flexural for yttria-stabilized zirconia specimens with different surface finishing. For polished surfaces, 3 mol % YSZ of the VIPI Block Zirconn Translucen manufacturer showed an average flexural strength of 861 ± 81 MPa. Further, White S. N. et al. (2005) [249] studied the flexural strength of layered zirconia and porcelain all-ceramic system beams through 3-point flexural strength. The specimens tested had dimensions of 4.0 × 4.0 × 45.0 mm in a sequence of width × thickness × length. The module of rupture, or simply MOR, obtained for a solely zirconia layered beam, was 786 MPa. The authors namely reported a significant discrepancy between the manufacturer's technical specification product profile and the experimentally obtained data. In other words, 1272 MPa versus 786 MPa. Based on these figures, it is concluded that the value of 740 MPa for YSZ ceramic composite samples with 5.0 × 4.5 × 45.0 mm developed, tested, and studied is therefore conceivable and likely to be obtained.

Nonetheless, due to the vast dissimilarities in the values announced in the literature and commercial manufacturers, it is thus concluded that the inconsistency in the flexural strength of yttria-stabilized zirconia is dependent on several considerations. These are the chemical composition under study, the fabrication process adopted, the surface preparation, the nature of the test conducted, the methodology of analysis, and the experimental conditions, among many others. Moreover, the concentration of the stabilizing or doping agent heavily influences and plays a significantly decisive role in the mechanical performance of zirconia. Being yttria the dopant, the following should be retained as explained by Amarante V. J. E. et al. (2019) [256]. For 3 – 4 % mol of Y_2O_3, the tetragonal toughening phase is stabilized. This zirconia alloy, i.e., yttria partially stabilized zirconia, is characterized by exceptional toughness and flexural strength. Nevertheless, by further increasing the concentration of yttrium oxide, a higher concentration of the cubic phase arises, compromising, therefore, the amount of tetragonal phase available for the so-called transformation-toughening process – manipulation of the tetragonal to monoclinic martensitic phase transformation [257]. With an even greater content of yttria, i.e., 8 – 12 mol %, a fully stabilized zirconia may be obtained which does not possess the toughening capacity of the tetragonal grains, however, still offers extremely high resistance to thermal shock, excellent fracture toughness, corrosion resistance, and, particularly, allows the passing of oxygen ions, making it applicable as active membranes.

Table 5.9 demonstrates the flexural strength figures as well as standard deviations of the different ceramic systems under investigation, i.e., MA1, MA2, MCZ, and YSZ.

Table 5.9: Flexural strength determined by the 3–point bend test for MA1, MA2, MCZ, and YSZ ceramic composites.

Ceramic Composite	**Flexural strength,** σ **[MPa]**
MA1	101 ± 6.5
MA2	103 ± 8.8
MCZ	318 ± 16.5
YSZ	740 ± 31.4

As well-known, ceramics are vulnerable to brittle fracture, particularly, when cracks or flaws arbitrarily oriented exist, concerning the applied stress. The ceramic cracks may be generated during the manufacturing, and machining processes or/and due to mechanical and thermal loads application during in-service lifetime. The evaluation of fracture toughness (assessed in the forthcoming section) and the crack growth direction is an integral component of designing and producing advanced ceramics for engineering structures. It is usually common to adapt as a frame of reference three basic modes of deformation inside engineering components, including *opening*, or simply *mode I*, *in-plane sliding*, or just *mode II*, and, lastly, *out-off plane tearing*, or *mode III*. A combination of these modes is recognized and announced as mixed mode deformation. For reliability analysis of such engineering structures, physically realistic mixed mode fracture evaluation must be performed [258, 259]. **Figures 5.14**, **5.15**, and **5.16** show the fracture modes geometries of the specimens after testing from the top and side – for better fracture profile visualization – views.

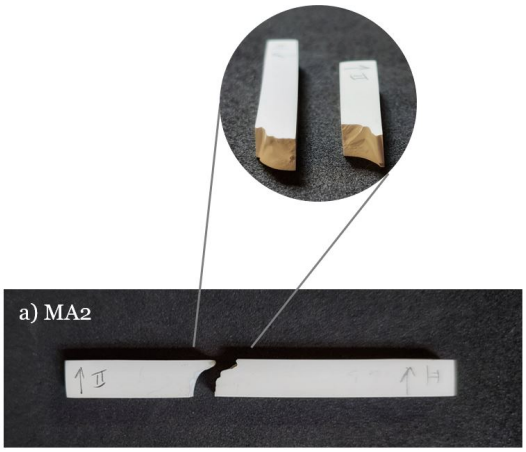

Figure 5.14: Fracture mode geometry of MA2 ceramic composites.

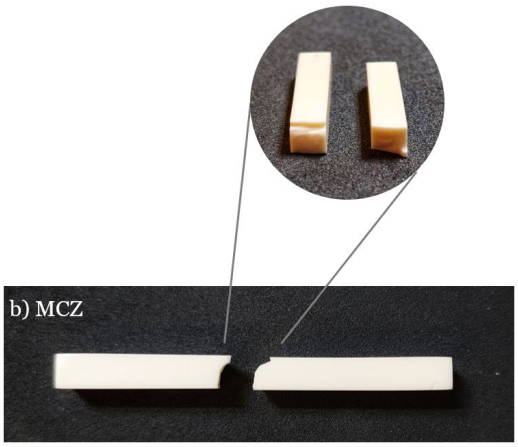

Figure 5.15: Fracture mode geometry of MCZ ceramic composites.

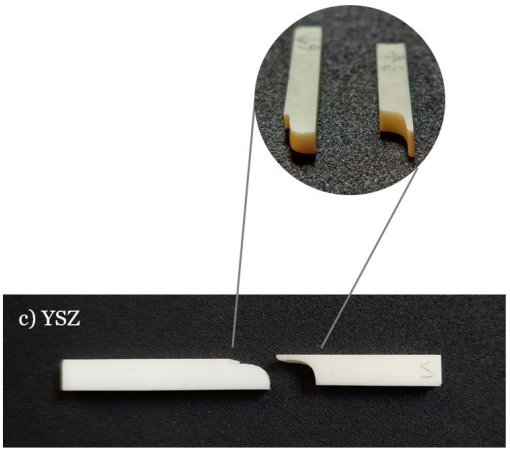

Figure 5.16: Fracture mode geometry of YSZ ceramic composites.

5.3.3 Hardness and Fracture Toughness

Hardness and fracture toughness are two characteristics of advanced ceramics which are namely commonly discussed in the context of the strength of both functional and structural ceramics – nevertheless with a slightly special focus for the latter one, i.e., structural purposes.

Figure 5.17 and **Table 5.10** show the Vickers hardness of the different ceramic systems manufactured, i.e., MA2, MCZ, and YSZ. The hardness parameter is crucially useful since it measures the resistance of the materials to plastic deformation, which potentially may incorporate effects such as material displacement and fracture [248]. In ceramic materials, Vickers hardness is of high importance since it allows to assess and evaluate the wear, abrasion, and friction resistance of the surface and structure.

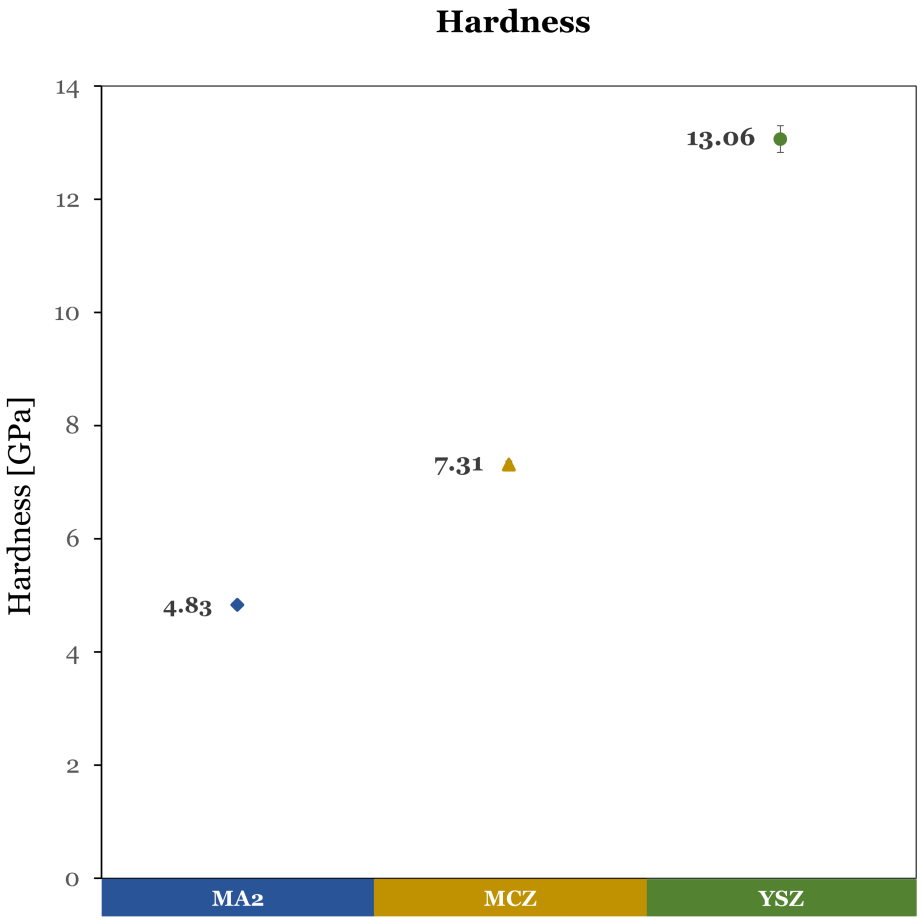

Figure 5.17: Hardness, HV, experimentally obtained for MA2, MCZ, and YSZ ceramic composites.

By studying the graph in **Figure 5.17**, it is possible to infer that of the three ceramic compositions investigated, the YSZ shows the highest value of hardness of, approximately,

13.06 GPa, whereas MCZ follows with 7.31 GPa and, lastly, MA2 has the lowest experimentally obtained value of 4.83 GPa. The graph shown in **Figure 5.17** omits MA1 ceramics due to its very high porosity content and, therefore, unlikely plausible results. Based on **Table 5.10** it is possible to conclude that the dispersion in data acquired associated with the measurements taken for the ceramic composite was very low, which indicates that the results were consistent. Solely for YSZ with a fairly short – but even so slightly higher than of the MA2 and MCZ – dispersion in data attained is represented by the vertical (black) error bar. Contrastingly, whenever no vertical bar is associated with each marker of each specimen type this means that the dispersion of data is very low and, therefore, it is contained inside the marker.

By getting deeper into detail, the experimental data presented in **Figure 5.17** must be carefully discussed on the following grounds. The average hardness value recorded for alumina ceramic composite is considerably lower than expected. Based on other investigations or commercially available alumina, the hardness value of this material should fall within a range of 15 – 22 GPa [248, 251, 260, 261, 262, 263]. It is strongly believed that the porosity content of 7 % present in these ceramic samples conditioned the final results of some parameters. Besides, even if considering the lowest Vickers hardness value of MgO of 12 GPa [264], this doping material feature is not capable to lower the final sintered ceramic composition hardness to the degree described.

In their article, Ternero F. et al. (2021) [265] discussed the influence of the total porosity on the overall properties of sintered materials. It is contextualized that, for the indentation hardness study, whenever porosity is detected in a material, it is necessary to differentiate between true hardness and apparent hardness. True hardness, also known as microhardness, is attained through single particle indentation using very low loads. Naturally, the hardness this way studied depends uniquely on the local composition and the microstructural state that does not differ from the hardness of analogous fully dense material. However, in the presence of porosity, microhardness does not provide correct insight into the porous true hardness. The apparent hardness, contrastingly, results of measurements made with higher loads and therefore considers the effect of porosity, and this relationship is far from linear. Thus, the relative hardness of 4.83 GPa experimentally obtained is presented, however, it does not represent an accurate reflection of the potential of alumina-based ceramics due to the incomplete sintering process and not fully compacted bulk ceramic, as shown in **Figure 5.17**. In other words, the porosity filling beneath the loaded indenter compromises the Vickers hardness indentation testing, analysis, and, ultimately, discussion.

Further, the MCZ value of hardness of 7.31 GPa shows a more confident value when compared to other studies. For instance, Nunes-Pereira J. et al. (2020) [264] reported a Vickers hardness of 7.5 GPa and 7.8 GPa for $CaZrO_3$–MgO composites sintered at tem-

peratures of 1450 ºC and 1500 ºC. In line with these results, Mamede et al. (2022) [253] reported namely a hardness experimental value of 7.8 GPa for a $CaZrO_3$−MgO composition with 0.02 % of porosity. As a result, it is concluded that the relative hardness of MCZ ceramic composite, with a porosity of 0.05, is assumed quite achievable and valid.

For the YSZ ceramic composite, the highest value of Vickers hardness was recorded, i.e., 13.06 GPa. Balça F. (2021) [170] who investigated several YSZ compositions, reported slightly lower values of about 10 – 11 GPa. According to the Tosoh powder manufacturer datasheet, YSZ's typical hardness is 12.5 GPa [243]. Other datasheets [262, 263] of commercially available YSZ ceramics point out a 12 – 14.5 GPa interval range. Thus, the value obtained is believed conceivable via ceramic sample experimental fabrication.

In turn, **Figure 5.18** and **Table 5.10** illustrate the fracture toughness of the different ceramic systems under investigation, i.e., MA2, MCZ, and YSZ. Essentially, fracture toughness is utilized to assess the resistance to the extension of cracks on a material [248].

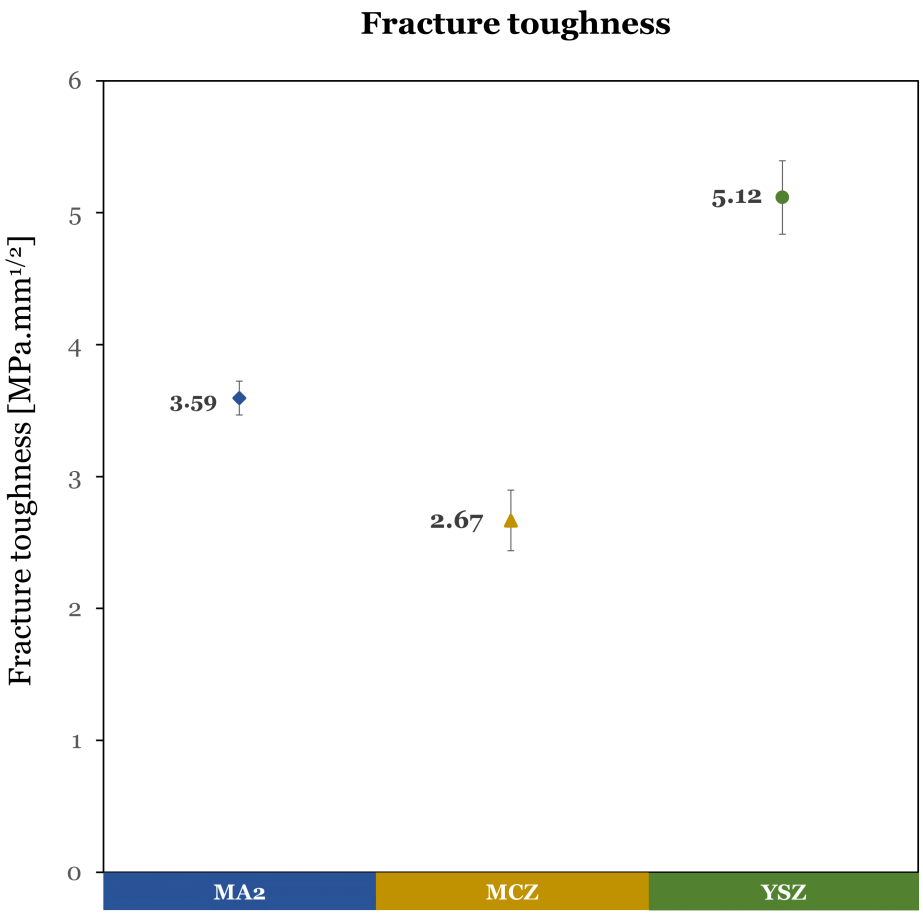

Figure 5.18: Fracture toughness, K_c, experimentally obtained for MA2, MCZ, and YSZ ceramic composites.

For the fracture toughness parameter, a different tendency was registered when compared to the Vickers hardness. In other words, the ability of a material to resist the propagation of flaws under applied stress was highest for YSZ with a magnitude value of, approximately, 5.12 MPa.mm$^{1/2}$, then MA2 with 3.39 MPa.mm$^{1/2}$, and, lastly, MCZ had the lowest experimentally obtained figure of 2.67 MPa.mm$^{1/2}$. Similarly, as in hardness measurements, **Table 5.10** indicates that the deviations encountered in the tests conducted were low, which implies that the data gathered was congruous. Once again and identically to the hardness graph, if no vertical bar is associated with each marker of each specimen type this means that the dispersion of data is very low and, therefore, it is housed inside the marker.

Particularly, for MA2, fracture toughness of 3.59 MPa.mm$^{1/2}$ curiously enough is consistent with the values mentioned in the literature. At room temperature, Heimann R. (2010) [250] indicates a range of 3 – 4 MPa.mm$^{1/2}$ for the fracture toughness parameter of high-alumina ceramics. Additionally, Auerkari P. (1996) [246] defends that, based on other studies, engineering alumina of 99 % purity and a porosity content of 1 – 5 % shall have a fracture toughness of about 3.5 – 5.5 MPa.mm$^{1/2}$. Some commercially available manufacturers namely point out an interval varying from 3 to 5 MPa.mm$^{1/2}$. Based on the diversity in fracture toughness data, considering the 7 % of porosity, the MA2's fracture toughness may be assessed well grounded.

Fracture toughness of 2.67 MPa.mm$^{1/2}$ of MCZ is consistent with the one reported by Nunes-Pereira J. et al. (2020) [264] for $CaZrO_3$−MgO ceramic composites of 2.6 and 2.5 MPa.mm$^{1/2}$ for a sintering temperature of 1450 ºC and 1500 ºC, respectively. In addition, Cabral A. (2021) [252] that studied the enhancement of the mechanical resistance of $CaZrO_3$−MgO, for a purely standard sample, indicated an experimentally achieved fracture toughness of 2.30 MPa.mm$^{1/2}$. Consequently, and bearing in mind possible experimental fluctuations – represented by a standard deviation of ± 0.5 – the MCZ fracture toughness parameter is considered consistent with the reported by other investigations and therefore envisioned as rational.

To finalize, the remaining ceramic composite YSZ, as mentioned previously, recorded the highest value among all ceramics fabricated at 5.12 MPa.mm$^{1/2}$. For the same composition investigated, i.e., 33.3 wt. % t-3YSZ, 33.3 wt. % c-8YSZ, and 33.3 wt. % m-ZrO_2, Balça F. (2021) [170] recorded slightly lower value of 4.09 MPa.mm$^{1/2}$. Datasheets of the manufacturers of the powder used, however, indicate an optimum value of 6.0 MPa.mm$^{1/2}$ [243]. It is remarked that the three-phase ceramic system YSZ, has an interesting composition in which the monoclinic, tetragonal, and cubic phases are ubiquitous. Consequently, and considering that each of these phases has its characteristic benefits, it is expected that slight variations may prevail. Additionally, once experimental deviation always occurs due to several different factors, the in-between 5.12 MPa.mm$^{1/2}$ achieved

is thus considered an enthusiastic result for YSZ's fracture roughness feature.

Table 5.10: Vickers hardness and fracture toughness determined from the Vickers indentation for MA2, MCZ, and YSZ ceramic composites.

Ceramic Composite	**Hardness,** HV [GPa]	**Fracture toughness,** K_c [MPa.mm$^{1/2}$]
MA2	4.83 ± 0.1	3.59 ± 0.1
MCZ	7.31 ± 0.5	2.67 ± 0.5
YSZ	13.06 ± 0.6	5.12 ± 0.6

Figures 5.19, **5.20**, and **5.21** illustrate the SEM micrographs representation of the Vickers indentation – of MA2, MCZ, and YSZ ceramic composites – performed for hardness and fracture toughness determination. In these figures, auxiliary red lines were drawn to facilitate the identification of the two diagonal cracks that emerge from the marks of the indentations made. The MA2 micrograph was achieved with a magnification of 350X, whilst the MCZ and YSZ micrographs with 250X.

Broadly speaking, an overall assessment of the mechanical elastic properties, in addition to the mechanical strength features of the four ceramic composites manufactured was investigated throughout this section. More specifically, the elastic properties were analyzed owing to the dynamic Young's modulus and the dynamic shear modulus collected data, whereas mechanical strength was characterized by flexural strength, hardness, and fracture toughness figures. As already explained, in the section on the Microstructure and Physical analysis, the direct comparison among the ceramic systems (MA1, MA2, MCZ, and YSZ) is not conceivable, but, on the other hand, it does not signify that a trade-off cannot be made. In terms of the module of rupture (i.e., flexural strength) and Vickers hardness YSZ showed the best results, followed by MCZ and lastly, MA2. In the fracture toughness test, however, MA2 is depicted to have a better capacity in resisting crack propagation than MCZ. Both ceramic systems, still fall behind taking into account the improved performance of YSZ. Contrastingly, in the elastic features, an inverse trend is observed. In other words, MA2 shows to have higher elastic and shear modulus than MCZ and YSZ. Nevertheless, it is emphasized the conditioning porosity content of the alumina-based ceramics strongly influenced the data results achieved.

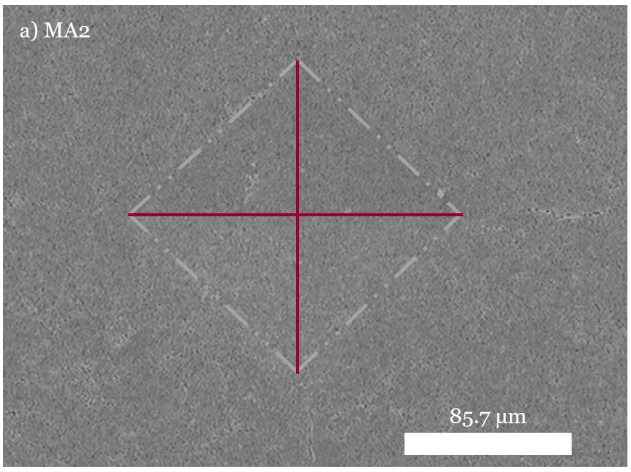

Figure 5.19: SEM micrographs of the characteristic results from Vickers indentation for MA2 hardness and fracture toughness determination.

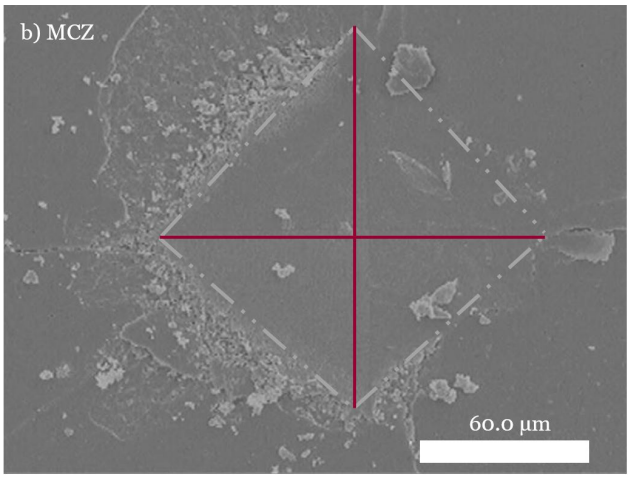

Figure 5.20: SEM micrographs of the characteristic results from Vickers indentation for MCZ hardness and fracture toughness determination.

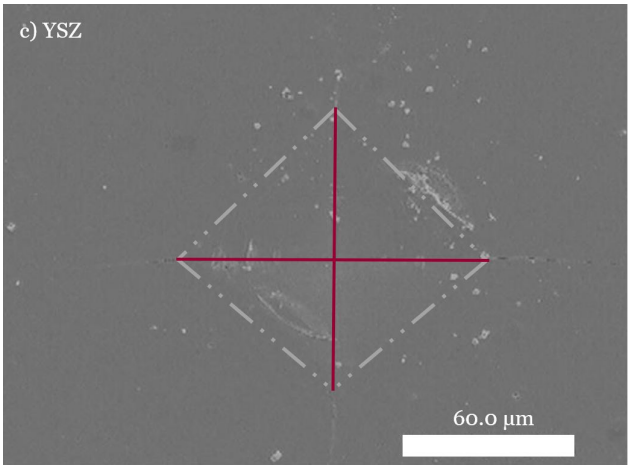

Figure 5.21: SEM micrographs of the characteristic results from Vickers indentation for YSZ hardness and fracture toughness determination.

Otitoju T. A. et al. (2020) [5] emphasized in their article review about advanced ceramics that in the last decades, research efforts have been focused on the investigation and development of ceramic components exhibiting a vast domain of applications owing to their unique features [5]. Accordingly, the pushing conditions of aeronautical and aerospace fields make it undeniably essential to study the mechanical properties of advanced ceramics both carefully and extensively. A set of needs evolved into real engineering requirements will dictate and shape the desired attributes to be fulfilled for a specific real application. Moreover, considering the multifunctional advanced ceramic aim and focus of this dissertation work, the mechanical evaluation developed throughout this section of MA1, MA2, MCZ, and YSZ in parallel to the microstructural and physical analysis is the first step key in the extensive characterization process of this ceramic material systems.

5.4 Thermal Properties

This section provides a thermal analysis of the manufactured ceramic composites. The thermal analysis is comprised of both, thermal conductivity – determined through flash method standard test – as well as thermal expansion coefficient – conducted by thermomechanical analysis, as explained in section 4.3.4, i.e., Thermal Properties of Chapter 4, Experimental Procedure. The assessment of thermal properties of the MA2, MCZ, and YSZ ceramic composites is of utmost importance, considering the high thermal wide range of applications in view. In other words, Thermal Protection Systems, Thermal Barrier Coating, in addition to Dielectric Barrier Discharges applications require a comprehensive analysis – of the thermal influence – on the performance of ceramic systems due to their desirable characteristics to provide both thermal insulation and environmental stability for engineering structures, or parts. Therefore, considering aeronautical and aerospace applications, in which hazard conditions to ceramics are continuously imposed, thermal analysis becomes mandatory. It is henceforth remarked that, in the present Thermal Analysis section, MA1 ceramic composite was not considered due to its high porosity and equipment (sample changer, as depicted in **Figure 4.16** limitations.

5.4.1 Thermal Conductivity

The property of thermal conductivity of the ceramic composites MA2, MCZ, and YSZ was achieved by initial *specific heat* and *thermal diffusivity* experimental determination through flash method standards and by data computation via **Equation 4.26**. As explained in section 4.3.4.1 Thermal Conductivity, thermal conductivity may be defined as "the rate at which heat is transferred by conducting through a unit cross-section area of a material when a temperature gradient exists perpendicular to the area" [211].

The following **Figures 5.22** and **5.23** represent the specific heat capacity and thermal diffusivity evolution with increase of temperature from 30 ^{o}C to 700 ^{o}C. It is remarked that the temperature interval mentioned above is slightly different from the referred in the Thermal Properties section 4.3.4, which is grounded on the need to adjust the conditions of the experimental analysis. This is, the controlled argon atmosphere was exploited rather than the nitrogen one, once it offered more consistent results. However, conversely, the argon atmosphere measurements were considered not feasible above 700 ^{o}C, owing to infra–red opacity at elevated temperatures.

On its basis, as well-known, equal masses of different materials require different amounts of heat to raise them through the same temperature interval. Accordingly, specific heat concept represents this phenomenon that consists of the quantity of heat necessary to raise the temperature of one gram of a substance by one Celsius degree. By examining **Figure 5.22**, MA2 ceramic composite is the ceramic system under analysis with higher specific heat, followed by MCZ, and lastly YSZ. In other words, MA2 requires an increased

amount of heat, than MCZ, which in turn will need a higher quantity of heat than YSZ to rise these three materials at the same temperature interval.

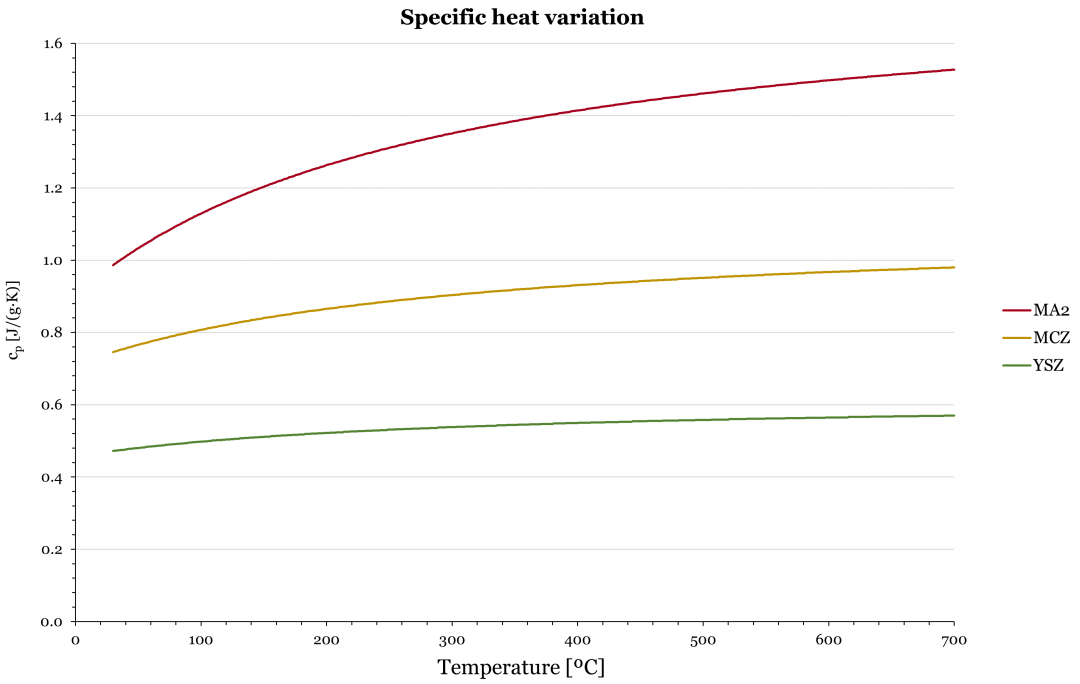

Figure 5.22: Specific heat, c_p, variation in function of temperature of MA2, MCZ, and YSZ ceramic composites.

In addition, with the growth of the temperature from 30 ºC to 700 ºC, the three ceramic composites increase to some degree their specific heat figures: MA2 in a more accentuated way, and with YSZ rise contrastingly being almost constant.

The following **Table 5.11** summarizes the experimentally obtained specific heat values at 30 ºC – room temperature – and 700 ºC – high-temperature – regimes.

Table 5.11: Specific heat of MA2, MCZ, and YSZ ceramic composites at 30 ºC and 700 ºC.

Ceramic Composite	**Specific heat capacity** [J/(g·K)]	
	Room temperature (30 ºC)	High-temperature (700 ºC)
MA2	0.986	1.53
MCZ	0.745	0.980
YSZ	0.472	0.570

As already referred, **Figure 5.23** depicts the evolution of the thermal diffusivity variation with temperature in the interval range of 30 ºC to 700 ºC.

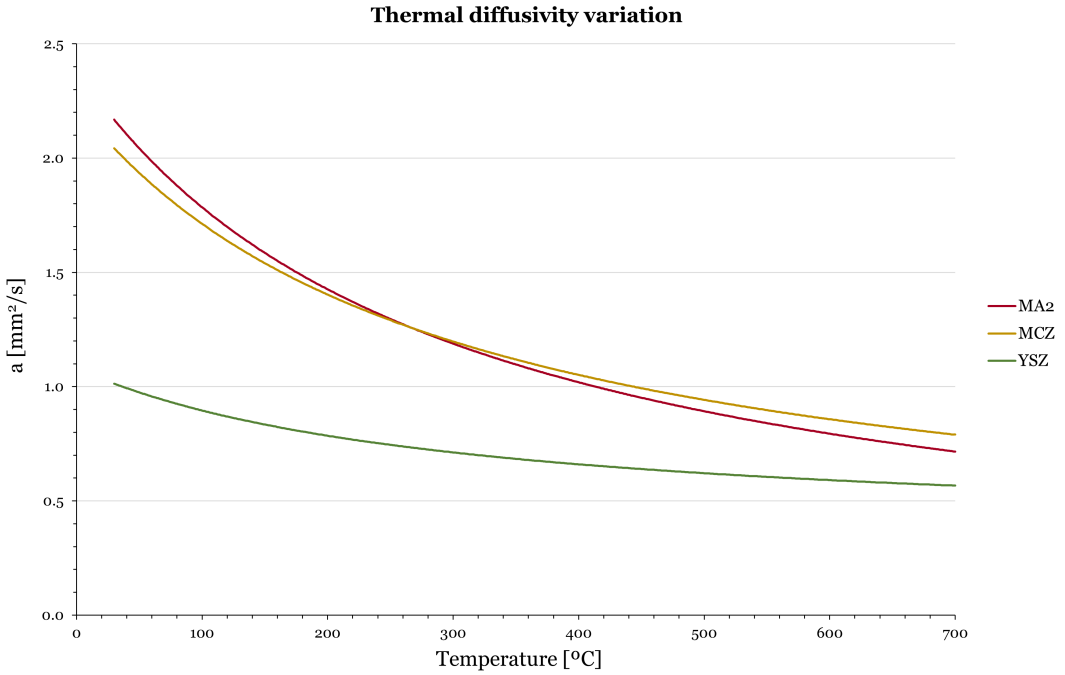

Figure 5.23: Thermal diffusivity, a, variation in function of temperature of MA2, MCZ, and YSZ ceramic composites.

The feature *thermal diffusivity* can be depicts as the parameter that describes the rate of temperature spread through a material. Consequently, thermal diffusivity is a material's property that gives an insight into the ability of a material to conduct thermal energy relative to its ability to store it [212]. **Figure 5.23** allows to conclude that of the three studied materials, MA2 and MCZ ceramic samples are more prone to spread heat energy through the specimen than YSZ. More accurately, MA2, at lower temperatures tested possesses a higher thermal diffusivity than MCZ, however this trend inverts at, approximately, 240 ºC until 300 ºC (i.e., the thermal diffusivity of MA2 and MCZ overlap). From approximately, 300 ºC to 700 ºC MCZ has a higher thermal diffusivity than MA2.

Moreover, **Figure 5.23** shows that with the increase of the temperature, in general, the three ceramic systems decrease their thermal diffusivity.

The **Table 5.12** below sums up the experimentally obtained thermal diffusivity values at 30 °C – room temperature, and 700 °C – high-temperature regimes.

Table 5.12: Thermal diffusivity of MA2, MCZ, and YSZ ceramic composites at 30 °C and 700 °C.

Ceramic Composite	**Thermal diffusivity** [mm^2/s]	
	Room temperature (30 °C)	High-temperature (700 °C)
MA2	2.17	0.716
MCZ	2.04	0.790
YSZ	1.01	0.567

Finally, **Figure 5.24** illustrates the thermal conductivity of MA2, MCZ, and YSZ ceramic composite materials, computed, as mentioned, through Equation 4.26 from 30 °C to 700 °C.

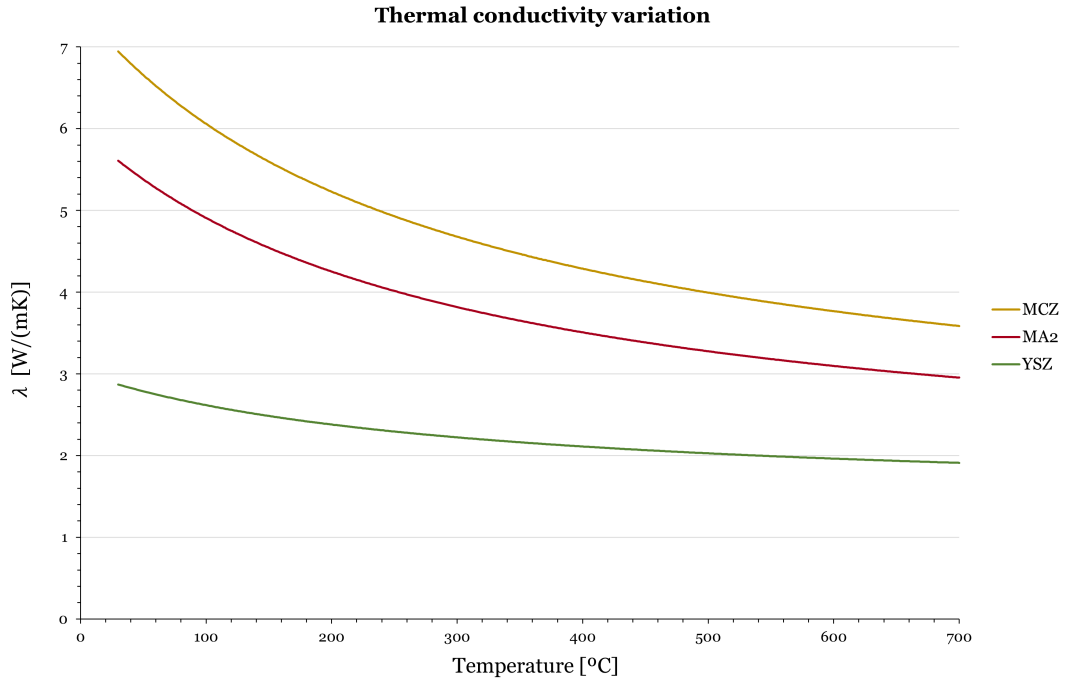

Figure 5.24: Thermal conductivity, λ, variation in function of temperature of MA2, MCZ, and YSZ ceramic composites.

By observing **Figure 5.24**, two major conclusions may be withdrawn. Primarily, it is evidenced that MCZ has a higher thermal conductivity than MA2, which in turn has an increased thermal conductivity than YSZ. Secondly, similarly to the thermal diffusivity behavior, the thermal conductivity tends to diminish with the growth of the temperature.

The following **Table 5.13** summarizes the experimentally obtained thermal conductivity values at 30 ºC – room temperature – and 700 ºC – high-temperature – regimes.

Table 5.13: Thermal conductivity of MA2, MCZ, and YSZ ceramic composites at 30 ºC and 700 ºC.

Ceramic Composite	**Thermal conductivity** [W/(mK)]	
	Room temperature (30 ºC)	High-temperature (700 ºC)
MA2	5.61	2.95
MCZ	6.95	3.59
YSZ	2.87	1.91

Considering the MA2 ceramic material, the thermal conductivity recorded for this sample is remarkably low. Typical figures of thermal conductivity for alumina, at room temperature, vary from 30 to 40 W/(mK) [250, 251, 262, 263]. Therefore, it is concluded that for MA2 a significant gap exist among the values reported by the literature and, approximately, 5.61 W/(mK) experimentally obtained. As a rule, the thermal conductivity parameter of porous ceramic materials is known to decrease with increasing porosity content [266]. More specifically, Sun J. et al. (2014) [267] explain that if increasing the porosity (i.e., lowering the density), ceramic's solid-phase heat conduction decreases regardless the temperature range studied, whilst the gas-phase heat conduction and thermal radiation rises. Thus, the overall thermal conductivity diminishes [267]. Furthermore, it has been shown in the literature that a modified exponential relationship for the description of the porosity dependence of the Young's modulus may alike be exploited with appropriate modifications of the numerical coefficient for the porosity dependence of the thermal conductivity [268]. The typical tendency curves shown for porous alumina ceramics studied by Živcová Z. et al. (2009) [268] of thermal conductivity behavior variation with temperature are resembling to the one represented of MA2 in **Figure 5.24**.

For the magnesium oxide-doped calcium zirconate, Carneiro P. et al. (2021) [241] performed a complete thermal characterization of composite materials with different $CaZrO_3$/MgO fractions. In their study – for the CZ2M1 ceramic, i.e., 1/3 MgO and 2/3 $CaZrO_3$ – experimental results, in addition to finite element method (FEM) simulations, and analytical model comparison showed a thermal conductivity rough variation between 3 and 7 W/(mK) for, approximately, [20; 500] ºC. Accordingly, these values are in line with the ones obtained for MCZ ranging from 3.59 W/(mK) and 6.95 W/(mK) as announced in **Table 5.13**. In terms of tendency behavior, alike graph line to the ones reported in Carneiro P. et al. (2021) [241] investigation may be observed, i.e., with increasing temperature, thermal conductivity diminishes.

Lastly, for the YSZ ceramic composite, satisfactory results were achieved. From the commercially available datasheets, it is recognized that YSZ has a very low thermal conductivity of, approximately, 2 – 3 W/(mK) [57, 262, 269]. Additionally, Zhao H. et al. (2006) [270] reported an interval range for thermal conductivity of yttria stabilized zirconia of 2.2 – 2.9 W(mK). Balça F. [170], clarifies that the cubic, tetragonal and monoclinic phases that coexist in the YSZ ceramic composites have dissimilar thermal conductivities of, approximately, 1.8 W/(mK), 3 W/(mK), and 7 W/(mK), respectively. Adopting different analytical studies, the results for the conductivity feature pointed out in Balça F. [171] study to vary between 2.93 and 3.57 W/(mK) at room temperature. Bearing this in mind, the values of 2.87 W(mK) and 1.91 W(mK) for 30 ºC and 700 ºC, respectively, are considered congruent and in agreement within the figures reported in the literature. On top, for fully dense yttria-stabilized zirconia, Schlichting K. W. et al. (2001) [271] research supports the behavior of lower thermal conductivity with increase of temperature depicted in **Figure 5.24**.

5.4.2 Coefficient of Thermal Expansion

As explained in the latter Chapter 4, the linear expansion coefficient, CTE, is an essential and indispensable parameter to be investigated once it grants insights into the ceramic's response to a change of temperature, and thus provides information if the failure of a part, or structure, may occur due to imposed thermal stress.

The following **Figure 5.25** depicts the evolution of the dimensional percentage change of MA2, MCZ, and YSZ ceramic composites for an interval range of -110 ºC to 980 ºC.

From a broad perspective, it can be stated that the dimensional evolution of ceramic composites is approximately close to linear over the temperature range evaluated, i.e., it rises continuously from -110 ºC to 980 ºC. Nevertheless, a slight decrease – for the three ceramic samples – is pointed out at, about, 650 ºC with no further strong oscillations recorded.

It should be namely emphasized the behavioral tendencies that are opposite in the below 0 ºC and the above 0 ºC regimes. In other words, up to 0 ºC, the MA2 curve has higher dimensional percentage change in magnitude – than both zirconia-based ceramics, i.e., MCZ and YSZ. On the other hand, after 0 ºC, this tendency inverts, being zirconia-based ceramics, the materials with a greater dimensional percentage both in magnitude during the course of temperature rise from 0ºC to, approximately, 980 ºC, and variation - verified by its increased slope. Curiously, at, approximately, 900 ºC, MCZ and YSZ ceramic systems overlap in their corresponding dimensional variation. Moreover, in both delineated (positive and negative temperatures) regimes, the MA2 curve shows a reasonable gap between the MCZ and YSZ curves which may be justified by not only its chemical composition difference but as well relatively accentuate porosity content.

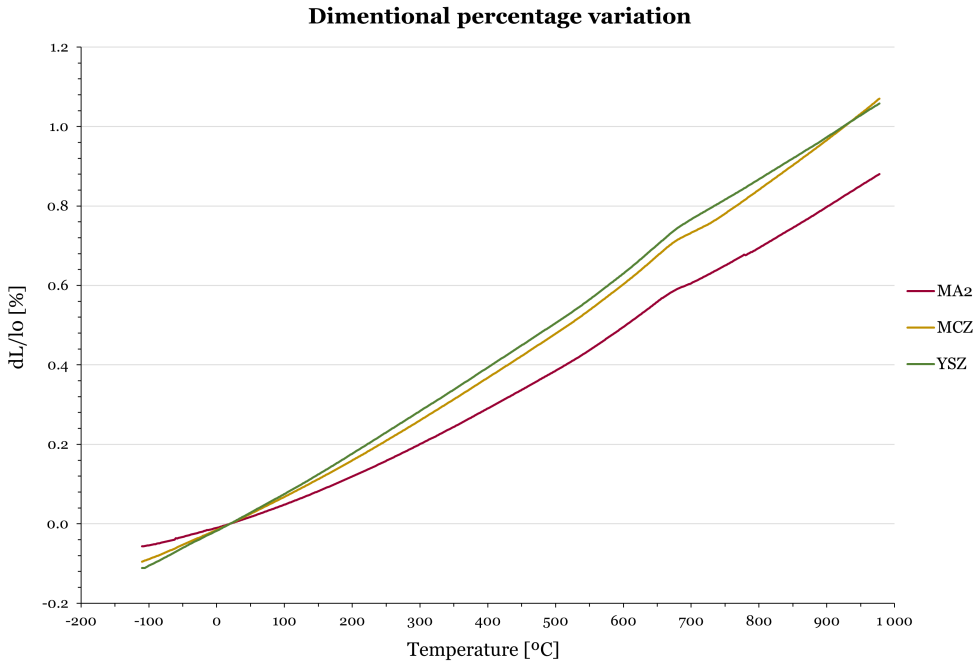

Figure 5.25: Dimensional percentage, dL/lo, variation in function of temperature of MA2, MZC, and YSZ ceramic composites.

Figure 5.26 below describes the evolution of the CTE variation of MA2, MCZ, and YSZ ceramic composites similarly analyzed in an interval range of -100 ºC to 980 ºC.

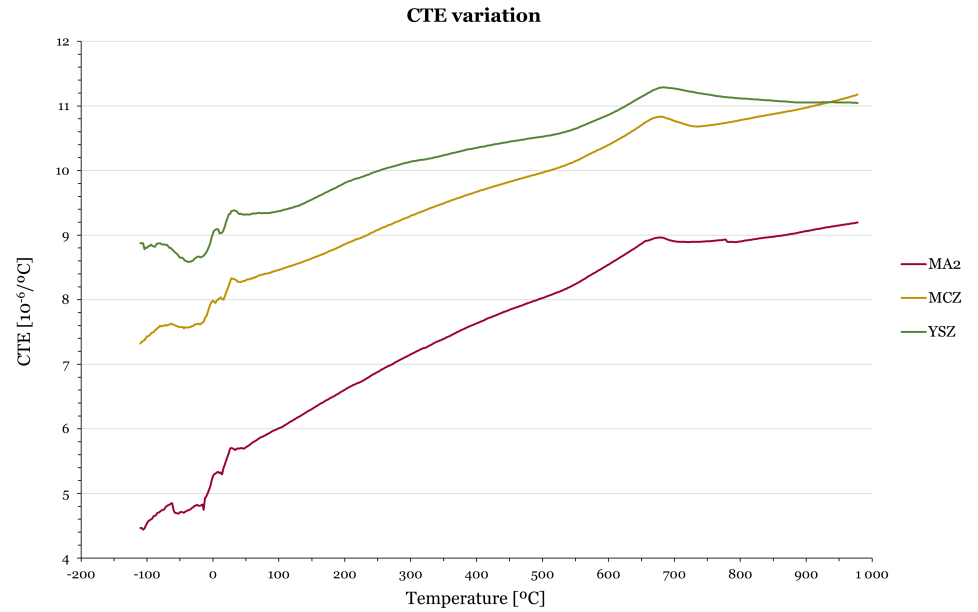

Figure 5.26: Coefficient of thermal expansion, CTE, variation in function of temperature of MA2, MCZ, and YSZ ceramic composites.

By analyzing **Figure 5.26**, a similar tendency is identified for all ceramic composites – MA2, MCZ, and YSZ. Their behavior starts with initial strong unsteady oscillations in CTE values in the temperature interval of -110 ºC until, approximately, 0 ºC. Worth being noted that MA2 ceramic is the ceramic system (of three) with the most volatile variations in CTE values. Subsequently, a sharp fluctuating increase in CTE until approximately 50 ºC temperature figure is identified, after which a steadier growth is observed up to the end of the whole evaluated temperature range – with the exceptions already verified in **Figure 5.25** – at 650 ºC.

Accordingly, based on the data behavior described, it is concluded that from -100 ºC to 0 ºC the samples suffered contraction – **Figure 5.25** – and thus the unsteady values in CTE for all samples. The ceramic's overall dimensions are diminished as well as the coefficient of thermal expansion. Further, from 0 ºC to 650 ºC, an expansion of the material was observed which consequently contributed to the determination of higher CTE values. Within the highest range of temperatures under investigation, i.e., from 650 ºC to 980 ºC, the dimensional expansion of the sample decreased to some degree which in turn led the coefficient of thermal expansion to stabilize. It is remarked that, for the last analyzed temperature value, approximately, 980 ºC, YSZ's overlaps with the MCZ's CTE feature being, approximately, $11.0 \times 10^{-6}/^{\circ}C$.

Additionally, **Table 5.14** contains data with an average CTE for three temperature intervals: a low (negative) of -50 to -100 ºC; an average room temperature considered from 20 to 30 ºC, and, lastly, a high–temperature from 800 to 980 ºC.

Table 5.14: Average CTE values for three temperature regimes: low, room, and high temperatures.

Ceramic Composite	**Coefficient of thermal expansion, CTE** $[10^{-6}/\,^{\circ}C]$		
	Low temperature range [-50; -100]	Room temperature range [20; 30]	High–temperature range [50; 980]
MA2	4.71	7.56	7.91
MCZ	5.63	8.24	9.94
YSZ	9.04	10.96	10.5

Reading the values of **Table 5.14**, it is concluded that the values of CTE are characteristic for every ceramic material under study, once they are considerably chemically, microstructurally, and physically dissimilar. Nevertheless, a common tendency for MA2, MCZ, and YSZ, as previously analyzed in **Figure 5.26**, is stressed out, i.e., with the growth in temperature, a rise in thermal expansion coefficient is recorded.

Considering the MA2 ceramic composite, the values obtained regardless of the temperature regimes studied, i.e., low temperature, room temperature and high temperature ranges, in **Table 5.14**, may be perceived as coherent with the data reported in the literature. More precisely, Auerkari P. (1996) [246] pointed out in his research that, at room temperature, for engineering alumina ceramic of 99 % purity with 1 – 5 % porosity level, the CTE is, approximately, 5.4×10^{-6}/°C. If considering the value listed on **Table 5.14** for the room temperature regime from 20 °C to 30 °C, MA2 possesses a very identical figure of 5.6×10^{-6}/°C. Additionally, Munro R. G. (1997) [248], outlined a CTE of, approximately, 4.6×10^{-6}/°C, 7.1×10^{-6}/°C, and 8.1×10^{-6}/°C for [0; 20] °C, [0; 500] °C, and [0; 1000] °C temperature intervals. If computing an average of the determined discrete values of CTE for the announced specific temperatures ranges, the corresponding values are, approximately, 5.4×10^{-6}/°C, 6.8×10^{-6}/°C, and 7.8×10^{-6}/°C.

Moreover, it is emphasized and recognized that a solid understanding of the variations of the material properties with the porosity consists of a useful tool for an adequate application of the porosity dependent relations in real engineering structures [272]. Nevertheless, for the CTE feature, conflicting and non-concordant data is provided [273]. Depending on several parameters – chemical composition, fabrication process, analysis performed – the thermal expansion coefficient may increase or decrease with the porosity content. It is claimed that a unique thermal expansion-porosity relationship does not exist [272]. Accordingly, the apparent porosity of MA2 of 7 % was not considered for the evaluation, validation and verification purposes in the CTE conducted tests. In short, it is therefore concluded that the variation among the experimentally obtained values and the cited in the literature is consistent.

Bearing in mind values indicated in the literature, it was concluded that MCZ have satisfactory final results. More precisely, Schafföner S. et al. (2013) [274] reported values of CTE collected from other previous studies of $CaZrO_3$ ceramics to be about $8.5 – 11.8 \times 10^{-6}$/°C between 20 °C and 900 °C. For the sake of completeness, and within the same framework of thought, an average computation of the experimental MCZ's CTE feature obtained in between 20 °C and 900 °C was performed. The result determined was approximately 9.8×10^{-6}/°C. Moreover, in its study about dense $CaZrO_3$ produced by electric arc melting, Schafföner et al. (2017) [275] experimentally obtained a CTE of 10.45×10^{-6}/°C [275]. Contrastingly, Hou Z. F. (2008) [242] highlighted a relatively rather lower thermal expansion coefficient $6.5 – 8.5 \times 10^{-6}$/°C. The slightly disparate values found in the bibliography may be justified by the anisotropic structure of MgO–doped $CaZrO_3$. More accurately, a thermal mismatch may be verified between the dopant agent MgO that has a CTE of 13.5×10^{-6}/°C and $CaZrO_3$ average CTE of 10.4×10^{-6}/°C (result of large thermal expansion anisotropy, i.e., α_{ma}=4.9×10^{-6}/°C, α_{mb}=10.9×10^{-6}/°C, and α_{mc}= 15.1×10^{-6}/°C) [276]. Therefore, considering the data provided, it is believed that the CTE result for MCZ ceramic composite is in line with other studied.

Lastly, for YSZ material the following was established. As previously, in the mechanical properties analysis, some values provided by manufacturer's datasheets varying considerably. Naturally, it depends on the compositions of yttria-stabilized zirconia used, the methodologies of manufacturing and testing applied, as well as the conditions in which the tests were conducted. Overall, some datasheets indicate values for CTE of 9.1×10^{-6}/°C between 20 and 100 °C; 9.9×10^{-6}/°C between 20 and 200 °C, and 10.1×10^{-6}/°C between 20 and 300 °C [277]; whereas others show lesser values, for instance, 6.9×10^{-6}/°C between 25 and 100 °C; 8.1×10^{-6}/°C between 25 and 300 °C, and 10.5×10^{-6}/°C between 25 and 600 °C [278]. Cao X. Q. et al. (2004) [57] that summarized the basic properties for thermal barrier coatings from studies available in the literature listed a CTE of 11.5×10^{-6}/°C for the 3YSZ and a slightly lower 10.7×10^{-6}/°C for 8YSZ. As described on **Table 5.15**, the acquired experimentally fabricated, tested and evaluated YSZ ceramic depicts reasonable and more constant (than of some references) values in terms of CTE parameter over the temperature interval studied.

Table 5.15: CTE figures considering different temperature interval ranges of YSZ ceramic composite.

Temperature intervals [°C]	**CTE** [10^{-6}/ °C] (from literature)	**CTE** [10^{-6}/ °C] (experimentally computed)
[20; 100] [277]	9.1	9.3
[20; 200] [277]	9.9	9.5
[20; 300] [277]	10.1	9.7
[25; 100] [278]	6.9	9.3
[25; 300] [278]	8.1	9.7
[25; 600] [278]	10.5	10.1
[0; 1000] [57]	11.5	10.4
[0; 1000] [57]	10.7	10.4

To summarize, in this section, two major thermal properties of ceramic materials, i.e., thermal conductivity and coefficient of thermal expansion were examined and evaluated for the manufactured MA2, MCZ and YSZ ceramic systems. Briefly, in terms of thermal conductivity, MCZ showed a higher capacity to conduct heat when a temperature gradient exists perpendicular to the area of the sample, followed by MA2, and thenceforth YSZ. On the whole, the three ceramic composites analyzed tend to decrease their respective thermal conductivity values with the increase of temperature from 30 °C to 700 °C. Further,

considering the CTE feature, a totally different behavior was ascertained. This is, the material that showed a higher coefficient of thermal expansion was YSZ, followed by MCZ, and lastly MA2. Broadly speaking, the three materials increased their CTE values from room temperature up to 980 ºC with a slight change in this tendency at, approximately, 650 ºC. In the CTE study, additionally, data was computed and studied for negative temperatures. In this regime, a more scattered and frequently changing variations in CTE were recorded.

Overall, from an application perspective, in aeronautical and aerospace fields, ceramics present interesting thermal properties. Particularly, backtracking to the discussed TPS, TBC and DBD purposes, thermal features such as thermochemical stability, thermal conductivity, as well as thermal expansion coefficient are crucial. In high temperature applications – both TPSs and TBCs – ceramic materials protect aerospace structures from aerothermal *cooling* and *heating* imposed under harsh environmental conditions. More specifically, TPSs rise challenges in adequate ceramic material selection due to loads, high temperatures as well as shock phenomena associated with hypersonic flight and re-entry into atmosphere. Furthermore, TBCs not only serve as protection mean to the underlying metallic substrate, as well as metallic bond coat – both with elevated coefficient of thermal expansion (about $15 \times 10^{-6}/°C$) – from corrosive and erosive conditions, but namely as thermal insulator in high-temperature regimes [78]. Accordingly, assessment of thermal coefficients of the several layers that comprise a TBC structure allows to predict and prevent adhesive failure from thermal interlayer stress, and cohesive failures as microcracks and/or spalling. In case of DBDs, different ceramic-based insulators are useful for high voltage applications due to their high resistivity and thermal conductivities.

All in all, it may be concluded that the tailorable properties of ceramics make them suitable for extremely demanding application in low and high-temperature. Consequently, the full comprehension of their thermal properties, such as conductivity and expansion coefficients become mandatory to not only improve the performance of engineering structures, or parts, but also extend their useful lifetime.

5.5 Electrical Properties

The present section focuses on the proof-of-concept evaluation and validation regarding the feasibility of the different ceramic composites produced – MA1, MA2, MCZ, and YSZ – as dielectric barriers for DBD plasma actuators. Within this framework, the following sequence is adopted to progressively discuss the results obtained. To start with, the electrical analysis composed of the average power consumption, the Lissajous curves as well as the capacitance variance are presented and examined. Then, a trade-off among the distance of the Pitot tube to the edge of the exposed electrode and the velocity – in function of the applied voltage – is performed for induced flow velocity study purposes. Lastly, thermographs (infra-red) images taken of the ceramic composite dielectrics during plasma discharge are namely shown. Additionally, to the thermographic pictures, the variations of the temperature along the $x-$ and $y-$directions across the dielectric material are provided to better understand the temperature influence on the overall ceramic DBD plasma actuator performance. Lastly, to finalize and sum up, some general conclusions are highlighted.

5.5.1 Average Power Consumption Analysis

Before initializing the discussion about the experimental data results obtained, it should be accentuated the importance of the power consumptions parameter in the all-embracing DBD plasma actuator analysis. As explained by Ashpis D. (2017) [223] the characterization of the power consumption of the DBD actuators is a key feature for the following reasons. Initially, and shortly put, it is essential in comparative characterization of performance of different actuators designs. Nevertheless, the comparisons are considered meaningful only in case they are conducted at constant powers. Next, in terms of practical implementations of flow control systems for aeronautical and aerospace aims, actuators power consumption is required for cost-benefit analysis of the system they are part of. Lastly, it is fundamental to acknowledge the magnitude of power consumptions to properly understand how to implement an efficient and lightweight high-voltage power supplies as well as through real-time sensors health monitor the actuator itself. All in all, as demonstrated, accurate power measurements of DBD plasma actuators are of vital relevance to the DBD research community for the technological advance of the engineering structures that are being focus of study.

Consequently, and as a starting point of this section, the average power consumed by the four manufactured ceramic composites DBD plasma actuators – MA1, MA2, MCZ and YSZ – are shown in the following **Figure 5.27** as function of the wide range of applied voltages at the frequency of 24 kHz. The represented average power consumed was calculated, as explained in section 4.3.5.1, this is, through **Equation 4.33** enunciated on the Electrical Current Method section. Although both methods, i.e., the Electric Current Method and the Electric Charge Method are coherent and reasonable for the electric average power

consumption estimation, once the capacitor's tolerance of 10 % (used in the Electrical Charge Method setup) is considerably higher than the resistor's tolerance of 1 % (applied in the Electrical Current Method setup), it becomes natural to exploit the average electrical consumption from the Current Method.

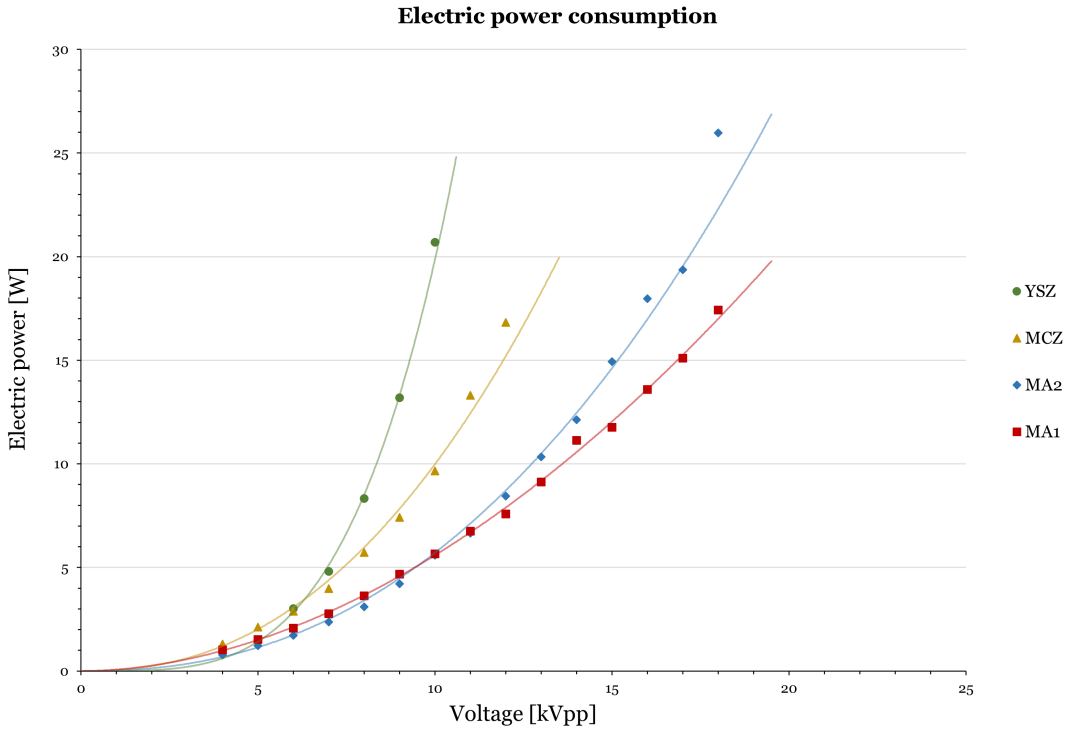

Figure 5.27: Electric power consumption for MA1, MA2, MCZ and YSZ ceramic composites.

On the whole, and by evaluating **Figure 5.27**, it can be assessed that the average power consumed by the four ceramic dielectrics increased with the increase of the input voltage. It is noted that for a better illustration of the evolution of the experimental data results, a fitting line was added for the four ceramic composites. Until, approximately, 6 kVpp, i.e., for low-voltages range, the power consumption shows a similar behavior for MA1, MA2, MCZ and YSZ ceramic samples. Afterward, however, different tendencies – depicted by the fitting curves – arise for each dielectric. It must be emphasized that although the behavior for low-voltages range mentioned is claimed to be similar, the magnitude of the values measured of the average power consumed – by the ceramic composites – is quite heterogeneous, this is, at 6 kVpp the corresponding power consumptions are, approximately, 3.0 W for YSZ, 2.9 W for MCZ, 2.1 W for MA1, and 1.7 W for MA2.

Moreover, at higher level voltages, i.e., from 7 kVpp on, it is noticeable that the power consumed by each DBD plasma actuator device strongly depends on the dielectric ceramic composite material. More precisely, YSZ curve depicts the sharpest increase of power consumptions of all materials for different input voltages analyzed, whereas MCZ shows a slightly slower (than YSZ) but still somehow rapid rise. Subsequently, MA1 and MA2

ceramics represent a more regular growth in power consumed for the voltage interval applied. It must be highlighted that MA2 ceramic composite presents a higher power consumption values for applied voltages above 12 kVpp than MA1. In short, from described tendencies and observations, and by considering a broadest perspective, the conclusion reached was that the ceramic composite that requires the highest amount of average power for the same range of applied voltages is the YSZ, and the lowest one the MA1. Additionally, it is possible to conclude that the zirconia–based ceramic composites tend to consume more power than the alumina–based ceramic composites, when operated at same input voltage level.

Besides the discussed, owing to both **Figure 5.27** and **Table 5.16**, it is also possible to infer that the YSZ ceramic has the lowest operating limit of 10 kVpp, followed by MCZ with a maximum input limit of 12 kVpp, and, lastly, MA2 and MA1 showing both the highest operating limit of 18 kVpp. It should be highlighted that the operating limits stated were evaluated and judged by considering the transition of the plasma discharge to an unstable and markedly filamentary regime, since, at this stage, for the wide range of input voltages tested, none of specimens fractured or deteriorate to a level that they could no longer be tested. Therefore, the highest the input voltage the ceramic material is capable to support without causing marked, or profound degradation, the broadest the operating range of the actuator.

Table 5.16 summarizes the operating limits in terms of input voltage for each ceramic composite as enunciated, in addition to the corresponding average electric power consumption.

Table 5.16: Operating limits of the four ceramic composites and the associated average power consumption.

Ceramic Composite	**Operating limit** [kVpp]	**Average electric power consumption** [W]
MA1	18	17.4
MA2	18	26.0
MCZ	12	16.8
YSZ	10	20.7

Furthermore, the registered operating limits were considered to be significant among the different ceramic composites studied, once the observed variation in maximum input voltage values is quite diverse. More specifically, from the conducted testes, MA1 and MA2 demonstrated to be the most robust ceramic composites since their maximum input voltage was almost two times higher than the YSZ.

The following provided and delineated information aims to contextualize and further describe the complexity of power consumption analysis for DBD plasma actuator devices considering the exposed on the literature.

From the extensive research undertaken on the DBD plasma actuators, and as already expected, it was concluded that it is extremely difficult, if not impossible, to perform an accurate, or precise, comparison with other studies on the field. In other words, bearing in mind the ceramic composites research as dielectrics barriers in surface DBD geometry (adopted in this dissertation work) – which is particularly linked to active flow control and icing mitigation – investigations in the literature do not report similarities. Consequently, power consumption comparison or even an assessment of this parameter with the found information becomes unlikable to add any significant validation, verification, or major conclusion to the present subsection.

Generally, SDBD power consumption is mostly considered and reported as a function of electrical, geometrical, and material features. Some authors emphasize and give detailed information about electrical parameters, i.e., input peak-to-peak voltage, frequency, and type of AC waveform as a determining parameter on the power consumption of DBD plasma actuators. Others, tend to lean to a more material-oriented perspective, for instance, the electrical properties of the dielectric being studied, for example, permittivity, dielectric strength, and thickness relationships [279]. Moreover, the electrical characteristics of the power supply are as well influenced by the environmental condition, such as temperature, pressure, humidity, and ambient gas [223].

On one hand, alumina composite – which is considered a state-of-art ceramic as dielectric barrier – comprises commonly recognized application such as surface treatment [157], adhesion improvement for film deposition [156], and CO_2 decomposition [165]. Nevertheless, the geometry designs adopted in these processes are very different from the one adopted in this dissertation work. For instance, Pribyl R. et al. (2020) [157] studied spinel-doped alumina ceramics sintered through gel-casting and mounted on a coplanar geometry (CDBD) with several electrodes and embedded in cooling and an insulating system. Likewise, Kelar J et al. (2020) [156] investigated alumina as dielectric barrier but instead of doping it with spinel – which was claimed by the authors to be highly insoluble in alumina – oxides such as cerium dioxide (CeO_2), chromium (III) oxide (CeO_3), and ferric oxide (Fe_2O_3) were added. Explicitly, in these studied, besides the varying chemical composition, which is different of the MA1 and MA2 samples (magnesium oxide doped alumina), the CDBD design exploited does not match with the geometry adopted. Even though, CDBD is considered a surface DBD, both ground and high-voltage electrodes were placed in refrigerating oil and covered by a ceramic insulator. This is considerably different from the asymmetric surface DBD design adopted and described in the previous Experimental Procedure Chapter 4.

On the other hand, and considering this time the MCZ ceramic composite, the most similar case studies encountered, were of other perovskites. For example, Li R. et al. (2004) [165] investigated the $Ca_{0.7}Sr_{0.3}TiO_3$ with $Li_2Si_2O_5$ as a sintering additive for CO_2 decomposition, whereas, in turn, Song X. et al. (2016) [158] analyzed the feasibility of using $Ca_{0.8}Sr_{0.2}TiO_3$ for the same aim. Besides the different chemical composition, a volume (planar) DBD geometry was chosen in both studies.

Lastly, YSZ ceramic composite as an asymmetric surface dielectric barrier discharge consists of a purely proof-of-concept, i.e., an establishment of the feasibility and rationale to use this ceramic composite as a product to DBD plasma actuator integration. In the literature, solely 8 % mol yttria-stabilized Zr_2O_3 microtubes has been reported to be implemented as dielectric barrier material in a micro atmospheric pressure micro-plasma jet by Talviste R. et al. (2021) [280]. Nevertheless, the authors highlighted that a quantitative description of the effect of the microtube material's dielectric constant on the electric fields, as well as plasma parameters, such as electron density and temperature, are still topics of further research.

On this basis, and as abovementioned, it is not plausible or cogent to evaluate power consumptions of different experiments especially when their features are not compatible and greatly divergent.

5.5.2 Lissajous Curves Analysis

The subsequent **Figures 5.28**, **5.29**, **5.30**, and **5.31** show Lissajous curves computed by the Electrical Charge Method (announced in the section 4.3.5.2) for four different selected voltage levels at which induced flow velocity (discussed in the next section) was registered for the ceramic composites DBD plasma actuators. It should be remarked that only four levels were selected for each ceramic DBD actuator to ease the Lissajous curve figures visualization once plotting all the data obtained would most certainly difficult the interpretation of the results to the reader.

In short, Lissajous figures for plasma actuators assembled were obtained by plotting the charge flowing into the circuit as function of the voltage differences between the electrodes. The measurement of the charge was performed by means of the ceramic probe capacitor E222M placed in series in the Current Charge Method, as shown in **Figure 4.21**. As explained in detail by Biganzoli I. et el. (2014) [281], if the input voltage is on a *low-level range*, the imposed electrical field is weak and therefore incapable to generate plasma. In this case, the Lissajous figure consists of a straight line once the charge varies proportional to the voltage and the system assumes a purely capacitive behavior. Contrastingly, if the input voltage is on a considerable *high-level range*, and, thus, is capable of inducing a high electrical field, the Lissajous plot opens (spreads) in a geometry

of a convex figure. Lissajous figures also known as voltage-charge cyclograms allow to infer about the power consumed by any actuators per cycle by computing the area inside a particular closed curve for that specific cycle period. What is more, it must be noted that in the SDBD plasma actuators – contrarily to volume or planar geometries – the discharge process is not characterized by a constant geometrical plasma shape. It is much more complex since it is *time-varying* in terms of discharge properties and behavior. In other words, the geometric shape of the overall discharge for this type of DBD plasma actuators, may change throughout the *discharge active phase*. This is owing to the accumulation of charges on the dielectric material surface which will dictate the electric fields of the future discharges of the voltage AC sinusoid supply. Accordingly, changes in shape of the (physical) discharge region occur and have a direct influence on the discharge capacitance, leading to so-called *almond-shape* Lissajous curves.

Figure 5.28 represents the Lissajous curves for MA1 ceramic composite for four – 12 kV, 14 kV, 16 kV and 18 kV – voltage levels.

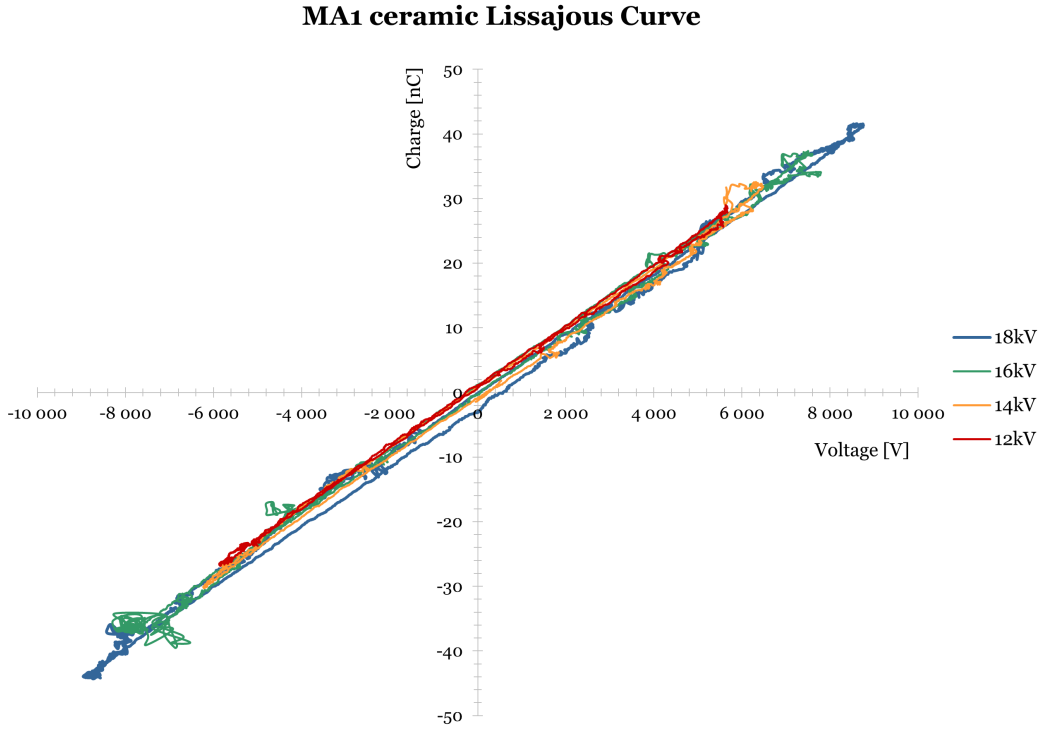

Figure 5.28: Lissajous curves of MA1 DBD plasma actuator at 24 kHz for different applied voltages.

The Lissajous curves for MA1 ceramic composite show a very closed shape and an especially sharp transition from the capacitance regime (in which no plasma discharge occurs) to the discharge regime (in which plasma discharge occurs). Besides, by increasing the input voltages, the cyclogram extends to a certain extent. Worth noting, that for the lowest

shown input voltage of 12 kV, the Lissajous curve is almost a straight line. Despite the characteristic geometry of the cyclogram, the represented behavior is concordant to the data of the power consumption, this is, by increasing the voltage, a higher electric field is originated, and, consequently, a higher amount of power is necessary to generate plasma. In addition, this type of ceramic presented the lowest power consumption values and, thus, it shows also very close Lissajous curves which is translated into low power consumption.

Figure 5.29 represents the Lissajous curves for MA2 ceramic composite for four – 12 kV, 14 kV, 16 kV and 18 kV – voltage levels.

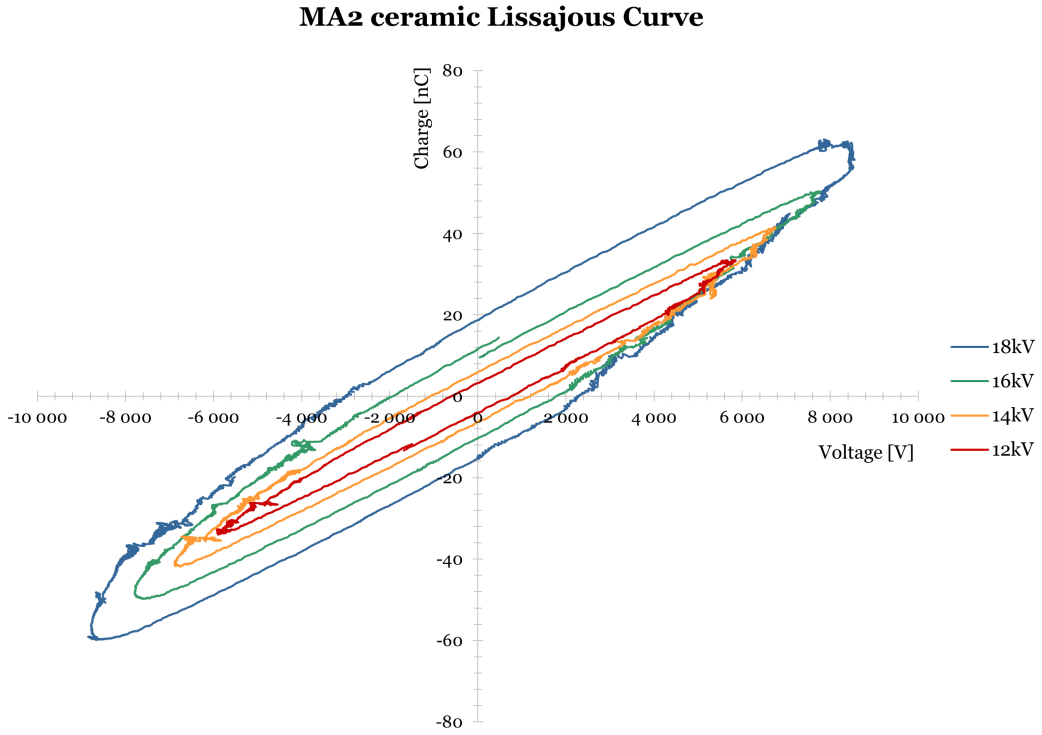

Figure 5.29: Lissajous curves of MA2 DBD plasma actuator at 24 kHz for different applied voltages.

The Lissajous curves for MA2 ceramic composite depict a profoundly round shape and a much smoothest transition from the capacitance regime to the discharge regime when compared to the less dense MA1 . This last consideration regarding the transition between the capacitance and discharge regimes induces into the idea that the MA2 dielectric is able to continue, at least to some degree, of providing plasma discharge in the passive i.e., capacitance regime. In addition, by increasing the input voltages, the cyclogram extends (broaden) quite significantly. From this observation, it is concluded that MA2 required a higher power consumption than the significantly porous alumina based ceramic MA1 for the same input voltages.

Taheraslani M. and Gardeniers H. (2021) [282] investigated the conversion of methane in a packed-bed dielectric barrier discharge, at ambient conditions, and analyzed the impact of different packed materials on the process. The materials studied were silica, barium titanate ($BaTiO_3$), in addition to α– and γ–alumina. Lissajous figures for the different listed materials packed inside the DBD plasma reactor were provided. Curiously enough, the geometry of the voltage-charge plot of both alumina ceramics, resembled the presented oval shapes figures on **Figure 5.29**. The authors attributed this special rounded form to the occurrence of a combination of filamentary discharges accompanied with further surface discharges. The effect of further partial surface discharge in DBDs is alike to having stray capacitance in the circuit, i.e., unintentional manifestation of electric charge or non-capacitive components. This stray capacitance can also be represented by a non-discharging capacitance [282].

Figure 5.30 represents the Lissajous curves for MCZ ceramic composite for – 7 kV, 8 kV, 9 kV and 10 kV – four voltage levels.

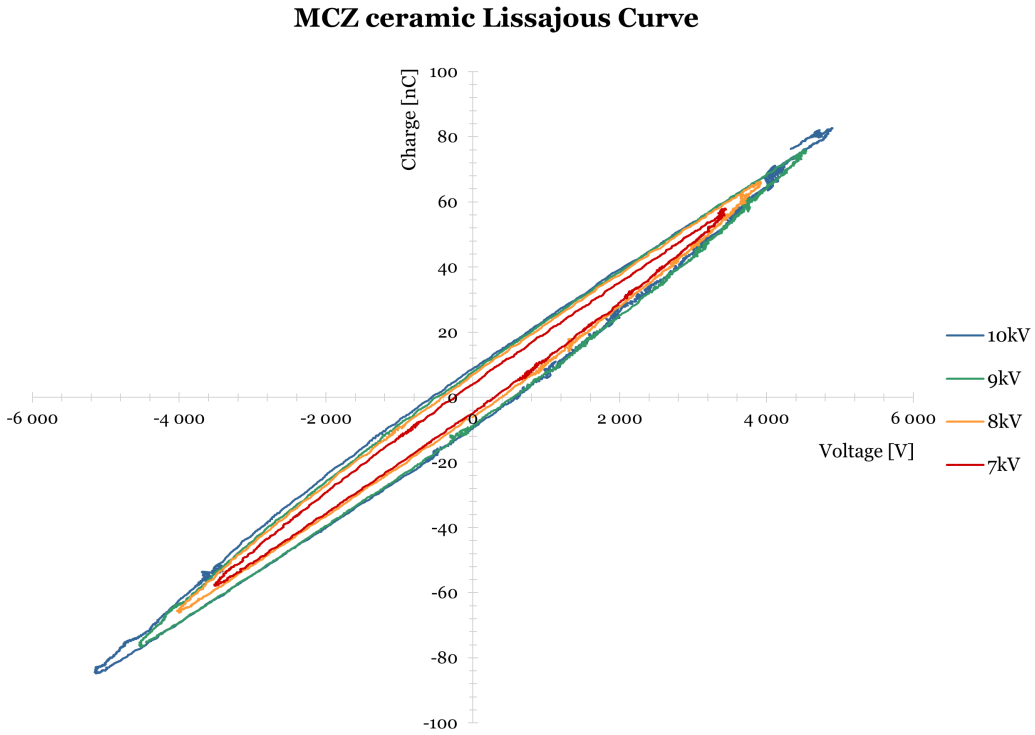

Figure 5.30: Lissajous curves of MCZ DBD plasma actuator at 24 kHz for different applied voltages.

The Lissajous curves for MCZ ceramic similarly to the MA1, represent a narrow shape and a distinctly sharp transition from the capacitance regime to the discharge regime. Furthermore, by rising the input voltage, the cyclogram contained area slightly expands,

agreeing therefore with the tendency of higher power consumption for higher voltage values. It must be emphasized that the expansion of the cyclogram for consecutive higher voltage inputs, does not occur in a sound way, i.e., the Lissajous curves are very close to each other, and in turn this agrees with the power consumption behavior shown by **Figure 5.27**. To put it in another way, smalls (steps) amount in power increases by rising the input voltage – the MCZ tendency line (yellow line) growths in a much slower way than the rest of the ceramic dielectrics and the spacing between the markers (triangles) is relatively evenly distanced without abrupt jumps. Moreover, the main differences between the alumina-based ceramic and the MCZ, independently of the input voltage values considered, geometrically consist of the following: the Lissajous curves of MCZ shows a bigger central area than MA1, i.e., they do not behave in the straight-line format; and when compared to MCZ, MA2 dielectric continues to show an acutely round shape. In addition, despite MA2 appears to present wider Lissajous curves when compared with MCZ, the values of charge in MCZ are quite larger which justifies the higher power consumption observed previously in **Figure 5.27**. Although, the Lissajous curves of MCZ does not present a convex geometry well-defined, slopes were subsequently determined to draw conclusions regarding cold and effective capacitances of this DBD plasma actuator.

Figure 5.31 represents the Lissajous curves for YSZ ceramic composite for four – 7 kV, 8 kV, 9kV, and 10 kV – voltage levels.

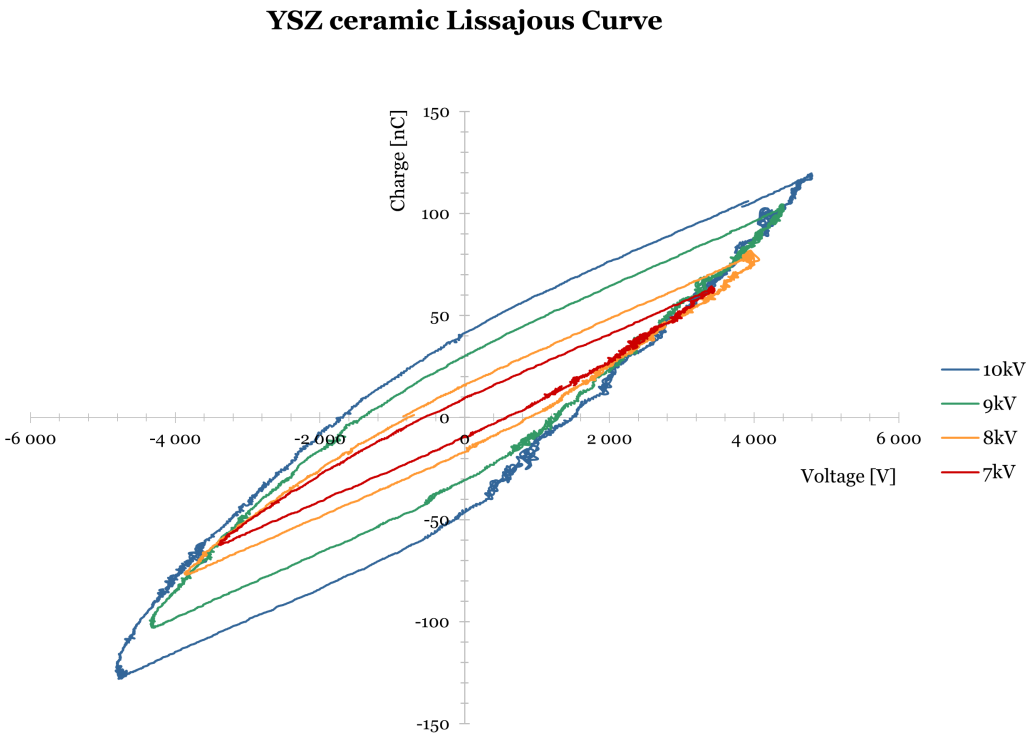

Figure 5.31: Lissajous curves of YSZ DBD plasma actuator at 24 kHz for different applied voltages.

Lastly, the Lissajous curves for the YSZ ceramic composite depict a more commonly recognized – in the literature [283] – shape and behavior among the four dielectrics. This is to say, that YSZ's cyclograms have a convex geometry, which was not observed for the alumina-based ceramics, nor for the calcium zirconate (MCZ). Contrastingly to **Figures 5.28**, and **5.29**, the Lissajous curves of YSZ have well-defined slopes to easily assess the cold and effective capacitances of the assembled DBD plasma actuator device. Similarly, to all previously reported materials, with the increase of input voltage, an increase in power consumption is verified. Additionally, the areas enclosed by the cyclograms become wider and with a more precise characteristic convex form. Thus, the power consumed abruptly increases, as suggested by **Figure 5.27**.

To ease the comparisons made throughout the Lissajous curves presentation and discussion, the following **Figure 5.32** plots the four different ceramic material Lissajous figures for 10 kV.

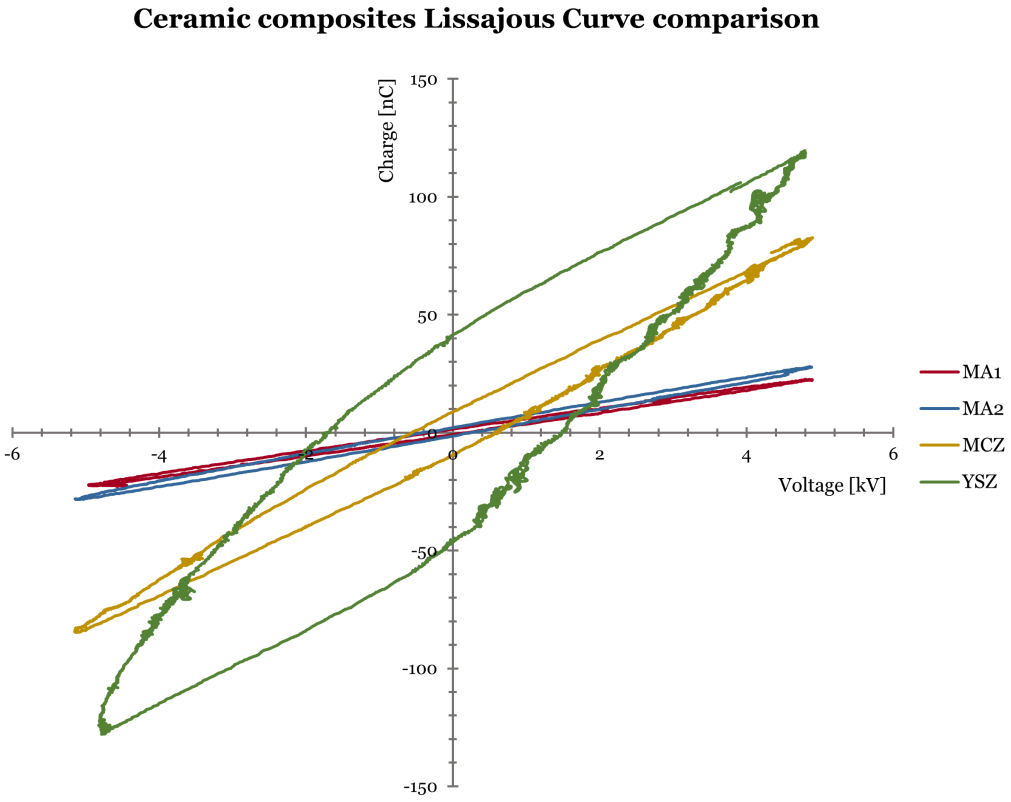

Figure 5.32: Lissajous curves comparison of the MA1, MA2, MCZ and YSZ ceramics dielectric for 10 kVpp.

Figure 5.32 confirms and supports the conclusions drawn from the analysis of **Figures 5.27**, **5.28**, **5.29**, **5.30**, and **5.31**. In short, for the alumina-based ceramics, MA1 Lissajous curve depicts a very closed shape and almost a straight-lined geometry, whilst MA2 cyclogram is more rounded shape with the transition of the capacitance regime to the dis-

charge regime more prolonged – which induces to the assumption that, when plasma is created, electrical charges are continuously transported during capacitance regime through the gap (between the electrodes) and accumulated on the insulating surfaces. Finally, for zirconia-based ceramic composites, MCZ has a higher area embodied by its Lissajous figure than both alumina ceramics which agrees with the power consumption results since MCZ presented higher power consumption. Nonetheless, the MCZ's Lissajous curve area is still slimmer than of the YSZ's material that in turn has the most trending behavior reported on the literature considering other dielectric materials. Moreover, owing to **Figure 5.32**, the total charge transferred (assessed through y–axis) to the ceramic composites is, approximately, as follows: roughly 25 nC to MA1 and MA2, about 80 nC to MCZ, and 120 nC to YSZ. The breakdown voltage (analyzed through x–axis), that determines the onset ignition of the plasma discharge, is highest for the YSZ (approximately, 1.5 kV), followed by MCZ (approximately, 0.6 kV), and, finally, by MA2 and MA1 (approximately, 0.2 kV).

As an additional feature, besides the Lissajous figures, maximum and minimum charge variations for the four ceramic composites were also computed through the Electrical Charge Method and depicted in the graphs of **Figure 5.33**.

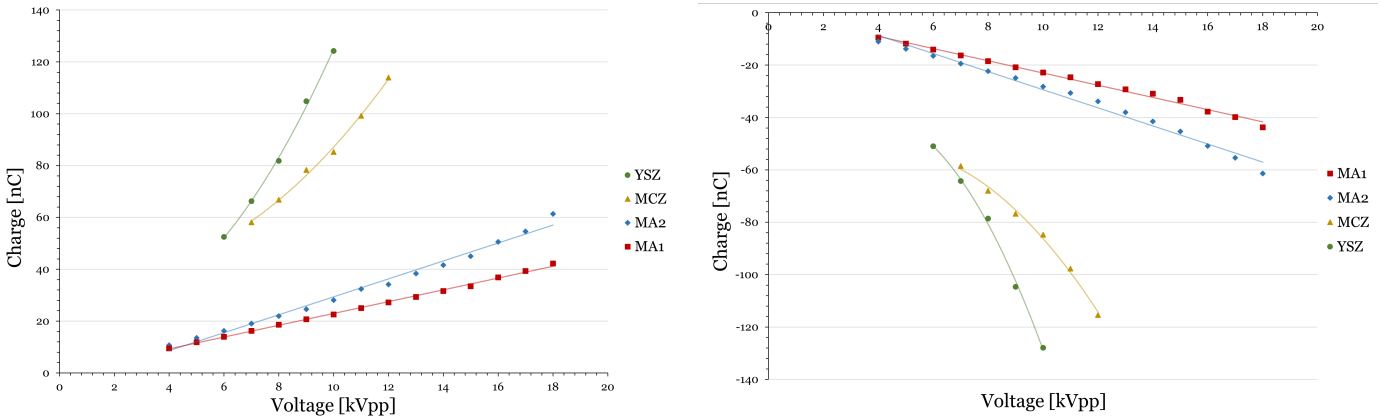

(a) Maximum charge variation.

(b) Minimum charge variation.

Figure 5.33: Maximum (a) and minimum (b) charge variation for the four sintered ceramic composites, i.e., MA1, MA2, MCZ, and YSZ[15].

Figure 5.33 represents the different maximum and minimum charges values for different input voltages for MA1, MA2, MCZ and YSZ sintered ceramic composites. It is remarked that for a better illustration of the evolution of the experimental data results, a trendline was added for the four ceramic composites. In detail, the maximum and minimum charge values oscillate considerably for the YSZ material, in a range of, about [-130, 125] nC, as shown in **Figure 5.31**, i.e., during the plasma discharge phenomenon, the

[15]In some of the Lissajous curves (i.e.., the ones related to the highest input voltages) of **Figures 5.28**, **5.29**, **5.30**, and **5.31**, the maximum charge values reached by the plot may be a little lower than the values shown in **Figure 5.33** since, as explained, some tests were omitted for clearer results presentation.

total charge transferred to this ceramic was higher when comparing to other manufactured materials. Besides, considerable charge amount was transmitted to MCZ, varying in between [-115, 115] nC interval, as illustrated by **Figure 5.30**. Both alumina ceramics had their maximum and minimum variations considerable lesser when compared to the zirconia-based ceramics, i.e., [-40; 40] nC for MA1, and [-60; 60] nC for MA2, as can be visualized in **Figure 5.28** and **5.28**, respectively.

Additionally, if considering the particular event of 10 kVpp input voltage – for the individual case of Lissajous curves represented by **Figure 5.32** – the maximum charge transferred to the alumina ceramic recorded was roughly 40 nC, 84 nC in case of MCZ, and 124 nC for YSZ. Therefore, it is concluded that the graphs shown in **Figure 5.33** agree with the data depicted in **Figure 5.32**.

As previously mentioned, in terms of Lissajous figures, MA1's extremely sharp and narrow characteristic geometry, as well as MA2's very round almond-shape, did not allow to differentiate the two – capacitive and discharge – regimes, nor in turn compute the cold and effective capacitances. Therefore, cold and effective capacitances were only possible to compute for the MCZ and YSZ ceramics due to the existence of a clear slope on the Lissajous curve profile.

This way, **Figures 5.34** represent the cold (C_{cold}) and the effective (C_{eff}) capacitances for zirconia–based ceramic composites – MCZ and YSZ – extracted from the voltage-charge filtered data graphs (Lissajous diagrams) of the DBD plasma actuators discharge process by considering their local slopes, as explained in **Figure 4.22**.

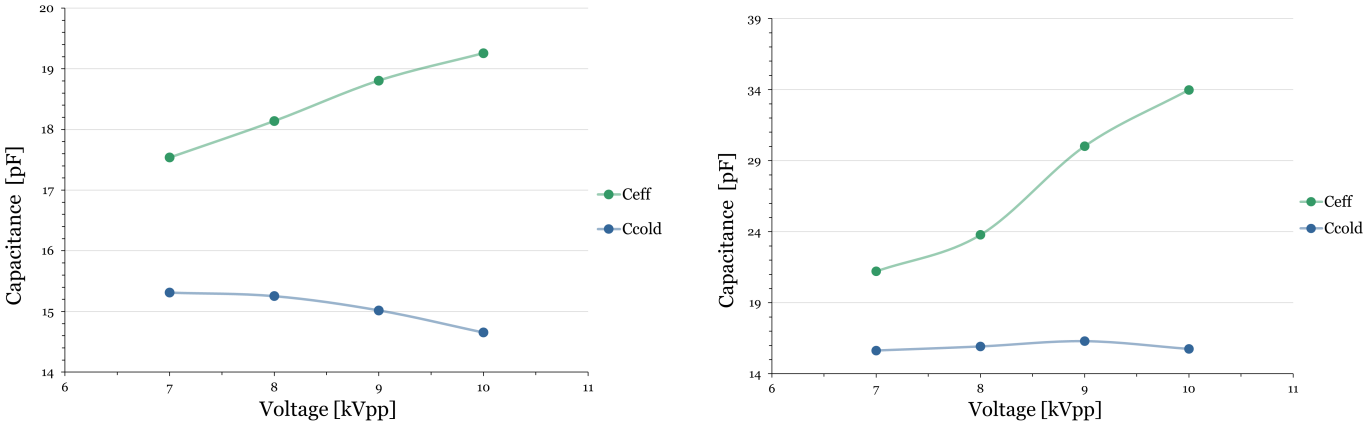

(a) MCZ cold and effective capacitance variation.

(b) YSZ cold and effective capacitance variation.

Figure 5.34: Cold and effective capacitances determined for the positive and negative half-cycles from the Lissajous curves for MCZ (a) and YSZ (b) ceramic composites

Figure 5.34 represents the cold and effective capacitances of both zirconia-based ceramic, i.e., MCZ (left side graph) and YSZ (right side graph). As anticipated, for both ceramic composites, the cold capacitance (C_{cold}), represented with blue lines, remained more or less stable over the applied range of input voltages, from 7 kVpp to 10 kVpp. This happens once *cold capacitance* refers to a purely passive component of the device's capacitance, and, as a result, should not change with the applied voltage rise. Although a wider range of input values was tested for MCZ, for consistency of results presentation, 7 to 10 kVpp is shown.

Moreover, the variations of effective capacitance (C_{eff}) illustrated by green lines show a higher variation for YSZ in the interval of [21; 34] pF than for MCZ ranging [17.5; 19.2] pF. These variation in effective capacitance – which correspond to the capacitance of the DBD device with the influence of the plasma discharge – are reasonable. As depicted by the Lissajous figures of MCZ, little variation (very closed cyclograms) was computed with increasing input voltages, whilst YSZ's Lissajous figures showed wider intervals (bigger cyclograph areas). To put it in another way, the higher effective capacitance for both ceramic composites is congruent with increased slopes of the voltage-charge curves. Notably, the visible inflation in capacitance at 8 kVpp is sustained by the larger gap between the yellow (8 kVpp) and green (9 kVpp) cyclogram lines represented in **Figure 5.31**.

5.5.3 Induced Flow Velocity Analysis

To evaluate the efficiency of the different DBD plasma actuators for active flow control applications in aeronautical and aerospace fields, the induced flow velocities were measured by the Pitot tube technique, as explained in the Electrical Properties section of the Experimental Procedure chapter and illustrated by **Figure 4.23**.

The induced velocities experimentally obtained were tested for – horizontal ($x-$direction) distances between the exposed electrode and Pitot tube – of 1.0 cm shown in **Figure 5.35**, and 1.5 cm, depicted in **Figure 5.36**. The purpose was to establish by using a micromanometer in which of these two positions higher velocity values would be recorded. In addition, the velocity was acquired during a time interval of 10 s, at a sampling rate of 1 sample per second, and the final presented results were computed by performing the overall average of the attained data. **Table 5.17** serves as a summary support resource for the shown graphs understanding and critical analysis.

As referred, **Figure 5.35** presents the recorded induced velocities as functions of the applied voltages for alumina-based (left side graph), i.e., MA1 and MA2, and zirconia-based (right side graph), i.e., MCZ and YSZ ceramic composites.

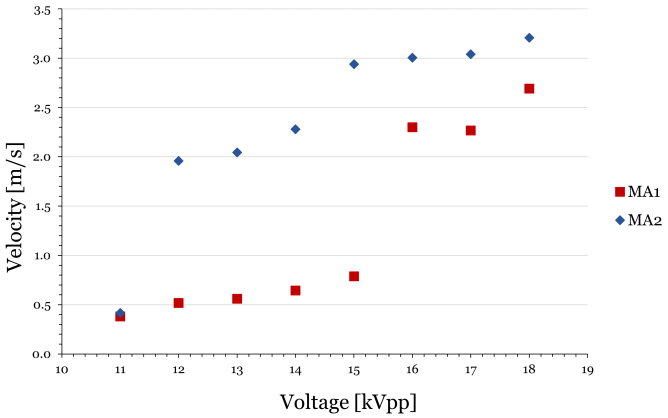

(a) Velocity of alumina–based ceramics.

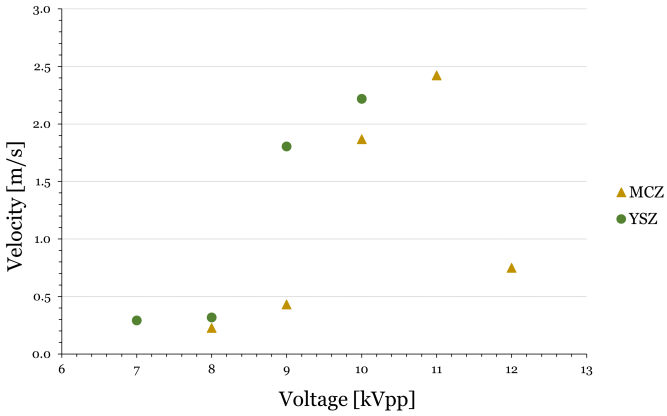

(b) Velocity of zirconia–based ceramics.

Figure 5.35: Maximum induced flow velocity for alumina–based ceramics (a) and zirconia–based (b) with a distance between the exposed electrode and Pitot tube of 1.0 cm.

According to **Figure 5.35**, the following conclusions were driven for 1.0 cm setup. MA2 alumina was the ceramic system, which was capable of inducing higher velocities, this is, approximately 3.2 m/s in comparison to the maximum achieved velocities of, about, 2.7 m/s, 2.4 m/s and 2.2 m/s by MA1, MCZ and YSZ ceramic dielectrics, respectively.

Nevertheless, it is noted that alumina-based ceramic required higher input voltages to generate flow velocities, i.e., the micromanometer was only able to register data starting from input voltages in the range of 8 kVpp for MCZ and YSZ, and 11 kVpp for the MA1 and MA2. Worth noting that once the difference between the induced velocities for 7 kVpp and 8 kVpp of MCZ is practically negligible, 8 kVpp is referred to as a starting point voltage of evaluation and analysis.

On one hand, considering the overall evolution of MA1 and MA2 flow velocities – despite starting to produce similar flow velocities for 11 kVpp voltage – these become considerably different when increasing to 12 kVpp, in the sense that MA2 jumps to velocities in order of 2.0 m/s and tends to increase, whilst MA1 continue with much lower results, this is, below 1.0 m/s threshold. After 16 kVpp, MA1 achieves higher velocities but is still overall lower than the ones presented by the denser MA2 ceramic composite. On the other hand, taking into account the evolution of MCZ and YSZ, it is straightforward to infer that MCZ has a significantly nonuniform and unstable behavior. For voltages between 8 and 10 kVpp, MCZ induces lower velocities than YSZ. Nevertheless, at 11 kVpp this material achieves its maximum, after which it drops sharply. Similarly, to the alumina ceramics, YSZ starts to provide low velocities for low applied voltages, but after a particular value, in this case, 9 kVpp, this parameter rises considerably. The very filamentary discharge verified on the YSZ surface was considered a strong limitation factor to further proceed with additional tests for higher voltages.

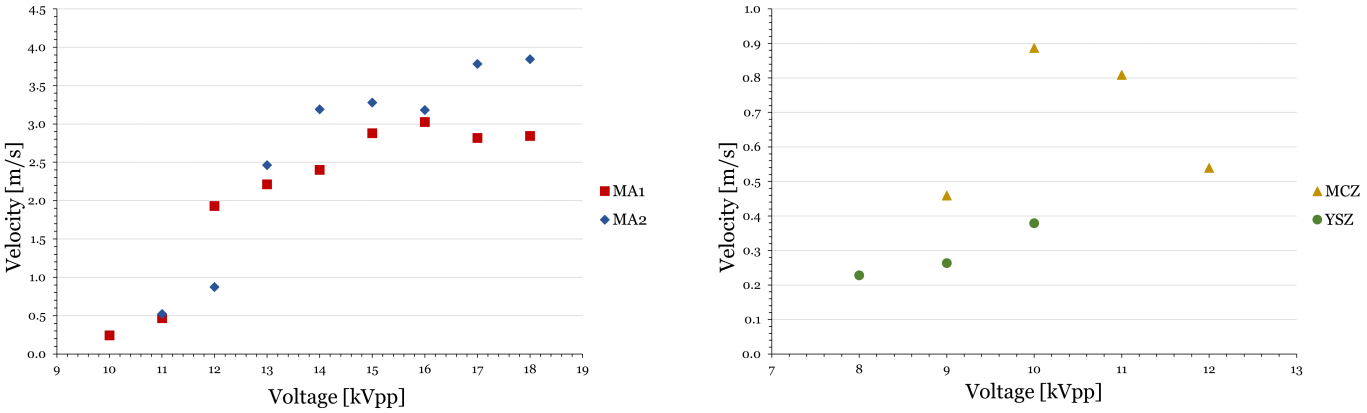

(a) Velocity of alumina–based ceramics.

(b) Velocity of zirconia–based ceramics.

Figure 5.36: Maximum induced flow velocity for alumina–based ceramics (a) and zirconia–based (b) with a distance between the exposed electrode and Pitot tube of 1.5 cm.

According to **Figure 5.36**, the following conclusions were driven for the 1.5 cm setup. MA2 alumina was once again the ceramic system that succeeded in inducing higher velocities, this is, approximately 3.8 m/s in comparison to the maximum achieved velocities of, about, 3.0 m/s, 0.90 m/s and 0.38 m/s by MA1, MCZ, and YSZ ceramic dielectrics, respectively.

In parallel to the results of the setup with 1.0 cm, higher voltages were necessary to apply to start recording any evidence of induced flow velocity for alumina ceramic composites than for MCZ or YSZ.

Similarly, to before, for the left side graph, MA1 and MA2 start to show analog results but generally, MA2 is able to achieve higher flow velocities than MA1 with the clear exception at 12 kVpp. For the right-side graph of **Figure 5.36**, MCZ and YSZ depict much divergent behaviors and values than in the 1.0 cm setup. In this configuration, contrary to the previous, MCZ tends to produce higher induced velocities than YSZ but still decreases after reaching its maximum. Once more, the very filamentary discharge observed on the YSZ dielectric surface was found a solid limitation factor to further rise the applied voltage.

Taking into consideration both **Figure 5.35** and **Figure 5.36** some further general conclusions are emphasized. Broadly speaking, despite the configuration analyzed, i.e., 1.0 cm and 1.5 cm, MA2 manifested to be the sintered ceramic composite that was able to supply the plasma actuator device with higher induced flow velocities. Therefore, it is possible to claim that, in view of active flow control focus, MA2 is the most efficient ceramic composite material. Furthermore, alumina-based ceramics were more efficient in the 1.5 cm arrangement, whilst zirconia-based ceramics tended to improve in the 1.0 cm layout.

Table 5.17: Maximum induced flow velocities for different dielectric materials sintered.

Ceramic Composite	**Maximum velocity** [m/s]	
	1.0 cm	**1.5 cm**
MA1	2.69	3.03
MA2	3.21	3.85
MCZ	2.42	0.89
YSZ	2.22	0.38

Ultimately, it must be highlighted that further investigation is suggested to better comprehend the MCZ and YSZ variations of induced flow velocities since very dissimilar behaviors were verified for these two ceramic composites. In greater detail, it is necessary to more clearly understand if YSZ ceramic composite is capable of supplying in a continuous manner increased flow velocities than MCZ or if the tendency inverts for higher applied voltages. In addition to ascertaining whether the efficiency of MCZ, from an active flow control perspective, improves with the increase of the distance from the exposed electrode. Further velocity profile construction of the flow induced by each DBD plasma actuator is namely advised once the maximum reached flow velocities may not be encountered at 1.5 mm in height (y–direction) position. Lastly, the higher input voltages necessary for the alumina-based ceramics in comparison to the zirconia ones may be justified by the sightless higher thickness of these samples. Since, as discussed in the literature [154, 163], this parameter (thickness) is strictly related to the input voltage recorded and has a strong influence on its magnitudes, this interdependency must be clarified and dissected.

5.5.4 Thermographic Analysis

The heating of a DBD plasma actuator is considered one of the limiting factors of the operation performance during the plasma discharge process. More precisely, the variation of electrical power consumed by the device with the voltage increase may be a trade-off with the dielectric heating power oscillation during the discharge phenomenon, since a significant part of the power consumed is dissipated in form of thermal energy [283, 284, 285].

To greater extend the fundamental knowledge of the thermal behavior of the different ceramic dielectric composites and, as consequence, the overall DBD actuator device, infrared dielectric surface thermographic measurements were made. It is essential to understand at this point that the plasma discharge is nonuniform and with characteristic filamentary regions (random oscillations in discharge filaments and their corresponding color intensity), and thus the emissivity of the plasma varies along the discharge area. In turn, it becomes impossible to obtain the plasma's temperature through infrared tech-

niques. On this basis, to acquire the temperature field of the plasma actuator, the temperature of the dielectric surface was considered. Considering that a surface of a body with its temperature above absolute zero, is capable of emitting electromagnetic radiation proportional to its inherent temperature, infrared thermography in quiescent air was conducted. Additionally, the infrared, i.e., thermographic images, were experimentally taken after an interval of time of operation of 300 s to ensure temperature stabilization as complete as possible.

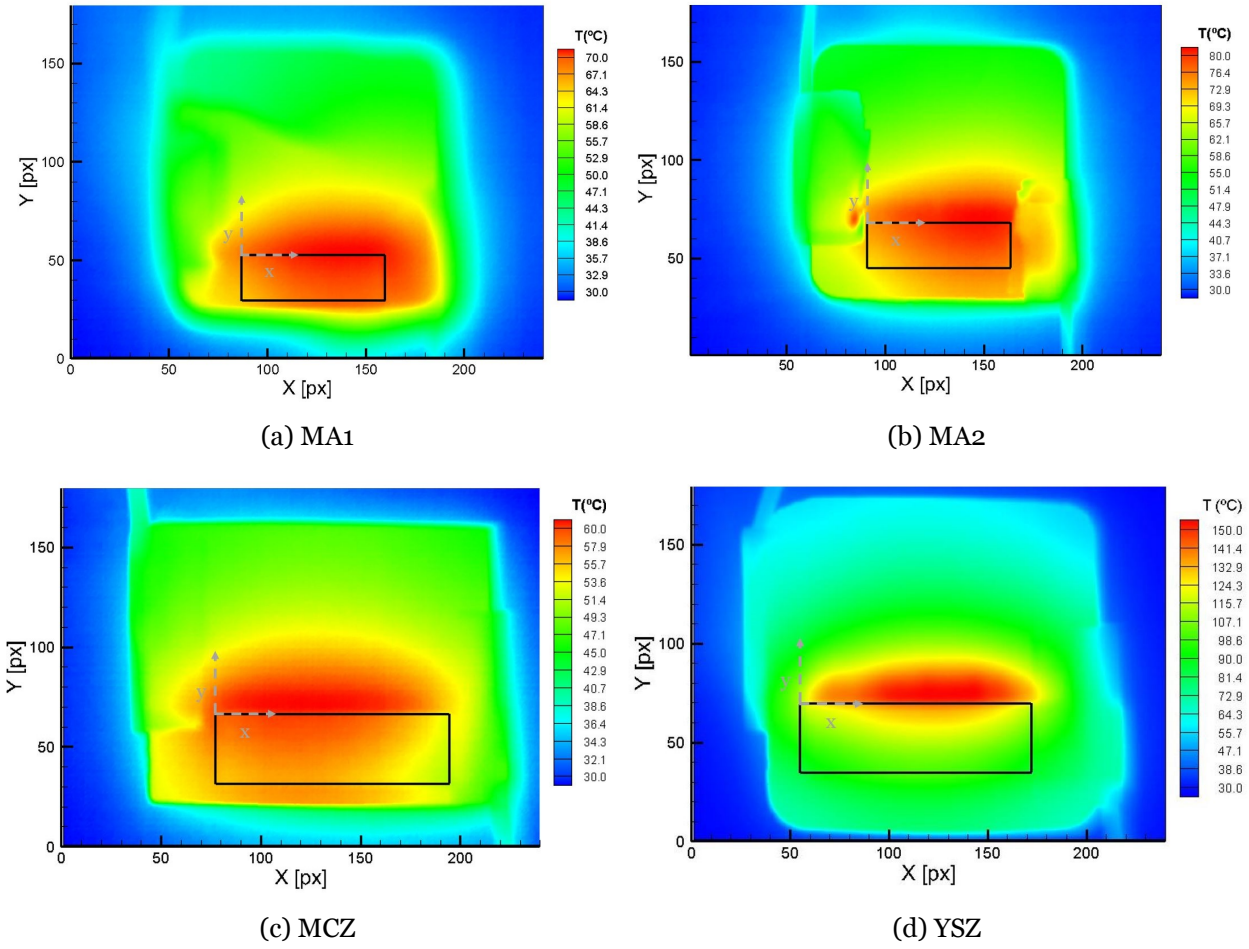

Figure 5.37: Thermographic (infra-red) images obtained for DBD plasma actuators with different dielectric materials: (a) MA1, (b) MA2, (c) MCZ and (d) YSZ.

Figure 5.37 shows the thermographic images captured during temperature effect examination on the plasma discharge for each ceramic composite acting as a dielectric barrier for the DBD plasma actuator. It is remarked that the delimited rectangle with a black line corresponds to the exposed electrode position and that the asymmetry direction of the electrodes is according to the positive direction of the y-direction illustrated referential. In **Figure 5.37**, the infrared images obtained of each ceramic composite manufactured are coincident with the *operating conditions for which the maximum induced flows were recorded* in the previously described efficiency tests for active flow control aim. More precisely, the thermographs of MA1, MA2, MCZ, and YSZ were taken for an input voltage of

16 kVpp, 18 kVpp, 11 kVpp and 10 kVpp, respectively, and a frequency of 24 kHz.

By analyzing **Figure 5.37**, it was concluded, first and foremost, that the temperature asymmetries and irregularities shown along both sides of the exposed electrodes are attributed to the effects of the connections of the electrode with the cables used in the mounted circuit, which tend to increase the temperature on their corresponding locations. Additionally, high discrepancies in terms of temperature magnitudes, i.e., maximum recorded temperatures for each ceramic system were noted. In other words, MCZ showed a lowest achieved maximum temperature near the edge of the exposed electrode of, approximately, 60 ºC, followed by MA1 and MA2 in the range of 70º C and 80 ºC. Lastly, it is highlighted that YSZ ceramic composite evidenced the considerably higher maximum ceiling value of 150 ºC. The discrepancies verified in the temperature fields may be justified by several factors, such as dielectric thicknesses, dielectric permittivity, and, above all, particular dielectric material thermal properties. It must be contextualized that, although the direct influence of the dielectrics' thickness was *a priori* undertaken as a firmly influencing factor, the sintering process and, furthermore, the shrinkage phenomenon dictated the final achieved geometrical properties of the samples. A common parameter considered was the total mass of 40 g used in the die uniaxial pressing of the specimens. Additionally, it is strongly emphasized that the order of the maximum temperature achieved depicted by **Figure 5.37** is not coincident with the power consumption order indicated by **Figure 5.27** since, as previously explained, the infrared images shown are corresponding to the operating conditions in which the maximum induced flow velocities were recorded, i.e., 16 kV (MA1), 18 kV (MA2), 11 kV (MCZ), and 10 kV (YSZ).

The temperature fields of the different ceramic dielectrics showed dissimilarities in function of the dielectric material. In detail, the YSZ temperature distribution field was much more concentrated than of the rest of the materials. Contrastingly, MCZ depicted the vastest and broadly distributed temperature levels across the dielectric surface. MA1 and MA2 – in spite of the connector cables interference – had somehow identical temperature levels dispersal. In addition, it is remarked that the highest temperatures in the YSZ material were mainly recorded at the edge of the exposed electrode (its frontal region), whilst for the remaining ceramic materials, it was more dispersed around the edge's area. The rate of spread of temperature across the ceramic samples described above is consistent to the thermal diffusivity results discussed in the Thermal Analysis 5.4. As **Figure 5.23** depicts, MCZ and MA2 ceramic systems are more prone to spread heat energy through the specimen than the YSZ composite.

On top of the presented, an analysis of the spatial temperature variation along the $x-$ and $y-$axis follows below.

As previously stated, part of the applied power is converted in the generation of flow velocities, whereas the remaining part is dissipated in the form of heat. Therefore, the dielectrics that registered a higher electrical power consumption tendentially will be the ceramic composites which dissipate the higher amount of energy in the form of heat, that, in turn, increases the overall temperature of their surfaces. The exposed above is parallel and concordant to the discussion provided about the power consumption tendencies in **Figure 5.27**. In the following analysis, as expected, YSZ which has a higher maximum temperature level achieved of almost 150 ºC, had also an abrupt rise in power consumed, pursued then by the MCZ, MA2, and, finally, MA1 ceramics that has the slowest increase rate of power consumption with the increase of applied voltages. Even more interestingly, it is noted that this sequence of the maximum temperature achieved by YSZ, MCZ, and MA2 ceramic composite is concordant to the study performed of the specifc heat variation in the Thermal Analysis 5.4. More precisely, as was ascertain through **Figure 5.22**, YSZ requires a lesser amount of heat to raise its temperature than MCZ, which, in turn, needs an even reduced one than MA2.

Figure 5.38 represents the spatial variation of the temperature along the $x-$axis for the alumina-based ceramics sintered, i.e., MA1 and MA2, between $x/l = -0.2$ and $x/l = 1.2$. In this section, l is the length of the exposed electrodes, whereas $0 < x/l < 1$ is their frontal region. The extended interval of [-0.2; 1.2] was adopted to accomplish a completer and more comprehensive investigation of the $x-$axis spatial temperature variation. Once again, it should be noted that part of the total test cases (applied voltages) is shown below for graphics interpretation easing purposes.

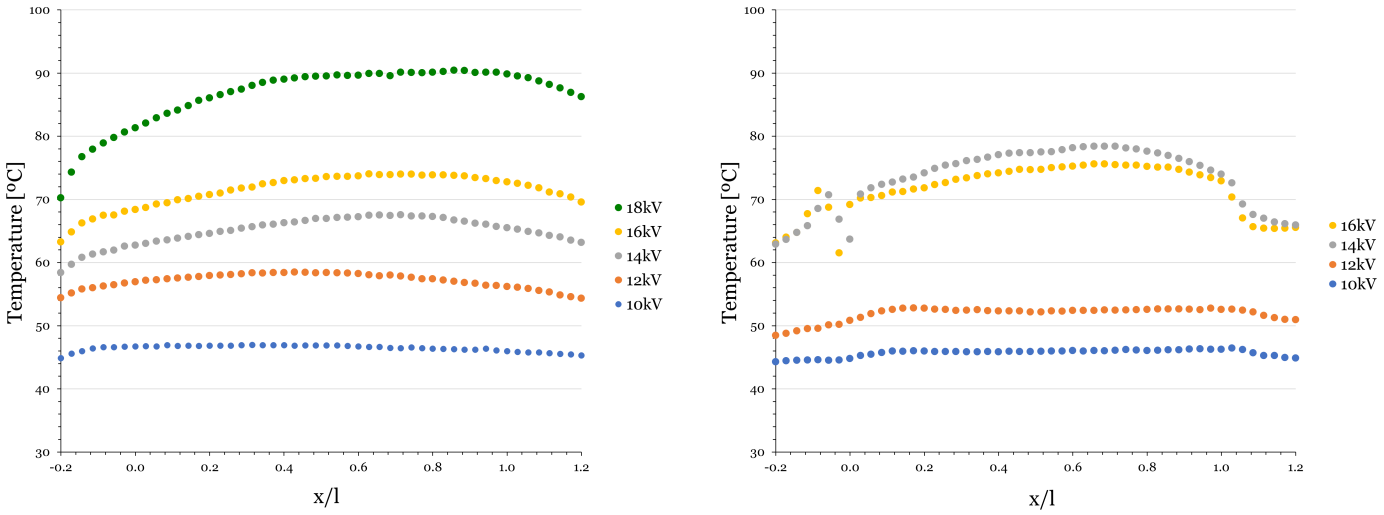

(a) MA1 spatial temperature variation along the $x-$axis.

(b) MA2 spatial temperature variation along the $x-$axis.

Figure 5.38: Spatial temperature variation along the $x-$axis for MA1 (a) and MA2 (b) ceramic composites.

The temperature variations along the $x-$axis were analyzed on the adjacent points of the exposed electrode edge, which is considered to be the region where the maximum tem-

perature levels are located. For alumina-based ceramics, and owing to **Figure 5.38**, it is possible to infer that – for the same applied *low-level* voltage values of 10 kV and 12 kV – the temperature distribution across x–axis presented similar behaviors. More specifically, the temperature magnitudes were distinctly stable. The main difference that stands out between the MA1 and MA2 ceramics – for 12 kV case study – is in the maximum temperature achieved was slightly lower for MA2 (up to, approximately, 54 ºC) than for MA1 (up to, approximately, 60 ºC).

Furthermore, for the same applied *high-level* voltage values of 14 kV and 16 kV trenchant differences are remarked in the temperature variation profiles of MA1 and MA2. In other words, curiously enough, for 16 kV, MA1 ceramic achieved higher temperatures (approximately, 74 ºC) whereas this was not verified for the denser MA2 material that achieved contrastingly higher temperatures for 14 kV (approximately, 78 ºC).

Additionally, and as stated previously, the same vast applied voltage range was not possible to test in every ceramic composite sample due to their diverse limiting capacity in a plasma discharge. In detail, some ceramics showed unstable filamentary behavior much sooner than others. This is the reason behind the fact that the analysis of MA1 was further extended to 18 kV and MA2 stayed at a maximum of 16 kV. On top of this, MA2 temperature profile depicted a relatively slightly more pronounced variation modification in temperature levels from distances of x/l in the ranges of [-0.2; 0.0] and [1.0; 1.2]. This ceramic composite (MA2) exhibit namely scattered values for x/l of [-0.08; 0.04]. The visualized phenomenon is justified by the progressive degradation –with the application of higher voltages of the several tests conducted – of the Kapton tape that was used to fix, glue and electrically insulate the connection cables of the circuit mounted to the dielectric material, as illustrated on **Figures 4.19** and **4.23**.

Lastly, in **Figure 5.38**, both left and right side plots do not have incident fluctuations along the temperature profiles which may be created by the nonuniformity of the plasma distribution across the actuator. These irregularities (nonuniformities) caused by hot spots, that are usually observable in the filamentary plasma discharge for higher voltages, are steep spikes that indicate that plasma is close to the limit of the dielectric material. To reinforce, these particularities were not found on these temperature profiles, but are commonly present in other dielectric materials investigations, such as, for example, Kapton, PLA (polylactic acid), and PIB (poly-isobutylene) rubbers [141, 283].

Figure 5.39 represents the spatial variation of the temperature along the x–axis for the zirconia-based ceramics sintered, i.e., MCZ and YSZ, between $x/l = -0.2$ and $x/l = 1.2$. Once again, l is the length of the exposed electrodes, whereas $0 < x/l < 1$ is their frontal region. The extended interval of [-0.2; 1.2] was also adopted to accomplish a wholly and more proper investigation of the x-axis spatial temperature variation. Similarly, solely

part of the total test cases (applied voltages) is shown below to ease the graphics reading.

As previously stated, the temperature variations along the x-axis were analyzed on the adjacent points of the exposed electrode edge, which is considered to be the region where the maximum temperature levels are located. For zirconia-based ceramics, and through **Figure 5.39** interpretation, it is possible to infer that – for the same applied *low-level* voltage values of 8 kV and 9 kV– the temperature distribution across x-axis presented alike behaviors. More specifically, the temperature magnitudes were quite stable. However, for a higher input voltage of 10 kV (and 11 kV for MCZ) a significant change can be observed for the YSZ ceramic when compared to the smooth MCZ's temperature profile variation. In terms of maximum achieved temperatures, MCZ ceramic slightly surpasses 60 °C, whereas YSZ reaches over 150 °C. Additionally, YSZ had profound dissimilarity between the temperature of electrode's frontal central region ($0.2 < x/l < 0.8$) and its edges ($-0.2 < x/l < 1$ and $1 < x/l < 1.2$).

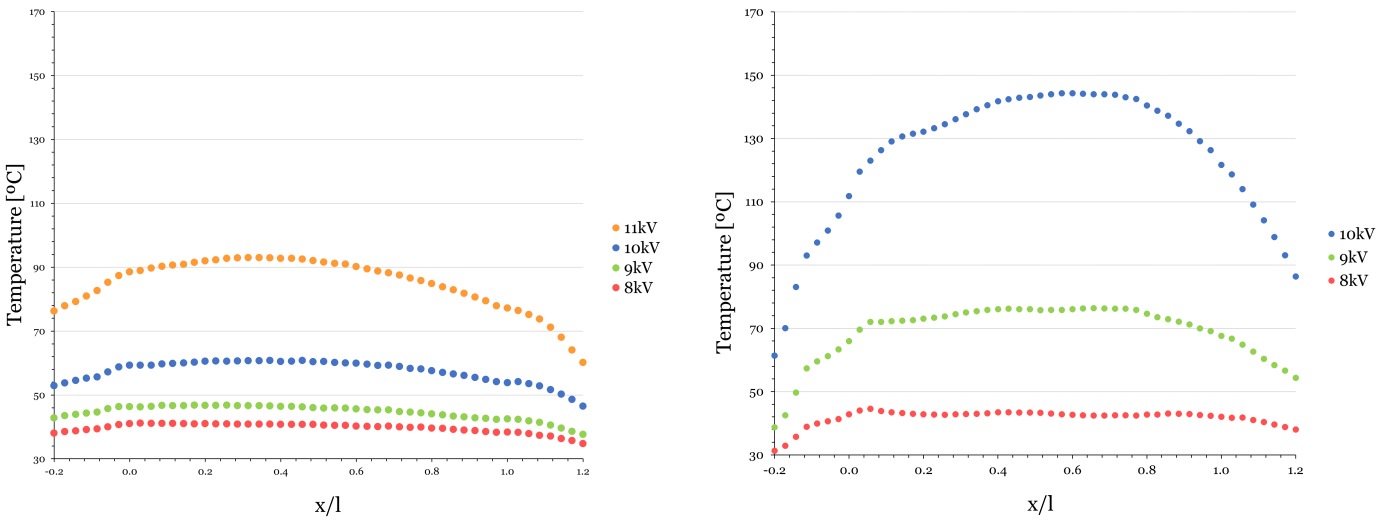

(a) MCZ spatial temperature variation along the x–axis.

(b) YSZ spatial temperature variation along the x–axis.

Figure 5.39: Spatial temperature variation along the x–axis for MCZ (a) and YSZ (b) ceramic composites.

Moreover, and as stated previously for alumina ceramic, an equally broad applied voltage range was not possible to test both enunciated zirconia-based ceramic composite specimens due to their diverse limiting capacity in plasma discharge. This is to say that YSZ showed an unstable and remarkably filamentary behavior much sooner than MCZ.

Lastly, in **Figure 5.39**, as well as in previous **Figure 5.38** no evidence of nonuniformities caused by hot spots – that are usually observable in the filamentary plasma discharge for higher voltages for the state-of-art polymers – were recorded in the form of sharp oscillation in the temperature profile along the x–axis.

Figure 5.40 depicts the spatial variation of the temperature across the y–axis (perpendicularly to the exposed electrode length, i.e., outwards) for the *alumina-based* sintered ceramics, i.e., MA1 and MA2, between $y/w = 0.0$ and $y/w = 2.5$. In this section, w is the width of the exposed electrodes. As before, it should be remarked that just part of the total test cases (applied voltages) is shown below for clear and objective graphics reading purposes.

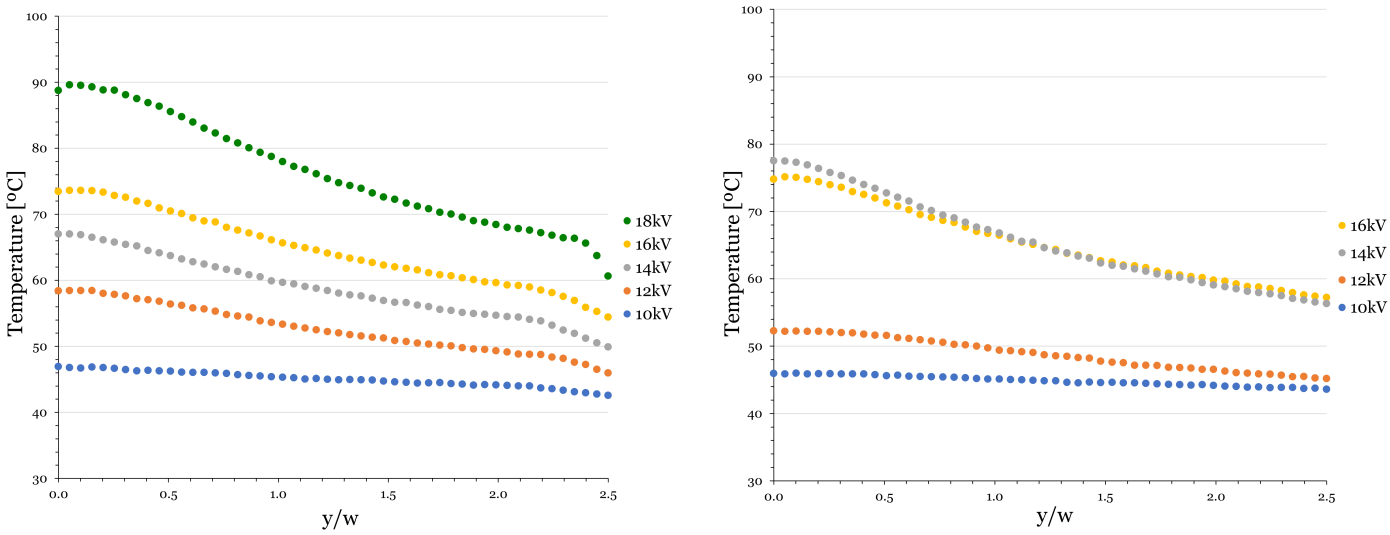

(a) MA1 spatial temperature variation along the y–axis.

(b) MA2 spatial temperature variation along the y–axis.

Figure 5.40: Spatial temperature variation along the y–axis for MA1 (a) and MA2 (b) ceramic composites.

From the experimental tests performed, **Figure 5.40**, allows to infer that along the y-axis, the temperature recorded was higher, more or less, near the exposed electrode edge, i.e., $y/w = 0.0$, in the onset of plasma discharge formation. A very little increase in temperature however is noted for y/w marginally over the start of the axis reference, i.e., for $0.0 < y/w < 0.2$ interval. This rise in temperature across the y-axis is especially verified for higher voltages applied for both MA1 and MA2 materials. Additionally, for MA1 after $y/w > 2.2$, a (to a certain degree) steeped decrease in temperature is observed.

Figure 5.41 represents the spatial variation of the temperature across the y-axis (perpendicularly to the exposed electrode length, i.e., outwards) for the *zirconia-based* sintered ceramics, i.e., MCZ and YSZ, between $y/w = 0.0$ and $y/w = 2.5$. In this section, as stated before for **Figure 5.40**, w is the width of the exposed electrodes. Once more, it should be remarked that just part of the total test cases (applied voltages) is shown below for graphics interpretation easing purposes.

Resembling behavior to the one described based on **Figure 5.40** for MA1 and MA2 ceramic may be detected in **Figure 5.41** for MCZ and YSZ samples as well. This is to say that the maximum verified temperature was measured near the onset of the edge of the

exposed electrode. The main dissimilarity between the alumina-based ceramics and the zirconia ones, is that the latest had a much more pronounced increase (than MA1 and MA2) in temperature for a little increased interval distance outwards the exposed electrode, i.e., of, approximately, $0.0 < y/w < 0.3$.

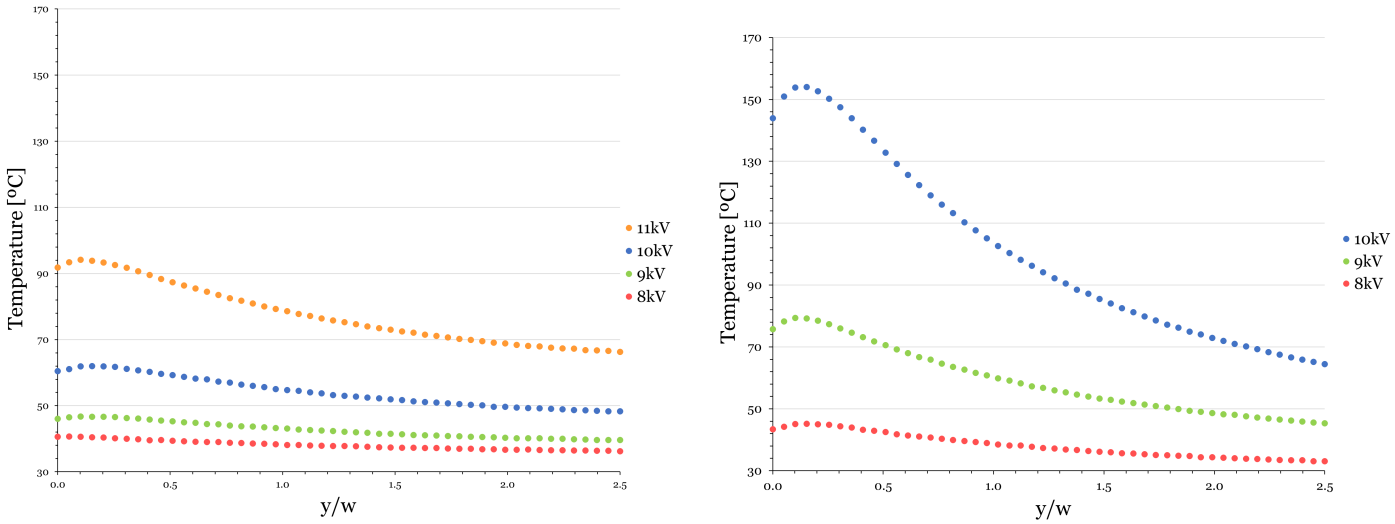

(a) MCZ spatial temperature variation along the y–axis.

(b) YSZ spatial temperature variation along the y–axis.

Figure 5.41: Spatial temperature variation along the y–axis for MCZ (a) and YSZ (b) ceramic composites.

As a last remark, the ceiling temperatures for both x–axis and y–axis spatial analyses of each ceramic composite case were very alike, i.e., for the highest applied voltage tested of 18 kV for MA1, the maximum temperature reached at x– and y–directions were of, approximately, 90 °C; for MA2 at 16 kV, the maximum temperature recorded as well in both directions was of, approximately, 80 °C; afterward, for 11 kV of the MCZ material a top value was of, more or less, 95 °C; and lastly, YSZ recorded the highest maximum temperature in both axis studies in a range varying from, approximately, 150 °C to 160 °C.

Although not part of the initial scope of the investigation aimed to be conducted in the electrical analysis section presented throughout this subchapter, it is extremely compelling to present the following obtained phenomenon. Last tests performed on YSZ ceramic material induced a major crack on the sample exploited. The subsequent **Figure 5.44** displays the YSZa (first YSZ sample tested) specimen's crack profile, as well as the location of the exposed electrode that burnt. As a consequence, another ceramic plate was fabricated from the original powder mixture. Notably, after being subject to the whole round of tests described throughout this subchapter, the second sample YSZb (second YSZ sample tested) fractured as well in a *very identical way*.

It is emphasized that YSZ was the only ceramic composite produced, aimed to act as a dielectric for DBD plasma actuator, that fractured. Moreover, both YSZ samples, i.e., YSZa

and YSZb, cracked in the same way. In other words, the fracture along the ceramic had a very alike profile in which the crack "points" to the electrode's burning location. It is believed and supposed that the breakage of the yttria-stabilized zirconia can be justified through the linkage of its microstructural, physical, electrical, and thermal properties.

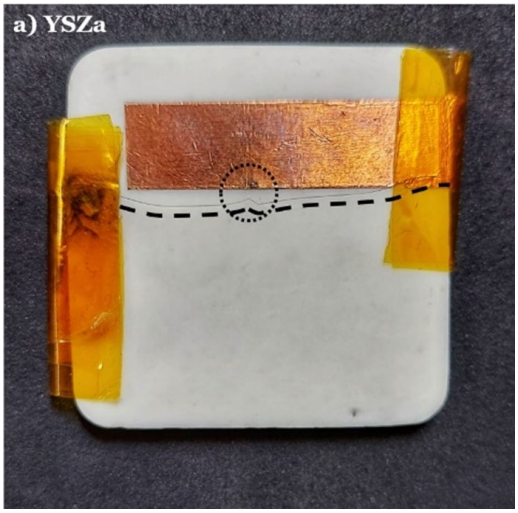

Figure 5.42: YSZa sample after fracture, crack profile (dashed black line), and electrode's burn location (encapsulated in dashed black circle).

The following **Figure 5.43** shows the second YSZb ceramic composite specimen, equally, fractured.

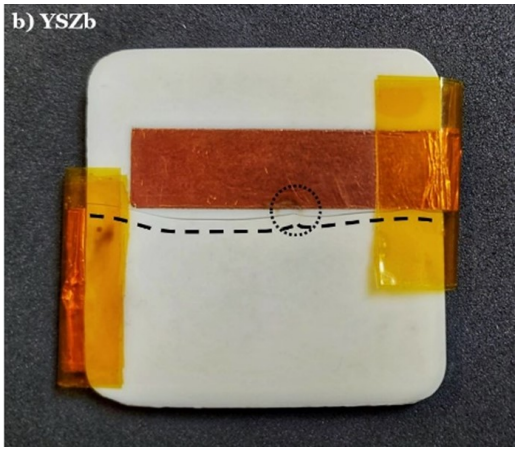

Figure 5.43: YSZb sample after fracture, crack profile (dashed black line), and electrode's burn location (encapsulated in dashed black circle).

As announced in Microstructural Analysis, both SEM imaging as well as PSD tests allowed to conclude that YSZ was a ceramic composite that exhibited a very small particles size, and consequently, was the material with a very high shrinkage percentage, which, in turn, translated into low porosity. The low porosity of the bulk YSZ ceramic made it extremely dense, i.e., compact. Once the material does not possess empty voids or pores, the material grains are the ones responsible for withstanding all the electrical, thermal, and

mechanical interferences related to the plasma discharge process. Regarding the electrical properties of YSZ, Lanagan M. T. et al. (1989) [286] reported that with the increase of yttria content of the yttria-doped zirconia material, both dielectric constant and dielectric loss parameters increased. Once, the dielectric constant (related to the ability of the dielectric that is acting as an insulating material to store electrical energy) and the dielectric loss (associated with the loss of the overall input energy to the circuit in the form of heat) increase, this means that the YSZ not only is responsible for storing the electrical energy in the electric field generated to obtain the plasma discharge, but it also loses a considerable amount of the provided power in form of thermal energy that heats the dielectric surface. Furthermore, bearing in mind this temperature rise of the ceramic, both relatively *high thermal expansion coefficient* (approximately, $10.0 \times 10^{-6}/^{o}C$) [287] and *low thermal conductivity* (2.2–2.9 W/(m K)) [270] condition limit the material's response to the cyclic imposed harsh environmental thermal conditions.

In greater detail, ceramic like yttria-stabilized zirconia (YSZ) is solid-state crystalline materials in which the crystal structure of zirconium dioxide is stabilized at room temperature by addition of yttrium oxide (Y_2O_3). The addition of Y_2O_3 into intrinsic ZrO_2 (both crystalline) substitutes Zr^{4+} ions with Y^{3+} ions within the lattice. This process produces anionic vacancies where three O^{2-} ions replace four O^{2-} ions. Thus, YSZ is able to conduct O^{2-} ions (electrical current) by means of vacancy site mobility, a property that increases with temperature. This ability to conduct O^{2-} ions is what makes YSZ a potential material to be used as solid electrolyte in energy cells, i.e., solid oxide fuel cells (SOFC) and solid oxide electrolysis cells (SOEC), usually in form of thin films [288, 289].

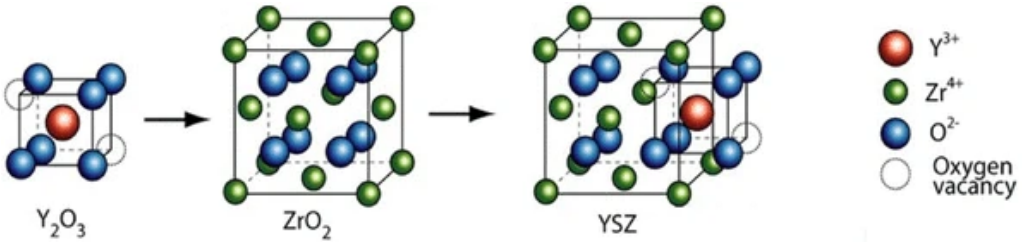

Figure 5.44: Illustration of oxygen vacancy formation in YSZ after addition of Y_2O_3 into ZrO_2 [288].

Moreover, the development of cracks in ceramics could be due to stresses remaining in the sample as consequence of the manufacture process, such us microcracking, strain contours, and nanoporosity. However, due to exposure to high electrical current density, as in flash sintering, the bibliography also reports common degradation in YSZ. Typically, the flash, and consequently the first microstructural defect, starts from the anode side but soon the entire section between the two electrodes is noted to lit up to red hot. The electrode protrusion is a field/current concentrator, it often initiated the flash [289, 290].

The first defect is reported near of the negative electrode as grain boundary cracking and spherical “dimpling” of the internal grain bulk structure was observed from a transgranular fracture. This morphology suggests a plastic-like behavior of the ceramic during the flash that remains locked into the microstructure after quenching by turning off the electric field [289].

From the micromechanical point of view, in YSZ ceramic composition with a greater fraction of the cubic and tetragonal phases, compared to the classic 8YSZ, the resistance to crack propagation provided by the deformation absorption capacity of the monoclinic phase, due to the martensitic transformation of the tetragonal phase into monoclinic, is not sufficient to withstand the variations in thermal expansion generated by the electric current [291].

Thereby, all combined, i.e., dense YSZ bulk ceramic, with an accumulated electrical field and considerably heated surface – **Figures 5.37**, **5.39** and **5.41** – lead to profound degradation of this ceramic composite. As an ultimate result, extensive spalling, and major longitudinal crack on the YSZ (a and b) specimens took place.

To conclude this section, and from a general point of view, a dielectric barrier in the atmospheric pressure discharge has two main functions. First and foremost, the dielectric barrier material limits the amount of charge transported by a single microdischarge; furthermore, it distributes the microdischarges over the total area of the electrode [292]. Commonly found in the literature, investigations with Kapton tape, which may be comprised of alternating layers of polyimide film and silicone adhesive, are applied as a dielectric of plasma actuators for asymmetric surface DBD geometry aimed to be applied in aerodynamic research regarding active flow control. Even though this approach is reported and proven to work, it has several limitations, including discrete thickness handling difficulties, partial discharge between layers, and, more markedly, material rapid degradation.

Consequently, ceramic dielectric appears as an excellent candidate (when compared to the widely and commonly used polymer dielectrics), due to their overall favorable properties. For instance, their physical stability, chemical inertness, low and high-temperature resistance, and insulative to conductive electrical properties turn them into a great candidate for this – DBD plasma actuators – category of application [154].

Considering all the parameters investigated, studied, analyzed, and reported throughout this section, it is possible to say with a high degree of confidence that, in general, DBD plasma actuator are *quite complex* and *sensible* devices. This may be foreseeable as follows: a special focus shall be given to the fact that the history of a DBD plasma actuator discharge is heavily reliant on various factors. These factors may be the *geometry and setup of the actuator* (position and number of both electrode and dielectric); *elec-*

trode's shape, size, gap distance; *dielectric's* material (chemical composition in addition to microstructural and physical properties), thickness, dielectric properties, among others. The *environmental conditions* – room temperature, humidity, pressure, and ambient gas composition – namely have an impact on the performance of these devices.

By virtue of the electrical, mechanical and thermal vast research performed on the ceramic samples sintered – MA1, MA2, MCZ and YSZ – through their implementation as DBD plasma actuators devices, it was not only possible to prove that these ceramics are plausible candidates as dielectrics materials since plasma discharge was achieved, but also showed favorable results. In greater detail, as expected, ceramic dielectrics showed much higher longevity than some polymeric dielectrics applied to this end. Furthermore, solely one material (YSZ) suffered a longitudinal crack at the end of the whole cycle of tests, whilst the others (MA1, MA2, MCZ) remained intact.

Moreover, to ascertain the efficiency of these ceramic composites as dielectrics for aerodynamic active flow control, induced flow velocities recorded were found to not lag behind from reported induced flow velocities of, for instance, remarkably tested, Kapton tape.

On top of that, besides their electrical features, thermal properties and data results of MA1, MA2, MCZ and YSZ ceramic composites, are believed to be an indicator of their ability to offer a reasonable solution for the recent trends of DBD plasma actuators applications for de- and anti-acing purposes. In other words, to take advantage of the heating phenomenon of the DBD plasma actuators – considered a limiting factor of plasma actuators technology – ceramic dielectrics could be evaluated for both high and low-temperature thermal protection systems, and this could be an interesting path of research to explore in the future.

Correspondingly, further research and investigation are forecast to be vital to answering some of the questions raised thanks to the extensive work already undertaken and fully reported.

Chapter 6

Conclusions and Future Perspectives

6.1 Conclusions

The premise that materials permeate all aspects of our day–a–day lives is well established. At present, in material science and engineering, among the major classes of existing materials, the advanced ceramics field is believed to be an enabling technology with the potential to deliver high-value contributions for meeting both future needs and challenges. Moreover, the advanced ceramics industry is quite distinctive due to its high diversity and interdisciplinary nature that encompasses an engaging number of different processing methodologies and a variety of applications.

Particularly, the relentless pursuit for increased performance in aeronautical and aero–space industries over the years has provided a solid driving force for the study, research, and investigation of fine ceramics for several future investments. It can be naturally justified and foreseen due to these materials' ability to accomplish an attractive, extreme, and distinguished arrangement of thermomechanical, thermoelectric, and electromechanical properties.

Within this framework of thought, this dissertation project focused on the concept of multifunctional advanced ceramic material systems that can be adapted to a multitude of requirements. Therefore, an extensive and comprehensive review of thermal protection systems, thermal barrier coatings, and dielectric barrier discharges was perceived and adopted as a jumping-off point. Fundamental knowledge was acquired regarding the current challenges pertaining to TPS, TBC, and DBD fields in parallel to the window of opportunity scrutiny for advanced ceramics in each of the announced applications.

Thereafter, once the research task was considered satisfactory to proceed, three ceramic compositions – $MgO-Al_2O_3$, $MgO-CaZrO_3$, and YSZ – were chosen to be objects of extensive investigation and, thus, the experimental phase took place. For the sake of completeness and to recall, the selection was made in the sense that, whenever possible, one of the functions of each candidate ceramic system was grounded on their nowadays state-of-art usage, the second employment consisted of an alternative one according to the literature revision, and, lastly, the third and remaining application, served as a suggestion and target of further assessment study.

Within the experimental procedure, a step-by–step approach was adopted. Primarily, $MgO-Al_2O_3$, $MgO-CaZrO_3$, and YSZ ceramic composite samples were manufactured via a four stages process, i.e., material preparation, processing, sintering, and finishing. After the rectangular plates, bars, and disc specimens were obtained for the three referred compositions, the in–depth study under the microstructural, physical, mechanical, thermal, and electrical characterization followed. Accordingly, the following conclusions were established.

One of the most common and well–known use cases for high-performance ceramics in aeronautical and aerospace sectors is as part of the thermal protection systems and thermal barrier coatings. On one hand, thermal protection systems play a crucial role as they are single-point-failure systems that work above all as thermal shields from severe aerothermodynamic heating, but namely as structural components and aerodynamic bodies in aviation and rocketry. The thermal protection systems of the next generation must offer a combination of suitable properties, among them a high melting point, high impact resistance, ability to withstand radiative heating, high ablation resistance, superior oxidation resistance, high fracture toughness, high–temperature strength, and low to moderate thermal conductivity. On the other hand, thermal barrier coatings systems are generally explored to enhance energy durability and therefore efficiency of hot components of aeroengines, gas turbines, and part of combustion power plants. Within the TBC structure, the ceramic top layer provides thermal protection to the metallic bond coat and substrate, in addition to strain tolerance, and thermal shock resistance. Consequently, to decrease particularly the temperature of the superalloy substrate material, the top coat shall have very high mechanical strength, wear, erosion impact, corrosion, and chemical resistance, as well as very low thermal conductivity, and a relatively high coefficient of thermal expansion. This way, microstructural and physical analysis come to the fore accompanied by mechanical and thermal studies.

The microstructure analysis allied to the physical properties assessment remarked that many specific features of ceramics depend critically on the manufacturing conditions, including grain size, and purity of the material, in addition to apparent porosity and relative density. The particle size distribution test which consists of a quality assessment tool parameter, allowed to infer through number–weighting and volume weighting analysis that the YSZ sample showed a highly homogeneous composition, whereas $Mg-CaZrO_3$ tended to contain some occasional bigger particles. Contrastingly, $Mg-CaZrO_3$ samples evidenced higher than expected particle sizes. Therefore, a second MA2 mixture with a doubled milling interval time (6 h), when compared to the first one (MA1), was produced. The adopted process was considered successful since it diminished the overall size of the MA2 mixture. The data read in the PSD results were consolidated by the SEM imaging which revealed the presence of pores in alumina micrographs that induced the conclusion that incomplete densification during sintering processes was carried out. With the XRD

patterns, the crystalline phases of the composites under research were identified and confirmation was secured about the chemical composition of the specimens. Furthermore, physical properties investigation through diametrical linear shrinkage, apparent porosity, as well as relative density, allowed to surmise the following. The sintering process, which is primarily responsible for the achievement of the final dimensions of ceramics lead to an increased shrinkage of the YSZ (27 %) sample, followed by Mg−$CaZrO_3$ (24 %), and this, in turn, by MA2 (13 %). Additionally, apparent porosity data reinforced the expected, this is, the MA1 sample was the sample with the highest degree of porosity (35 %). Considerably improved porosity results, i.e., much decreased values were obtained for MA2 (7 %), MCZ (0.04 %) and YSZ (0.2 %) specimens. The relative density reflected the porosity data, i.e., the ratio between bulk and theoretically computed densities was, approximately, 63 % (MA1), 71 % (MA2), 99.95 % (MCZ), and 97.95 (YSZ). Thus, it is highlighted that the primary properties of ceramic systems – apparent porosity and relative density – were in line. On the whole, it is remarked that naturally the overall performance of an engineering structure, or component, that the ceramic composites studied may integrate is directly influenced by their microstructural and physical characteristics.

From a scientific field perspective, this is, both functional and structural ceramics possess mechanical properties of fundamental importance. More accurately, among many features, ceramics stand out due to their high hardness, high wear, fatigue, and corrosion resistance. Nevertheless, a significant predisposition to brittle fraction and low endurance limits – when compared to metal and engineering plastics – strongly condition their performance. Thereby, the mechanical characterization followed the microstructural and physical studies. The mechanical assessment of fabricated ceramics was achieved through dynamic Young's modulus, dynamic shear modulus, flexural strength, hardness, and fracture toughness. For the dynamic Young's and shear modulus, satisfactory results were obtained and considered congruent with the reported by the literature. As expected MA1 and MA2 composites showed inconsistencies due to the high and relatively high, respectively, porosity content. Notwithstanding, by adopting existing models for ceramic materials dedicated to the estimation of the porosity impact on these properties, it was proved that the experimental results acquired were reasonable. For the flexural strength parameter, the experimental figures are concordant with the reported by the bibliography, even for alumina–based ceramics specimens with their respective porosities. Lastly, considering hardness property, as expected, alumina ceramic samples did not represent an accurate reflection of their true potential due to the incomplete sintering and, therefore, not fully compact bulk ceramic. Both MCZ and YSZ reported data values foreseen and agreeable with other studies and investigations. Curiously enough, fracture toughness figures were coincident with the intervals mentioned in the literature for the three ceramic systems under study. It is remarked that in hardness and fracture toughness tests MA1 sample was not considered once the vast porosity filling beneath the loaded indenter heavily compromised these parameters examination.

The assessment of thermal properties of ceramic composites is of utmost importance given the critical role that fine ceramics have and continue to play in all aspects of energy storage, distribution, conservation, and efficiency via thermal insulation and environmental stability means. The study of thermal properties of the MA2, MCZ, and YSZ ceramic composites was done through the thermal conductivity (from 30°C to 700 °C temperature range) and coefficient of thermal expansion parameters (from -100 °C to 980 °C temperature range). It is remarked that typically, low (negative) temperature ranges are not studied for the coefficient of thermal expansion. Nevertheless, considering the aeronautical and aerospace applications, in which engineering structures are prone to both negative (low), and positive (high) temperatures, as well as temperature strong oscillations, it is believed that the test undertaken adds significant value to the scientific community. In short, MA2 ceramic had lower thermal conductivity figures than expected due to the porosity of 7 %, whereas zirconia–based ones were in line and therefore congruent with the exposed in the literature. Contrastingly, experimentally obtained data for the coefficient of thermal expansion was consistent with the reported investigations in the bibliography. All in all, it is highlighted that the comprehension of thermal properties of ceramic composites is believed to be compulsory due to the extremely demanding application they are tailored to in low–, room– and high-temperature regimes.

Over the last years, plasma actuators based on the dielectric barrier discharge mechanism have attracted much attention for aeronautical and aerospace applications. Broadly, the DBD plasma actuators may be applied in conducting research regarding aerodynamic active flow and heat transfer purposes. DBD plasma actuators' performance may be predominantly considered in terms of their three major features, i.e., their electrical parameters, the geometry chosen, and material properties. One of the major weaknesses of these devices is their longevity due to degradation or even premature electric breakdown phenomena. Studies in the literature focus their research mainly on polymeric dielectric barriers. Nevertheless, polymers are reported to be susceptible to material degradation or even burnout. As a result, ceramics appear a suitable substitute for the widely applied polymers, since this type of material offers several superior traits such as corrosion resistance, high- and low-temperature resistance, and excellent dielectric properties. Within this train of thought, an experimental study was conducted regarding the feasibility of the different materials manufactured – MA1, MA2, MCZ, and YSZ – as dielectric barriers for DBD plasma actuators. To start, the electrical analysis composed of the average power consumption, the Lissajous curves, as well as the capacitance variance were tested and examined via Electric Current Method and Electric Charge Method. The experimental data acquired through Electric Current Method allowed inferring that alumina–based ceramic had a higher operating limit (18 kVpp) than both MCZ (12 kVpp) and YSZ (10 kVpp). Additionally, Lissajous figures, known as voltage-charge cyclograms, were computed. On the whole, Lissajous cyclograms allow ascertaining the power consumed by the

actuators per cycle by computing the area inside a particular closed curve. On this basis, it is possible to state that both methods applied were consistent. In other words, the YSZ ceramic composite that showed a wider cyclogram (with an increased enclosed area) was the material that had also a sharper increase in power consumption, followed by MCZ, MA2, and MA1 ceramic systems. Afterward, a trade-off between the distance of the Pitot tube to the edge of the exposed dielectric and the maximum velocity in the function of the applied voltage achieved was performed for induced flow velocity study purposes. Interestingly, alumina–based ceramics were capable of achieving higher induced flow velocities than zirconia–based ones for the two setups studied, i.e., 1.0 cm and 1.5 cm between the Pitot tube and the exposed electrode. Moreover, in the view of active flow control focus, MA2 specifically, was the most efficient material once it achieved velocities of 3.85 m/s. Finally, thermographic images were taken during the plasma discharge useful to infer the properties of the discharge and its implication on the performance of the DBD actuators. Additionally, to the infra-red pictures, the variations of temperature along the x– and y–directions across the dielectric material were conducted. Worth noting that part of the applied power to the DBD devices is converted in the generation of flow velocities, whereas the remaining amount is dissipated in the form of heat. Through the variations of temperature along the x– and y–directions, it was remarked that the ceramic system with higher power consumption was the one with higher surface temperature achieved. This is, YSZ was the ceramic that heated the most, i.e., achieved the highest surface temperatures, followed by MCZ, MA2, and MA1 ceramics just as in the power consumption sequence.

To conclude, many fine ceramics are multifunctional and therefore predestined to solve the forthcoming technological and engineering challenges. It is believed that ceramic composites offer an enormous potential to be exploited with the knowledge of material science, i.e., through correlations between microstructural, physical, mechanical, thermal, and electrical features. Future needs and requirements for innovative and multifunctional advanced ceramic material systems, system-level performance studies, system reliability, and durability, as well as lifecycle extension, have to be addressed. From a general point of view, all in all, it is outlined that the objectives of this dissertation work were successfully accomplished.

6.2 Future Perspectives

In consideration of the extensive and in-depth research conducted in the present dissertation work, a wide range of forthcoming studies may be identified to continuously engage innovative and relevant investigation in the multifunctional ceramic composite field for aeronautical and aerospace applications. Therefore, the following topics are suggested for future work research guidelines:

- Optimize the manufacturing process of $MgO-Al_2O_3$ specimens for reduced porosity content achievement.
- Conduct mechanical and thermal experimental tests for $MgO-Al_2O_3$ samples to assess their true capabilities as reported by the literature.
- Retake the three–point flexural strength examination to investigate the fracture locus and the direction of the crack initiation under the mixed mode deformation in the ceramics studied.
- Perform ballistic testing to evaluate the protective strength of the ceramic composites manufactured.
- Particularly, conduct an experimental test analysis of the coefficient of thermal expansion, for the compositions studied, to investigate the implications of porosity in this ceramic composites' feature. Additionally, provide clarity on the described conflicting data in the bibliography.
- Carry out thermal cycling articulated with vibrational tests to simulate the ceramics' performance, in both cooling and heating environments, during ascent and re–entry atmosphere conditions simulation to establish these compositions' robustness.
- Additionally, ascertain the combination of convective and radiative heat transfer mechanisms on the surface of ceramic composites that instigate chemical reactions and gas dynamics phenomena, resulting in constraints for TPS and TBC design and material selection.
- Execute surface topography measurements for the ceramic composition samples under study to infer the influence of the surface roughness in mechanical, thermal, and electrical research.
- Exploit corrosion, erosion, and oxidation testing methodologies to evaluate the robustness and stability of $MgO-Al_2O_3$, $MgO-CaZrO_3$, and YSZ systems.
- With produced denser $MgO-Al_2O_3$ specimens, repeat the electrical experimental studies, via Electrical Current Method and Electrical Charge methods, to further extent examine the implication of the porosity content on the plasma microdischarge process through the *charge traps* phenomenon.

- Optimize the fabrication process of specimens of the ceramic composites under study, i.e., thinner thickness, to perform for each a comparison of their capabilities as dielectric barriers more easily.
- Carry out dielectric properties acquisition tests for the $MgO-Al_2O_3$, $MgO-CaZrO_3$, and YSZ ceramic composites and crosscheck with their respective performance.
- Perform comparison research on ceramic systems dielectric materials versus polymers under analogous conditions, to fulfill an existing gap in the literature specifically for surface dielectric barrier discharge geometry.
- Conduct induced velocity analysis through the development of velocity profiles for the $MgO-Al_2O_3$, $MgO-CaZrO_3$, and YSZ ceramic materials to analyze their mechanical efficiency more clearly.
- Under the same electrical operating parameters, i.e., constant input voltage, investigate the aging process of the ceramic dielectric barriers.
- Moreover, gather SEM imaging of the aged ceramic dielectric to investigate the individual impact of high–voltage AC cycles on $MgO-Al_2O_3$, $MgO-CaZrO_3$, and YSZ composites.
- Further perform velocity research of the MCZ and YSZ zirconia–based ceramic systems' capability to provide induced flow velocities, due to dissimilarities found over the evaluated range of input voltages. In other words, confirm, via testing repetition, if with higher voltages, the induced flow velocity of zirconia–based ceramics decreases. Additionally, assess if MCZ delivers in fact higher flow velocities than YSZ for the two setups, i.e., 1.0 cm and 1.5 cm.
- In–depth investigation of the fracturing phenomenon of YSZ samples through SEM analysis to greater comprehend the reasoning behind it and to determine accurately the location of initiation of fracturing.
- Implement numerical simulation methodologies through FEM analysis to simulate the different $MgO-Al_2O_3$, $MgO-CaZrO_3$, and YSZ systems' mechanical, thermal, and electrical features.
- Validation of the experimental investigation and research conducted throughout this dissertation work by applying $MgO-Al_2O_3$, $MgO-CaZrO_3$, and YSZ layers on engineering structures.

Bibliography

[1] R. B. Heimann, "**Classic and Advanced Ceramics: From Fundamentals to Applications**." Wiley & Sons, 2010, pp. XV–XIX. 1, 2, 11, 12, 13

[2] F. Froes, "**Aerospace Materials for the Twenty-First Century**," *Materials Design*, vol. 10, no. 3, pp. 110–120, 1989. [Online]. Available: https://doi.org/10.1016/S0261-3069(89)80026-3 1, 2

[3] R. Browning, "**Fundamentals of Ceramics**," in *Series in Materials Science and Engineering*, 2nd ed., R. Browning and M. Barsoum, Eds. CRC Press, 2020, p. 1–3. 1, 2

[4] P. Boch and J. C. Nièpce, "**Ceramic Materials: Processes, Properties, and Applications**." Wiley–ISTE, 2007, p. 3–8. 1

[5] T. A. Otitoju, P. U. Okoye, G. Chen, Y. Li, M. O. Okoye, and S. Li, "**Advanced Ceramic Components: Materials, Fabrication, and Applications**," *Journal of Industrial and Engineering Chemistry*, vol. 85, pp. 34–65, 2020. [Online]. Available: https://doi.org/10.1016/j.jiec.2020.02.002 2, 67, 75, 76, 122, 134, 144

[6] A. Goulas and R. Friel, "**Laser Sintering of Ceramic Materials for Aeronautical and Astronautical Applications**," in *Laser Additive Manufacturing*, M. Brandt, Ed. Woodhead Publishing, 2017, pp. 373–398. [Online]. Available: https://doi.org/10.1016/B978-0-08-100433-3.00014-2 3, 19

[7] The American Ceramic Society, "**Ceramics and Glass in the Aerospace Industry: Engineered Ceramics and Glasses Serve Essential Roles in Flight**," 2019, Retrieved November 3, 2021. [Online]. Available: https://ceramics.org/about/what-are-engineered-ceramics-and-glass/ceramics-and-glass-in-the-aerospace-industry 3

[8] B. Coffey and R. Kennedy, "**Hotter Air: Ceramics are the Secret to Lighter, Faster Jet Engines**," GE News, 2019, Retrieved November 10, 2021. [Online]. Available: https://www.ge.com/news/reports/hotter-air-ceramics-are-the-secret-to-lighter-faster-jet-engines 3

[9] D. Benningfield, "**Shuttle Tiles**," Smithsonian Magazine, Air and Space Magazine, 2006, Retrieved November 10, 2021. [Online]. Available: https://www.airspacemag.com/air-space-magazine/shuttle-tiles-12580671/ 4

[10] Y. Smith, "**Heat Shield Milestone Complete for First Orion Mission with Crew**," NASA, Humans in Space, 2020, Retrieved November 10, 2021. [Online]. Available: https://www.nasa.gov/image-feature/heat-shield-milestone-complete-for-first-orion-mission-with-crew/ 4

[11] Morgan Advanced Materials, "**Role of Advanced Ceramics in Aerospace Industry**," Technische Artikel, 2021, Retrieved November 11, 2021. [Online]. Available: https://www.morganbrazealloys.com/de-de/datenunterlagen/technische-artikel/role-of-advanced-ceramics-in-aerospace-industry/ 4, 19

[12] J. Rödel, A. B. Kounga, M. Weissenberger-Eibl, D. Koch, A. Bierwisch, W. Rossner, M. J. Hoffmann, R. Danzer, and G. Schneider, "**Development of a Roadmap for Advanced Ceramics: 2010–2025**," *Journal of the European Ceramic Society*, vol. 29, no. 9, pp. 1549–1560, 2009. [Online]. Available: https://doi.org/10.1016/j.jeurceramsoc.2008.10.015 9, 15, 16, 17

[13] European Defence Agency, "**EDA Technology Watch & Foresight**," 2021, Retrieved November 28, 2021. [Online]. Available: https://eda.europa.eu/what-we-do/research-technology/technology-watch-foresight 9

[14] Encyclopedia Britannica, "**Advanced Ceramics**," 2021, Retrieved November 28, 2021. [Online]. Available: https://www.britannica.com/technology/advanced-ceramics 9, 10

[15] R. B. Heimann, "**Classic and Advanced Ceramics: From Fundamentals to Applications**." Wiley & Sons, 2010, p. 157–163. 10, 12, 14, 15

[16] K. Singh, M. Kaur, and A. Kumar, "**Progress in Advanced Ceramics: Energy and Environmental Perspective**," in *Advanced Ceramics for Energy and Environmental Applications*, 1st ed., A. Kumar, Ed. CRC Press/Taylor & Francis Group, 2021, p. 1–12. [Online]. Available: https://doi.org/10.1201/9781003005155 11, 12

[17] T. D. Taylor, "**Advanced Ceramics – The Evolution, Classification, Properties, Production, Firing, Finishing and Design of Advanced Ceramics**," AZO Materials (AZoM), 2017, Retrieved November 28, 2021. [Online]. Available: https://www.azom.com/article.aspx?ArticleID=2123 15

[18] W. O. Soboyejo, J. Obayemi, E. Annan, E. Ampaw, L. Daniels, and N. Rahbar, "**Review of High Temperature Ceramics for Aerospace Applications**," *Advanced Materials Research*, vol. 1132, pp. 385–407, 2016. [Online]. Available: https://doi.org/10.4028/www.scientific.net/AMR.1132.385 19

[19] Lockheed Martin, "**Space Age Technologies for Down to Earth Applications**," Thermal Protection Materials, 2021, Retrieved November 11, 2021. [Online]. Available: https://www.lockheedmartin.com/en-us/products/thermalprotection.html 19

[20] P. K. Panda, "**Piezoceramic Materials and Devices for Aerospace Applications**," in *Aerospace Materials and Material Technologies: Aerospace Materials*, N. E. Prasad and R. J. H. Wanhill, Eds. Springer, 2017, pp. 501–518. 20

[21] A. Riccio, F. Raimondo, A. Sellitto, V. Carandente, R. Scigliano, and D. Tescione, "**Optimum Design of Ablative Thermal Protection Systems for Atmospheric Entry Vehicles**," *Applied Thermal Engineering*, vol. 119, pp. 541–552, 2017. [Online]. Available: https://doi.org/10.1016/j.applthermaleng.2017.03.053 21, 23, 24

[22] V. E. Zarko, "**Chapter 1 – The Prospects of Using Nanoenergetic Materials in Solid Rocket Propulsion**," in *Nanomaterials in Rocket Propulsion Systems*, Q. L. Yan, G. Q. He, P. J. Liu, and M. Gozin, Eds. Elsevier, 2019, pp. 3–30. [Online]. Available: https://doi.org/10.1016/B978-0-12-813908-0.00001-0 21

[23] E. Venkatapathy, C. E. Szalai, B. Laub, H. H. Hwang, J. L. Conley, J. Arnold, and N. ARC, "**Thermal Protection System Technologies for Enabling Future Sample Return Missions**," *White Paper submitted to the Planetary Science Decadal Survey, National Research Council, Washington, DC*, 2009. [Online]. Available: https://citeseerx.ist.psu.edu/viewdoc/download?doi=10.1.1.580.8037&rep=rep1&type=pdf 21

[24] O. Uyanna and H. Najafi, "**Thermal Protection Systems for Space Vehicles: A Review On Technology Development, Current Challenges and Future Prospects**," *Acta Astronautica*, vol. 176, pp. 341–356, 2020. [Online]. Available: https://doi.org/10.1016/j.actaastro.2020.06.047 21, 22, 23, 24

[25] R. D. Launius and D. R. Jenkins, "**Coming Home: Reentry and Recovery From Space (NASA/Sp)**," *NASA Aeronautics Book Series*, pp. 26–28, 2012. [Online]. Available: https://repository.si.edu/bitstream/handle/10088/24974/201210SH.pdf 21, 22, 23

[26] A. Ortona, C. Badini, V. Liedtke, C. Wilhelmi, C. D'Angelo, D. Gaia, and W. Fischer, "**Hetoroporous Heterogeneous Ceramics for Reusable Thermal Protection Systems**," *Journal of Materials Research*, vol. 28, no. 17, pp. 2273–2280, 2013. [Online]. Available: https://doc.rero.ch/record/290798/files/S0884291413000708.pdf 21, 24

[27] D. Glass, "**Ceramic Matrix Composite (CMC) Thermal Protection Systems (TPS) and Hot Structures for Hypersonic Vehicles**," *15th AIAA International Space Planes and Hypersonic Systems and Technologies Conference*, p. 2682, 2008. [Online]. Available: https://doi.org/10.2514/6.2008-2682 21, 28

[28] D. Sziroczak and H. Smith, "**A Review of Design Issues Specific to Hypersonic Flight Vehicles**," *Progress in Aerospace Sciences*, vol. 84, pp. 1–28, 2016. [Online]. Available: https://doi.org/10.1016/j.paerosci.2016.04.001 22

[29] H. Jouhara, A. Chauhan, T. Nannou, S. Almahmoud, B. Delpech, and L. Wrobel, "**Heat Pipe Based Systems – Advances and Applications**," *Energy*, vol. 128, pp. 729–754, 2017. [Online]. Available: https://doi.org/10.1016/j.energy.2017.04.028 22

[30] P. Sengupta and I. Manna, "**Advanced High–Temperature Structural Materials for Aerospace and Power Sectors: A Critical Review**," *Transactions of the Indian Institute of Metals*, vol. 72, no. 8, pp. 2043–2059, 2019. [Online]. Available: https://doi.org/10.1007/s12666-019-01598-z 23, 25, 26

[31] Y. Zhu, W. Peng, R. Xu, and P. Jiang, "**Review on Active Thermal Protection and its Heat Transfer for Airbreathing Hypersonic Vehicles**," *Chinese Journal of Aeronautics*, vol. 31, no. 10, pp. 1929–1953, 2018. [Online]. Available: https://doi.org/10.1016/j.cja.2018.06.011 23

[32] A. Harpale, S. Sawant, R. Kumar, D. Levin, and H. B. Chew, "**Ablative Thermal Protection Systems: Pyrolysis Modeling by Scale–Bridging Molecular Dynamics**," *Carbon*, vol. 130, pp. 315–324, 2018. [Online]. Available: https://doi.org/10.1016/j.carbon.2017.12.099 24, 25

[33] B. Laub and E. Venkatapathy, "**Thermal Protection System Technology and Facility Needs for Demanding Future Planetary Missions**," in *Planetary Probe Atmospheric Entry and Descent Trajectory Analysis and Science*, vol. 544, 2004, pp. 239–247. [Online]. Available: https://adsabs.harvard.edu/pdf/2004ESASP.544..239L 24

[34] P. G. I. Meseguer, J. and A. Sanz–Andrés, "**Spacecraft Thermal Control**," in *Woodhead Publishing in Mechanical Engineering*, 1st ed. Woodhead Publishing, 2012, pp. 305–325. 24

[35] M. Natali, J. M. Kenny, and L. Torre, "**Science and Technology of Polymeric Ablative Materials for Thermal Protection Systems and Propulsion Devices: A Review**," *Progress in Materials Science*, vol. 84, pp. 192–275, 2016. [Online]. Available: https://doi.org/10.1016/j.pmatsci.2016.08.003 24, 25

[36] M. S. Johnson, "**Engineered Ceramics: Current Status and Future Prospects**," T. Ohji and M. Singh, Eds. Wiley–American Ceramic Society, 2016, pp. 224–243. 24

[37] N. P. Padture, "**Advanced Structural Ceramics in Aerospace Propulsion**," *Nature Materials*, vol. 15, no. 8, pp. 804–809, 2016. [Online]. Available: https://doi.org/10.1038/nmat4687 25

[38] B. Clauß, "**Ceramic Matrix Composites: Fiber Reinforced Ceramics and their Applications**," W. Krenkel, Ed. John Wiley & Sons, 2008, p. 1–11. 26

[39] R. Naslain and M. Pomeroy, "**Ceramic Matrix Composites: Matrices and Processing**," in *Reference Module in Materials Science and Materials Engineering*. Elsevier, 2016, pp. 1060–1066. [Online]. Available: https://doi.org/10.1016/B978-0-12-803581-8.02317-1 26

[40] J. Cho, A. R. Boccaccini, and M. S. Shaffer, "**Ceramic Matrix Composites Containing Carbon Nanotubes**," *Journal of Materials Science*, vol. 44, no. 8, pp. 1934–1951, 2009. [Online]. Available: https://doi.org/10.1007/s10853-009-3262-9 27

[41] H. Porwal, S. Grasso, and M. J. Reece, "**Review of Graphene–Ceramic Matrix Composites**," *Advances in Applied Ceramics*, vol. 112, no. 8, pp. 443–454, 2013. [Online]. Available: https://doi.org/10.1179/174367613X13764308970581 27

[42] L. Li, Y. Song, and Y. C. Sun, "**Modeling the Tensile Behavior of Unidirectional C/SiC Ceramic–Matrix Composites**," *Mechanics of composite materials*, vol. 49, no. 6, pp. 659–672, 2014. [Online]. Available: https://doi.org/10.1007/s11029-013-9382-y 27

[43] K. Wei, K. Wang, X. Cheng, Y. Peng, M. Li, and X. Yang, "**Structural and Thermal Analysis of Integrated Thermal Protection Systems with C/Sic Composite Cellular Core Sandwich Panels**," *Applied Thermal Engineering*, vol. 131, pp. 209–220, 2018. [Online]. Available: https://doi.org/10.1016/j.applthermaleng.2017.12.009 27

[44] B. Heidenreich, H. Kraft, N. Bamsey, and M. Such-Taboada, "**Shear Properties of C/C–SiC Sandwich Structures**," *International Journal of Applied Ceramic Technology*, vol. 19, no. 1, pp. 54–61, 2022. [Online]. Available: https://doi.org/10.1111/ijac.13818 28

[45] Y. Shi, S. Li, E. Sitnikova, D. Cepli, and D. Koch, "**Experimental Evaluation and Theoretical Prediction of Elastic Properties and Failure of C/C–SiC Composite**," *International Journal of Applied Ceramic Technology*, vol. 19, no. 1, pp. 7–21, 2022. [Online]. Available: https://doi.org/10.1111/ijac.13775 28

[46] J. Huang and L. Guo, "**SiC Coating with High Crack Resistance Property for Carbon/Carbon Composites**," *Ceramics International*, vol. 48, no. 2, pp. 1740–1744, 2022. [Online]. Available: https://doi.org/10.1016/j.ceramint.2021.09.253 28

[47] D. Ni, Y. Cheng, J. Zhang, J. X. Liu, J. Zou, B. Chen, H. Wu, H. Li, S. Dong, J. Han, X. Zhang, Q. Fu, and G. J. Zhang, "**Advances in Ultra-High Temperature Ceramics, Composites, and Coatings**," *Journal of Advanced Ceramics*, vol. 11, no. 1, pp. 1–56, 2022. [Online]. Available: https://doi.org/10.1007/s40145-021-0550-6 28, 29

[48] E. Opila, S. Levine, and J. Lorincz, "**Oxidation of ZrB_2– and HfB_2–Based Ultra–High Temperature Ceramics: Effect of Ta Additions**," *Journal of Materials Science*, vol. 39, no. 19, pp. 5969–5977, 2004. [Online]. Available: https://doi.org/10.1023/B:JMSC.0000041693.32531.d1 28

[49] A. Chamberlain, W. Fahrenholtz, G. Hilmas, and D. Ellerby, "**Characterization of Zirconium Diboride for Thermal Protection Systems**," in *Key Engineering Materials*, vol. 264. Trans Tech Publ, 2004, pp. 493–496. [Online]. Available: https://doi.org/10.4028/www.scientific.net/kem.264-268.493 28

[50] H. Zhang, D. Jayaseelan, I. Bogomol, M. Reece, C. Hu, S. Grasso, and W. Lee, "**A Novel Microstructural Design to Improve the Oxidation Resistance of ZrB_2–SiC Ultra–High Temperature Ceramics (UHTCs)**," *Journal of Alloys and Compounds*, vol. 785, pp. 958–964, 2019. [Online]. Available: https://doi.org/10.1016/j.jallcom.2019.01.208 29

[51] D. Sciti, L. Silvestroni, F. Monteverde, A. Vinci, and L. Zoli, "**Introduction to H2020 Project C^3HARME – Next Generation Ceramic Composites for Combustion Harsh Environment and Space**," *Advances in Applied Ceramics*, vol. 117, no. 1, pp. s70–s75, 2018. [Online]. Available: https://doi.org/10.1080/17436753.2018.1509822 29

[52] S. Tang and C. Hu, "**Design, Preparation and Properties of Carbon Fiber Reinforced Ultra–High Temperature Ceramic Composites for Aerospace Applications: A Review**," *Journal of Materials Science Technology*, vol. 33, no. 2, pp. 117–130, 2017. [Online]. Available: https://doi.org/10.1016/j.jmst.2016.08.004 29

[53] Y. Arai, R. Inoue, K. Goto, and Y. Kogo, "**Carbon Fiber Reinforced Ultra–High Temperature Ceramic Matrix Composites: A Review**," *Ceramics International*, vol. 45, no. 12, pp. 14 481–14 489, 2019. [Online]. Available: https://doi.org/10.1016/j.ceramint.2019.05.065 30

[54] S. Mungiguerra, L. Silvestroni, R. Savino, L. Zoli, B. Esser, M. Lagos, and D. Sciti, "**Qualification and Reusability of Long and Short Fibre–Reinforced Ultra–Refractory Composites for Aerospace Thermal Protection Systems**," *Corrosion Science*, vol. 195, p. 109955, 2022. [Online]. Available: https://doi.org/10.1016/j.corsci.2021.109955 30

[55] Y. G. Jung, "**Science and Technology of Thermal Barrier Coatings**," in *Coatings*. MDPI, 2021, p. ix. [Online]. Available: https://doi.org/10.3390/books978-3-0365-0319-6 31, 34

[56] K. Mondal, L. Nuñez, C. M. Downey, and I. J. Van Rooyen, "**Thermal Barrier Coatings Overview: Design, Manufacturing, and Applications**

in High-Temperature Industries," *Industrial & Engineering Chemistry Research*, vol. 60, no. 17, pp. 6061–6077, 2021. [Online]. Available: https://doi.org/10.1021/acs.iecr.1c00788 31, 32, 33, 34, 35, 36

[57] X. Cao, R. Vassen, and D. Stoever, "**Ceramic Materials for Thermal Barrier Coatings**," *Journal of the European Ceramic Society*, vol. 24, no. 1, pp. 1–10, 2004. [Online]. Available: https://doi.org/10.1016/S0955-2219(03)00129-8 31, 37, 38, 40, 82, 150, 154

[58] M. Kilic, D. Ozkan, M. S. Gok, and A. C. Karaoglanli, "**Room– and High–Temperature Wear Resistance of MCrAlY Coatings Deposited by Detonation Gun (D-Gun) and Supersonic Plasma Spraying (SSPS) Techniques**," *Coatings*, vol. 10, no. 11, p. 1107, 2020. [Online]. Available: https://doi.org/10.3390/coatings10111107 31, 33, 34

[59] P. Ctibor, "**Interaction of Strontium Zirconate Plasma Sprayed Coating with Natural Silicate (CMAS) Dust—Origin of Luminescent Phases**," *Coatings*, vol. 10, no. 8, p. 738, 2020. [Online]. Available: https://doi.org/10.3390/coatings10080738 31, 32, 33

[60] D. Song, T. Song, U. Paik, G. Lyu, Y. G. Jung, B. G. Choi, I. S. Kim, and J. Zhang, "**Crack–Resistance Behavior of an Encapsulated, Healing Agent Embedded Buffer Layer on Self–Healing Thermal Barrier Coatings**," *Coatings*, vol. 9, no. 6, p. 358, 2019. [Online]. Available: https://doi.org/10.3390/coatings9060358 31, 32

[61] Q. Liu, S. Huang, and A. He, "**Composite Ceramics Thermal Barrier Coatings of Yttria Stabilized Zirconia for Aero-Engines**," *Journal of Materials Science Technology*, vol. 35, no. 12, pp. 2814–2823, 2019. [Online]. Available: https://doi.org/10.1016/j.jmst.2019.08.003 32, 34, 35, 40

[62] W. N. Harrison, D. G. Moore, and J. C. Richmond, "**Review of an Investigation of Ceramic Coatings for Metallic Turbine Parts and Other High-temperature Applications**," *National Advisory Committee for Aeronautics*, 1947. [Online]. Available: https://ntrs.nasa.gov/api/citations/19930082087/downloads/19930082087.pdf 32

[63] R. A. Miller, "**History of Thermal Barrier Coatings for Gas Turbine Engines: Emphasizing NASA's Role from 1942 to 1990**," *Thermal Barrier Coatings II*, no. NASA/TM–2009–215459, 2009. [Online]. Available: https://ntrs.nasa.gov/api/citations/20090018047/downloads/20090018047.pdf 32

[64] R. A. Miller, "**Thermal Barrier Coatings for Aircraft Engines: History and Directions**," *Journal of Thermal Spray Technology*, vol. 6, no. 1, pp. 35–42, 1997. [Online]. Available: https://doi.org/10.1007/BF02646310 32

[65] Superior Technical Ceramics, "**Yttria Stabilized Zirconia (YTZP)**," (n.d.), Retrieved February 2, 2022. [Online]. Available: https://www.ceramics.net/ceramic-materials-solutions/zirconias/ytzp 33

[66] D. Song, T. Song, U. Paik, G. Lyu, Y. G. Jung, B. G. Choi, I. S. Kim, and J. Zhang, "**Crack–Growth Behavior in Thermal Barrier Coatings with Cyclic Thermal Exposure**," *Coatings*, vol. 9, no. 6, p. 365, 2019. [Online]. Available: https://doi.org/10.3390/coatings9060365 34

[67] Z. Lu, G. Lyu, A. Gulhane, H. M. Park, J. S. Kim, Y. G. Jung, and J. Zhang, "**Experimental and Modeling Studies of Bond Coat Species Effect on Microstructure Evolution in EB-PVD Thermal Barrier Coatings in Cyclic Thermal Environments**," *Coatings*, vol. 9, no. 10, p. 626, 2019. [Online]. Available: https://doi.org/10.3390/coatings9100626 34

[68] E. Bakan and R. Vaßen, "**Ceramic Top Coats of Plasma–Sprayed Thermal Barrier Coatings: Materials, Processes, and Properties**," *Journal of Thermal Spray Technology*, vol. 26, no. 6, pp. 992–1010, 2017. [Online]. Available: https://doi.org/10.1007/s11666-017-0597-7 34, 37, 38, 40

[69] J. G. Thakare, C. Pandey, M. Mahapatra, and R. Mulik, "**Thermal Barrier Coatings — A State of the Art Review**," *Metals and Materials International*, vol. 27, no. 7, pp. 1947–1968, 2021. [Online]. Available: https://doi.org/10.1007/s12540-020-00705-w 34

[70] D. R. Clarke, M. Oechsner, and N. P. Padture, "**Thermal–Barrier Coatings for More Efficient Gas–Turbine Engines**," *MRS bulletin*, vol. 37, no. 10, pp. 891–898, 2012. [Online]. Available: https://doi.org/10.1557/mrs.2012.232 35

[71] Z. Cheng, J. Yang, F. Shao, X. Zhong, H. Zhao, Y. Zhuang, J. Ni, and S. Tao, "**Thermal Stability of YSZ Coatings Deposited by Plasma Spray–Physical Vapor Deposition**," *Coatings*, vol. 9, no. 8, p. 464, 2019. [Online]. Available: https://doi.org/10.3390/coatings9080464 35

[72] W. Beele, G. Marijnissen, and A. van Lieshout, "**The Evolution of Thermal Barrier Coatings — Status and Upcoming Solutions for Today's Key Issues**," *Surface and Coatings Technology*, vol. 120-121, pp. 61–67, 1999. [Online]. Available: https://doi.org/10.1016/S0257-8972(99)00342-4 35

[73] K. P. Jonnalagadda, "**Thermal Barrier Coatings: Failure Mechanisms and Life Prediction**," Ph.D. dissertation, Linköping University, Linköping, Sweden, 2019. [Online]. Available: https://www.diva-portal.org/smash/record.jsf?pid=diva2%3A1291953&dswid=7394 36, 37, 39, 40

[74] V. Kumar and K. Balasubramanian, "**Progress Update on Failure Mechanisms of Advanced Thermal Barrier Coatings: A Review**," *Progress*

in Organic Coatings, vol. 90, pp. 54–82, 2016. [Online]. Available: https://doi.org/10.1016/j.porgcoat.2015.09.019 36, 37

[75] N. R. Kadam, G. Karthikeyan, P. M. Jagtap, and D. M. Kulkarni, "**An Atmospheric Plasma Spray and Electron Beam–Physical Vapour Deposition for Thermal Barrier Coatings: A Review**," *Australian Journal of Mechanical Engineering*, vol. 0, no. 0, pp. 1–26, 2022. [Online]. Available: https://doi.org/10.1080/14484846.2022.2030088 37, 38, 39, 40, 42, 46, 47

[76] G. Mauer, M. O. Jarligo, D. E. Mack, and R. Vaßen, "**Plasma–Sprayed Thermal Barrier Coatings: New Materials, Processing Issues, and Solutions**," *Journal of Thermal Spray Technology*, vol. 22, no. 5, pp. 646–658, 2013. [Online]. Available: https://doi.org/10.1007/s11666-013-9889-8 37, 38, 39, 40, 43, 47

[77] S. Bose, "**High Temperature Coatings**." Butterworth-Heinemann, 2017, pp. 155–162. [Online]. Available: https://www.elsevier.com/books/high-temperature-coatings/bose/978-0-12-804622-7 38, 39

[78] R. Vaßen, M. O. Jarligo, T. Steinke, D. E. Mack, and D. Stöver, "**Overview on Advanced Thermal Barrier Coatings**," *Surface and Coatings Technology*, vol. 205, no. 4, pp. 938–942, 2010. [Online]. Available: https://doi.org/10.1016/j.surfcoat.2010.08.151 40, 43, 155

[79] D. Zhu and R. A. Miller, "**Advanced Low Conductivity Thermal Barrier Coatings: Performance and Future Directions**," *35th International Conference On Metallurgical Coatings and Thin Films*, 2008. [Online]. Available: https://ntrs.nasa.gov/api/citations/20080047729/downloads/20080047729.pdf 40, 41

[80] D. Zhu, J. A. Nesbitt, C. A. Barrett, T. R. McCue, and R. A. Miller, "**Furnace Cyclic Oxidation Behavior of Multicomponent Low Conductivity Thermal Barrier Coatings**," *Journal of Thermal Spray Technology*, vol. 13, no. 1, pp. 84–92, 2004. [Online]. Available: https://doi.org/10.1007/s11666-004-0053-3 40, 41

[81] D. Zhu and R. A. Miller, "**Development of Advanced Low Conductivity Thermal Barrier Coatings**," *International Journal of Applied Ceramic Technology*, vol. 1, no. 1, pp. 86–94, 2004. [Online]. Available: https://doi.org/10.1111/j.1744-7402.2004.tb00158.x 41

[82] R. Vassen, X. Cao, F. Tietz, D. Basu, and D. Stöver, "**Zirconates as New Materials for Thermal Barrier Coatings**," *Journal of the American Ceramic Society*, vol. 83, no. 8, pp. 2023–2028, 2000. [Online]. Available: https://doi.org/10.1111/j.1151-2916.2000.tb01506.x 42

[83] M. O. Jarligo, D. E. Mack, R. Vassen, and D. Stöver, "**Application of Plasma-Sprayed Complex Perovskites as Thermal Barrier Coatings**," *Journal of Thermal Spray Technology*, vol. 18, no. 2, pp. 187–193, 2009. [Online]. Available: https://doi.org/10.1007/s11666-009-9302-9 42, 43

[84] J. Yuan, J. Sun, J. Wang, H. Zhang, S. Dong, J. Jiang, L. Deng, X. Zhou, and X. Cao, "**$SrCeO_3$ as a Novel Thermal Barrier Coating Candidate for High–Temperature Applications**," *Journal of Alloys and Compounds*, vol. 740, pp. 519–528, 2018. [Online]. Available: https://doi.org/10.1016/j.jallcom.2018.01.021 42, 43

[85] Z. Qiao, S. Li, Y. Li, N. Xu, and K. Xiang, "**Structure, Mechanical Properties, and Thermal Conductivity of $BaZrO_3$ Doped at the A–B Site**," *Ceramics International*, vol. 48, no. 9, pp. 12 529–12 536, 2022. [Online]. Available: https://www.sciencedirect.com/science/article/pii/S0272884222001328 42, 43

[86] R. Vassen, A. Stuke, and D. Stöver, "**Recent Developments in the Field of Thermal Barrier Coatings**," *Journal of Thermal Spray Technology*, vol. 18, no. 2, pp. 181–186, 2009. [Online]. Available: https://doi.org/10.1007/s11666-009-9312-7 42

[87] N. Vourdas, E. Marathoniti, P. Pandis, C. Argirusis, G. Sourkouni, C. Legros, S. Mirza, and V. Stathopoulos, "**Evaluation of $LaAlO_3$ as Top Coat Material for Thermal Barrier Coatings**," *Transactions of Nonferrous Metals Society of China*, vol. 28, no. 8, pp. 1582–1592, 2018. [Online]. Available: https://doi.org/10.1016/S1003-6326(18)64800-9 42

[88] W. Ma, D. E. Mack, R. Vaßen, and D. Stöver, "**Perovskite–Type Strontium Zirconate as a New Material for Thermal Barrier Coatings**," *Journal of the American Ceramic Society*, vol. 91, no. 8, pp. 2630–2635, 2008. [Online]. Available: https://doi.org/10.1111/j.1551-2916.2008.02472.x 42

[89] W. Ma, M. Jarligo, D. Mack, D. Pitzer, J. Malzbender, R. Vaßen, and D. Stöver, "**New Generation Perovskite Thermal Barrier Coating Materials**," *Journal of Thermal Spray Technology*, vol. 17, no. 5, pp. 831–837, 2008. [Online]. Available: https://doi.org/10.1007/s11666-008-9239-4 42, 43, 56, 65

[90] E. Garcia, C. Cano, T. Coyle, M. Osendi, and P. Miranzo, "**Thermally Sprayed $CaZrO_3$ Coatings**," *Journal of Thermal Spray Technology*, vol. 17, no. 5, pp. 865–871, 2008. [Online]. Available: https://doi.org/10.1007/s11666-008-9224-y 43, 65

[91] N. Ejaz, L. Ali, F. Ahmed, K. M. Ghauri, and A. N. Khan, "**Hot Corrosion Behavior of YSZ and $CaZrO_3$/YSZ Composite Tthermal Barrier Coatings in Contact with 50 V_2O_5 + 50 Na_2SO_4 Salts**," *Journal of Thermal Spray*

Technology, vol. 26, no. 5, pp. 913–928, 2017. [Online]. Available: https://doi.org/10.1007/s11666-017-0568-z 43

[92] B. Saruhan, K. Fritscher, U. Schulz, and D. G. A. Center, "**Y–doped $La_2Zr_2O_7$ Pyrochlore EB–PVD Thermal Barrier Coatings**," in *Ceramic Engineering and Science Proceedings*, vol. 24, no. 3. The American Ceramic Society, 2003, pp. 491–496. [Online]. Available: https://doi.org/10.1002/9780470294802.ch70 43, 44

[93] H. Wang, Z. Sheng, E. Tarwater, X. Zhang, and J. W. Fergus, "**Function of Reaction Layer in Pyrochlore Thermal Barrier Coatings Against CMAS Corrosion**," *ECS Transactions*, vol. 66, no. 18, p. 53, 2015. [Online]. Available: https://doi.org/10.1149/06618.0053ecst 44

[94] M. P. Schmitt, A. K. Rai, R. Bhattacharya, D. Zhu, and D. E. Wolfe, "**Multilayer Thermal Barrier Coating (TBC) Architectures Utilizing Rare Earth Doped YSZ and Rare Earth Pyrochlores**," *Surface and Coatings Technology*, vol. 251, pp. 56–63, 2014. [Online]. Available: https://doi.org/10.1016/j.surfcoat.2014.03.049 44

[95] R. Vaßen, F. Traeger, and D. Stöver, "**New Thermal Barrier Coatings Based on Pyrochlore/YSZ Double–Layer Systems**," *International Journal of Applied Ceramic Technology*, vol. 1, no. 4, pp. 351–361, 2004. [Online]. Available: https://doi.org/10.1111/j.1744-7402.2004.tb00186.x 44

[96] N. P. Bansal and D. Zhu, "**Effects of Doping on Thermal Conductivity of Pyrochlore Oxides for Advanced Thermal Barrier Coatings**," *Materials Science and Engineering: A*, vol. 459, no. 1, pp. 192–195, 2007. [Online]. Available: https://doi.org/10.1016/j.msea.2007.01.069 44

[97] J. Yang, Y. Han, M. Shahid, W. Pan, M. Zhao, W. Wu, and C. Wan, "**A Promising Material for Thermal Barrier Coating: Pyrochlore–Related Compound Sm_2FeTaO_7**," *Scripta Materialia*, vol. 149, pp. 49–52, 2018. [Online]. Available: https://doi.org/10.1016/j.scriptamat.2018.02.005 44

[98] J. Che, X. Wang, X. Liu, G. Liang, and S. Zhang, "**Outstanding Sintering Resistance in Pyrochlore–Type $La_2(Zr_{0.7}Ce_{0.3})_2O_7$ for Thermal Barrier Coatings Material**," *Ceramics International*, vol. 47, no. 5, pp. 6996–7004, 2021. [Online]. Available: https://doi.org/10.1016/j.ceramint.2020.11.050 44

[99] R. Gadow and M. Lischka, "**Lanthanum Hexaaluminate — Novel Thermal Barrier Coatings for Gas Turbine Applications — Materials and Process Development**," *Surface and Coatings Technology*, vol. 151-152, pp. 392–399, 2002. [Online]. Available: https://doi.org/10.1016/S0257-8972(01)01642-5 45

[100] M. K. Cinibulk, "**Thermal Stability of Some Hexaluminates at 1400°C**," *Journal of Materials Science Letters*, vol. 14, no. 9, pp. 651–654, 1995. [Online]. Available: https://doi.org/10.1007/BF00586168 45

[101] N. P. Bansal and D. Zhu, "**Thermal Properties of Oxides with Magnetoplumbite Structure for Advanced Thermal Barrier Coatings**," *Surface and Coatings Technology*, vol. 202, no. 12, pp. 2698–2703, 2008. [Online]. Available: https://doi.org/10.1016/j.surfcoat.2007.09.048 45

[102] S. R. Choi, N. P. Bansal, and D. Zhu, "**Mechanical and Thermal Properties of Advanced Oxide Materials for Higher–Temperature Coatings Applications**," *Advances in Ceramic Coatings and Ceramic-Metal Systems: Ceramic Engineering and Science Proceedings*, vol. 26, pp. 11–19, 2005. [Online]. Available: https://doi.org/10.1002/9780470291238.ch2 45

[103] X. Cao, Y. Zhang, J. Zhang, X. Zhong, Y. Wang, H. Ma, Z. Xu, L. He, and F. Lu, "**Failure of the Plasma–Sprayed Coating of Lanthanum Hexaluminate**," *Journal of the European Ceramic Society*, vol. 28, no. 10, pp. 1979–1986, 2008. [Online]. Available: https://doi.org/10.1016/j.jeurceramsoc.2008.01.023 45

[104] X. Xie, H. Guo, S. Gong, and H. Xu, "**Lanthanum–Titanium–Aluminum Oxide: A Novel Thermal Barrier Coating Material for Applications at 1300°C**," *Journal of the European Ceramic Society*, vol. 31, no. 9, pp. 1677–1683, 2011. [Online]. Available: https://doi.org/10.1016/j.jeurceramsoc.2011.03.036 45

[105] X. Chen, Y. Zhao, W. Huang, H. Ma, B. Zou, Y. Wang, and X. Cao, "**Thermal Aging Behavior of Plasma Sprayed $LaMgAl_{11}O_{19}$ Thermal Barrier Coating**," *Journal of the European Ceramic Society*, vol. 31, no. 13, pp. 2285–2294, 2011. [Online]. Available: https://doi.org/10.1016/j.jeurceramsoc.2011.05.036 46

[106] X. Chen, Y. Zhao, X. Fan, Y. Liu, B. Zou, Y. Wang, H. Ma, and X. Cao, "**Thermal Cycling Failure of New $LaMgAl_{11}O_{19}$/YSZ Double Ceramic Top Coat Thermal Barrier Coating Systems**," *Surface and Coatings Technology*, vol. 205, no. 10, pp. 3293–3300, 2011. [Online]. Available: https://doi.org/10.1016/j.surfcoat.2010.11.059 46

[107] X. Chen, L. Gu, B. Zou, Y. Wang, and X. Cao, "**New Functionally Graded Thermal Barrier Coating System Based on $LaMgAl_{11}O_{19}$/YSZ Prepared by Air Plasma Spraying**," *Surface and Coatings Technology*, vol. 206, no. 8-9, pp. 2265–2274, 2012. [Online]. Available: https://doi.org/10.1016/j.surfcoat.2011.09.076 46

[108] X. Chen, Y. Sun, J. Hu, J. Li, C. Deng, D. Wu, D. Zeng, W. Li, Y. Liu, B. Zou, and X. Cao, "**Thermal Cycling Failure of the Multilayer Thermal Barrier Coatings Based on $LaMgAl_{11}O_{19}$/YSZ**," *Journal of the European*

Ceramic Society, vol. 40, no. 4, pp. 1424–1432, 2020. [Online]. Available: https://doi.org/10.1016/j.jeurceramsoc.2019.12.039 46

[109] K. Ollegott, P. Wirth, C. Oberste-Beulmann, P. Awakowicz, and M. Muhler, "**Fundamental Properties and Applications of Dielectric Barrier Discharges in Plasma–Catalytic Processes at Atmospheric Pressure**," *Chemie Ingenieur Technik*, vol. 92, no. 10, pp. 1542–1558, 2020. [Online]. Available: https://doi.org/10.1002/cite.202000075 48, 49, 50, 52, 53

[110] M. L. Carreon, "**Plasma Catalysis: A Brief Tutorial**," *Plasma Research Express*, vol. 1, no. 4, p. 043001, 2019. [Online]. Available: https://doi.org/10.1088/2516-1067/ab5a30 48, 49

[111] S. Gershman, "**Pulsed Electrical Discharge in Gas Bubbles in Water**," Ph.D. dissertation, Rutgers State University, New Jersey, USA, 2008. [Online]. Available: https://doi.org/doi:10.7282/T30Z73K8 48, 49, 51

[112] S. U. Kalghatgi, "**Mechanisms of Interaction of Non–Thermal Plasma with Living Cells**," Ph.D. dissertation, Drexel University, Philadelphia, USA, 2010. [Online]. Available: https://doi.org/10.17918/etd-3208 48, 49

[113] P. Bruggeman and R. Brandenburg, "**Atmospheric Pressure Discharge Filaments and Microplasmas: Physics, Chemistry and Diagnostics**," *Journal of Physics D: Applied Physics*, vol. 46, no. 46, p. 464001, 2013. [Online]. Available: https://doi.org/10.1088/0022-3727/46/46/464001 48, 50

[114] J. Li, C. Ma, S. Zhu, F. Yu, B. Dai, and D. Yang, "**A Review of Recent Advances of Dielectric Barrier Discharge Plasma in Catalysis**," *Nanomaterials*, vol. 9, no. 10, p. 1428, 2019. [Online]. Available: https://doi.org/10.3390/nano9101428 49, 54

[115] R. Brandenburg, "**Dielectric Barrier Discharges: Progress on Plasma Sources and on the Understanding of Regimes and Single Filaments**," *Plasma Sources Science and Technology*, vol. 26, no. 5, p. 053001, 2017. [Online]. Available: https://doi.org/10.1088/1361-6595/aaced9 49, 50, 52, 54

[116] U. Kogelschatz, "**Dielectric–Barrier Discharges: Their History, Discharge Physics, and Industrial Applications**," *Plasma Chemistry and Plasma Processing*, vol. 23, no. 1, pp. 1–46, 2003. [Online]. Available: https://doi.org/10.1023/A:1022470901385 49, 50, 54

[117] A. Schulz and S. Merli, "**Dielectric Barrier Discharge (DBD)**," Institute of Interfacial Process Engineering and Plasma Technology, University of Stuttgart, (n.d.), Retrieved February 22, 2022. [Online]. Available: https://www.igvp.uni-stuttgart.de/en/research/plasma-technology/sources/barrier/ 50, 52

[118] Matsusada Precision Inc., "**Dielectric Barrier Discharge (DBD)**," Matsusada Precision, 2022, Retrieved February 22, 2022. [Online]. Available: https://www.matsusada.com/application/ps/dielectric_barrier_discharge/#:%7E:text=Dielectric%20Barrier%20Discharge%20(DBD)%20is,and%20covered%20with%20an%20insulator.&text=This%20is%20why%20it%20is,observed%20in%20the%20discharge%20area 50, 51

[119] P. Shrestha, D. P. Subedi, and U. M. Joshi, "**Electrical Characterization of Atmospheric Pressure Dielectric Barrier Discharge in Air**," *International Conference on the Frontiers of Plasma Physics and Technology*, 2013. [Online]. Available: https://www-pub.iaea.org/MTCD/publications/PDF/TE-1713-CD/talks/posters/Shrestha-paper.pdf 50

[120] M. Bryjak, I. Gancarz, and K. Smolinska, "**Plasma Nanostructuring of Porous Polymer Membranes**," *Advances in Colloid and Interface Science*, vol. 161, no. 1, pp. 2–9, 2010. [Online]. Available: https://doi.org/10.1016/j.cis.2010.09.004 50

[121] D. F. Opaits, "**Dielectric Barrier Discharge Plasma Actuator for Flow Control**," Ph.D. dissertation, Princeton University, New Jersey, USA, 2010. [Online]. Available: https://ntrs.nasa.gov/api/citations/20120015252/downloads/20120015252.pdf 51, 52

[122] U. Kogelschatz, B. Eliasson, and W. Egli, "**Dielectric–Barrier Discharges. Principle and Applications**," *Le Journal de Physique IV*, vol. 7, no. C4, pp. C4–47, 1997. [Online]. Available: https://doi.org/10.1051/jp4:1997405 52, 54

[123] N. D. Wilde, H. Xu, N. Gomez-Vega, and S. R. Barrett, "**A Model of Surface Dielectric Barrier Discharge Power**," *Applied Physics Letters*, vol. 118, no. 15, p. 154102, 2021. [Online]. Available: https://doi.org/10.1051/jp4:1997405 52, 53

[124] F. M. F. Rodrigues, "**Modelação Experimental para Otimização de Atuadores a Plasma com Ações em Termofluidodinâmica**," Ph.D. dissertation, Universidade da Beira Interior, Covilhã, Portugal, 2018. [Online]. Available: https://doi.org/10.13140/RG.2.2.20759.21929 52, 54, 56, 57, 58, 59

[125] F. F. Rodrigues, J. C. Pascoa, and M. Trancossi, "**Experimental Analysis of Alternative Dielectric Materials for DBD Plasma Actuators**," in *ASME International Mechanical Engineering Congress and Exposition*, vol. 52002. American Society of Mechanical Engineers, 2018, p. V001T03A005. [Online]. Available: https://doi.org/10.1115/IMECE2018-87455 53

[126] U. Kogelschatz, B. Eliasson, and W. Egli, "**From Ozone Generators to Flat Television Screens: History and Future Potential of Dielectric–Barrier Discharges**," *Pure and Applied Chemistry*, vol. 71, no. 10, pp. 1819–1828, 1999. [Online]. Available: https://doi.org/10.1351/pac19997110181 54

[127] T. Abe, Y. Takizawa, S. Sato, and N. Kimura, "**Experimental Study for Momentum Transfer in a Dielectric Barrier Discharge Plasma Actuator**," *AIAA Journal*, vol. 46, no. 9, pp. 2248–2256, 2008. [Online]. Available: https://doi.org/10.2514/1.30985 54

[128] K. Shimizu, Y. Mizuno, and M. Blajan, "**Basic Study on Force Induction Using Dielectric Barrier Microplasma Array**," *Japanese Journal of Applied Physics*, vol. 54, no. 1S, p. 01AA07, 2014. [Online]. Available: https://doi.org/10.7567/JJAP.54.01AA07 54, 55

[129] K. Shimizu and M. Blajan, "**Dielectric Barrier Discharge Microplasma Actuator for Flow Control**," *IntechOpen*, p. 1, 2018. [Online]. Available: http://dx.doi.org/10.5772/intechopen.75802 54, 55

[130] F. F. Rodrigues, J. C. Pascoa, and M. Trancossi, "**Analysis of Innovative Plasma Actuator Geometries for Boundary Layer Control**," vol. 50510, p. V001T03A007, 2016. [Online]. Available: https://doi.org/10.1115/IMECE2016-66495 55

[131] F. F. Rodrigues, J. C. Pascoa, and M. Trancossi, "**Experimental Thermal Characterization of DBD Plasma Actuators**," *ASME International Mechanical Engineering Congress and Exposition*, vol. 58349, p. V001T03A004, 2017. [Online]. Available: https://doi.org/10.1115/imece2017-70541 55, 56, 57

[132] A. Duchmann, B. Simon, C. Tropea, and S. Grundmann, "**Dielectric Barrier Discharge Plasma Actuators for In–Flight Transition Delay**," *AIAA Journal*, vol. 52, no. 2, pp. 358–367, 2014. [Online]. Available: https://doi.org/10.2514/1.J052485 55

[133] C. Lai, H. Fu, B. Hu, Z. Ling, and L. Jiang, "**Aerodynamic Drag Reduction and Optimization of MIRA Model Based on Plasma Actuator**," *Actuators*, vol. 9, no. 3, p. 64, 2020. [Online]. Available: https://doi.org/10.3390/act9030064 55

[134] S. Roy, P. Zhao, A. DasGupta, and J. Soni, "**Dielectric Barrier Discharge Actuator for Vehicle Drag Reduction at Highway Speeds**," *AIP Advances*, vol. 6, no. 2, p. 025322, 2016. [Online]. Available: https://doi.org/10.1063/1.4942979 55

[135] S. Karimi, A. Zargar, M. Mani, and A. Hemmati, "**The Effect of Single Dielectric Barrier Discharge Actuators in Reducing Drag on an Ahmed Body**," *Fluids*, vol. 5, no. 4, 2020. [Online]. Available: https://doi.org/10.3390/fluids5040244 55

[136] Z. Su, H. Zong, H. Liang, J. Li, and X. Chen, "**Characteristics of a Dielectric Barrier Discharge Plasma Actuator Driven by Pulsed-DC High Voltage**,"

Journal of Physics D Applied Physics, vol. 55, no. 7, p. 075203, 2022. [Online]. Available: https://doi.org/10.1088/1361-6463/ac30bc 55

[137] P. R. C. Souza, A. R. Proenca, O. de Almeida, and R. H. Self, "**Aerodynamics and Aeroacoustics Investigation of a Low Speed Subsonic Jet**," *International Journal of Acoustics and Vibration*, vol. 22, no. 1, pp. 121–130, March 2017. [Online]. Available: https://doi.org/10.20855/ijav.2017.22.1458 55, 56

[138] G. Pereira Gouveia da Silva, J. P. Eguea, J. A. Garcia Croce, and F. Martini Catalano, "**Slat Aerodynamic Noise Reduction Using Dielectric Barrier Discharge Plasma Actuators**," *Aerospace Science and Technology*, vol. 97, p. 105642, 2020. [Online]. Available: https://doi.org/10.1016/j.ast.2019.105642 56

[139] X. Huang and X. Zhang, "**Plasma Actuators for Noise Control**," *International Journal of Aeroacoustics*, vol. 9, no. 4-5, pp. 679–703, 2010. [Online]. Available: https://doi.org/10.1260/1475-472X.9.4-5.679 56

[140] V. F. Kopiev, V. A. Bityurin, I. V. Belyaev, S. M. Godin, M. Y. Zaitsev, A. I. Klimov, V. A. Kopiev, I. A. Moralev, and N. N. Ostrikov, "**Jet Noise Control Using the Dielectric Barrier Discharge Plasma Actuators**," *Acoustical Physics*, vol. 58, no. 4, pp. 434–441, 2012. [Online]. Available: https://doi.org/10.1134/S1063771012040100 56

[141] F. F. Rodrigues, J. C. Pascoa, and M. Trancossi, "**Experimental Analysis of Dielectric Barrier Discharge Plasma Actuators Thermal Characteristics Under External Flow Influence**," *Journal of Heat Transfer*, vol. 140, no. 10, 05 2018. [Online]. Available: https://doi.org/10.1115/1.4040152 56, 175

[142] P. Audier, M. Fénot, N. Bénard, and E. Moreau, "**Film Cooling Effectiveness Enhancement Using Surface Dielectric Barrier Discharge Plasma Actuator**," *International Journal of Heat and Fluid Flow*, vol. 62, pp. 247–257, 2016. [Online]. Available: https://doi.org/10.1016/j.ijheatfluidflow.2016.10.009 57

[143] S. Roy and C. C. Wang, "**Plasma Actuated Heat Transfer**," *Applied Physics Letters*, vol. 92, no. 23, p. 231501, 2008. [Online]. Available: https://doi.org/10.1063/1.2938886 57

[144] J. L. Yu, L. M. He, Y. F. Zhu, W. Ding, and Y. G. Wang, "**Numerical Simulation of the Effect of Plasma Aerodynamic Actuation on Improving Film Hole Cooling Performance**," *Heat and Mass Transfer*, vol. 49, no. 6, pp. 897–906, 2013. [Online]. Available: https://doi.org/10.1007/s00231-013-1157-4 57

[145] C. Kolbakir, H. Hu, Y. Liu, and H. Hu, "**An Experimental Study on Different Plasma Actuator Layouts for Aircraft Icing Mitigation**,"

Aerospace Science and Technology, vol. 107, p. 106325, 2020. [Online]. Available: https://doi.org/10.1016/j.ast.2020.106325 57, 58

[146] K. Petty and C. Floyd, "**A Statistical Review of Aviation Airframe Icing Accidents in the U.S**," *Proceedings of the 11th Conference on Aviation*, 2004. [Online]. Available: https://ams.confex.com/ams/11aram22sls/techprogram/paper_81425.htm 57

[147] Y. Jia, H. Liang, H. Zong, B. Wei, L. Xie, W. Hua, and Z. Li, "**Ice Shape Modulation with Nanosecond Pulsed Surface Dielectric Barrier Discharge Plasma Actuator Towards Flight Safety**," *Aerospace Science and Technology*, vol. 120, p. 107233, 2022. [Online]. Available: https://doi.org/10.1016/j.ast.2021.107233 57, 58

[148] W. Zhou, Y. Liu, H. Hu, H. Hu, and X. Meng, "**Utilization of Thermal Effect Induced by Plasma Generation for Aircraft Icing Mitigation**," *AIAA Journal*, vol. 56, no. 3, pp. 1097–1104, 2018. [Online]. Available: https://doi.org/10.2514/1.J056358 57, 58

[149] C. Kolbakir, Y. Liu, H. Hu, A. Starikovskiy, and R. B. Miles, "**An Experimental Investigation on the Thermal Effects of NS–DBD and AC–DBD Plasma Actuators for Aircraft Icing Mitigation**," *AIAA Aerospace Sciences Meeting*, 2018. [Online]. Available: https://doi.org/10.2514/6.2018-0164 57, 58

[150] H. Hu, X. Meng, J. Cai, W. Zhou, Y. Liu, and H. Hu, "**Optimization of Dielectric Barrier Discharge Plasma Actuators for Icing Control**," *Journal of Aircraft*, vol. 57, no. 2, pp. 383–387, 2020. [Online]. Available: https://doi.org/10.2514/1.C035697 57, 58

[151] E. Moreau, "**Airflow Control by Non–Thermal Plasma Actuators**," *Journal of Physics D: Applied Physics*, vol. 40, no. 3, pp. 605–636, 2007. [Online]. Available: https://doi.org/10.1088/0022-3727/40/3/S01 58

[152] T. Corke, M. Post, and D. Orlov, "**Single Dielectric Barrier Discharge Plasma Enhanced Aerodynamics: Physics, Modeling and Applications**," *Experiments in Fluids*, vol. 46, pp. 1–26, 2009. [Online]. Available: https://doi.org/10.1007/s00348-008-0582-5 58, 59

[153] N. Benard and E. Moreau, "**Electrical and Mechanical Characteristics of Surface AC Dielectric Barrier Discharge Plasma Actuators Applied to Airflow Control**," *Experiments in Fluids*, vol. 55, p. 1846, 2014. [Online]. Available: https://doi.org/10.1007/s00348-014-1846-x 58

[154] D. L. Bian, Y. Wu, M. Jia, C. B. Long, and S. B. Jiao, "**Comparison Between AlN and Al_2O_3 Ceramics Applied to Barrier Dielectric of Plasma**

Actuator," *Chinese Physics B*, vol. 26, no. 8, p. 084703, 2017. [Online]. Available: https://doi.org/10.1088/1674-1056/26/8/084703 58, 59, 62, 171, 181

[155] J. Pons, L. Oukacine, E. Moreau, and J. M. Tatibouet, "**Observation of Dielectric Degradation After Surface Dielectric Barrier Discharge Operation in Air at Atmospheric Pressure**," *IEEE Transactions on Plasma Science*, vol. 36, no. 4, pp. 1342–1343, 2008. [Online]. Available: https://doi.org/10.1109/TPS.2008.926856 59

[156] J. Kelar, R. Přibyl, M. Pazderka, Z. Kelar Tučeková, M. Zemánek, and M. Černák, "**Change of Fundamental Properties of Dielectric Barrier Discharge due to the Alumina–Based Barrier Layer Composition**," *Vacuum*, vol. 174, p. 109180, 2020. [Online]. Available: https://doi.org/10.1016/j.vacuum.2020.109180 59, 62, 126, 159

[157] R. Pribyl, P. Stastny, M. Pazderka, J. Kelar, Z. K. Tucekova, M. Zemanek, M. Trunec, and M. Cernak, "**Properties of MgAl2O4 Doped Alumina Barrier Layers for Dielectric Barrier Discharge**," *Journal of Physics D: Applied Physics*, vol. 53, no. 50, p. 505202, 2020. [Online]. Available: https://doi.org/10.1088/1361-6463/abb0ba 59, 62, 64, 118, 159

[158] S. Xiaozhen, Z. Yong, Q. Fuyang, and W. Xiangrong, "**Effect of Glass Additions on $Ca_{0.8}Sr_{0.2}TiO_3$ Ceramics as Dielectrics for a Cylindrical Dielectric Barrier Discharge Reactor in CO_2 Plasma**," *Rare Metal Materials and Engineering*, vol. 45, no. 12, pp. 3037–3042, 2016. [Online]. Available: https://doi.org/10.1016/S1875-5372(17)30050-4 59, 61, 65, 160

[159] J. Zito, D. P. Arnold, R. J. Durscher, and S. Roy, "**Exploration of Ceramic Dielectrics for Microscale Dielectric Barrier Discharge Plasma Actuators**," *44th AIAA Plasmadynamics and Lasers Conference*, p. 2495, 2013. [Online]. Available: https://doi.org/10.2514/6.2013-2495 59, 60

[160] N. E. Fine and S. J. Brickner, "**Plasma Catalysis for Enhanced–Thrust Single Dielectric Barrier Discharge Plasma Actuators**," *AIAA Journal*, vol. 48, no. 12, pp. 2979–2982, 2010. [Online]. Available: https://doi.org/10.2514/1.J050729 60

[161] M. Neumann, C. Friedrich, J. Czarske, J. Kriegseis, and S. Grundmann, "**Determination of the Phase–Resolved Body Force Produced by a Dielectric Barrier Discharge Plasma Actuator**," *Journal of Physics D: Applied Physics*, vol. 46, no. 4, p. 042001, 2012. [Online]. Available: https://doi.org/10.1088/0022-3727/46/4/042001 60

[162] T. Segawa, H. Furutani, H. Yoshida, T. Jukes, and K. S. Choi, "**Wall Normal Jet Under Elevated Temperatures Produced by Surface Plasma Actuator**,"

45th AIAA Aerospace Sciences Meeting and Exhibit, p. 784, 2007. [Online]. Available: https://doi.org/10.2514/6.2007-784 60

[163] J. Ran, C. Li, D. Ma, H. Luo, and X. Li, "**Homogeneous Dielectric Barrier Discharges in Atmospheric Air and Its Influencing Factor**," *Physics of Plasmas*, vol. 25, no. 3, p. 033511, 2018. [Online]. Available: https://doi.org/10.1063/1.5019989 60, 171

[164] J. Ran, X. Zhang, D. Ge, X. Li, and X. Li, "**Effect of Dielectric Surface Morphology on Dielectric Barrier Discharge Mode in Air at Atmospheric Pressure**," *IEEE Transactions on Plasma Science*, vol. 49, no. 1, pp. 214–218, 2021. [Online]. Available: https://doi.org/10.1109/TPS.2020.3043580 61

[165] R. Li, Q. Tang, S. Yin, Y. Yamaguchi, and T. Sato, "**Decomposition of Carbon Dioxide by the Dielectric Barrier Discharge (DBD) Plasma Using $Ca_{0.7}Sr_{0.3}TiO_3$ Barrier**," *Chemistry Letters*, vol. 33, no. 4, pp. 412–413, 2004. [Online]. Available: https://doi.org/10.1246/cl.2004.412 61, 65, 159, 160

[166] I. Moralev, V. Sherbakova, I. Selivonin, V. Bityurin, and M. Ustinov, "**Effect of the Discharge Constriction in DBD Plasma Actuator on the Laminar Boundary Layer**," *International Journal of Heat and Mass Transfer*, vol. 116, pp. 1326–1340, 2018. [Online]. Available: https://doi.org/10.1016/j.ijheatmasstransfer.2017.09.121 62

[167] J. D. Mackenzie, "**Multifunctional Ceramic Materials–Review and Projections**," *MRS Online Proceedings Library*, vol. 175, 1989. [Online]. Available: https://doi.org/10.1557/PROC-175-149 63

[168] J. Mollá, R. Moreno, and A. Ibarra, "**Effect of Mg Doping on Dielectric Properties of Alumina**," *Journal of Applied Physics*, vol. 80, no. 2, pp. 1028–1032, 1996. [Online]. Available: https://doi.org/10.1063/1.362836 64

[169] J. Ramírez-González and A. R. West, "**Electrical Properties of Mg-doped and Mg, Si Co-Doped Alumina**," *Journal of the European Ceramic Society*, vol. 41, no. 6, pp. 3512–3519, 2021. [Online]. Available: https://doi.org/10.1016/j.jeurceramsoc.2020.12.040 64

[170] F. Balça, "**Otimização de Compósitos Multifásicos de Zircónia para Aplicações Termomecânicas Aeronáuticas**," Master's dissertation, Universidade da Beira Interior, Covilhã, Portugal, 2022. 66, 120, 122, 140, 141, 150

[171] International Syalons, "**Manufacturing Advanced Ceramics**," Articles & Guides, 2020, Retrieved May 30, 2022. [Online]. Available: https://www.syalons.com/resources/articles-and-guides/manufacturing/ 67

[172] R. Yerly, "**Better Together: XRF and XRD**," ThermoFisher Scientific, 2016, Retrieved May 30, 2022. [Online]. Available: https://www.thermofisher.com/blog/mining/better-together-xrf-and-xrd/ 70, 71

[173] B. L. Dutrow and C. M. Clark, "**X–Ray Powder Diffraction (XRD)**," Instruments and Analytical Methods Common to Nano, Montana State University, (n.d), Retrieved May 30, 2022. [Online]. Available: https://serc.carleton.edu/msu_nanotech/index.html 70, 71

[174] E. Zolotoyabko, "**Basic Concepts of X–Ray Diffraction**." John Wiley & Sons, 2014, pp. 155–160. 70, 71, 72

[175] M. Birkholz, "**Thin Film Analysis by X–Ray Scattering**." John Wiley & Sons, 2006, pp. 1–5. 71, 72

[176] M. Ermrich and D. Opper, "**XRD for the Analyst: Getting Acquainted with the Principles**," in *XRD Powder Diffraction*, 2013. [Online]. Available: https://imf.ucmerced.edu/sites/imf.ucmerced.edu/files/page/documents/x-ray_powder_diffraction.pdf 71, 72

[177] M. Gonon, "**Case Studies in the X–Ray Diffraction of Ceramics**," in *Encyclopedia of Materials: Technical Ceramics and Glasses*, M. Pomeroy, Ed. Elsevier, 2021, pp. 560–577. [Online]. Available: https://doi.org/10.1016/B978-0-12-818542-1.00005-9 71, 72

[178] T. A. Saleh, "**Chapter 8 – Surface and Morphological Characterization of Hybrid Materials**," in *Polymer Hybrid Materials and Nanocomposites*, T. A. Saleh, Ed. William Andrew Publishing, 2021, pp. 241–283. [Online]. Available: https://doi.org/10.1016/B978-0-12-813294-4.00003-0 71, 72

[179] Encyclopaedia Britannica, "**Bragg Law**," Matter & Energy, Retrieved June 1, 2022. [Online]. Available: https://www.britannica.com/science/Bragg-law 71, 72

[180] Izasa Scientific, "**Laser Diffraction**," Particle Technology and Molecular Interaction, 2022, Retrieved June 1, 2022. [Online]. Available: https://www.izasascientific.com/pt-pt/tecnicas/tecnicas/tecnologia-de-particulas-e-interacoes-moleculares/tecnologia-de-particulas/difracao-laser 74

[181] Malvern Panalytical, "**Laser Diffraction (LD)**," Particle Size Distributions from Nanometers to Millimeters, 2022, retrieved June 1, 2022. [Online]. Available: https://www.malvernpanalytical.com/en/products/technology/light-scattering/laser-diffraction 74

[182] Anton Paar, "**Laser Diffraction for Particle Sizing**," Anton Paar Wiki, (n.d.), retrieved June 1, 2022. [Online]. Available: https://wiki.anton-paar.com/uk-en/laser-diffraction-for-particle-sizing/ 74

[183] S. Nimesh, "**3 – Tools and Techniques for Physico-Chemical Characterization of Nanoparticles**," in *Gene Therapy*, S. Nimesh, Ed. Woodhead Publishing, 2013, pp. 43–63. [Online]. Available: https://www.sciencedirect.com/science/article/pii/B9781907568404500038 74

[184] Particle Technology Labs, "**Laser Diffraction**," Particle Size Distribution, Testing, (n.d.), Retrieved June 1, 2022. [Online]. Available: https://particletechlabs.com/analytical-testing/particle-size-distribution-analyses/laser-diffraction 74

[185] K. Pye and S. J. Blott, "**Particle Size Analysis of Sediments, Soils and Related Particulate Materials for Forensic Purposes Using Laser Granulometry**," *Forensic Science International*, vol. 144, no. 1, pp. 19–27, 2004. [Online]. Available: https://doi.org/10.1016/j.forsciint.2004.02.028 75

[186] L. F. Francis, "**Chapter 5 – Powder Processes**," in *Materials Processing*, L. F. Francis, Ed. Boston: Academic Press, 2016, pp. 343–414. [Online]. Available: https://doi.org/10.1016/B978-0-12-385132-1.00005-7 75

[187] D. Kopeliovich, "**Materials Engineering**," Graphite Manufacturing Process, SubsTech Substances & Technologies, 2020, Retrieved June 4, 2022. [Online]. Available: http://www.substech.com/dokuwiki/doku.php?id=graphite_manufacturing_process 76

[188] Colorado State University, "**Mass Transfer**," Introduction to Chemical and Biological Engineering, 2021, Retrieved June 4, 2022. [Online]. Available: https://www.engr.colostate.edu/CBE101/topics/mass_transfer.html 76

[189] J. S. Moya, C. Baudín, and P. Miranzo, "**Sintering**," in *Encyclopedia of Physical Science and Technology*, R. A. Meyers, Ed. Academic Press, 2003, pp. 865–878. [Online]. Available: https://doi.org/10.1016/B0-12-227410-5/00694-3 76

[190] Breviary Technical Ceramics, "**From Forming to Firing**," Think Ceramic Technische Keramik, 2004, Retrieved June 4, 2022. [Online]. Available: http://www.keramverband.de/brevier_engl/4/1/4_1_4.htm#:~:text=Through%20reactions%20that%20occur%20during,this%20is%20called%20sintering%20shrinkage. 77

[191] ***Standard Test Methods for Apparent Porosity, Water Absorption, Apparent Specific Gravity, and Bulk Density of Burned Refractory Brick and Shapes by Boiling Water***. ASTM International, 2005. [Online]. Available: https://doi.org/10.1520/C0020-00R22 79

[192] ***Standard Test Method for Dynamic Young's Modulus, Shear Modulus, and Poisson's Ratio for Advanced Ceramics by Sonic Resonance***. ASTM International, 2020. [Online]. Available: https://10.1520/C1198-20 81

[193] A. P. Silva, F. Booth, L. Garrido, E. Aglietti, P. Pena, and C. Baudín, "**Young's Modulus and Hardness of Multiphase $CaZrO_3$−MgO Ceramics by Micro and Nanoindentation**," *Journal of the European Ceramic Society*, vol. 38, no. 4, pp. 2194–2201, 2018. [Online]. Available: https://doi.org/10.1016/j.jeurceramsoc.2017.11.007 82, 130

[194] M. Bauccio, "**ASM Engineering Materials Reference Book**," in *Technology & Engineering*, 2nd ed. CRC Press, 1994. 82, 130

[195] ***Standard Test Method for Flexural Strength of Advanced Ceramics at Ambient Temperature***. ASTM International, 2018. [Online]. Available: https://doi.org/10.1520/C1161-18 84

[196] ***Standard Test Method for Vickers Indentation Hardness of Advanced Ceramics***. ASTM International, 2018. [Online]. Available: https://doi.org/10.1520/C1327-15R19 87

[197] G. R. Anstis, P. Chantikul, B. R. Lawn, and D. B. Marshall, "**A Critical Evaluation of Indentation Techniques for Measuring Fracture Toughness: I, Direct Crack Measurements**," *Journal of the American Ceramic Society*, vol. 64, no. 9, pp. 533–538, 1981. 88

[198] K. Akhtar, S. A. Khan, S. B. Khan, and A. M. Asiri, "**Scanning Electron Microscopy: Principle and Applications in Nanomaterials Characterization**," in *Handbook of Materials Characterization*, S. K. Sharma, Ed. Springer International Publishing, 2018, pp. 113–145. [Online]. Available: https://doi.org/10.1007/978-3-319-92955-2_4 89

[199] First Faculty of Medicine, Charles University, "**Resolution of Human Eye**," WikiLectures, Project of the First Faculty of Medicine, Charles University, 2017, retrieved June 5, 2022. [Online]. Available: https://www.wikilectures.eu/w/Resolution_of_human_eye 89

[200] B. R. Masters, "**Optical Resolution and Resolving Power: What It Is, How to Measure It, and What Limits It**," in *Confocal Microscopy and Multiphoton Excitation Eicroscopy: The Genesis of Live Cell Imaging*. SPIE Press, 2006, p. Abstract. [Online]. Available: https://doi.org/10.1117/3.660403.ch4 89

[201] Thermo Fisher Scientific, "**The Difference Between SEM and Optical Microscopes**," Scanning Electron Microscopy, Optical Microscopy, (n.d.), Retrieved June 5, 2022. [Online]. Available: https://www.thermofisher.com/pt/en/home/materials-science/learning-center/applications/sem-optical-microscopes-difference.html 90

[202] Medical Device Testing Services Incorporated, "**Optical Microscopy vs. Scanning Electron Microscopy: How Scanning Electron Microscopy Can**

Take Your Medical Device Inspections to the Next Level," Medical Device Testing Services Incorporated, (n.d.). [Online]. Available: https://devicetesting.com/pdfFiles/Benefits%20of%20SEM%20and%20Optical%20Microscopy.pdf 90

[203] Thermo Fisher Scientific, "**Principles of Scanning Electron Microscopy**," Scanning Electron Microscopy, Principles of Scanning Electron Microscopy, (n.d.), Retrieved June 5, 2022. [Online]. Available: https://www.thermofisher.com/pt/en/home/materials-science/learning-center/applications/scanning-electron-microscope-sem-electron-column.html#:~:text=Contact%20us-,Scanning%20electron%20microscopy%20principles,beam%20in%20the%20electron%20source. 90

[204] W. Zhou, R. Apkarian, Z. L. Wang, and D. Joy, "**Fundamentals of Scanning Electron Microscopy (SEM)**," in *Scanning Microscopy for Nanotechnology: Techniques and Applications*, W. Zhou and Z. L. Wang, Eds. Springer, 2007, pp. 1–40. [Online]. Available: https://doi.org/10.1007/978-0-387-39620-0_1 90

[205] B. Inkson, "**2 – Scanning Electron Microscopy (SEM) and Transmission Electron Microscopy (TEM) for Materials Characterization**," in *Materials Characterization Using Nondestructive Evaluation (NDE) Methods*, G. Hübschen, I. Altpeter, R. Tschuncky, and H. G. Herrmann, Eds. Woodhead Publishing, 2016, pp. 17–43. [Online]. Available: https://www.sciencedirect.com/science/article/pii/B978008100040300002X 91

[206] G. Höflinger, "**Brief Introduction to Coating Technology for Electron Microscopy**," Leica Microsystems, 2013, Retrieved June 5, 2021. [Online]. Available: https://www.leica-microsystems.com/science-lab/brief-introduction-to-coating-technology-for-electron-microscopy/ 92

[207] Shimadzu, "**Fundamentals of Thermal Analysis**," Technical Support, (n.d.), Retrieved June 14, 2021. [Online]. Available: https://www.shimadzu.com/an/service-support/technical-support/analysis-basics/fundament_thermal/1/index.html 93

[208] T. Lever, P. Haines, J. Rouquerol, E. Charsley, P. Eckeren, and D. Burlett, "**ICTAC Nomenclature of Thermal Analysis (IUPAC Recommendations 2014)**," *Pure and Applied Chemistry*, vol. 86, no. 4, pp. 545–553, 2014. [Online]. Available: https://doi.org/10.1515/pac-2012-0609 93, 98

[209] M. S. H. Akash and K. Rehman, "**Introduction to Thermal Analysis**," in *Essentials of Pharmaceutical Analysis*, M. S. H. Akash and K. Rehman, Eds. Springer, 2020, pp. 195–198. [Online]. Available: https://doi.org/10.1007/978-981-15-1547-7_16 93

[210] ***Standard Test Method for Thermal Diffusivity by the Flash Method***. ASTM International, 2013. [Online]. Available: https://doi.org/10.1520/E1461-13R22 93, 94, 95

[211] D. Ratna, "**3 – Thermal Properties of Thermosets**," in *Thermosets*, Q. Guo, Ed. Woodhead Publishing, 2012, pp. 62–91. [Online]. Available: https://doi.org/10.1533/9780857097637.1.62 93, 145

[212] A. Salazar, "**On Thermal Diffusivity**," *European Journal of Physics*, vol. 24, p. 351, 2003. [Online]. Available: https://doi.org/10.1088/0143-0807/24/4/353 94, 147

[213] NETZSCH, "**Thermal Diffusivity and Thermal Conductivity: Method Techniques and Applications**," in *Laser Flash Apparatus LFA 457 MicroFlash*. NETZSCH Analyzing & Testing, (n.d.). [Online]. Available: https://analyzing-testing.netzsch.com/_Resources/Persistent/3/5/4/3/354397eabf4de16f634a19ef016d4ffc3870aedc/LFA_457_MicroFlash_en_web_01.pdf 94, 95

[214] W. J. Parker, R. J. Jenkins, C. P. Butler, and G. L. Abbott, "**Flash Method of Determining Thermal Diffusivity, Heat capacity, and Thermal Conductivity**," *Journal of Applied Physics*, vol. 32, no. 9, pp. 1679–1684, 1961. [Online]. Available: https://doi.org/10.1063/1.1728417 94

[215] NETZSCH, "**Determination of the Specific Heat by Means of LFA**." NETZSCH Thermal Academy, 2020. [Online]. Available: https://academy.netzsch.com/ 97

[216] PerkinElmer, "**Thermomechanical Analysis: A Beginners Guide to TMA 4000**," in *Thermomechanical Analysis*. PerkinElmer Inc., 2013. [Online]. Available: https://resources.perkinelmer.com/lab-solutions/resources/docs/FAQ_TMA_4000.pdf 97, 98

[217] J. James, "**Thermomechanical Analysis and Its Applications**," *Thermal and Rheological Measurement Techniques for Nanomaterials Characterization*, pp. 159–171, 2017. [Online]. Available: https://www.sciencedirect.com/science/article/pii/B9780323461399000074 97, 98

[218] ***Standard Test Method for Linear Thermal Expansion of Solid Materials by Thermomechanical Analysis***. ASTM International, 2019. [Online]. Available: https://doi.org/10.1520/E0831-06 98, 99

[219] NETZSCH, "**Thermomechanical Analysis – TMA: Method, Technique and Applications**," in *TMA 402 F1/F3 Hyperion*. NETZSCH Analyzing & Testing, (n.d.). [Online]. Available: https://paralab.pt/wp-content/uploads/2019/09/TMA_402_F1_F3_Hyperion_en_web.pdf 99

[220] J. R. Roth and X. Dai, "**Optimization of the Aerodynamic Plasma Actuator as an Electrohydrodynamic (EHD) Electrical Device**," *44th AIAA Aerospace Sciences Meeting and Exhibit*, p. 1203, 2006. [Online]. Available: https://doi.org/10.2514/6.2006-1203 101

[221] M. Forte, J. Jolibois, J. Pons, E. Moreau, G. Touchard, and M. Cazalens, "**Optimization of a Dielectric Barrier Discharge Actuator by Stationary and Non-Stationary Measurements of the Induced Flow Velocity: Application to Airflow Control**," *Experiments in Fluids*, vol. 43, no. 6, pp. 917–928, 2007. [Online]. Available: https://doi.org/10.1007/s00348-007-0362-7 101

[222] A. R. H. Rigit, K. C. Lai, and D. B. L. Bong, "**Degradation of a Dielectric Barrier Discharge Plasma Actuator**," *IEEE 9th International Conference on the Properties and Applications of Dielectric Materials*, pp. 569–572, 2009. [Online]. Available: https://doi.org/10.1109/ICPADM.2009.5252365 101

[223] D. Ashpis, M. Laun, and E. Griebeler, "**Progress Toward Accurate Measurements of Power Consumption of DBD Plasma Actuators**," *50th AIAA Aerospace Sciences Meeting Including the New Horizons Forum and Aerospace Exposition*, p. 823, 2012. [Online]. Available: https://doi.org/10.2514/6.2012-823 102, 156, 159

[224] F. Rodrigues, A. Mushyam, J. Pascoa, and M. Trancossi, "**A New Plasma Actuator Configuration for Improved Efficiency: the Stair-Shaped Dielectric Barrier Discharge Actuator**," *Journal of Physics D: Applied Physics*, vol. 52, no. 38, p. 385201, 2019. [Online]. Available: https://doi.org/10.1088/1361-6463/ab2584 102, 106

[225] M. Abdollahzadeh, F. Rodrigues, J. Nunes-Pereira, J. Pascoa, and L. Pires, "**Parametric Optimization of Surface Dielectric Barrier Discharge Actuators for Ice Sensing Application**," *Sensors and Actuators A: Physical*, vol. 335, p. 113391, 2022. [Online]. Available: https://doi.org/10.1016/j.sna.2022.113391 104

[226] J. Kriegseis, B. Möller, S. Grundmann, and C. Tropea, "**Capacitance and Power Consumption Quantification of Dielectric Barrier Discharge (DBD) Plasma Actuators**," *Journal of Electrostatics*, vol. 69, no. 4, pp. 302–312, 2011. [Online]. Available: https://doi.org/10.1016/j.elstat.2011.04.007 106

[227] K. Somton, K. Dateraksa, P. Laoratanakul, and R. McCuiston, "**Shrinkage and Properties of Die Pressed Alumina Produced from Different Granule Sources**," *AIP Conference Proceedings, AIP Publishing LLC*, vol. 2279, no. 1, p. 060003, 2020. [Online]. Available: https://doi.org/10.1063/5.0023313 118, 120

[228] I. Ropuš, L. Ćurković, V. Mandić, K. M. Musfata, and I. Gabelica, "**Conventional and Non–Conventional Sintering Techniques of High Purity Alumina**

Ceramics," *Tehnički Vjesnik*, vol. 28, no. 5, pp. 1526–1531, 2021. [Online]. Available: https://doi.org/10.17559/TV-20200825223809 120, 121

[229] A. Shui, N. Uchida, and K. Uematsu, "**Origin of Shrinkage Anisotropy During Sintering for Uniaxially Pressed Alumina Compacts**," *Powder Technology*, vol. 127, no. 1, pp. 9–18, 2002. [Online]. Available: https://doi.org/10.1016/S0032-5910(02)00004-9 120, 121

[230] J. Szczerba, Z. Pdzich, and D. Madej, "**Synthesis of Spinel – Calcium Zirconate Mterials**," *Materiały Ceramiczne*, vol. 63, pp. 27–33, 2011. [Online]. Available: https://www.infona.pl/resource/bwmeta1.element.baztech-article-AGH1-0028-0013 120, 121

[231] L. F. Hu and C. A. Wang, "**Effect of Sintering Temperature on Compressive Strength of Porous Yttria–Stabilized Zirconia Ceramics**," *Ceramics International*, vol. 36, no. 5, pp. 1697–1701, 2010. [Online]. Available: https://doi.org/10.1016/j.ceramint.2010.03.009 120, 121, 122

[232] W. B. Zhao, G. J. Zhang, Y. Yang, and Z. Yan, "**Correlation Between Trapping Parameters and Surface Insulation Strength of Solid Dielectric Under Pulse Voltage in Vacuum**," *IEEE Transactions on Dielectrics and Electrical Insulation*, vol. 14, no. 1, pp. 170–178, 2007. [Online]. Available: https://doi.org/10.1109/TDEI.2007.302885 126

[233] F. Ren, E. Case, A. Morrison, M. Tafesse, and M. Baumann, "**Resonant Ultrasound Spectroscopy Measurement of Young's Modulus, Shear Modulus and Poisson's Ratio as a Function of Porosity for Alumina and Hydroxyapatite**," *Philosophical Magazine*, vol. 89, no. 14, pp. 1163–1182, 2009. [Online]. Available: https://doi.org/10.1080/14786430902915388 129

[234] R. W. Rice, "**The Porosity Dependence of Physical Properties of Materials: A Summary Review**," *Key Engineering Materials*, vol. 115, pp. 1–20, 1996. 129, 130

[235] A. Boccaccini and Z. Fan, "**A New Approach for the Young's Modulus-Porosity Correlation of Ceramic Materials**," *Ceramics International*, vol. 23, no. 3, pp. 239–245, 1997. [Online]. Available: https://doi.org/10.1016/S0272-8842(96)00033-8 129

[236] W. Pabst, E. Gregorová, and G. Tichá, "**Elasticity of Porous Ceramics -— A Critical Study of Modulus–Porosity Relations**," *Journal of the European Ceramic Society*, vol. 26, no. 7, pp. 1085–1097, 2006. [Online]. Available: https://doi.org/10.1016/j.jeurceramsoc.2005.01.041 129

[237] K. Phani and D. Sanyal, "**The Relations Between the Shear Modulus, the Bulk Modulus and Young's Modulus for Porous Isotropic Ceramic**

Materials," *Materials Science and Engineering: A*, vol. 490, no. 1, pp. 305–312, 2008. [Online]. Available: https://doi.org/10.1016/j.msea.2008.01.030 130, 132

[238] E. Bruschini, S. Speziale, G. B. Andreozzi, F. Bosi, and U. Hålenius, "**The Elasticity of $MgAl_2O_4$–$MnAl_2O_4$ spinels by Brillouin Scattering and an Empirical Approach for Bulk Modulus Prediction**," *American Mineralogist*, vol. 100, no. 2-3, pp. 644–651, 2015. [Online]. Available: https://doi.org/10.2138/am-2015-4993 130

[239] A. Kushwaha, "**Vibrational and elastic properties of aluminate spinel $MgAl_2O_4$**," *Physica B: Condensed Matter*, vol. 405, no. 13, pp. 2795–2798, 2010. [Online]. Available: https://doi.org/10.1016/j.physb.2010.03.068 130

[240] O. Burgos-Montes, R. Moreno, and C. Baudín, "**Effect of Mullite Additions on the Fracture Mode of Alumina**," *Journal of the European Ceramic Society*, vol. 30, no. 4, pp. 857–863, 2010. [Online]. Available: https://doi.org/10.1016/j.jeurceramsoc.2009.10.013 130

[241] P. M. Carneiro, P. V. Gamboa, C. Baudín, and A. P. Silva, "**Modelling of Elastic Modulus of a Biphasic Ceramic Microstructure Using 3D Representative Volume Elements**," *Journal of the European Ceramic Society*, vol. 40, no. 3, pp. 901–910, 2020. [Online]. Available: https://doi.org/10.1016/j.jeurceramsoc.2019.10.046 130, 149

[242] Z. Hou, "***Ab Initio* Calculations of Elastic Modulus and Electronic Structures of Cubic $CaZrO_3$**," *Physica B: Condensed Matter*, vol. 403, no. 17, pp. 2624–2628, 2008. [Online]. Available: https://www.sciencedirect.com/science/article/pii/S0921452608000446 130, 153

[243] TOSOH Corporation, "**Zirconia**," Zirconia Brochure, (n.d), Retrieved August 28, 2022. [Online]. Available: https://www.rbhltd.com/wp-content/uploads/2019/05/Tosoh-Zirconia-Brochure.pdf 130, 135, 140, 141

[244] L. Jin, Q. Yu, A. Rauf, and C. Zhou, "**Elastic, Electronic and Thermal Properties of YSZ from First Principles**," *Solid State Sciences*, vol. 14, no. 1, pp. 106–110, 2012. [Online]. Available: https://doi.org/10.1016/j.solidstatesciences.2011.11.003 130

[245] R. W. Rice and M. Dekker, "**Porosity of Ceramics**," A. R. Boccaccini, Ed. Materials Science and Engineering: A, 2000, vol. 280, no. 2, pp. 358–359. [Online]. Available: https://doi.org/10.1016/S0921-5093(99)00696-6 131

[246] P. Auerkari, "**Mechanical and Physical Properties of Engineering Alumina Ceramics. VTT Manufacturing Technology**," Ph.D. dissertation, ESPOO: Technical Research Centre of Finland, 1996. [Online]. Available: https:

//www.vttresearch.com/sites/default/files/pdf/tiedotteet/1996/T1792.pdf 131, 134, 141, 153

[247] M. Asmani, C. Kermel, A. Leriche, and M. Ourak, "**Influence of Porosity on Young's Modulus and Poisson's Ratio in Alumina Ceramics**," *Journal of the European Ceramic Society*, vol. 21, no. 8, pp. 1081–1086, 2001. [Online]. Available: https://doi.org/10.1016/S0955-2219(00)00314-9 131

[248] M. R. G, "**Evaluated Material Properties for a Sintered α-Alumina**," *Journal of the American Ceramic Society*, vol. 80, no. 8, pp. 1919–1928, 1997. [Online]. Available: https://doi.org/10.1111/j.1151-2916.1997.tb03074.x 132, 138, 139, 140, 153

[249] S. White, V. Miklus, E. McLaren, L. Lang, and A. Caputo, "**Flexural Strength of a Layered Zirconia and Porcelain Dental All–Ceramic System**," *The Journal of Prosthetic Dentistry*, vol. 94, no. 2, pp. 125–131, 2005. [Online]. Available: https://doi.org/10.1016/j.prosdent.2005.05.007 133, 135

[250] R. B. Heimann, "**Classic and Advanced Ceramics: From Fundamentals to Applications**." Wiley & Sons, 2010, p. 176. 134, 141, 149

[251] STC Material Solutions, "**High Purity Alumina (99.5%, 99.8%, 99.96%)**," Caramic Materials Solutions, (n.d), Retrieved August 28, 2022. [Online]. Available: https://precision-ceramics.com/materials/comparison/ 134, 139, 149

[252] A. R. S. Cabral, "**Melhoria da Resistência Mecânica do Compósito Cerâmico $CaZrO_3$–MgO com a Adição de 3YSZ e 8YSZ**," Master's dissertation, Universidade da Beira Interior, Covilhã, Portugal, 2021. 134, 141

[253] J. Mamede, D. F. Macedo, A. Maceiras, and A. P. Silva, "**Reinforcement of the Ceramic Matrix of CaO–ZrO_2–MgO with Al_2O_3 Coarse Particles**," *Ceramics*, vol. 5, no. 1, pp. 148–160, 2022. [Online]. Available: https://doi.org/10.3390/ceramics5010013 134, 140

[254] J. F. Lang, J. G. You, X. F. Zhang, X. D. Luo, and S. Y. Zheng, "**Effect of MgO on Thermal Shock Resistance of $CaZrO_3$ Ceramic**," *Ceramics International*, vol. 44, no. 18, pp. 22 176–22 180, 2018. [Online]. Available: https://doi.org/10.1016/j.ceramint.2018.08.333 134

[255] R. B. Heimann, "**Classic and Advanced Ceramics: From Fundamentals to Applications**." Wiley & Sons, 2010, p. 361. 135

[256] J. E. V. Amarante, M. V. S. Pereira, G. M. de Souza, M. F. R. Pais Alves, B. G. Simba, and C. dos Santos, "**Roughness and Its Effects on Flexural Strength of Dental Yttria–Stabilized Zirconia Ceramics**," *Materials Science and Engineering: A*, vol. 739, pp. 149–157, 2019. [Online]. Available: https://doi.org/10.1016/j.msea.2018.10.027 135

[257] E. P. Butler, "**Transformation–Toughened Zirconia Ceramics**," *Materials Science and Technology*, vol. 1, no. 6, pp. 417–432, 1985. [Online]. Available: https://doi.org/10.1179/mst.1985.1.6.417 135

[258] D. Singh and D. K. Shetty, "**Fracture Toughness of Polycrystalline Ceramics in Combined Mode I and Mode II Loading**," *Journal of the American Ceramic Society*, vol. 72, no. 1, pp. 78–84, 1989. [Online]. Available: https://doi.org/10.1111/j.1151-2916.1989.tb05957.x 136

[259] M. Aliha and M. Ayatollahi, "**Analysis of Fracture Initiation Angle in Some Cracked Ceramics Using the Generalized Maximum Tangential Stress Criterion**," *International Journal of Solids and Structures*, vol. 49, no. 13, pp. 1877–1883, 2012. [Online]. Available: https://doi.org/10.1016/j.ijsolstr.2012.03.029 136

[260] X. Teng, H. Liu, and C. Huang, "**Effect of Al_2O_3 Particle Size on the Mechanical Properties of Alumina–Based Ceramics**," *Materials Science and Engineering: A*, vol. 452-453, pp. 545–551, 2007. [Online]. Available: https://doi.org/10.1016/j.msea.2006.10.073 139

[261] C. Piconi and G. Maccauro, "**Zirconia as a Ceramic Biomaterial**," *Biomaterials*, vol. 20, no. 1, pp. 1–25, 1999. [Online]. Available: https://doi.org/10.1016/S0142-9612(98)00010-6 139

[262] Precision Ceramics USA, "**Ceramic Materials Comparison**," Ceramic Materia Comparison Chart, (n.d), Retrieved August 28, 2022. [Online]. Available: https://precision-ceramics.com/materials/comparison/ 139, 140, 149, 150

[263] KYOCERA, "**Extreme Hardness Surpassing that of Metals**," Fine Ceramic World, (n.d), Retrieved August 28, 2022. [Online]. Available: https://global.kyocera.com/fcworld/charact/strong/hardness.html 139, 140, 149

[264] J. Nunes-Pereira, P. M. Carneiro, A. Maceiras, C. Baudín, and A. P. Silva, "**Modelling of Elastic Modulus of $CaZrO_3$–MgO Composites Using Isotropic Elastic and Anisotropic Models**," *Journal of the European Ceramic Society*, vol. 40, no. 15, pp. 5882–5890, 2020. [Online]. Available: https://doi.org/10.1016/j.jeurceramsoc.2020.05.050 139, 141

[265] F. Ternero, L. G. Rosa, P. Urban, J. M. Montes, and F. G. Cuevas, "**Influence of the Total Porosity on the Properties of Sintered Materials — - A Review**," *Metals*, vol. 11, no. 5, 2021. [Online]. Available: https://doi.org/10.3390/met11050730 139

[266] S. Rhee, "**Porosity-—Thermal Conductivity Correlations for Ceramic Materials**," *Materials Science and Engineering*, vol. 20, pp. 89–93, 1975. [Online]. Available: https://doi.org/10.1016/0025-5416(75)90134-2 149

[267] J. Sun, Z. Hu, J. Zhuo, X. Wang, and C. Sun, "**Thermal Properties of Highly Porous Fibrous Ceramics**," *5th International Conference on Porous Media and Their Applications in Science, Engineering and Industry*, 2014. [Online]. Available: https://dc.engconfintl.org/cgi/viewcontent.cgi?article=1002&context=porous_media_V 149

[268] Z. Živcová, E. Gregorová, W. Pabst, D. S. Smith, A. Michot, and C. Poulier, "**Thermal Conductivity of Porous Alumina Ceramics Prepared Using Starch as a Pore-Forming Agent**," *Journal of the European Ceramic Society*, vol. 29, no. 3, pp. 347–353, 2009. [Online]. Available: https://www.sciencedirect.com/science/article/pii/S0955221908003233 149

[269] KYOCERA, "**Thermal Conductivity Easily Transmits Heat**," Fine Ceramic World, (n.d), Retrieved September 24, 2022. [Online]. Available: https://global.kyocera.com/fcworld/charact/heat/thermalcond.html 150

[270] H. Zhao, F. Yu, T. D. Bennett, and H. N. Wadley, "**Morphology and Thermal Conductivity of Yttria–Stabilized Zirconia Coatings**," *Acta Materialia*, vol. 54, no. 19, pp. 5195–5207, 2006. [Online]. Available: https://doi.org/10.1016/j.actamat.2006.06.028 150, 180

[271] K. Schlichting, N. Padture, and P. Klemens, "**Thermal Conductivity of Dense and Porous Yttria–Stabilized Zirconia**," *Journal of Materials Science*, vol. 36, no. 12, pp. 3003–3010, 2001. [Online]. Available: https://link.springer.com/content/pdf/10.1023/A:1017970924312.pdf 150

[272] S. Ghabezloo, "**Effect of Porosity on the Thermal Expansion Coefficient of Porous Materials**," *Poromechanics V*, pp. 1857–1866, 2013. [Online]. Available: https://doi.org/10.1061/9780784412992.220 153

[273] Ghabezloo S., "**Effect of Porosity on the Thermal Expansion Coefficient: A discussion of the paper 'Effects of mineral admixtures on the thermal expansion properties of hardened cement paste' by Z.H. Shui, R. Zhang, W. Chen, D. Xuan, Constr. Build. Mater. 24 (9) (2010) 1761–1767**," *Construction and Building Materials*, vol. 24, no. 9, pp. 1796–1798, 2010. [Online]. Available: https://www.sciencedirect.com/science/article/pii/S095006181000098X 153

[274] S. Schafföner, C. G. Aneziris, H. Berek, J. Hubálková, and A. Priese, "**Fused Calcium Zirconate for Refractory Applications**," *Journal of the European Ceramic Society*, vol. 33, no. 15, pp. 3411–3418, 2013. [Online]. Available: https://www.sciencedirect.com/science/article/pii/S0955221913003385 153

[275] S. Schafföner, J. Fruhstorfer, C. Faßauer, L. Freitag, C. Jahn, and C. G. Aneziris, "**Influence of In Situ Phase Formation on Properties of**

Calcium Zirconate Refractories," *Journal of the European Ceramic Society*, vol. 37, no. 1, pp. 305–313, 2017. [Online]. Available: https://doi.org/10.1016/j.jeurceramsoc.2016.08.017 153

[276] F. Booth, L. Garrido, E. Aglietti, A. Silva, P. Pena, and C. Baudín, "**$CaZrO_3$–MgO Structural Ceramics Obtained by Reaction Sintering of Dolomite–Zirconia Mixtures**," *Journal of the European Ceramic Society*, vol. 36, no. 10, pp. 2611–2626, 2016. [Online]. Available: https://doi.org/10.1016/j.jeurceramsoc.2016.03.027 153

[277] Nishimura Advanced Ceramics, "**Compare by Thermal Expansion Coefficient**," Compare Material Properties, 2021, Retrieved September 24, 2022. [Online]. Available: https://nishimuraac.com/propertie/compare-by-thermal-expansion-coefficient 154

[278] STC Material Solutions, "**Yttria Stabilized Zirconia (YTZP)**," Caramic Materials Solutions, (n.d), Retrieved September 24, 2022. [Online]. Available: https://www.ceramics.net/ceramic-materials-solutions/zirconias/ytzp 154

[279] N. D. Wilde, H. Xu, N. Gomez Vega, and S. R. H. Barrett, "**A Model of Surface Dielectric Barrier Discharge Power**," *Applied Physics Letters*, vol. 118, no. 15, p. 154102, 2021. [Online]. Available: https://doi.org/10.1063/5.0043339 159

[280] R. Talviste, I. Jõgi, T. Tätte, M. Part, J. Raud, and P. Paris, "**Application of Y–ZrO_2 Microtubes as Dielectric Barrier Material in a He Atmospheric Pressure Micro-Plasma Jet**," *SN Applied Sciences*, vol. 3, no. 2, pp. 1–9, 2021. [Online]. Available: https://doi.org/10.1007/s42452-020-03981-8 160

[281] I. Biganzoli, R. Barni, A. Gurioli, R. Pertile, and C. Riccardi, "**Experimental Investigation of Lissajous Figure Shapes in Planar and Surface Dielectric Barrier Discharges**," *Journal of Physics: Conference Series*, vol. 550, no. 1, p. 012039, 2014. [Online]. Available: https://doi.org/10.1088/1742-6596/550/1/012039 160

[282] M. Taheraslani and H. Gardeniers, "**Coupling of CH_4 to C_2 Hydrocarbons in a Packed Bed DBD Plasma Reactor: The Effect of Dielectric Constant and Porosity of the Packing**," *Energies*, vol. 13, no. 2, 2020. [Online]. Available: https://doi.org/10.3390/en13020468 163

[283] J. Nunes-Pereira, F. F. Rodrigues, M. Abdollahzadehsangroudi, J. C. Páscoa, and S. Lanceros-Mendez, "**Improved Performance of Polyimide Cirlex-Based Dielectric Barrier Discharge Plasma Actuators for Flow Control**," *Polymers for Advanced Technologies*, vol. 33, no. 4, pp. 1278–1290, 2022. [Online]. Available: https://doi.org/10.1002/pat.5600 165, 171, 175

[284] F. Peeters and M. Van de Sanden, "**The Influence of Partial Surface Discharging on the Electrical Characterization of DBDs**," *Plasma Sources Science and Technology*, vol. 24, no. 1, p. 015016, 2014. [Online]. Available: https://doi.org/10.1088/0963-0252/24/1/015016 171

[285] J. Pons, E. Moreau, and G. Touchard, "**Asymmetric Surface Dielectric Barrier Discharge in air at Atmospheric Pressure: Electrical Properties and Induced Airflow Characteristics**," *Journal of Physics D: Applied Physics*, vol. 38, no. 19, p. 3635, 2005. [Online]. Available: https://doi.org/10.1088/0022-3727/38/19/012 171

[286] M. Lanagan, J. Yamamoto, A. Bhalla, and S. Sankar, "**The Dielectric Properties of Yttria–Stabilized Zirconia**," *Materials Letters*, vol. 7, no. 12, pp. 437–440, 1989. [Online]. Available: https://doi.org/10.1016/0167-577X(89)90047-5 180

[287] H. Hayashi, T. Saitou, N. Maruyama, H. Inaba, K. Kawamura, and M. Mori, "**Thermal Expansion Coefficient of Yttria Stabilized Zirconia for Various Yttria Contents**," *Solid State Ionics*, vol. 176, no. 5, pp. 613–619, 2005. [Online]. Available: https://doi.org/10.1016/j.ssi.2004.08.021 180

[288] J. Molina-Reyes, H. Tiznado, G. Soto, M. Vargas-Bautista, D. Dominguez, E. Murillo, D. Sweeney, and J. Read, "**Physical and Electrical Characterization of Yttrium–Stabilized Zirconia (YSZ) Thin Films Deposited by Sputtering and Atomic–Layer Deposition**," *Journal of Materials Science: Materials in Electronics*, vol. 29, no. 18, pp. 15 349–15 357, 2018. [Online]. Available: https://doi.org/10.1007/s10854-018-8909-3 180

[289] H. Charalambous, S. K. Jha, K. Vikrant, R. E. García, X. L. Phuah, H. Wang, H. Wang, A. Mukherjee, and T. Tsakalakos, "**Electric Field–Induced Grain Boundary Degradation Mechanism in Yttria Stabilized Zirconia**," *Scripta Materialia*, vol. 204, p. 114130, 2021. [Online]. Available: https://doi.org/10.1016/j.scriptamat.2021.114130 180, 181

[290] A. Alvarez, Y. Dong, and I.-W. Chen, "**DC Electrical Degradation of YSZ: Voltage-Controlled Electrical Metallization of a Fast Ion Conducting Insulator**," *Journal of the American Ceramic Society*, vol. 103, no. 5, pp. 3178–3193, 2020. [Online]. Available: https://doi.org/10.1111/jace.17004 180

[291] D. J. Green, H. R. H. J., and S. M. V., "**Transformation Toughening of Ceramics**." CRC Press, Taylor & Francis, 1989, pp. 17–41. 181

[292] A. Garamoon, D. El-Zeer, A. Abd El-Ghany, D. Ghoneem, and F. El-Hossary, "**Influences of the Barrier Types and Arrangements on Dielectric Barrier Discharge Characteristics**," *The European Physical Journal-Applied Physics*, vol. 53, no. 2, 2011. [Online]. Available: https://doi.org/10.1051/epjap/2010100196 181